Gas-Solid interactions and its influence in electronic structure evolution and heterogeneous catalysis

by

Ravi Ranjan
10CC17A26022

A thesis submitted to the
Academy of Scientific & Innovative Research
for the award of the degree of
DOCTOR OF PHILOSOPHY
in
SCIENCE

Under the supervision of
Dr. Chinnakonda S. Gopinath

CSIR-National Chemical Laboratory, Pune

Academy of Scientific and Innovative Research
AcSIR Headquarters, CSIR-HRDC campus
Sector 19, Kamla Nehru Nagar,
Ghaziabad, U.P. – 201002, India

September, 2023

Certificate

This is to certify that the work incorporated in this Ph.D. thesis entitled, "*Gas-Solid interactions and its influence in electronic structure evolution and heterogeneous catalysis*", submitted by *Ravi Ranjan* to the Academy of Scientific and Innovative Research (AcSIR), in partial fulfillment of the requirements for the award of the Degree of *Doctor of Philosophy in Science*, embodies original research work carried-out by the student. We further certify that this work has not been submitted to any other University or Institution in part or full for the award of any degree or diploma. Research material(s) obtained from other source(s) and used in this research work has/have been duly acknowledged in the thesis. Image(s), illustration(s), figure(s), table(s) etc., used in the thesis from other source(s), have also been duly cited and acknowledged.

Ravi Ranjan

(Signature of Student)

Ravi Ranjan

C.S. 25/9/23

(Signature of Supervisor)

Dr. C.S. Gopinath

STATEMENTS OF ACADEMIC INTEGRITY

I, Ravi Ranjan, a Ph.D. student of the Academy of Scientific and Innovative Research (AcSIR) with Registration No.10CC17A26022 hereby undertake that the thesis entitled *"Gas-Solid interactions and its influence in electronic structure evolution and heterogeneous catalysis*" has been prepared by me and that the document reports original work carried out by me and is free of any plagiarism in compliance with the UGC Regulations on *"Promotion of Academic Integrity and Prevention of Plagiarism in Higher Educational Institutions (2018)"* and the CSIR Guidelines for "*Ethics in Research and in Governance (2020)*".

Ravi Ranjan

Signature of the Student

Date 25/09/23

Place: Pune

It is hereby certified that the work done by the student, under my/our supervision, is plagiarism-free in accordance with the UGC Regulations on *"Promotion of Academic Integrity and Prevention of Plagiarism in Higher Educational Institutions (2018)"* and the CSIR Guidelines for "*Ethics in Research and in Governance (2020)*".

C.S. Gopinath 25/9/23

Signature of the Supervisor

Name: Dr. C.S Gopinath

Date:

Place: Pune

DECLARATION

The research work embodied in this thesis has been carried out in CSIR-National Chemical Laboratory, Pune under the supervision of Dr. Chinnakonda S. Gopinath, Catalysis and Inorganic Chemistry Division, CSIR-National Chemical Laboratory, Pune -411008. This work is original and has not been submitted in part or full, for any degree or diploma of this or any other university.

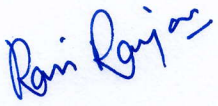

25/09/2023

Ravi Ranjan

CSIR-NCL, Pune

Catalysis and Inorganic chemistry Division,

CSIR-NCL, Pune

Dedicated to my Parents

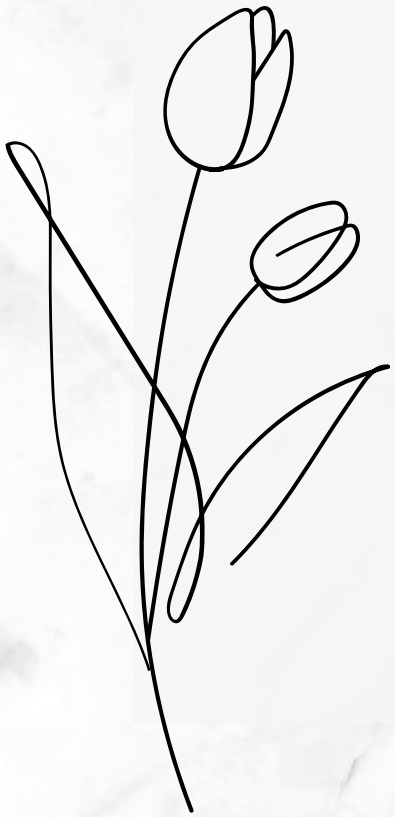

Acknowledgements

The journey embarked on the 2nd of August 2010 when I commenced my BS-MS program at IISER Mohali. At that point, the notion of pursuing a Ph.D. seemed distant and unfamiliar. Today, it marks the culmination of this extensive Ph.D. expedition. Time has elapsed so swiftly that my Ph.D. research is now nearing its conclusion; it feels like just yesterday when I sent my initial email to Dr. Chinnakonda S. Gopinath, expressing my desire to join as a Ph.D. student under his mentorship. Throughout these years, I have accumulated a wealth of knowledge and cultivated a profound understanding, all thanks to the insights and perspectives shared by those I have encountered on this journey. Numerous individuals have played pivotal roles in achieving significant life goals, particularly those related to the realization of one's most cherished aspirations. Their support, inspiration, and encouragement have been invaluable, and I wish to take this opportunity to express my heartfelt gratitude and appreciation to each of them.

Most significantly, I extend my profound gratitude to my Ph.D. supervisor, Dr. Chinnakonda S. Gopinath, for granting me the privilege to work within his research group. This would not have been possible without his unwavering support, guidance, motivation, and constructive criticism throughout my Ph.D. voyage. He has consistently offered invaluable advice and encouragement, and I have gained an immense wealth of knowledge during my tenure under his mentorship. His assistance in interpreting experimental data, coupled with his priceless insights and engaging discussions has proven to be of immense help. I am genuinely thankful for his kindness, patience, and encouragement, especially during the initial stages of my Ph.D., when I grappled with the complexities of research. His meticulous attention to detail and his logical explanations of experimental outcomes will continue to inspire me in all my future research endeavors. His profound expertise and extensive experience have laid the foundation for my research career, and without his supervision and constant guidance, this thesis would not have come to fruition. Under his mentorship, I have acquired the skills to become an independent researcher, and I wholeheartedly appreciate his continuous support and encouragement.

I would also like to extend my sincere thanks to my doctoral advisory committee members, Drs. C.P. Vinod, Suresh Bhat, Ashok Giri, and Ekambaram Balaraman, for their consistent evaluation of my work, academic discussions, and encouragement.

My heartfelt thanks go out to the current and former heads of the Catalysis and Inorganic Chemistry Division, namely Dr. Shubhangi B. Umbarkar, and Dr. Chinnakonda S.

Gopinath, and Dr. D. Srinivas, respectively, for providing all the divisional facilities essential for my research work. I am deeply appreciative of DST-India for their timely financial support and for granting me a research fellowship throughout my Ph.D. tenure. My gratitude extends to Prof. A.K. Nangia, the former director, and Dr. Ashish Lele, the current director, for their institutional support during my Ph.D. journey. I also wish to express my thanks to the Academy of Scientific and Innovative Research (AcSIR) for affording me the opportunity to achieve this significant milestone in my life.

I extend my heartfelt thanks to Dr. T. Raja and Dr. Nandini Devi for allowing me to conduct reactor studies in completing my experiments in their laboratory. I would also like to express my appreciation to Dr. Kushal Bhatte and Dr. Avishek Saha for their valuable help and support.

I am also grateful to the technical teams at Prevac, Poland and AnarghyaInnotech, Bangalore, for their assistance and support during the repair and maintenance of the NAPPES system. Their support throughout my research journey has been invaluable, and I wish to offer special recognition to Mr. Marcin Dzierzega for his consistent availability and online assistance. Additionally, I would like to convey my gratitude to all the scientific and technical staff members, including Mr. Madhu, Mr. Purushothaman, Mr. Milind, Dr. Tejas, and Mr. Dhutraj in the division, for their direct and indirect assistance on various occasions.

I want to extend my sincere thanks to senior colleagues who played a crucial role in facilitating my journey by providing training and support. I am deeply grateful to Dr. Ruchi Jain, Dr. Kasala Prabhakar Reddy, Dr. Manoj Kumar Ghosalaya, and Dr. Sadhu Kolekar for their constant guidance, valuable suggestions, and support, both professionally and personally.

I am also immensely appreciative of the remarkable community of colleagues who have also become dear friends during my Ph.D. journey at NCL, Pune. I wish to express my gratitude to all the past and current students of the CSG research group, including Dr. Kanak, Dr. Devaraj, Dr. Kshirodra Patra, Dr. Naresh (alongside Swathy mam), Dr. Ruchi, Dr. Manoj, Dr. Prabhakar, Dr. Pradnya, Dr. Sadhu, Dr. Nitin, Dr. Himanshu, Kranti, Inderjeet, Subhashree, Arindam, Nivedhitha, for fostering a fantastic working atmosphere in our laboratory. Much of my research insights stem from the discussions with those who generously shared their time. I would also like to extend my thanks to Sreeya, Athira, Akhila, Sarika, Sibo, Rahul, Hamid, Madhusudan, Nikita, Sarika, Onkar, Dr. Priyabrata, Dr. Abhaya, Dr. Ashok Patil, Dr. Pranjal Saikia, Layna, Elsa, Shinto, Nashwa, Vasundhara, Vijay, Avani, Garima, Chnimay, Sudipto, Tejas, and others who collaborated alongside me, contributing to the cheerful and cooperative

environment in the lab. Many of the concepts in catalysis and spectroscopy that I have learned were a result of group meetings and general discussions. I cherish the unforgettable lab trips and gathering outside or sir's home, made possible by our wonderful labmates and our cool supervisor, Dr. ChinnakondaS. Gopinath.

I wish to express my gratitude to all my friends within the division, including Shiva, Aakash, Gorab, Shweta, Smurudhi, Mayuri, Sheetal, Archana, Dr. Ashwathi, Eeswar, Dr. Pranjal, Dr. Prabhu, Prabhu, Nittan, Dr. Govind, Sumanta, Dr. Yogita, Dr. Sharad, Mahesh, Anuradha, Pavan, Jyotsna, Betsy, Pooja, Sanket, Dr. Gargi, Dr. Rohit, Kritika, Ajith, Kajal, Viplab, Kailash, Sonu, Dr. Shibin, Priyanka, Seema, Akshay, Rushi, Wassi, Vipul da, Jyoti T., Akshay, Deepali, Priya, Kalyani, Moshin, Subham, Lavanya, Jyoti, and Tufeil, for their invaluable assistance and support.

I'd like to offer a special thanks to my friends Pavan Dongapure, Vikas Chaturvedi, Dr. Mahendra Wagh, Dr. Anupam Tripathi, Dr. Naru, Pankaj, and Dr. Sayantan Aacharya and Late. Vipin for the countless nights of parties, outings and discussions, both scientific and political, which often turned into memorable gatherings. I owe a special debt of gratitude to Vikas, Pavan, and Sayantan for being there with unwavering support throughout my Ph.D. journey, much like brothers. Your love and encouragement were indispensable for the success of this journey. I cherish the fond memories of our unforgettable Himalayan tour with Dr. Sayantan, Pavan, Rahul, and Dr. Amit, and I am grateful for those experiences. My sincere thanks also extend to all the members of RSM-2019. Your assistance and support were vital, and organizing such a significant event in the early stages of my Ph.D. journey was truly a great experience.

I wish to express my gratitude to my friends from the NCL Cricket team, including Manish, Rohit Sr., Siddharth, Dr. Arun, Dr. Ashish, Dr. Nirshaad, Dr. Rajan, Dr. Mahendra Pawar, Shabaaz Bhai, Bharath, Ashish (NCIM), Dharmendra, Pinkabhai, Prashant Bhai, Kapil, Nitin (polymer), Prashant, Priyam, Kush, Dr. Rahul Jagtap, Sandy Bhai, Saumya, and Umasharan. Your camaraderie and joyful environment during GJPL and daily matches have been deeply appreciated.

Beyond the realm of scientific work lies a life enriched with friends, the most beautiful gift of my life in Pune. I also want to thank Jayram, Sangram, Akash, Pawan (Dr.Utpal Das), Kiran, Viksit, Geetu, Indranil, Vinita, Supriya, Monika, Monika ma'am, Subhra, Heena, Amrita, Rajni, Soumya, Smita, Aishwarya, Surya, Dr. Dipesh, Debjani, Dr. Kumar, Spurti, Jagjeevan, Dr.Priyanka Halder, Dr. Suhag, Dr. Zenoy, Ashvini, Pranali, Jayesh, Kundan,

Tripuranthaka, Mayur, Dr. Subhrashis, Sheena, Abha, Ajith and Apurva. Special thanks to Sujeet, Chotu, Subash for providing me with the best meals during my stay in Pune.

I'd like to express my gratitude to my friends from BS-MS (IISER Mohali), including Rahul, Nitin, Dr. Prashant, Dr. Piyush, Dr. Neeraj, Dr. Kuldeep, Dr. Nishant, Dr. Aaveg, Dr. Ashish, Dr. Lilit, Dr. Vikram, Dr. Akshay, Ravinder, Nishant, Ashish Thaur, Shiv Prajwal, Dr. Promit, Arul, Upakul, Nitish, Rahul Yadav, Debi bhaiya, Imran, Nitesh and Abhishek for maintaining our connection since Aug. 2010. I also want to extend my appreciation to my colleagues from IIP Dehradun and Azimpremji Foundation (Nainital), including Azeembhai, Priyanshu, Satendra, Chandrakala, Jitendra, Adarsh, Saurabh, Pramod, Neeraj, Anam, Shadab, Debarati, Sushant, and Samarpita, for their support and camaraderie.

I extend my special appreciation to my childhood friends from my hometown, including Rahul Bhardwaj, Manish, Mukesh, Pooja, Rahul Keshri, Divyam, Dheeraj, Rishu, Anant, Subhash, Ankit, Shashi, Gaurav, and Akash, for their unwavering support throughout this journey.

I want to convey my heartfelt gratitude to my father and my late mother for their limitless love and unwavering support throughout my life. I genuinely value my father's patience as we embarked on this lengthy journey together. His constant encouragement has been a steady presence in every facet of my life. I also wish to extend my appreciation to my elder sister (didi), who has consistently stood by my side, offering unwavering support through all the highs and lows. My sincere appreciation goes out to my elder brothers, Mantubhaiya and Pintubhaiya, and my sisters-in-law, Badibhabhi and Chhotibhabhi, as well as my nephews and nieces, Akshat, Shanu, Riddhi, Sarthak, and Chhota babu, for their steadfast moral support, care, and affection. Furthermore, I would like to express my gratitude to my brother-in-law for his encouragement and support over the years, as well as his enthusiasm as I approached my goal.

Thank You All

With Best Regards,

Ravi Ranjan

List of Abbreviations

NAPPES	Near Ambient Pressure Photoelectron Spectroscopy
XPS	X-ray Photoelectron Spectroscopy
UVPES/UPS	Ultra-violet Photoelectron Spectroscopy
NAPUPS/NAP-UPS	Near Ambient Pressure Ultraviolet Photoelectron Spectroscopy
UHV	Ultra High Vacuum
EEA	Electron Energy Analyzer
ELR	Electrostatic Lens Regime
FWHM	Full-width half maximum
QMS	Quadrupole Mass Spectrometer
RGA	Residual Gas Analyser/Analysis
KE	Kinetic Energy
BE	Binding Energy
RT	Room Temperature
VB	Valence Band
XRD	X-Ray Diffraction
HRTEM	High-Resolution Transmission Electron Microscopy
EDX	Energy Dispersive X ray
STEM	Scanning Tunneling Electron Microscopy
GC	Gas Chromatography
NC	Nanocube
GHSV	Gas Hourly Space Velocity

List of Symbols

ϕ	Work Function
h	Plank's Constant
E_F	Fermi Level/Energy
υ	Frequency
σ	Photoionization Cross Section
λe	Mean Free Path of Photoelectron

Table of Contents

Chapter 1

Introduction to Surface Science and Heterogeneous Catalysis

1.1 **Catalysis**

Catalysis plays a crucial role in driving efficient and sustainable chemical transformation. The fundamental principle of catalyst is explained, including the concept of catalyst, their activation energy reduction, and selectivity enhancement. Catalysis is a process that accelerates chemical reaction by lowering their activation energy, thus enabling faster reaction under milder conditions. It has extensive application in various fields, including petroleum refining, energy conversion, environmental remediation, pharmaceutical synthesis etc. The importance of catalyst and catalysis lies in promoting environmentally friendly process with minimum usage of material and energy, renewable energy, production and synthesis of valuable chemicals.

There are various types of catalysts, namely, (1) Homogeneous catalyst (2) Heterogeneous catalyst and (3) Enzymatic catalyst. As the name suggests, homogeneous catalysis involves reaction in the same phase, typically in solution; catalyst and reactants are in the same phase. Transition metal complexes and organocatalyst are commonly employed in such type of catalysis.on the other hand, heterogeneous catalysis involves two different phases. Generally, heterogeneous catalysis utilizes solid form of catalyst with reactants in gas-phase and/or liquid phase. Metal catalysts, supported by high-surface-area materials like zeolites, mesoporous substances, or metal oxides, find extensive use as heterogeneous catalysts. Enzymes function as catalysts within biological systems, facilitating specific chemical reactions. While homogeneous catalysts exhibit superior activity and selectivity compared to heterogeneous catalysts, the cost associated with separating them from the unreacted reactants and product mixtures renders them economically unfavorable within industrial contexts. The presence of unsaturated coordination sites on solid surfaces enables the facile adsorption of gases or liquid-phase reactants onto them. The porosity of solid catalysts permits the diffusion of reactants toward active sites, ultimately enabling the chemical transformation of reactants into products. All heterogeneous catalysts operate at the surface or interface of solid catalysts due to the high energy of solid surfaces, allowing reactants to effectively diffuse to active sites and maintain low surface tension.

The adsorption process can be categorized into two types based on the nature of the bonding between the surface (adsorbent) and the reactant (adsorbate): (1) Physisorption, which is characterized by weak van der Waals forces and typically takes place at low temperatures. In physisorption, the reactant can be easily desorbed from the surface, either in a molecular form or as it is, by simply heating it from low temperatures. (2) Chemisorption, as implied by its

name, involves the creation of a chemical bond with the catalyst surface. In this process, the reactant or adsorbate molecule dissociates on the catalyst surface and undergoes reactions with other adsorbate species, resulting in the formation of products. Subsequently, desorption occurs at the appropriate temperature. Reaction using solid catalyst follows surface phenomena like adsorption, desorption and surface reaction.

1.2 History of heterogeneous catalysis

The history of heterogeneous catalysis dates back to ancient times when humans used catalyst, but without realizing the scientific principles behind them. However, significant advancement in understanding and utilizing heterogeneous catalysis has been made over the centuries. In 18th century (1770s), the French chemist, St. Antoine Lavoiser, conducted oxidation experiments using platinum, and discovered its catalytic properties. This laid the foundation for the study of heterogeneous catalysis. In the early 1900s, the German chemist Firtz Haber, developed a catalytic process for synthesizing, ammonia from nitrogen and hydrogen gases. This Harbor-bosch process commercialized by Carl Bosch, revolutionised the production of ammonia-based fertilizers and played a crucial role in agriculture. In 1909, the French chemist, Paul Sebastian, and his collaborators team Jean-Baptiste Senderens, discovered the catalytic hydrogenation of organic compounds leading to the development of industrial hydrogenation process. In 1940, Eugene Houdry and Vladimir Haenselmade significant contribution to the development of catalytic cracking process for petroleum refining, which introduced the production of high-octane gasoline.

In 1950s, the British chemist, John Turkevich, introduced the concept of catalytic poisoning, where the activity of catalyst is decreased or eliminated due to the presence of certain impurities or poisons. In the 1960s, the commercialization of zeolite catalysts for various petrochemical processes begun; as mentioned earlier, It signifies a significant advancement in the field of heterogeneous catalysis. During the 1970s, the introduction and widespread adoption of catalytic converters in automobiles brought about a revolutionary change in the regulation of exhaust emissions.

Since late 20^{th} century, research and advancement in heterogeneous catalysis have continued at a rapid pace leading to the discovery of several new catalysts, and improvedthe understanding of catalytic mechanism due to the advancement of several spectral/structural/microscopy techniques. This also led to the development of novel applications in the catalysis field, such

as energy, environmental sustainability, pharmaceuticals. Certainly, these processes have enabled modern-day life to thrive with remarkable convenience. Nevertheless, the excessive utilization of natural resources, particularly fossil fuels, coupled with extensive global industrialization, has resulted in substantial pollution across various domains and subsequently contributed to climate change. It is anticipated that heterogeneous catalysis will assume a pivotal role in addressing these environmental challenges through the development of enhanced or novel catalysts.

The significance of a catalyst in gas-phase reactions is illustrated in **Fig. 1.1** through a potential energy diagram. The reaction rate for a heterogeneous catalyzed reaction is depicted as

$$A+B \xrightarrow{\text{Catalyst}} AB \qquad \text{Eq. (1.1)}$$

$$\text{Rate} = K\,[A][B] \qquad \text{Eq. (1.2)}$$

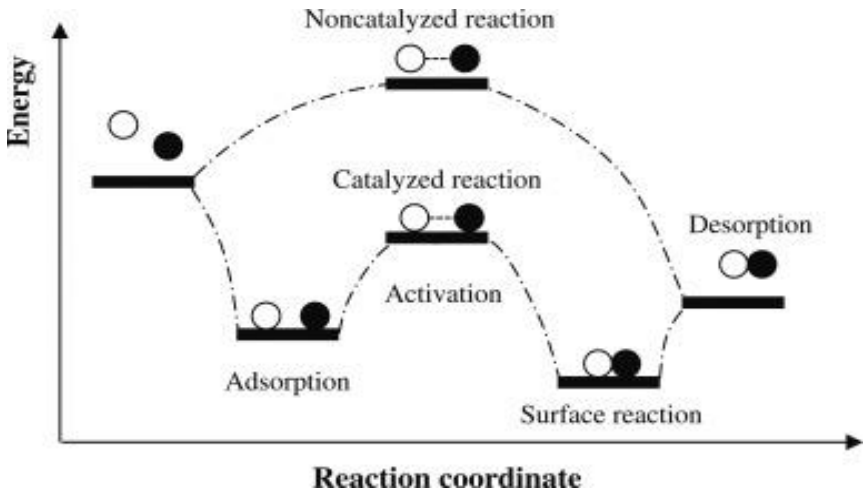

Figure 1.An energy diagram is employed to illustrate the function of a heterogeneous catalyst, showcasing the activation energy for both uncatalyzed and catalyzed reactions.

1.3 Surface science approach toward heterogeneous catalysis

Surface science plays a crucial role in understanding and advancing the field of heterogeneous catalysis. Heterogeneous catalysis refers to a process where a catalyst typical in solid phase, facilitate a chemical reaction and several fundamental/elementary steps occur over the surface within the process. The process involves the adsorption and diffusion of the reactant(s) on the surface, followed by the breaking of bonds within the reactant(s) molecule, the formation of intermediates (if applicable), and finally, the creation of bonds and the release of the product. These steps can be investigated using surface science techniques.

Surface science techniques primarily aim to explore processes taking place at the atomic and molecular scale on the catalyst surface. This involves understanding the reaction mechanisms, enhancing catalyst density, developing catalyst systems that are more efficient and selective, and studying electronic alterations. [**1**] Comprehending these various aspects could profoundly influence the reactivity of the catalyst in a specific reaction. Fig. 1.2 shows dynamic evolution of catalyst surface during interaction with reactants molecule as a function of reactant pressure. The surface structural evolution occurs, which is primarily triggered by alteration in the surface chemical potential during its interaction with the reactant molecules, and can be observed by *in-situ* methods. The observed changes in response to reactant pressure indicate that the density of the reactant molecule influence the surface chemical potential, this leads to alterations in the electronic configuration of the surface.

Under the catalytic conditions, various phenomena, such as, segregation, restructuring, sintering, encapsulation, occur on the catalyst surface. It is also crucial to examine the catalyst, before and after the experiment, to observe for any physical and chemical changes. The actual surface of the catalyst during operation may differ from the initial and final states, as they often exhibit dynamic behaviour. Considering the changes that take place on the catalyst surface and the reaction conditions, it is essential to gain a comprehensive understanding of the catalyst surface under actual working or near working

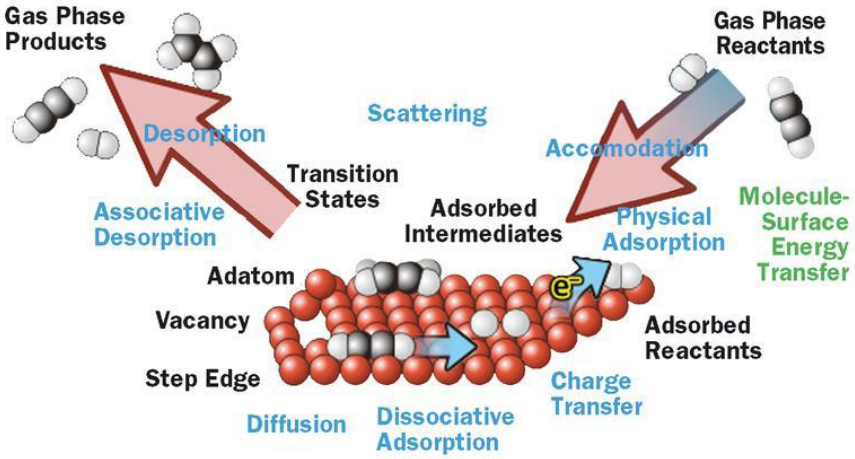

Figure 1.2. Various chemical phenomenon during a heterogeneous catalytic reaction. **Ref. 2**

conditions. The exploration of catalyst surfaces commenced with the introduction of surface science instruments capable of functioning under ultra-high vacuum (UHV) conditions, which became commercially available from 1960s and 1970s; this advancement facilitated significant

improvement in comprehending catalyst surface at atomic level. Surface science methodologies provide valuable insights into the fundamental process occurring at the surface/interface of catalyst under precisely controlled conditions. Primary tools in surface science arespectroscopy, Structural techniques and microscopy offer valuable insights into the electronic and geometric characteristics of catalyst surfaces. These methods encompass a range of techniques, including Photoelectron Spectroscopy (PES), Electron Energy Loss Spectroscopy (EELS), Low Energy Electron Diffraction (LEED), Scanning Tunneling Microscopy (STM), Ion Scattering Spectroscopy (ISS), Sum Frequency Generation (SFG), Polarized Modulation Infrared Reflection Absorption Spectroscopy (PM-IRRAS), Atomic Force Microscopy (AFM), and Secondary Ion Mass Spectrometry (SIMS).These methods are employed to investigate surface composition, depth-dependent composition variations, oxidation states, electronic properties of the surface, and the structural arrangement of catalyst materials. The information obtained from these techniques aids in identifying active sites, comprehending catalyst deactivation mechanisms, and designing catalysts with improved performance.

Another critical aspect of surface science in heterogeneous catalysis is towards understanding the interaction between reactant molecule(s)/species and the catalyst surface. Temperature programmed desorption (TPD) experiments, for instance, allow scientists to measure the adsorption and desorption energies of reacting molecule on the catalyst surface. This knowledge aids in determining the energy barrier for key reaction steps and provides insights into the reaction kinetics and rate determining steps. For real-time study various *in-situ* surface techniques, like infrared reflection absorption spectroscopy (IRAS) or Near-ambient pressure photoelectron spectroscopy (NAPPES) or related techniques are employed for tracking alterations in surface species and the electronic states of catalysts as catalytic reactions unfold. This information aids in understanding the catalyst's dynamic behaviour, identifying intermediates and reaction pathways, which helps in optimizing the reaction conditions.

In 2007, Gerhard Ertl was honored with the Nobel Prize for his significant contributions to the field of surface science. His pioneering work greatly advanced our understanding of oxidation on Pt catalysts. The groundbreaking research conducted by Gerhard Ertl and Gabor Somorjai laid the foundation for the fundamental principles of the surface science approach in the field of heterogeneous catalysis. Over the past four decades, the application of surface science tools

has provided the catalysis community with a profound understanding of this research area. [**4-6]**

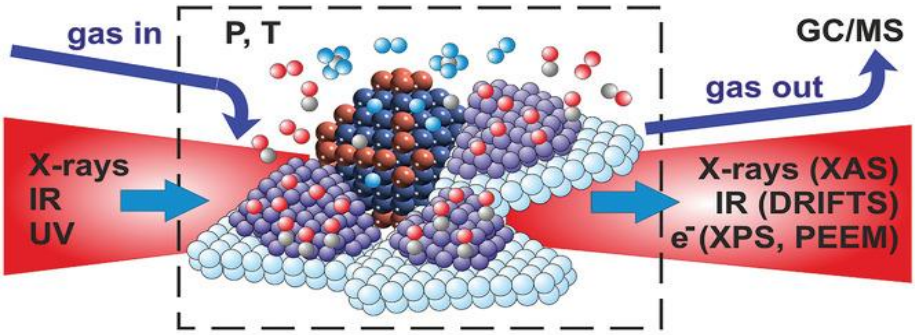

Figure 1.3. Various operando/*in-situ* technique shows, how the use of various technique enables structural and molecular ordering to be probed. Figure reproduced from **Ref. [3]** Copyright permission obtained from Wiley.

1.4. Pressure and material gap in heterogeneous catalysis

Understanding the factors that influence the catalytic activity is crucial for optimizing catalytic performance and developing efficient catalyst. Two significant factors that impact catalytic process are pressure gap and material gap. Conventional surface science technique has the capability to detect numerous surface processes, including absorption, desorption, surface reconstruction etc. Nevertheless, the majority of surface science technique requires UHV condition, as it is essential to ensure the cleanliness of the catalyst's surface by preventing contamination. Hence maintaining UHV conditions become crucial for conducting sensitive surface science experiments under controlled conditions. However, the real-world catalysis happens at ambient pressure and above, and at high temperatures. The direct applicability of data obtained, from surface science study conducted under UHV condition to real world process occurring at atmospheric pressure or higher is often questioned in the past. The disparity in pressure between measurements made under ideal condition in surface science studies and actual catalytic process taking place at atmospheric or elevated pressure, which is of several orders of mbar, is referred to as the "**pressure gap**" as shown in **Figure 1.4.** Other than UHV condition, the surface science studies invariably involve the use of single crystal or metal foil surfaces under carefully controlled circumstances. However, it is important to recognize the real-world catalysis, employs powder-based catalyst with properties, such as surface defects, porosity, high surface area and interaction between metal andsupport. These factors contribute to the complexity of the material and significantly impact catalytic process,

including reactant adsorption and diffusion over the catalyst surface. Consequently, the correlation between surface science results obtained from single crystal or simple metal foil surface and catalytic outcomes using complex powder catalyst under high pressure and temperature condition raises concern about the reliability of the conclusions from the former studies. The discrepancy between knowledge acquiredthrough surface science studies on the ideal surface and the practical application involving powder-basedcatalyst under real-world conditions constitutes the "**Material gap**". The material gap refers to thediscrepancy between the behaviour of model catalyst, often studied under ideal/controlled conditions and real-world catalyst employed in practical application conditions. Model catalysts are typically single crystal surface that provide detail insights into the fundamental mechanism, governing catalytic reactions. However, the real-world catalyst used in industrial process often, consists of complex, they often appear as inhomogeneously dispersed particles on porous oxide supports in powdered form, or they can take the form of multicomponent systems with sustainable surface area and porosity. Bridging the material gap requires understanding that behaviour of real catalyst and identifying structure activity relationship that can guide catalyst, design and optimization. [**8-10**].

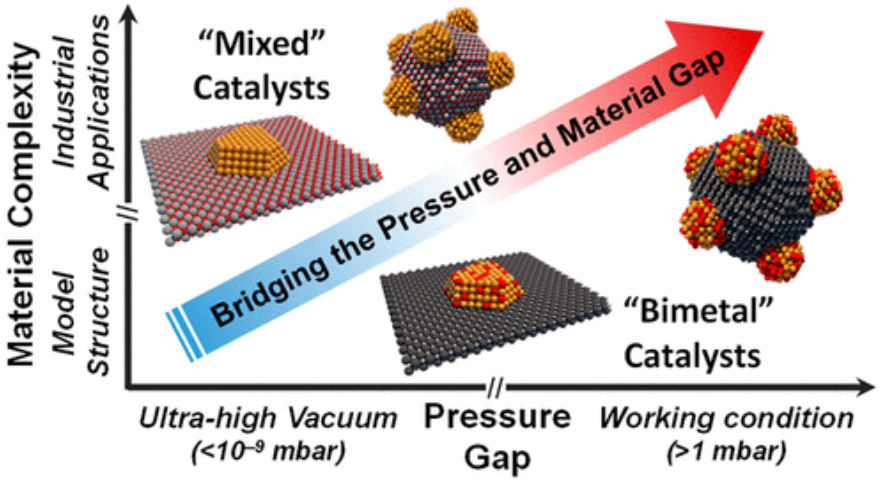

Figure 1.4. Schematic representation of bridging the material and pressure gap. Figure reproduced from **Ref. [7],** Copyright permission obtained from ACS.

This intricate nature stems from the existence of diverse defects, porosity, and steps on the catalyst surface. These characteristics notably augment the quantity of catalytically active sites and possess the capacity to elevate the overall catalytic activity.**[11]** The ultimate objective of the surface science involves investigating the atomic level interactions between various components of a catalyst and enhancing the efficiency of heterogeneously catalyzed reactions to the highest possible extent. However, achieving these goals is challenging due to highly

complex nature of the catalyst's surface structure. This complexity poses limitations on studying the catalyst under real working conditions, such as at near ambient or elevated gas pressures.

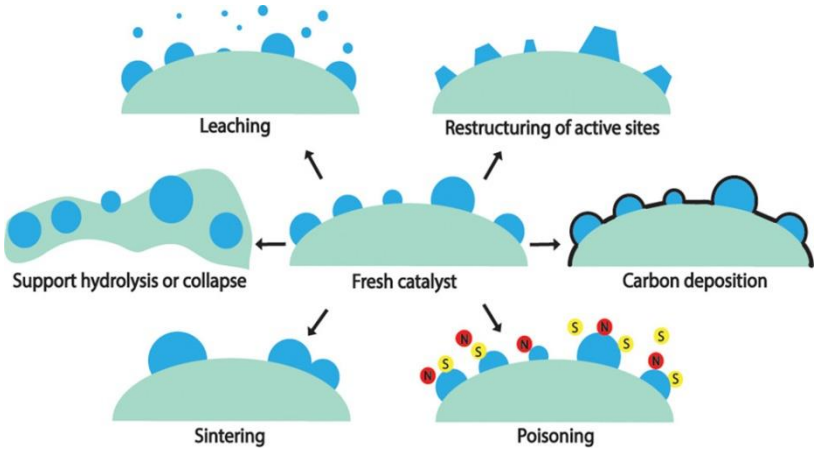

Figure 1.5 The illustration depicts the potential structural and compositional changes that catalyst may undergo during their transformation from the "as prepared" state to the active state. Figure reproduced from **Ref. [12]** Copyright permission obtained from ACS.

Throughout the catalytic process, numerous structural and compositional changes occur over the catalyst surface. These changes include sintering, carbon deposition, segregation and restructuring, as illustrated in **Figure 1.5**. Hence, many researchers are dedicated to studying surface processes under authentic conditions, aiming to eliminate the influence of disparities in pressure and material. Bridging these gaps has become a central focus, driving significant research endeavors aimed at advancing scientific knowledge and practical applications in these domains. Acquiring detailed insights into the atomic-scale, geometric, and electronic structures of surfaces and interfaces, particularly under conditions closely resembling real-world operating conditions in terms of pressure and temperature and on actual catalyst materials, is of utmost importance. Achieving this goal necessitates the application of various in-situ techniques that facilitate a molecular-level understanding of gas-solid and gas-liquid interfaces under ambient or atmospheric pressure, as well as the requisite temperature conditions. The primary aim of this thesis is to narrow, the pressure and material gaps as much as possible by utilizing advanced *in -situ* surface science tools capable of operating under ambient, or near ambient conditions. This will contribute to a more comprehension of the conditions utilized in surface science experiments and their applicability to real-world industrial catalytic processes. Additionally, it has the potential to establish a stronger connection between the outcomes obtained in practical catalysis and the discoveries made in the realm of surface science.

1.5. Photoelectron spectroscopy (PES)

Photoelectronspectroscopy has emerged as an advanced technology for characterizing surface science. PES, or Photoelectron Spectroscopy, is a technique in electron spectroscopy. In PES, a photon with enough energy is directed at a solid substance, causing electrons to be dislodged from the tightly bound orbitals of an atom. In simpler terms, these electrons can break free from the attractive forces holding them within their respective atoms or molecules. The foundation of PES lies in the discovery of the photoelectric effect, initially observed by J.J. Thomson **[13]** and later explained by Albert Einstein in 1920. **[14]** It really relies on a process where a single photon results in the emission of an electron. The phenomena in which an electron is ejected from an atom or molecule using the energy obtained from absorbed photons is referred to as "photoinonization". The electrons that are emitted in this process are known as photoelectron and their energy reflect the specific atomic or molecular orbital from which they originate. The conservation of energy in this process is described by a fundamental equation known as Einstein photoelectric effect, equation given as follows:

$$h\nu = \text{B.E} + \text{K.E} + \phi \tag{1.3}$$

Here, $h\nu$ represents the energy of the incident photon, while B.E stands for binding energy (BE), which is the energy necessary to excite an electron from an occupied level to the Fermi level (E_F) **[15]**. This BE corresponds to the energy level from which electrons are excited. The additional energy needed to extract an electron from E_F into the vacuum is known as the work function (ϕ) of the solid. The remaining energy possessed by the ejected electron is its kinetic energy (KE), which relies on the energy of the incoming photon. The total of the BE and ϕ is referred to as the ionization potential for a specific atomic shell. In other words, ionization potential energy represents the minimum energy required to dislodge an electron from a given orbital. To ensure that the ejected electron from the solid surface reaches the detector without experiencing any inelastic collisions with gas atoms or molecules present in the chamber or atoms within the surface layers of the solid, precautions are taken. So, it is important to maintain extremely low-pressure environment. This requirement is achieved by maintaining and UHV of the order of $\leq 10^{-9}$ mbar within the PES spectrometer. Thistechnique has been divided into two types based on the excitation energy employed, namely, x-ray photoelectron spectroscopy (XPS) and ultraviolet photoelectron spectroscopy (UPS).

X-ray photoelectron spectroscopy (XPS)- When employing soft X-rays as the photon source, typically with energy levels around 500 to 2000 eV, the technique is referred to as X-ray Photoelectron Spectroscopy (XPS) or Electron Spectroscopy for Chemical Analysis (ESCA)

[16]. The probing depth of XPS varies with the photon energy used. For instance, when using photon energies between 1200 and 1500 eV, the probing depth reaches approximately 10 nanometers. Higher photon energies are also available, and as the photon energy increases, the probing depth of XPS offers the capability to conduct quantitative analysis of surface composition, distinguishing between various oxidation states and chemical environments. Additionally, it proves valuable for assessing surface composition and acquiring insights into the electronic structure.

Ultraviolet Photoelectron Spectroscopy (UPS or UVPES):-

UPS, also referred to as Valence Band (VB) Photoelectron Spectroscopy or Molecular Photoelectron Spectroscopy, and furnishes valuable insights into the VB hybridization, the location of VB maxima, ionization energy, work function, and more. Notably, no other methods directly provide information about VB hybridization; instead, they often necessitate in-depth analysis to extract as much detail as possible. UPS harnesses a noble gas discharge lamp to produce UV radiations with varying wavelengths or energy levels. When Helium (He) is utilized as the source in the discharge lamp, it emits two distinct He radiations: He(I) radiation (21.2 eV) and He(II) radiation (40.4 eV) in the form of photons. By optimizing the conditions related to He pressure, it becomes possible to maximize one of the two He radiation energies. The resonance emission line He-I produced by transition from the first excited state to the ground state is the most intense line. Additional photon-lines (satellites) are generally generated in the He discharge; however, these are of low in intensity. By manipulating the He-gas pressure the relative proportion of singly ionized He-atoms in the discharge lamp can be modified to generate usable photon yields of He II. Due to low energy of the excitation source, capable of knocking out the electrons only from the outermost occupied levels or valence orbitals of any materials into the vacuum. **[17]**

UPS which employs low energy photons has a distinct advantage. UPS can only investigate top 2 nanometers of solid surfaces. Due to the low KE (<16 eV with He I) associated with ejected electrons by UPS, the electron escape depth is limited to top few atomic layers. This characteristic makes UPS, a highly surface sensitive technique, rendering it exceptionally sensitive to the surface contamination. In addition, UPS offers superior resolution relative to XPS.The relatively slim spectral width of He radiation and the generally elevated photoionization cross-section of valence orbitals in numerous elements contribute to achieving exceptional resolution. UPS proves highly effective in investigating solid surfaces, particularly when focusing on the VB and exploring the interactions between gases and solid surfaces,

especially on metals and solid materials. Furthermore, UPS plays a valuable role in determining the ϕ of a material, thereby expanding its applications in fields such as organic and inorganic photovoltaics, as well as organic light-emitting diodes (LEDs).

The UPS technique offers the capability to observe the intricate details of atomic and molecular vibrations. This fine structure results from a variety of vibrational and rotational transitions that occur in monoatomic, diatomic, and multiatomic gaseous molecules. For example, when examining gas-phase atomic elements such as Argon (Ar) using He(I) photonization, a doublet pattern is observed, as illustrated in **Figure 1.6**. The separation between the two doublets in the spectrum (176 meV) represents the spin-orbit interaction, while the line width of the singlet defines the resolution of the spectrometer. On the other hand, when dealing with diatomic molecules like H_2 (which are not detectable in XPS), photoionization with He-I results in multiple peaks due to vibration-induced transitions.

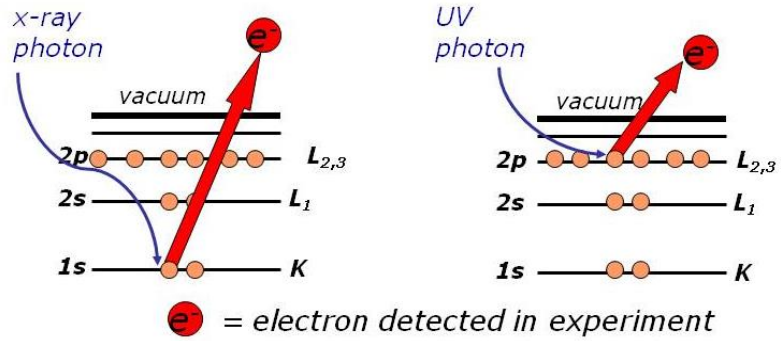

Figure1.6 Process of photoionisation in XPS and UPS. **Ref. 18**

1.6 Birth of Near Ambient pressure photoelectron spectroscopy (NAPPES)

Photoelectron spectroscopy stands as a versatile method for exploring the electronic and chemical makeup of solid surfaces. Nevertheless, because of the interplay between photons and electrons, most PES instruments, whether in laboratory settings or synchrotron-based, necessitate ultra-high vacuum (UHV) conditions, where pressures typically range from 10^{-9} mbar and below. This presents a challenge in various applications, notably in scenarios such as real-world catalysis that transpires under ambient or substantially higher pressures ($P \geq 1$ bar). This disparity in UHV conditions for surface science measurements and real-world catalysis pressure conditions is called "**Pressure gap**". However, there are three conventional justifications for the necessity of UHV condition for surface science measurements: **(a)** Inelastic scattering - Since PES relies on the energy of emitted photoelectrons providing

chemical/electronic information. It is crucial to collect the electrons without subjecting them to any elastic collision. Therefor, it becomes imperative to position detectors at a distance from the sample that is comparable to the inelastic mean free path (IMFP) or attenuation length of electrons. Secondly, maintaining a vacuum is critical both for the generation of X-rays through photon interactions and for the electron analysis by detectors. Detectors, often utilizing microchannel plates or charged-coupled devices, come with pressure limitations, requiring vacuum conditions of 10^{-6} mbar or lower. Thirdly, the preservation of a vacuum environment serves the purpose of keeping the sample surface atomically clean and devoid of contaminants. In accordance with the kinetic gas theory, the rate at which molecules (with mass M) collide with the sample surface, possessing an area (A), can be expressed as follows, considering the pressure (P) and temperature (T):

$$\frac{\Delta n}{A.\Delta t} = \sqrt{\frac{NA}{2\pi MKBT}}.\rho$$

When the pressure is at 10^{-6} torr, a metal surface (with a sticking coefficient of 1) can become completely covered by gas molecules in approximately 1 second. Even with a sticking coefficient of 0.01, the surface can be entirely coated with adsorbed molecules within 100 seconds. Gas contamination on a catalyst's surface has the potential to modify its electronic characteristics and can also act as a "poison" for the surface.

The origins of NAPPES can be traced back to Uppsala University, emerging shortly after the introduction of vacuum-based X-ray photoelectron spectroscopy (XPS). The initial NAPPES instrument was developed by Siegbahn and colleagues with a specific focus on studying vapor/liquid interfaces **[19]**. In the late 1970s, Joyner and Roberts at Cardiff University, England, also created a similar instrument tailored for investigating vapor/solid interfaces **[20]**. These early laboratory systems made use of X-ray sources and included differential pumping stages to isolate the sample compartment from the electrostatic lens system of a hemispherical analyzer. Both of these initiatives had relatively short lifespans, resulting in only a handful of research articles being published **[17, 19-21]**. Over time, various modifications were introduced to enhance electron collection efficiency while maintaining high spectral quality and bridging the pressure gap as effectively as possible. As the new century dawned, the increasing demands of environmental and catalysis science, combined with advancements in third-generation synchrotron technology, led to significant breakthroughs in the realm of high-pressure

photoelectron spectroscopy (HPPES). These developments enabled researchers to work at relatively higher pressures, addressing the evolving requirements of the scientific community. Pioneering research groups, located at the Advanced Light Source (ALS) and BESSY (Berliner Elektronenspeicherring-Gesellschaft für Synchrotronstrahlung) facilities, have made significant advancements in this field. They were the pioneers in integrating differentially pumped electrostatic lens systems into their electron energy analyzers, resulting in a significant enhancement in transmission for analyzers adapted to high-pressure conditions. The initial deployment of such an instrument took place at beamline 9.3.2 **[22]** of the ALS. Following this breakthrough, multiple synchrotron-based facilities around the world, including the Fritz Haber Institute (BESSY II) **[23]** in Berlin, ALS beamline 11.0.2.24 **[24]**, MAX-lab **[25]** in Shanghai, and Diamond, installed HPPES beamlines, further contributing to the progress in this field **[26]**.

Recent advancements in custom-built laboratory-based photon sources have significantly facilitated the proliferation of NAPPES systems. These advancements encompass improvements in small-spot, high-flux, monochromatized X-ray sources, which have proven capable of examining surfaces under realistic conditions, outside the constraints of ultra-high vacuum environments **[27-28]**. Consequently, there has been a resurgence of laboratory-based NAP-XPS instruments in recent years, with further growth anticipated in this field in the near future. An exemplary instance of a custom-built NAPPES instrument is the installation at CSIR NCL, Pune, in 2012, marking the first of its kind in India capable of operating under non-conventional conditions. This system features an enhanced analyzer with an aperture-free Electrostatic Lens System (ELS). With this setup, it becomes possible to investigate surfaces at pressures up to 1 mbar with XPS and 0.3 mbar with UPS, while reaching temperatures of up to 900 K **[29]**. More detailed information regarding the design aspects of this system will be discussed in Chapter 2. Subsequently, the following section provides a concise overview of fundamental concepts considered during the development of NAPPES, with further exploration of important applications in catalysis in the subsequent section.

1.7 Exploring Electronic Structure Evolution of Materials Using NAPPES and Its Significance in Catalysis

An analysis of the literature regarding NAPPES studies of heterogeneous catalytic reactions underscores the significance of exploring the surface chemistry of catalysts during catalysis to gain a comprehensive understanding of the catalytic processes. However, monitoring a catalyst's surface under the relevant catalytic conditions offers valuable insights into the surface electronic structure and catalyst properties, establishing a fundamental connection between

catalytic performance and mechanistic aspects of the reaction. Recent advancements in surface science and the advent of NAPPES technology provide an opportunity to investigate real-world catalytic surfaces under conditions that closely resemble actual catalytic scenarios. This breakthrough effectively bridges the existing gaps related to pressure and materials, ushering in a new and indispensable chapter in the field of surface science.

1.7.1 Gas-Solid interaction: The fundamental phenomenon of heterogeneous catalysis

Surface chemical reactions are pivotal across various fields of science and technology. Among these, gas-solid interactions form the foundation for numerous applications reliant on surfacephenomena, including heterogeneous catalysis, electrochemistry, sensors, semiconductors, and more. Understanding gas-solid interactions during redox processes holds particular significance in the realm of heterogeneous catalysis. One of these reactions, CO oxidation, holds particular importance, especially in three-way catalytic converters. Furthermore, it serves as a extensively studied model reaction in surface science, offering insights into surface properties and behavior. Turnel *et.al.* conducted an investigation into the temporal oscillations observed in CO oxidation reactions over a Pt surface, both under steady and non-steady state conditions, with a focus on low-pressure conditions **[30]**. Meanwhile, Ertl and his team pioneered the study of non-linear kinetic oscillations in CO oxidation on a Pt(111) surface under ultra-high vacuum (UHV) conditions. According to the proposed reaction mechanism, the elevated sticking coefficient of CO and subsequent surface reconstruction significantly hinder the dissociative adsorption of O_2. Conversely, clean or relatively sparsely covered CO surfaces facilitate O_2 adsorption and dissociation. However, under actual reaction conditions, both extreme scenarios can occur, resulting in oscillatory behavior of the reaction rate at a specific temperature, leading to non-linear kinetics. Consequently, to maintain continuous desorption of CO adsorbates and generate free adsorption sites, considerably high temperatures (above 400K) are required during steady-state flow conditions **[31-32]**.

Gopinath *et. al.* successfully demonstrated a shift in the catalysis regime through surface modification. By diffusing oxygen atoms into the sub-surface of Pd layers, they generated a significantly electron-deficient Pd surface, referred to as cationic δ+ or $Pd^{\delta+}$. This transformation weakened CO chemisorption, alleviated CO-poisoning effects, and enhanced CO mobility on the surface, even at lower temperatures around 350 K **[32]**.

Understanding gas-solid interactions during redox processes remains highly relevant in the context of heterogeneous catalysis. Various transition metals, including Cu, Co, Mo, and V, along with their respective oxides, play crucial roles in catalytic applications. Gaining a deeper

understanding of the temperature-dependent oxidation and reduction by O_2 and H_2 through the utilization of NAPPES can provide essential atomic-level insights. These insights, in turn, can be leveraged to enhance the design of catalysts for improved performance. Gopinath and his team conducted a comprehensive investigation into gas-solid interactions using NAP-XPS and NAP-UPS under near-ambient conditions, offering valuable explanations for changes in the VB and core-level surfaces during the reaction conditions. [**34-36]**

Within transition-metal oxides, the presence of water vapor on the catalyst surface hampers catalytic activity by obstructing active sites. These phenomenon posses significant challenges in heterogeneous catalysis, ultimately resulting in catalyst deactivation. In line with this concern, Ruchi Jain *et. al*. conducted a study that delved into the surface electronic alterations of Co_3O_4 nanorods during CO oxidation, both in the presence and absence of water vapor. Intriguingly, when water vapor was introduced (alongside CO and O_2) during the catalytic reaction, it followed a novel pathway, resulting in the emergence of carbonate and formate species. Nevertheless, at temperatures of 400 K and above, the surface managed to recover from the aforementioned contamination, enabling CO oxidation to proceed, even in the presence of water vapor. These findings shed light on the influence of water vapour on the catalytic mechanism, providing essential insights for understanding the reactivity of the catalyst in relevant reaction environment. This type of study contributes to our understanding of the complexities associated with water vapour induced modification in transition metal oxide catalyst, and open an avenue in surface science study especially in NPPES. [**37-38**].

1.7.2 Work function changes: ϕ is a fundamental concept in solid state physics and material science, playing a crucial role in understanding the material behaviour of solids. This term refers to the energy needed to displace an electron from the E_F (which represents the highest energy state occupied by electrons at absolute zero temperature) of a solid material and transport it to a position just beyond the material's surface. It is material specific property. Meaning each solid material has its own unique ϕ value. The ϕ depends on various factors, including the material’s electronic structure, crystal lattice, surface termination, and temperature.

Understanding these diverse factors significantly impact the reactivity of the surface and enhance catalyst design considerations. Furthermore, ϕ of the catalytic material holds significant importance in various microscopic phenomena linked to catalytic reactions. It's worth noting that chemisorption can result in changes to the ϕ of the solid surface due to the formation of chemical bonds, thereby altering the density of states on the solid surface. In

metals, the conduction band (CB) and VB directly adjoin each other without any energy gap, and the E_F aligns precisely at the interface between these two bands.

Conversely, semiconductors and insulators lack electronic states at and around the E_F, leading to distinction from metals in their electronic structure. As a result, the ϕ of semiconductors/insulators is not directly synonymous with ionization energy (E_{ion}) or electron affinity (χ). The ϕ of any surface can be attributed to two factors: (1) the electron chemical potential and (2) the surface dipole (δ). The electron chemical potential signifies the Fermi level's position relative to the absolute vacuum level and the extra energy needed to extract an electron from the surface, known as the dipole charge. **[39]**

The alteration of the vacuum level without a simultaneous shift in the E_F happens because of the existence of a surface dipole. Elements like oxidation state, impurities, and crystal structure defects have the potential to adjust the electron chemical potential, resulting in E_F changes. Conversely, the surface dipole charge is predominantly shaped by various factors, including surface reconstruction, surface orientation, and, importantly, the existence of adsorbates, especially chemisorbed species. Typically, the surface dipole charge emerges from the exchange of charges at the boundary between the material and its surroundings. One significant application is in the field of surface science, where the ϕ is utilised to characterise the surface properties of materials and investigate surface reactions and adsorption processes. As an illustration, when a solid material comes into contact with a gas or reaction environment, the shift in ϕ can offer valuable information about the charge transfer and chemical interplay occurring on the surface. This aspect was specifically assessed in studies related to solid-gas interactions. **[40-41]** The catalytic performance of a surface is affected by a multitude of factors, encompassing the BE of reactants, intermediates, products, co-adsorbates, impurities, and surface structure.

A negative surface charge results in an elevated surface dipole, which consequently lowers the ϕ, whereas a positive surface charge leads to a reduced surface dipole and an increased ϕ. It's important to recognize that the measured ϕ is significantly affected by the specific conditions of the material, rather than being an inherent material constant. Nonetheless, certain materials like Au, Cu, Mo exhibit reproducible ϕ values under ultra-high vacuum (UHV) conditions. A thorough explanation of how to measure changes in ϕ under reaction conditions using NAPPES will be provided in Chapter 2.

1.7.3 CO_2 reduction: Surface Science approach

To combat the climate change, numerous nations have pledge to decrease their CO_2 emissions. The 2015 Paris agreements witnessed the participation of 190 parties, including the EU and its member states, who united in their commitment to limit global warming to 2 °C. Additionally, the European Commission has established precise objectives, including a 40% reduction in greenhouse gas emissions by 2030 in comparison to 1990 levels, and a broader aim of attaining climate-neutrality by 2050. A crucial aspect of achieving these objectives involves a significant transition from fossil fuel to carbon-neutral energy in the realm of energy production. Green house gases mean those gaseous constituents of the atmosphere, both natural and anthropogenic, that adsorbs and remits infrared radiations. The greenhouse gas in atmosphere presents methane (CH_4), CO, CO_2, nitrous oxide, fluorinated gases and 76% of the greenhouse gas is CO_2. The huge quantity of CO_2 in atmosphere which acts as a blanket, trapping heat and warming the planet, is the main cause of global warming. In response to escalating global energy demand, there has been concurrent rise in atmospheric carbon dioxide concentration, leading to the detrimental effect on global warming and ocean acidification. As a result, there is an urgent need to address the elevated CO_2 levels in the atmosphere by either capturing and storing it or converting it into valuable chemicals. The concept of achieving carbon neutrality plays a pivotal role in recycling atmospheric CO_2 by activating it and transforming it in to a useful feedstock. However, due to high ionization energy and no positive electron affinity of CO_2 molecule, characterized by its linear and symmetric structure, the scientific community faces a formidable challenge in reducing and converting it into others value added product like CO, methanol, and formaldehyde. The stable nature of CO_2, high heat of formation and, strong C=O bond and high enthalpy of C=O breaking (+293KJ/mol) makes it difficult to activate [**42-43**]. To activate CO_2, it is essential to have a suitable catalyst that possesses active sites for CO_2 adsorption and the ability to provide the necessary energy for the adsorbed CO_2 molecules to undergo activation. Direct CO_2 conversion to various products is feasible; however, it frequently results in a mixture of various products, and overall conversion efficiency tends to be relatively low.

Methane formation from CO_2 is an exothermic process and relatively straightforward to accomplish. However, despite its ease of formation, the fuel values of methane is considerably lower compared to methanol. Methane is not preferred due to added cost and energy required for compression and transportation. On the other hand, Fischer-Tropsch synthesis is well

known and established technology for converting CO into various value-added products. The conversion of CO_2 into CO is referred as reverse water gas shift reaction (RWGS) and related CO_2 transformation leading to other value added-products. The conversion of CO_2 to CO serves as a widely recognised building block for the synthesis of value-added product such as methanol, acetic acid, ethanol etc.

$CO_2 + H_2 \rightarrow CO + H_2O$ ($\Delta H = 41$ kJ/mol) (1.4)

$CO_2 + 3H_2 \rightarrow CH_3OH + H_2O$ ($\Delta H = -49.5$ kJ/mol) (1.5)

$CO_2 + 4H_2 \rightarrow CH_4 + 2H_2O$ ($\Delta H = -165.0$ kJ/mol) (1.6)

$CO + 2H_2 \rightarrow CH_3OH$ ($\Delta H = -90.4$ kJ/mol) (1.7)

However, achieving high CO_2 conversion with exceptional selectivity towards CO presents a significant challenge due to the potential formation of methane. Mitigating the issue involves decreasing the H_2 and increasing the CO_2 contents to suppress methane and water formation; in fact, the adsorbed ratio reactants on the catalyst surface plays a more critical role than the input feed ratio of the reactant.

Transition metal-based catalysts have emerged as an attractive approach for catalyzing the conversion of CO_2. They offer improved conversion efficiency, enhanced product selectivity, and a more cost-effective alternative to precious metal catalysts. In response to the need for economically viable catalysis, numerous studies have explored the potential of transition metals in converting C1 molecules into liquid fuels. Among the various transition metals investigated, catalysts based on Co, Cu, and Ni have exhibited significant activity in CO_2 hydrogenation reactions. Cu-based catalysts, typically supported on a ZnO carrier, find widespread application in the RWGS reaction **[44-46]**. Salmeron and Somorjai conducted research using a Cu single crystal as a model catalyst to gain insights into the impact of surface termination on the adsorption and dissociation of CO_2. Notably, they employed synchrotron-based NAPPES in conjunction with high-pressure scanning tunneling microscopy (STM) to investigate the interaction of CO_2 with Cu(100) and Cu(111) surfaces at room temperature. The experiments were conducted at pressures of up to 10 Torr for NAP-XPS and 20 Torr for STM **[46].**

In the C1s region, two distinct adsorbed carbon species were identified: hydrocarbon species located at 284.4 eV and $CO_2^{\delta-}$ species at 288.1 eV. Furthermore, there is clear evidence of the contribution of CO_2 in the gas phase above the sample, which is noticeable at higher binding energies in the O1s and C1s spectra, approximately around 536 and 292 eV, respectively.

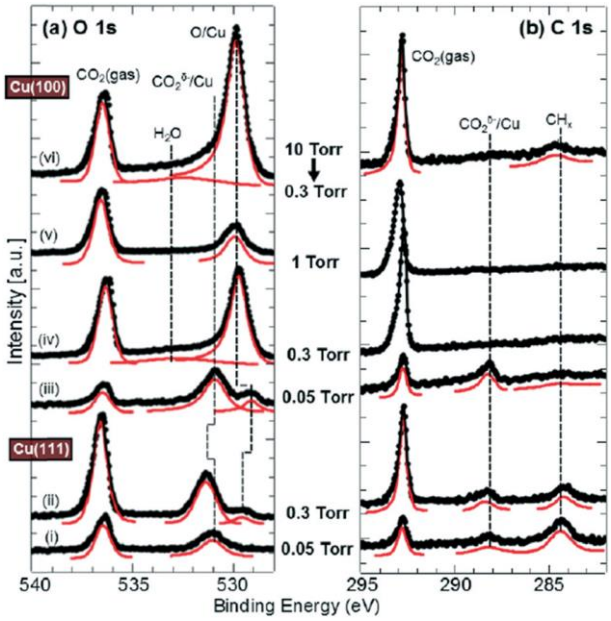

Figure 1.7 NAP-XPS spectra of O1s and C1s XPS in the presence of CO_2 at RT on the Cu (111) surface (lower two panels) and on the Cu(100) surface (upper four panels) (i) 0.05 Torr CO_2 on Cu(111) , (ii) 0.3 Torr CO_2 on Cu(111), (iii) 0.05 Torr CO_2 on Cu(100), (iv) 0.3 Torr CO_2 on Cu(100), (v) 1 Torr on Cu(100), and (vi) 0.3 Torr CO_2 on Cu (100), after the sample was exposed to 10 Torr CO_2 for 5 min. Figure reproduced from**Ref. 47,** Copyright permission obtained from American Chemical Society.

This observation led to the conclusion that on open Cu surface planes, such as Cu(100), there is a more efficient dissociation of CO_2 compared to close-packed Cu(111). This difference was attributed to the relatively high coverage of atomic oxygen (AO) and the relatively low signal intensity of $CO_2^{\delta-}$ species on Cu(100) as compared to Cu(111) **[48].**

Recently, the findings regarding CO_2 dissociation over Cu(100) were substantiated by a more recent study that focused on the atomic oxygen layer induced by CO_2 dissociation. This investigation, which utilized DFT calculations, suggested that CO_2 dissociation primarily takes place at step sites on the Cu surface, where Cu atoms have a lower coordination number **[49]**. This observation corroborated an earlier study involving CO_2 interactions with a well-defined vicinal Cu (997) substrate **[50]**. When exposed to CO_2 at 67 °C, carbonate species (CO_3^{2-}) were generated on the copper surface due to the reaction of CO_2 with oxygen resulting from CO_2 dissociation. Once adsorbed CO_3^{2-} reached saturation, the spectroscopic signature of atomic oxygen (AO) appeared, indicating that CO_2 dissociation into CO and O continues even after saturation **[51].** Similar CO_2 dissociation into CO and O was observed on Cu(111) after extended CO_2 exposure, leading to the formation of an AO layer that passivated the Cu(111) surface and hindered further CO_2 activation. However, when CO_2 was co-fed with H_2 and the adsorbed oxygen species were carefully controlled (e.g. by adjusting CO_2 and H_2 partial pressures), this process had a beneficial effect by preventing the formation of graphitic carbon

and sustaining Cu catalytic activity **[52].** Reports of similar oxygen species were noted during CO_2 interactions with polycrystalline Cu surfaces. Furthermore, when O_2 was introduced alongside CO_2, metallic Cu underwent oxidation to Cu_2O, resulting in a net increase in CO species. Additionally, bulk-dissolved oxygen in Cu could also participate in the reaction by diffusing to the surface at critical temperatures (around 580 °C) and forming chemisorbed oxygen **[53].**

Aside from Cu catalysts, nickel (Ni) and cobalt (Co) also exhibit significant potential for CO_2 utilization reactions, leading to several NAP-XPS investigations of CO_2 interactions with Ni and Co surfaces. Particularly noteworthy is the strong chemisorption of CO_2, which readily dissociates into CO and surface atomic oxygen (AO) on Ni(110) surfaces, even under ultra-high vacuum (UHV) conditions**[54]**. However, density functional theory (DFT) calculations have indicated that the adsorption of CO_2 on Ni(111) surfaces is not energetically favored, especially under low-pressure and low-temperature conditions **[55]**. A study conducted by Salmeron's group employed NAP-XPS to examine the changes in Ni(111) surface composition in the presence of CO_2 and CO_2 + H_2 atmospheres **[56]**. They initially emphasized the importance of the "**pressure gap**" in adsorption, dissociation, and methanation of CO_2 on Ni(111). Specifically, they found that CO_2 is activated over Ni(111) at millibar pressures but not under UHV conditions.The O1s spectra presented in Figure 1.8a illustrate that at 200 millitorr, CO_2 dissociates into CO and AO, resulting in the formation of CO_3^{2-} and NiO (characteristic O1s components at around 529.3 and 531.2 eV, respectively). In CO_2 + H_2mixtures (**Figure 1.8b**), NiO is reduced back to metallic Ni0 at 160 °C, followed by the elimination of adsorbed CO_3^{2-} species. A weak O1s peak at 531.1 eV (**Figure 1.8c**) suggeststhat the reverse water-gas shift (RWGS) reaction occurs under these conditions. Furthermore, the presence of atomic carbon at 283.3 eV (**Figure 1.8c**) indicates that the methanation reaction mechanism on the Ni(111) surface involves the reduction of CO to atomic carbon, which is subsequently hydrogenated to form methane. A more recent NAP-XPS investigation of zeolite-supported Ni catalysts has reported that the coexistence of Ni and NiO on the surface enhances the adsorption and conversion of CO_2. In a recent study by Liu *et. al*. **[58]**, they examined the activation of CO_2 over a polycrystalline Co foil in the presence of H_2O using NAP-XPS. Their observations revealed that the Co surface underwent partial oxidation, primarily due to the formation of carbonates resulting from the dissociative adsorption of CO_2 with H_2O. This led to the generation of methoxy, formate, and bulk carbonate species, with a surprisingly high methoxy/formate coverage ratio, which closely resembled previous findings related to Cu **[59]**. These findings suggest that Co and Cu may interact with CO_2: H2O mixtures in a similar

manner, carrying significant implications for the future development of highly selective Co-based catalysts for CO_2 reduction.

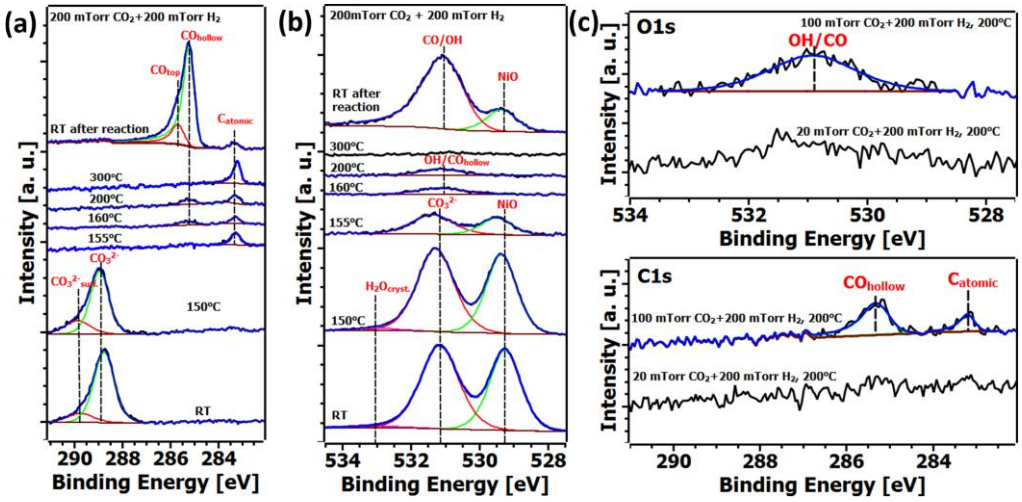

Figure 1.8 NAP-XPS spectra were collected using a Ni(111) model catalyst under various conditions :(a) O1s Spectra were recorded in 200 mTorr CO_2 at temperatures ranging from room temperature (RT) to 200 °C (b) O1s spectra were obtained in 200 mTorr CO_2 and 200 mTorr H_2 at temperatures ranging from RT to 300 °C. (c) O1s and C1s spectra were measured in 20 mTorr CO_2 + 200 mTorr H_2 and in 100 mTorr CO_2 + 200 mTorr H_2 environments. Figure reproduced from **Ref. [57],** Copyright permission obtained from American Chemical Society,

1.8 Objective of the Thesis

A thorough review of the literature on NAPPES studies of heterogeneous catalytic reactions underscores the importance of comprehending the chemistry occurring on a catalyst's surface during catalysis. Examining the catalyst's surface under conditions relevant to catalysis provides valuable insights into its electronic structure, properties, and establishes connections between catalytic performance and potential intermediates. Recent progress in surface science and the advancement of NAPPES techniques present a unique opportunity to explore actual catalyst surfaces under real-world catalysis conditions, effectively closing the gaps related to pressure and materials.

Transition metal oxides display a wide spectrum of oxidation states and varying ϕ, rendering them versatile for applications that entail interactions with adsorbed molecules through charge transfer. The exchange of charges at the interface, including the addition or extraction of electrons from the surface, is significantly influenced by surface properties, notably the ϕ. The manipulation of material surface ϕ holds significant relevance for devices and applications centered on surfaces and interfaces. It becomes especially crucial to grasp how surface ϕ evolves under reaction conditions, particularly in the domains of catalysis and

electrochemistry, where surface electronic characteristics wield substantial influence. The use of UVPES with low energy photons is limited in studying the changes in surface electronic structure during catalysis. Hence, it becomes imperative to investigate the alterations in the VB of catalysts through UVPES under various reaction conditions. This approach delves into nanoscale surface changes (approximately 2nm), which exert a substantial influence on catalytic and other surface-related properties. The utilization of NAPUPS facilitates the determination of crucial parameters, including shifts in the E_F and ϕ under differing pressure and temperature conditions, as elaborated in Chapters 3 and 4.

Tackling the reduction of carbon dioxide presents a formidable challenge for the scientific community, given its link to global warming. Discovering an efficient catalyst and sustainable energy source for converting CO_2 into value-added chemicals holds immense importance in reducing reliance on fossil fuels. However, the majority of catalysts employed in this process involve noble metals supported by or integrated with reducible oxides. These catalysts are often costly, intricate, and unstable at high temperatures, limiting their widespread industrial application. In the quest for an active and cost-effective alternative, catalysts based on transition metals like Co and Ni have emerged as promising options for CO_2 hydrogenation in comparison to noble metal-based counterparts. Chapters 5a and 5b delve into the role of surface structure and aim to identify the active state of the catalyst during catalysis while elucidating changes occurring under realistic conditions on the catalyst surface. These chapters offer valuable insights into the mechanistic pathways of CO_2 hydrogenation reactions.

1.9 Outline of the thesis

The central theme of this thesis revolves around the application of NAPPES to explore alterations in surface electronic properties throughout catalytic chemical processes. It delves into the mechanics of these transformations and aims to elucidate the genuine active states of the catalyst surface under conditions that are pertinent to catalysis. **Chapter 1** discuss the History and fundamental aspects of catalysis, surface science approach towards heterogeneous catalysis, basics of PES, birth of NAPPES system, and its applicability in bridging the pressure and material gaps.

Chapter 2 outlines various experimental methods employed for the synthesis and characterization of various materials during the research conducted and reported in the present thesis. Principle behind important characterizationsare briefly discussed in this chapter. The instrumentation details of the NAPPES facility available at CSIR-NCL, Pune are discussed along with the experimental conditions for In-situ experiments.

Oxidation and reduction reactions play a fundamental role in catalysis, and gaining insights into how catalysis behaves under these conditions is crucial for understanding subsequent catalytic processes. Furthermore, understanding the mechanisms of formation or transformation holds significant significance from both a material and catalysis perspective. In **Chapter 3**, we utilized VB and core-level photoelectron spectroscopy to examine electronic structural modifications as polycrystalline Vanadium (V) evolved into various vanadium oxides through systematic oxidation. This oxidation process involved varying O_2 partial pressures, temperatures, and durations. We assessed the oxidative interaction between O_2 and V in a gas-solid system using UV photons (He-I) under NAP conditions. Notably, we observed distinct VB features corresponding to V metal, V_2O_3, VO_2, and mixed phases such as V_2O-V_2O_3 and VO_2-V_2O_5, with the transitions between these features aligning consistently with core-level changes. We noticed significant and distinctive alterations in the V 3d features of the VB, and we also observed changes in the ϕ as we modified the surface properties. We established a significant correlation between variations in the ϕ and the oxidation state of the cation. Even minor changes in stoichiometry had a pronounced impact on the shift in the E_F. These reversible changes in ϕ, observed during oxidation and reduction conditions, directly influence the energy at the VB edge, thereby affecting the catalytic reaction. In summary, this research underscores the importance of comprehending electronic structural transformations during the oxidation process in catalysis, as they have a direct impact on catalytic behavior and can be effectively studied using the NAPPES technique.

In **Chapter 4**, we delved into the redox behavior of copper (Cu) through a systematic process of oxidation and reduction in the presence of oxygen (O_2) and hydrogen (H_2). We employed NAP-UPS to thoroughly investigate the progressive changes in the electronic structure of copper. This involved the transformation of Cu metal into Cu_2O and CuO, followed by reduction back to Cu_2O and Cu. These transformations occurred under various conditions, including variations in pressure, temperature, and the duration of oxidation and reduction processes in the presence of molecular oxygen and hydrogen, respectively. This study focuses on elucidating the modifications in the VB of a pristine polycrystalline Cu-metal foil during the processes of oxidation and subsequent reduction. We further explored the systematic oxidation and reduction processes by examining the vibrational characteristics of gaseous O_2 and H_2. This analysis was conducted using NAP-UPS, allowing us to monitor alterations in the ϕ as a means to gain insights into the mechanisms underlying oxidation and reduction pathways. Our observations revealed that systematic heating of Cu metal foil in the presence

of oxygen led to a systematic progression from Cu to Cu_2O and subsequently to CuO at 675K, with an increase in the pressure ranging from 10^{-6} to 1 mbar oxygen partial pressure. Notably, the overlapping of the Cu 3d with the oxygen 2p orbital was not observed with Cu_2O, while it is observed with CuO. The modifications in the VB features indicated the deeper advancement of oxidation across the Cu surface; while the reverse is observed during reduction, but not to the same extent, as that of oxidation. The control of surface energy, particularly the ϕ, is a topic of significant interest in the field of surface and interface-based devices and applications. It is crucial for both chemists and physicists, especially in disciplines that involve surface-dependent phenomena such as nanoscience, catalysis, and electrochemistry, to comprehend how the ϕ of a solid surface evolves under reaction conditions.

The challenge posed by the material gap can be mitigated to some extent by optimizing model systems like powdered metal oxides and alloys**. Chapter 5a** and **5b** provide an illustration of such a model system applied to CO_2 hydrogenation. Given the importance of converting carbon dioxide, a greenhouse gas, into valuable feedstocks like carbon monoxide and methanol, this research delves into the hydrogenation of CO_2 using hydrogen as the reducing agent through the RWGS process. To achieve this we employed morphology dependent low-cost transition metal based Co and Ni oxides catalyst. Co_3O_4NC and Co-Ni core shell morphology was used to investigate the CO_2 hydrogenation under varying conditions of temperature and CO_2:H_2 ratio. The study reveals that mix phase of Co (II) and Co(III) are responsible for the selective CO production, especially at 723 K and ambient pressure, with hydrogen deprived condition. In situ studies reveal that Co (II) is highly prone to the activation of CO_2 at lower temperature compared to spinel Co_3O_4 and Co metal. XRD also reveal the mixed-phase of Co oxide is responsible for the selective high conversion of CO_2 and selective CO production. In chapter 5b, similar experiments were performed with 1:3 ratio of CO_2:H_2 where we observed the synergistic effect between Co and Ni at 525 K. Under the reaction conditions, core Ni is segregated over the surface and it forms bimetallic alloy; along with CO, formic acid formation was also observed as products at 0.1 mbar CO_2+H_2 pressure. In addition, this research delved into the mechanistic aspects of the RWGS reaction by utilizing NAPPES. CoO and Co metal were *in-situ* generated through reduction with H_2, and NAPPES experiments were conducted at near-ambient pressures (0.1 mbar) and various temperatures. These investigations revealed a robust correlation between the catalytic activity observed under atmospheric pressure conditions and the electronic structural information derived from NAP-XPS results, thereby establishing a well-defined structure-activity relationship.

In general, the research covered in this thesis underscores the distinctive potential of NAPPES in detecting both subtle and significant alterations in the electronic structure of solid surfaces during typical oxidation and reduction processes. This capability renders NAPPES highly pertinent to a wide array of surface-related phenomena, encompassing catalysis and electrochemistry. **Chapter 6** offers an extensive overview of the findings presented in this thesis, coupled with prospective avenues for future research direction.

1.10 References

1. Nguyen, L.; Tao, F. F.; Tang, Y.; Dou, J.; Bao, X. J.*Chem. Rev.* **2019**, 119, 12, 6822–6905
2. https://www.psi.ch/swissfel/chemical-time-scales
3. Günther Rupprechter, *Small* **2021**, *17*, 2004289.
4. Ertl, G.*Angew. Chem. Int. Ed.***1990**, *29*, 1219-1227.
5. Ertl, G.*Angew. Chem. Int. Ed.* **2008**, *47*, 3524-3535.
6. Hind, A. R.; Bhargava, S. K.; McKinnon, A.*Adv. Colloid Interface Sci.* **2001**, *93*, 91-114.
7. Kim, J.; Choi, H.; Kim, D.; Park, J. Y.*ACS Catal.***2021**, *22*, 8645–8677.
8. Somorjai, G.A.*Introduction to Surface Chemistry and Catalysis.*John Wiley&Sons, 2010.
9. Yu, W.; Porosoff, M. D.; Chen, J. G.*Chem. Rev.***2012**, *26*, 5780–5817.
10. Choi, J. I. J.; Kim, T. S.; Kim, D.; Lee, S. W.; Park, J. Y. *ACS Nano* **2020**, *28*, 16392–16413.
11. Rupprechter, G.; Weilach, C.*J. Phys.: Cond. Matter*. **2008**, *20*, 184019/1.
12. Huo, J.; Tessonnier, J.-P.; Shanks, B. H.*ACS Catal.* **2021**, *11*, 5248−5270.
13. Thomson, J. J.*Proceedings of the Cambridge Philosophical Society* **1907**, 407.
14. Jentoft, F.*Angew. Chem., Int. Ed.* **2003**, *42*, 256.
15. Bürgi, T.*ChemPhysChem.* **2003**, *4*, 402–403.
16. Fadley, C. S.; Brundle, C. R.*Surface and Interface Analysis* **1978**, *2*, 1.
17. Fadley, C. S.; Brundle, C. R.*Surface and Interface Analysis* **1978**, *2*, 1.
18. http://cleanenergywiki.org
19. Siegbahn, H.*J. Phys. Chem.* **1985**, *89*, 897.
20. Eley, D. D., Pines, H., Weisz, P. B., Eds.; Academic Press: **1980**; Vol. 29, p 55.
21. Joyner, R. W.; Roberts, M. W.; Yates, K. A.*Surf. Sci.***1979**, *87*, 501−509.
22. Hussain, Z.; Huff, W. R. A.; Kellar, S. A.; Moler, E. J.; Heimann, P. A.; McKinney, W.; Padmore, H. A.; Fadley, C. S.; Shirley, D. A.*J. Electron Spectroscopy Rel. Phen.* **1996**, *80*, 401.
23. Sawhney, K. J. S.; Senf, F.; Gudat, W.*Nucl. Instr. Meth. Phys. Res.* **2001**, *467-468*, 466.
24. Ogletree, D. F.; Bluhm, H.; Lebedev, G.; Fadley, C. S.; Hussain, Z.; Salmeron, M.*Rev. Sci. Instrum.* **2002**, *73*, 3872.

25. Schnadt, J.; Knudsen, J.; Andersen, J. N.; Siegbahn, H.; Pietzsch, A.; Hennies, F.; Johansson, N.; Mårtensson, N.; Öhrwall, G.; Bahr, S.; Mähl, S.; Schaff, O.*J. Synchrotron Radiat.* **2012**, *19*, 701.
26. Starr, D. E.; Liu, Z.; Havecker, M.; Knop-Gericke, A.; Bluhm, H.*Chem. Soc. Rev.* **2013**, *42*, 5833.
27. Tao, F.*ChemCatChem.* **2012**, *4*, 583.
28. Eriksson, S. K.; Hahlin, M.; Kahk, J. M.; Villar-Garcia, I. J.; Webb, M. J.; Grennberg, H.; Yakimova, R.; Rensmo, H.; Edström, K.; Hagfeldt, A.; Siegbahn, H.; Edwards, 30. M. O. M.; Karlsson, P. G.; Backlund, K.; Åhlund, J.; Payne, D. J.*Rev. Sci. Instrum.* **2014**, *85*, 075119.
29. Roy, K.; Vinod, C. P.; Gopinath, C. S. *J. Phys. Chem. C.* **2013**, *117*, 4717.
30. Turner, J. E.; Sales, B. C.; Maple, M. B. *Surf. Sci.* **1981**, *103*, 54-74.
31. Ertl, G.; Norton, P. R.; Rüstig. *J. Phys. Rev. Lett.* **1982**, *49*, 177-180.
32. Nagarajan, S.; Thirunavukkarasu, K.; Gopinath, C. S. *J. Phys. Chem. C*, **2009**,*113*, 7385-7397.
33. Gopinath, C. S.; Roy, K.; Nagarajan, S.*ChemCatChem.* **2015**, *7*, 588-594.
34. Roy, K.; Gopinath, C. S.*Anal. Chem.* **2014**, *86*, 3683–3687.
35. Ranjan, R.; Mhamane, N. B.; Kolekar, S.; Gopinath, C. S. *J. Phys. Chem. C*, **2022**, *126*, 19136.
36. Reddy, K. P.; Mhamane, N. B.; Kumar Ghosalya, M.; Gopinath, C. S.*J. Phys. Chem. C.* **2018**, *122*, 23034–23044.
37. Gopinath, C. S.; Roy, K.; Nagarajan, S.*ChemCatChem.* **2015**, *7*, 588-594.
38. Jain, R.; Reddy, K. P.; Ghosalya, M. K.; Gopinath, C. S.*J. Phys. Chem. C.* **2017**, *121*, 20296-20305.
39. Eichelbaum, M.; Hävecker, M.; Heine, C.; Wernbacher, A. M.; Rosowski, F.; Trunschke, A.; Schlögl, R. *Angew. Chem. Int. Ed.* **2015**, *54*, 2922-2926.
40. Ranjan, R.; Tekawadia, J.; Jain, R.; Mhamane, N. B.; Raja, T.; Gopinath, C. S. *Chem. Eng. J.* **2023,** *471*, 144459.
41. Mhamane, N. B.; Chetry, S.; Ranjan, R.; Raja, T.; Gopinath, C.S. *ACS Sustainable Chem. Eng.* **2022**, 10, 3521−3531.
42. Nicot, J. P.; Duncan, I. J.*Greenh. Gases: Sci.***2012**, *2*, 352–368.
43. Freund, H. J.; Roberts, M. W.*Surf. Sci. Rep.***1996**, *25*, 225–273.
44. Rasmussen, P. B.; Holmblad, P. M.; Askgaard, T.; Ovesen, C. V.; Stoltze, P.; Nørskov, J. K.; Chorkendorff, I.*Catal. Lett.* **1994**, *26*, 373–381.
45. Chorkendorff, I.; Taylor, P. A.; Rasmussen, P. B.*J. Vac. Sci. Technol. A,* **2002**, *10*, 2277–2281.
46. Szanyi, J.; Goodman, D. W.*Catal. Lett.***1991**, *10*, 383–390.
47. Eren, B.; Weatherup, R. S.; Liakakos, N.; Somorjai, G. A.; Salmeron, M.*J. Am. Chem. Soc.* **2016**, *138*, 8207–8211.
48. Posada-Borbon, A.; Hagman, B.; Schaefer, A.; Zhang, C.; Shipilin, M.; Hellman, A.; Gustafson, J.; Grönbeck, H.*Surf. Sci.* **2018**, *675*, 64–69.
49. Hagman, B.; Posada-Borbón, A.; Schaefer, A.; Shipilin, M.; Zhang, C.; Merte, L. R.; Hellman, A.; Lundgren, E.; Grönbeck, H.; Gustafson, J.*J. Am. Chem. Soc.* **2018**, *140*, 12974–12979.

50. Koitaya, T.; Yamamoto, S.; Shiozawa, Y.; Takeuchi, K.; Liu, R.-Y.; Mukai, K.; Yoshimoto, S.; Akikubo, K.; Matsuda, I.; Yoshinobu, J.*Top. Catal.* **2016**, *59*, 526–531.
51. Koitaya, T.; Yamamoto, S.; Shiozawa, Y.; Takeuchi, K.; Liu, R.-Y.; Mukai, K.; Yoshimoto, S.; Akikubo, K.; Matsuda, I.; Yoshinobu, J.*Top. Catal.* **2016**, *59*, 526–531.
52. Ren, Y.; Yuan, K.; Zhou, X.; Sun, H.; Wu, K.; Bernasek, S. L.; Chen, W.; Xu, G. Q.*Chem. Eur. J.* **2018**, *24*, 16097–16103.
53. Regoutz, A.; Kerherve, G.; Villar-Garcia, I.; Williams, C. K.; Payne, D. J.*Surf. Sci.* **2018**, *677*, 121–127.
54. Vesselli, E.; De Rogatis, L.; Ding, X.; Baraldi, A.; Savio, L.; Vattuone, L.; Rocca, M.; Fornasiero, P.; Peressi, M.; Baldereschi, A.; Rosei, R.; Comelli, G.*J. Am. Chem. Soc.* **2008**, *130*, 11417–11422.
55. Freund, H.-J.; Roberts, M. W.*Surf. Sci. Rep.* **1996**, *25*, 225–273.
56. Bi, Q.; Huang, X.; Yin, G.; Chen, T.; Du, X.; Cai, J.; Xu, J.; Liu, Z.; Han, Y.; Huang, F.*Chem. Cat. Chem.* **2019**, *11*, 1295–1302.
57. Heine, C.; Lechner, B. A. J.; Bluhm, H.; Salmeron, M.*J. Am. Chem. Soc.* **2016**, *138*, 13246–13252.
58. Liu, Q.; Han, Y.; Cai, J.; Crumlin, E. J.; Li, Y. M.; Liu, Z.*Catal. Lett.* **2018**, *148*, 1686–1691.
59. Deng, X. Y.; Verdaguer, A.; Herranz, T.; Weis, C.; Bluhm, H.; Salmeron, M.*Langmuir*, **2008**, *24*, 9474–9478.

Chapter 2

Experimental Section

2.1 Introduction

The rational design and development of novel catalyst represent the foremost and most formidable aspects of heterogeneous catalysis. [**1-2]** Nevertheless, given that catalysis predominantly occurs on the surface, a profound comprehension of the surface structure and its correlation with activity demands the utilization of advanced surface science tools. [**3-4**] Numerous surface science techniques exist for characterizing catalyst surfaces. No single technique can offer a complete comprehension of surface structure. However, by combining these techniques, one can glean valuable insights. These insights encompass details regarding surface adsorption of reactants, their diffusion to active sites, the presence of intermediates, possible products, alterations in surface electronic structure and morphology, and correlations between catalytic performance and potential intermediates. Over the past several decades, photoelectron spectroscopy has gained widespread usage on a global level for investigating the surface electronic structure and chemical composition of catalytic materials in surface science. Among all the surface science technique, photoelectron spectroscopy stands out as a powerful technique due to its inherent surface sensitivity and ability to discern elemental and chemical specifics. Significantly it can also be employed as *in-situ* technique, known as NAPPES offering additional advantage for studying surface phenomenon.

However, global and persistent endeavours have contributed to the development of surface science technique capable of operating under realistic conditions, effectively bridging the gaps in pressure and material considerations. [**5-7**]. Such advancements have propelled the progress of surface science and evolution of NAPPES, facilitating the investigation of surface phenomenon at near ambient pressure (NAP) conditions. While majority of the surface science studies traditionally focussed on ideal single-crystal surfaces [**8-11]**, real-world catalysts exhibit several distinctive properties, including porosity, high surface area, surface defects, and interfaces between active metal and support. These complexities introduce materials that significantly influence catalytic processes, shaping the landscape of heterogeneous catalysis. Consequently, questions arise regarding the applicability of surface science studies conducted on single crystalunder ideal conditions to realworld catalysis that occur under harsh conditions. **[12]**

Moreover, the active phase of the catalyst may differ during the reaction due to adsorbate induced changes in the surface electronic structure. NAPPES provide an avenue to explore these aspects for various catalytic reactions. The primary objective of this thesis is to address and minimize the existing gaps inmaterial and pressure considerations between surface science

and real-world catalysis process such as CO_2 reduction reaction. To find the active states and electronic structure changes during catalysis we employed Co_3O_4 NC and Ni@Co core shell nano-particle. In **chapter 5a** and **5b**, we studied CO_2 hydrogenation overthese catalystat relevant temperature range and at atmospheric pressure with Co_3O_4 and at NAPPES conditions with Ni@Co. Our finding indicates that surface nature changes during the redox conditions and the electronic nature also changes along with the ϕ.

In the initial section of this thesis, we have addressed synthesis aspects of Co_3O_4 NC and Ni-Co core-shell nanoparticles. Accompanied by comprehensive synthesis techniques, several characterization methods pertaining to these catalysts are succinctly elucidated. Subsequent to the characterization techniques, experimental conditions governing the catalytic activity elucidation of spinel Co_3O_4 NC and Ni-Co core-shell nanoparticles has been optimized for CO_2 reduction. Following this, essential design aspects of the NAPPES system at CSIR-NCL will be deliberated, alongside the experimentalconditions for in situ experiments.

2.2 Synthesis of spinel Co_3O_4 NC

2.2.1 Chemical Required: All chemicals were of analytical grade and were employed without additional purification. Precursor $Co(OAC)_2.4H_2O$ was purchased from Alfa Aesar.

2.2.2 Synthesis procedure:

Co_3O_4 NC was prepared using a wet chemical synthesis method following procedures outlined in the literature **[13]**, as depicted in Figure 2.1. Specifically, a template-free hydrothermal approach was employed, utilizing $Co(OAC)_2 \cdot 4H_2O$ as the cobalt precursor. Initially, 2.5 mmol $Co(OAC)_2 \cdot 4H_2O$ was dissolved in 125 ml of water and stirred for 30 minutes. Aqueous ammonia was then added dropwise until the solution's pH reached 9, indicated by a color change from pink-red to blue. The solution was further stirred for 30 minutes and subsequently transferred into a 200 ml autoclave with a Teflon liner, where it was heated to 453 K for 10 hours. The resulting Co_3O_4 solid was filtered and subjected to multiple washes with deionized water. Finally, the sample was calcined in air at 623 K for 3 hours.

2.3 Synthesis of Ni-Co core-shell nanoparticles

2.3.1 All necessary chemicals, including $NiCl_2 \cdot 6H_2O$, $CoCl_2 \cdot 6H_2O$, ethylene glycol, NaOH, PVP, and hydrazine hydrate, were of analytical grade and were utilized without the need for additional purification. Precursor $NiCl_2.6H_2O$, $CoCl_2.\ 6H_2O$, ethylene glycol, NaOH , PVP, hydrazine hydrate.

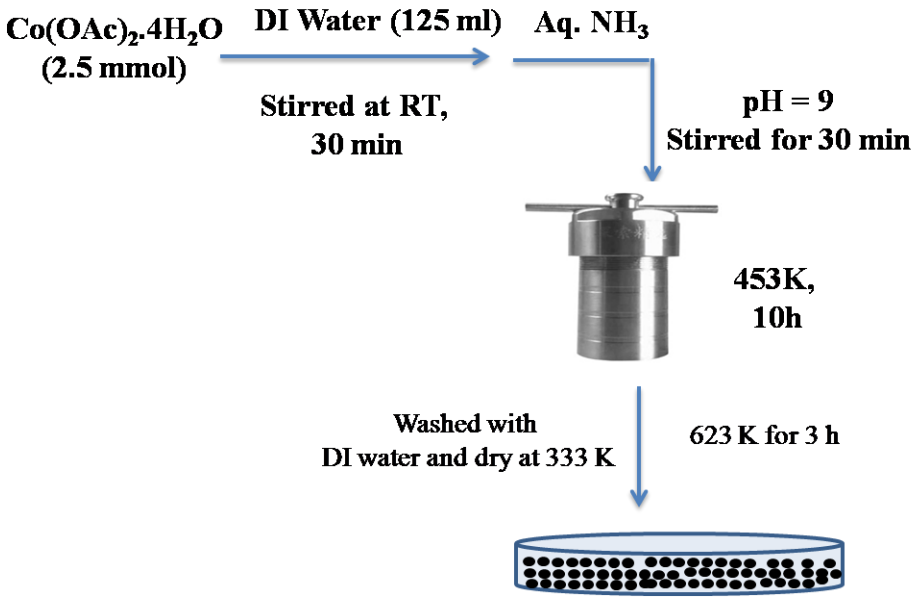

Figure 2.1: Schematic representation of Co_3O_4 NC catalyst synthesis by hydrothermal method.

2.3.2 Synthesis Procedure:

Ni@Co core-shell (NiCo) nanoparticles were prepared in a Ni:Co ratio of 2:1 using a reductant-free pH-assisted polyol method with ethylene glycol as the solvent and PVP as a surfactant. In this standard synthesis procedure, the $NiCl_2 \cdot 6H_2O$ precursor, along with PVP, was dispersed in ethylene glycol, 1M NaOH, and hydrazine hydrate (510 µl) under a nitrogen (N_2) atmosphere and stirred at room temperature for 15 minutes. This was followed by heating to 353 K for 30 minutes, during which the nickel precursor was reduced to form black Ni nanoparticles. Subsequently, the temperature was raised to 393 K, and the $CoCl_2 \cdot 6H_2O$ precursor, along with hydrazine hydrate (510 µl), was rapidly injected. This led to the reduction of cobalt ions, facilitated by the change in pH. The reaction mixture was allowed to age for 10 minutes to stabilize the Ni@Co nanoparticles and then cooled to room temperature. The prepared nanoparticles were easily separated using an external magnet. The surfactant PVP was removed by subjecting the separated nanoparticles to repeated sonication with isopropyl alcohol (IPA). Finally, the separated nanoparticles were dispersed in hexane (to prevent cobalt surface oxidation) and stored in desiccators. Just before reactions or any structural/spectral measurements, the nanoparticles were dried at 333 K and used.

2.4 CO_2 catalytic reduction on Co_3O_4 NC

The CO_2 reduction reaction was carried out in a fixed-bed down flow reactor with an internal diameter of 12 mm and a length of 40 cm, operating at atmospheric pressure. A thermocouple was positioned at the center of the 1 cm^3 catalyst bed. The catalyst particles, ranging in mesh

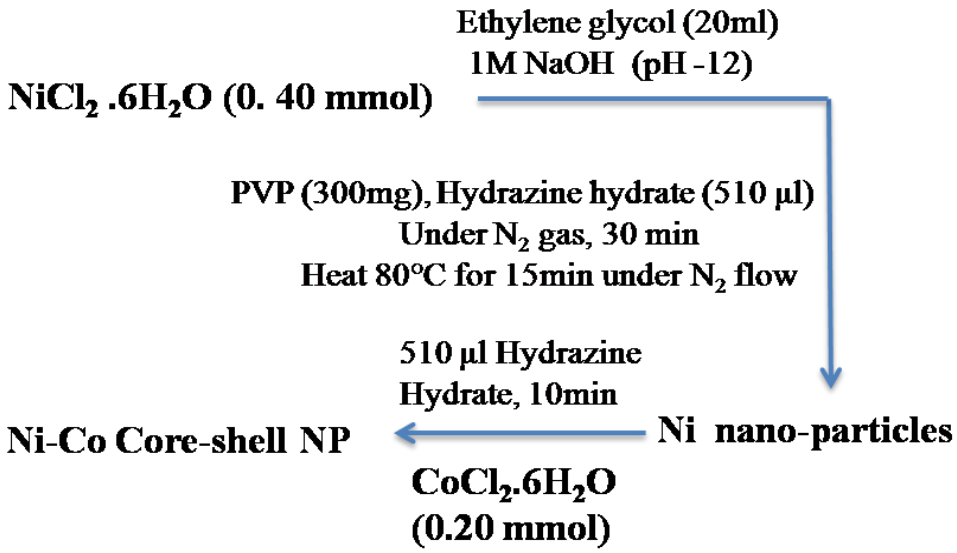

Figure 2.2: Schematic representation of NiCo core-shell catalyst synthesis by polyol method.

size from 35 to 50, were blended with alumina pieces of equal volume and particle size, and then placed in the uniformly heated section of the tubular reactor. Prior to the reaction, the catalyst was preheated in static air to 523 K at a rate of 5 K/min and held at this temperature for 2 hours. The experiment was conducted at desired reaction temperatures. The gaseous products were continuously monitored using a Trace 3110 gas chromatograph from Thermoscientific. This chromatograph was equipped with a thermal conductivity detector (TCD) and a Porapak Q column, which had a diameter of 0.2 mm and a length of 6 meters. Prior to conducting the experiment, a calibrated gas mixture was employed to identify the gas components. We evaluated the catalytic activity and selectivity of Co_3O_4 NC at temperatures of 450 and 823 K and with CO_2:H_2 ratios of 1:3, 1:2, 1:1, and 3:2. The CO_2 + H_2 gas mixture was generated using mass flow controllers specific for H_2 and CO_2. It is worth noting that no carrier gas was used with the reactant, which is advantageous from a process standpoint and indicates that product desorption does not require any carrier gas. Prior to commencing any GC analysis for reaction measurements, the reaction temperature was permitted to stabilize for roughly 30 minutes to achieve a steady state. The total gas mixture flow rate was set at 320 ml/min, and the gas hourly space velocity (GHSV) for the entire reactor studies was 19200 h^{-1} high GHSV ensures that mass transfer resistance has no significant role in the present studies. Time on stream (ToS) was also conducted for 12 h with 3:2 CO_2:H_2at 623 and 723 K. The reaction conversion and product selectivity were calculated using the following equations:

$$CO_2 \text{ Conversion } (\%) = \frac{nCO_2(in) - nCO_2(out)}{nCO_2\ (in)} \text{ X } 100 \qquad (2.1)$$

$$H_2 \text{ Conversion } (\%) = \frac{nH_2 \text{ (in)} - nH_2 \text{ (out)}}{nH_2 \text{ (in)}} \text{ X } 100 \quad (2.2)$$

$$CO \text{ Selectivity}(\%) = \frac{nCO \text{ (out)}}{nCO \text{ (out)} + nCH_4 \text{ (out)}} \text{ X } 100 \quad (2.3)$$

$$CH_4 \text{ Selectivity}(\%) = \frac{nCH_4 \text{(out)}}{nCO \text{ (out)} + nCH_4 \text{ (out)}} \text{ X } 100 \quad (2.4)$$

2.5 Ex-situ Characterization

2.5.1 X-Ray diffraction

X-Ray Diffraction (XRD) is a non-destructive analytical method used extensively for characterizing catalysts. It plays a crucial and highly important role in determining phases, crystal structures, interplanar distances, crystallite sizes, and the purity of crystalline materials. The smallest repetitive structural component within the crystal lattice is referred to as the 'unit cell', which imparts vital information about atomic arrangement and crystal geometry. Given that the wavelength of the X-rays employed in this technique, such as 1.54 Å (Cu Kα), is commensurate with the dimensions of atoms within the lattice, X-rays can effectively penetrate solids, rendering them ideally suited for probing the atomic arrangements within the bulk materials. **[14]**

Principle:

Let's examine a scenario where monochromatic plane X-ray wave strikes a crystal at an angle of incidence θ, as depicted in Figure 2.3. We denote the wavelength of the X-ray beam as λ (measured in m), and the crystal exhibits equidistance atomic planes are in phase, they combine constructively, resulting in what we call X-ray diffraction. To achieve a phase difference of zero, the disparity in optical path length between the top and bottom wave must equal an integer, denoted as 'n', times the wavelength λ. In Figure 2.3, this optical path difference is represented as ACB, with a length equal to 2d Sinθ. In simpler terms, the condition for diffraction can be expressed as follows:

When X-rays interact with a crystalline solid material, they can go through two processes: coherent scattering and incoherent absorption. Coherently scattered X-ray waves show interference effects, which create either bright or dark fringes. Bright fringes are the result of constructive interference, which happens when X-rays scatter at certain angles, and the path The equation referred to as the "Bragg Equation" is represented mathematically as follows: nλ = 2d Sin(θ), where "n" represents the order of reflection or diffraction, "θ" is the Bragg angle, "λ" is the wavelength of X-rays, "d" is the interplanar distance, and "n" is the order of

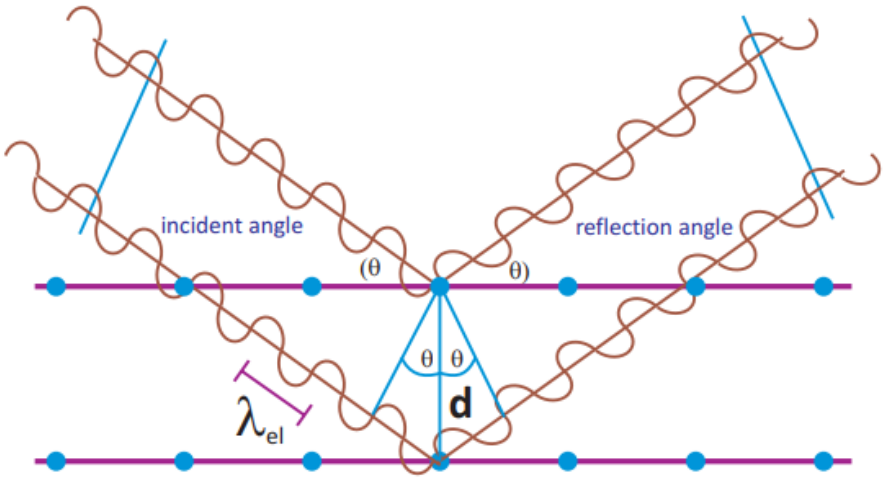

Figure 2.3 Schematic representation of the diffraction of X-ray in crystalline materials. Bragg reflection (diffraction) on a set of atomic planes. **Ref [15]**

difference between them is a whole-number multiple of the wavelength. This phenomenon is commonly known as X-ray diffraction Bragg's equation establishes a connection between the wavelength of the electromagnetic rays, the diffraction angle, and the lattice spacing. [**15**]

$$2d\ \mathbf{Sin\theta} = n\lambda \quad (2.5)$$

When various solid materials are examined at different 2θ angles ranging from 1 to 90°, distinct diffraction patterns emerge due to the random orientations of crystallites within the material. Since each material has its unique d-spacing value, Bragg's equation can be employed to calculate these d-values. By comparing these values with a reference pattern, such as the Joint Committee on Powder Diffraction Standards (JCPDS), it becomes possible to identify the structural characteristics of the material. Additionally, the Full Width at Half Maximum (FWHM) of a diffraction peak in the diffraction pattern provides information about the dimensions of the reflecting planes. The Scherer formula can be used to calculate the average crystallite size for monomaterials.

$$\mathbf{D = 0.9\lambda / \beta.\ Cos\theta\ (2.6)} \quad (2.6)$$

The formula used to calculate the thickness of the crystal involves several parameters: "D" represents the crystal's thickness, "λ" denotes the wavelength of the incident X-ray photon, "θ" signifies the angle between incident rays and the lattice plane, and "β" is determined through the Warren formula, where $\beta = \beta^2_M - \beta^2 s$. Here, "β" represents the FWHM difference between the studied materials and a standard sample (Silicon). In this thesis, XRD analysis was conducted on various materials, including as-synthesized Co_3O_4 NC powder, pure Co_3O_4, reduced Co_3O_4, and Ni@Co core-shell nanoparticles. The analysis employed powder XRD

with a Cu Kα X-ray photon source, which has a radiation wavelength of 1.5406 Å. The scanning rate was set at 3º per minute, covering a 2θ angle range from 10° to 85°.

2.5.2 H_2-Temperature-programmed reduction (H_2-TPR)

The technique of Temperature Programmed Reduction (TPR) is widely utilized in the field of heterogeneous catalysis for the characterization of various materials, including metal oxides, metal carbides, and metals supported on oxides. This method, initially developed by John Jenkins during his tenure at Shell petrochemical industries **[16]**, offers a quantitative assessment of the reducibility of these materials and the variability of their reducible surfaces. In TPR, a reducing gas, typically a mixture of H_2 or CO diluted with Argon (comprising 5/10% H_2/CO in Argon), is passed over the sample. Changes in the amount of the reducing gas result in alterations in thermal conductivity, which are subsequently detected by a thermal conductivity detector (TCD).

H_2-TPR experiments were carried out using a Micromeritics Autochem 2920 system equipped with a TCD detector. Initially, a freshly synthesized catalyst was subjected to heating at a rate of 5 K/min in a flow of helium gas (30 ml/min) until it reached 573K. The sample was held at a temperature of 573 K for a duration of 30 minutes and then gradually cooled to 325 K. Afterward, the gas stream was changed to a mixture of 10% H_2 in Argon gas (at a flow rate of 30 ml/min), and the catalyst underwent heating to reach 1173 K, following a heating rate of 5 K/min. The TCD detector was used to continuously monitor and record the consumption of H_2. A visual representation of the H_2-TPR instrumentation can be seen in Figure 2.4.

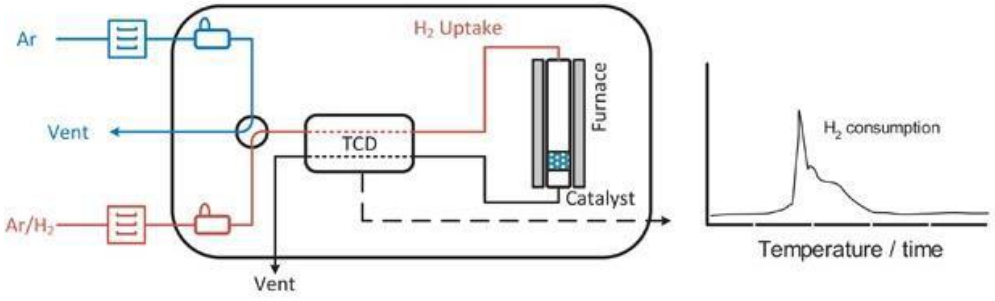

Figure 2.4 Schematic design for H_2-TPR design. Figure reproduced from **Ref. [17],** Copyright permission obtained from Science Direct.

2.5.3 High Resolution-Transmission Electron Microscopy (HR-TEM):

In adequate lighting conditions, the human eye can distinguish details in an image up to a precision of approximately 0.2 millimetres at an optimal viewing distance. In comparison, a light microscope enhances resolution by factor of up to 1000 times when compared to the

human eye. This improvement is quite significant because typical white light has an average wavelength of around 550 nm, which sets a theoretical limit on the resolution of light microscopes at approximately 200-250 nm. The resolving capability of a light microscope depends not only on the quality and quantity of its lenses but also on the wavelength of the photons it uses. To overcome this limitation, electron microscopy replaces white light with electrons, which have much shorter wavelengths, resulting in substantially enhanced resolution. This technological advancement has enabled the examination of specimens with much greater precision.**[18]** There are two primary types of electron microscopes used for material characterization: (1) Transmission Electron Microscopy (TEM) and (2) Scanning Electron Microscopy (SEM).

TEM is an advanced microscopy technique employed for the nanoscale analysis of materials. Its operational principal parallels that of traditional microscopes, but it distinguished itself by utilizing transmitted electrons, rather than light, to create images. When an electron beam traverses a thin specimen of materials, electron scattering phenomena become apparent. The electron microscope was originally conceived by Ernst Ruska and Max Knolls in 1931, and later in 1933; however, Ernst Ruska adapted it into the TEM. The capacity to generate exceptionally high-quality and finely resolved images primarily hinges on the interaction between the atoms within the sample and the electron beam.

High resolution TEM (HR-TEM) possesses the capability to characterize samples down to the atomic level, making it immensely valuable for examining nanostructures. In the course of its operation, electrons emitted by the electron source engage with the atoms within the sample, leading to scattering events. Among these, elastically scattered electrons assume a paramount role in the final data interpretation and the generation of high-quality, finely resolved images. Throughout the imaging process, the phase contrast and resolution of the data can be affected by the aberration effects steaming from the objective lenses. For the thesis research, high-resolution transmission electron microscopy (HR-TEM) analysis was conducted at 298 K using the JEOL JEM F-200 instrument, operating at an accelerating voltage of 200 kV. A beam energy of 511.8 pA/cm^2 and an emission current of 214.5 μA at a5° angle were utilized. Sample preparation involved dispersing a very small quantity of catalyst in isopropyl alcohol, followed by sonication for 1hour. The prepared samples were then drop-cast onto TEM grids.

2.5.4 Field-Emission Scanning Electron Microscopy (FESEM):

SEM is a microscopy technique extensively employed for the examination of morphology of solid materials.SEM operates by scanning a solid surface using a focused and highly energetic

electron beam, which in turn generates an image providing valuable insights into the material's morphology. The electron source, often composed of materials like tungsten or lanthanum hexaboride (LaB_6), is meticulously controlled through a series of lenses and apertures toprecisely target the sample's surface, typically under ultrahigh vacuum (UHV) conditions. Depending on factors such as the electron beam's accelerating voltage and the sample's density, the beam can penetrate a few microns into the material, resulting in the emission of secondary electrons, backscattered electrons (reflected), transmitted electrons, and characteristic X-rays. High-resolution images are predominantly generated by detecting the secondary electron emissions from atoms near the surface. The contrast in these images is typically influenced by the sample's orientation relative to the detector, with surface areas facing the detector appearing brighter than those oriented away from it. When an electron from the beam encounters a nucleus within the sample, the resulting coulombic attraction causes the electron's path to deviate, this phenomenon is referred to as Rutherford elastic scattering, where certain electronsexperience complete backscattering, emerging from the sample's incident surface. As the scattering angle depends on the atomic number of the nucleus, the primary electrons reaching a specific detector position can be utilized to create images that contain both topographical and compositional details. The energy of the characteristic X-rays can be quantified using energy dispersive X-ray spectroscopy (EDX analysis), which assists in both qualitative and quantitative assessments of the elements present in the sample. **[20]**

For SEM sample preparation, generally, the materials were dispersed in IPA via ultrasonication for 30 minutes. Following proper dispersion, the solution was drop-casted onto silicon wafer (or on sample holder) and allowed to dry at room temperature before analysis. Image acquisition was conducted utilizing an environmental scanning electron microscope (ESEM) Quanta-200 3D system operating at 20 kV. Additionally, the chemical composition of the catalyst was assessed via SEM-EDX by examining various random sample spots. Schematic diagram of the HR-TEM and SEM has given in Fig. 2.5 and Fig. 2.6 respectively.

2.6 Near-Ambient Pressure Photoelectron Spectroscopy (NAPPES)

To obtain a deeper understanding of the interaction between the catalyst's surface and gaseous molecules, and to address the current pressure disparity in the domains of catalysis and materials science , there is strong need for surface characterization technique that can operate effectively at or near ambient pressure conditions. However, surface-sensitive methodologies like PES encounter limitations when applied under high pressure environments, primarily

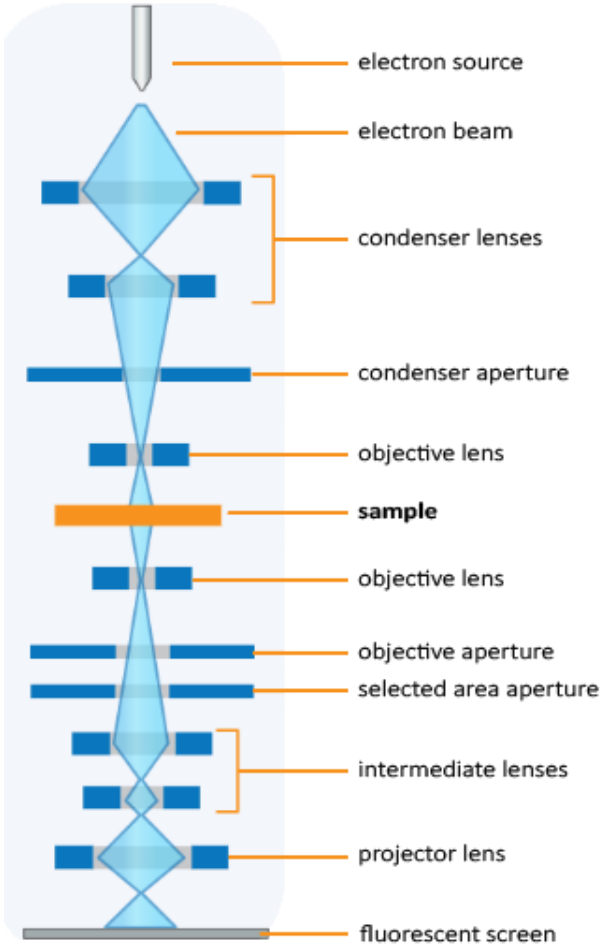

Figure 2.5 Schematic representation of HR-TEM. Figure reproduced from ref. **[19],** and permission was obtained from Micobenotes.

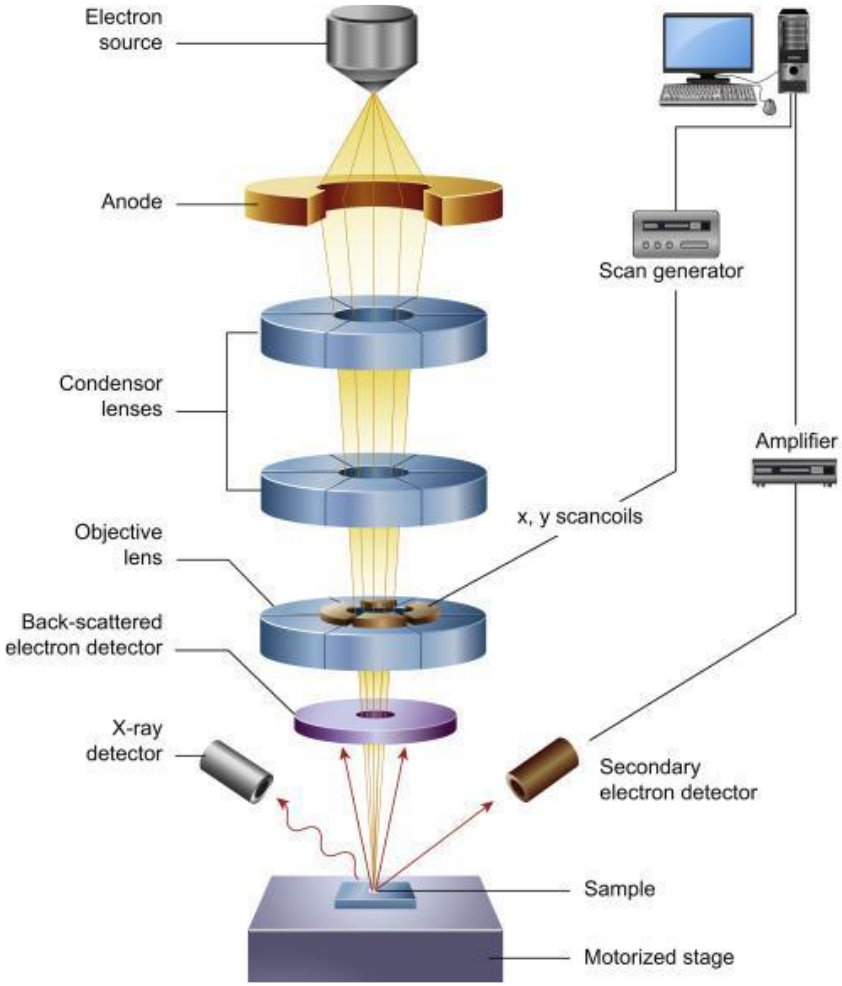

Figure 2.6 Schematic diagram of the core components of SEM microscope. Figure reproduced from ref. **[18]**

because gas-phase molecules cause substantial attenuation of photoelectrons. This attenuation phenomenon adheres to Beer's law, which governs the relationship between the absorption of light and the concentration of absorbing species in a medium.

$$I = I_0 e(-z\sigma_{K.E}\, P/kT) \quad (2.7)$$

The emitted electron intensity detected by the analyzer at a specific pressure (P) is represented by I, while I_0 stands for the emitted electron intensity detected by the analyzer in UHV. In this context, 'z' signifies the distance traveled by electrons in the gas at pressure P and temperature T, and 'k' represents the Boltzmann constant. The electron scattering cross-section, denoted as $\sigma_{K.E}$, depends on the kinetic energy of the electrons and the properties of the gas through which they traverse **[21]**. Under increased pressure conditions, photoelectrons may undergo elastic scattering, preserving their kinetic energy, and potentially scatter outside the analyzer's acceptance cone. Additionally, there can be inelastic scattering events caused by the excitation of gas molecules in their vibrational, rotational, and electronic states. As a result, inelastically scattered photoelectrons contribute to an elevated background signal at lower kinetic energies, leading to a reduction in the intensity of characteristic peaks.

The mean free path of electrons, referred to as λe, depends on both the energy of the electron and the gas pressure (P). With increasing pressure, λe decreases, making it necessary to position the sample in close proximity to the analyzer cone aperture. Additionally, maintaining an appropriate distance (d) between the solid sample surface and the analyzer cone is crucial to ensure consistent pressure at the sample surface. The inelastic mean free path (IMFP) of electrons within a solid is typically on the order of a few nanometers, whereas in a gas at 1 Torr pressure, it extends to the order of millimeters. Furthermore, electrons must travel a distance of approximately 1 meter to reach the detector, which requires the use of multiple efficient pumping stages within the electrostatic lens system and electron energy analyzer. Reducing the aperture diameter of the analyzer cone enhances the efficiency of differential pumping. These stages, as depicted in **Figure 2.7**, enable the solid sample to remain exposed to the gaseous environment pressure while maximizing the mean free path of emitted electrons, ensuring that they successfully reach the detector. Furthermore, by applying voltage to the electrostatic lenses within the apparatus, electrons are accelerated and directed toward the electron energy analyzer. To function at its best, the detector is configured as a standard hemispherical electron energy analyzer and must be maintained within a vacuum environment.

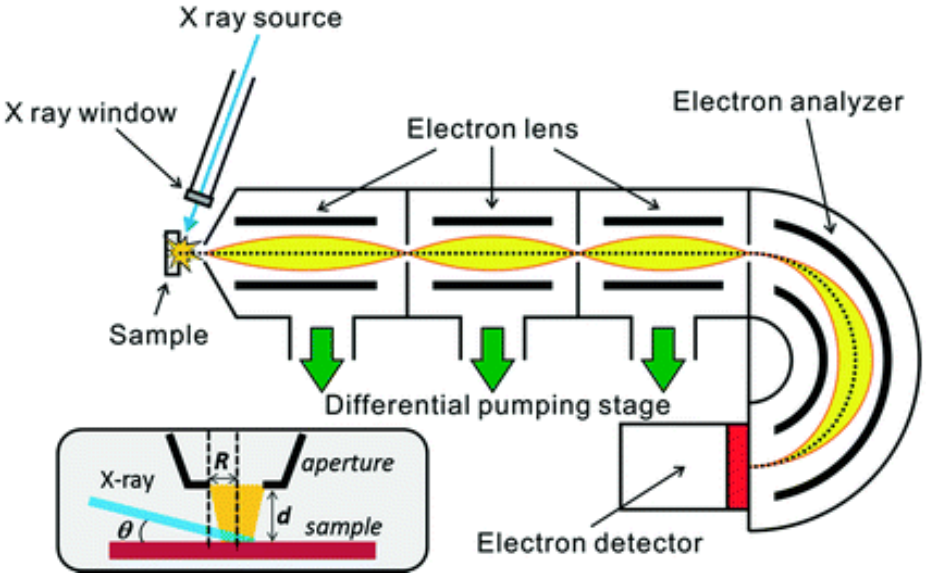

Figure 2.7 Principal layouts of the NAPPES. Figure reproduced from **Ref. [22]**

2.7 Gas-phase photoelectron spectroscopy and work function changes

Obtaining a thorough comprehension of the gas-phase spectra related to reactant molecules interacting with the surface is essential. To elucidate this point, it is worth noting that gas-phase photoelectron spectroscopy, as initially elucidates by Kai Siegbahn **[23]**, and provides valuable insights.

Figure 2.9 presents the NAP-UPS data for gaseous O_2 and H_2 molecules, which were recorded at a partial pressure of 0.1 mbar using He-I (21.2 eV) photons. This gas-phase photoelectron spectrum originates from electrons expelled from multitude of electronic states, as depicted in Figure 2.9.

$$E_{BE} = \hbar\upsilon - E_{KE} - \phi_{analyzer} \quad (2.8)$$

As soild sample placed on metallic sample holder is electrically connected (or grounded) to the earth through the spectrometer, the acquired BE isoften referenced to the E_F. In contrast, When analyzing gas-phase photoelectron spectra, the ionization energy (IE) of the gas molecule is compared to the vacuum level. Hence,

$$IE_{gas} = BE_{gas} + \phi_{sample} \quad (2.9)$$

The kinetic energy of gas-phase photoelectrons near the surface of a solid sample

$$KE_{gas} = \hbar\upsilon + BE_{gas} - \phi_{analyser} = \hbar\upsilon - IE_{gas} + \phi_{sample} - \phi_{analyser} \quad (2.10)$$

The ionization energy of a free gas molecule remains constant, but changes in the vacuum level of a particular gas molecule relative to the E_F correspond to variations in the ϕ of a given material. **[24]**

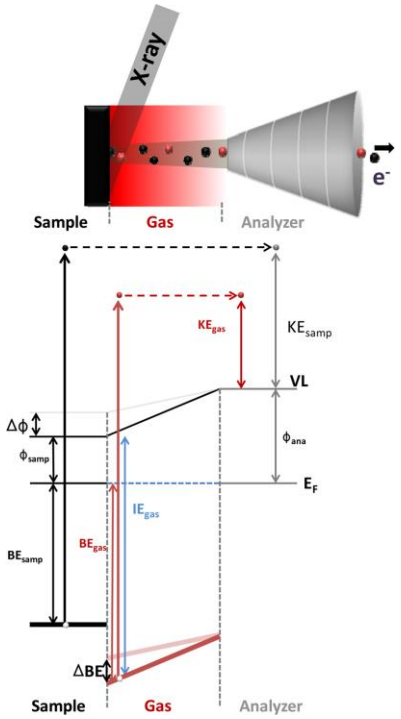

Figure 2.8 The schematic illustration, featuring a band energy diagram of the sample, gas, analyzer, and its alignment with the photoelectron process, depicts how the relative variation between the vacuum level and the sample's E_F produces alteration in the ϕ. These changes are discernible through shifts in gas-phase binding energies. Figure reproduced from **Ref. [24]**; Copyright permission obtained from ACS.

The excitation of electrons with 21.2 eV (He-I UV) photons results in the creation of photoelectron bands that exhibit vibrational features located around binding energies (BEs) of 8.0, 12.5, and 13.5 eV for oxygen and 11.2 eV for hydrogen. This excitation process originates from the photoexcitation of an electron from the valence orbitals Π*2p, Π2p, and 3σ in the case of oxygen, and from the σ1s orbital in the hydrogen molecule **[25]**. Each group of photoelectron bands displays closely spaced and well-defined fine structure, which is attributed to the formation of M_2+ ions having different degrees of vibrational excitation. At room temperature, most M_2 molecules are in their lowest vibrational ground states, denoted as V = 0,1,2,3, with higher states having lower population. The ionization process that leads to M+ ions can produce ions in various electronic states, each of which may exist in multiple allowed vibrational states represented as v'.

The resolution of vibrational features depends on the duration of molecule ion states or the density of available vibrational states. However, alterations occur in gas-phase spectra when gas-phase molecules reach adsorption equilibrium with a surface, engage in reactions with the surface, or closely interact with the solid surface. These changes are further influenced by surface heterogeneity resulting from varying surface potentials **[27]**. This phenomenon is

particularly relevant in the context of surface-dependent physicochemical phenomena like sensing, adsorption, catalysis, and electrochemistry. On solid surfaces, the vibrational features in BE can shift due to the influence of the solid surface potential on gas molecules.

2.8 Near-Ambient Pressure Photoelectron Spectroscopy (NAPPES) at CSIR-NCL, Pune:

The current thesis utilized a custom-made Lab-NAPPES unit fabricated by Prevac, Poland, capable of conducting *in-situ* PES analysis at pressures up to 1 mbar. Figure 2.10 displays a digital image of the NAPPES unit. A detailed description of the system is available in Gopinath's group publications. **[28]** However, a few crucial parameters of NAPPES are discussed below to appreciate the criticality of the research conducted in this thesis. The Lab-NAPPES instrument, illustrated in **Figure 2.10**, consists of four chambers, each of which is briefly described below.

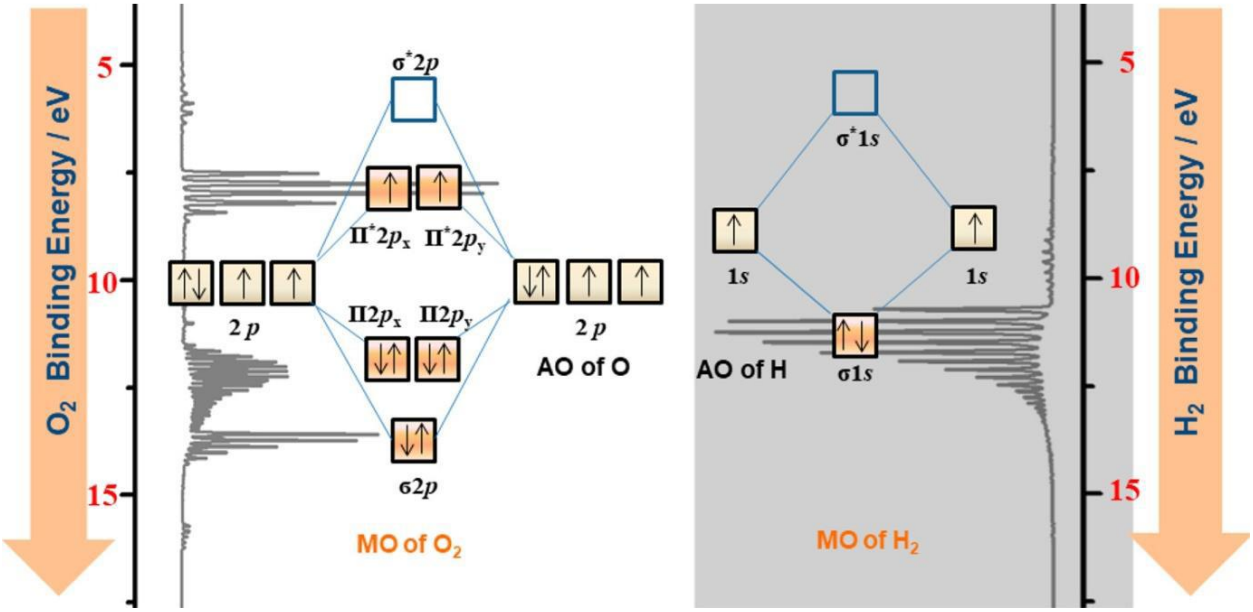

Figure 2.9 Schematic representations of the O_2 and H_2vibrational features. AO and MO stands for atomic and molecular orbitals. Figure reproduced from **Ref. [26]**, Copyright permission obtained from ACS.

2.8.1. Load lock:

This chamber is the most basic part of the instrument, functioning as the entry and exit point for inserting and removing samples. It enables quick sample replacement in the next vacuum chamber, eliminating the necessity of venting the preparation chamber.

2.8.2 Preparation chamber:

A simple load lock chamber attached to the preparation chamber enables the introduction of samples under ambient pressure conditions. Upon sample introduction, the chamber is evacuated to 10^{-9} mbar before transferring the sample into the preparation chamber. Similarly

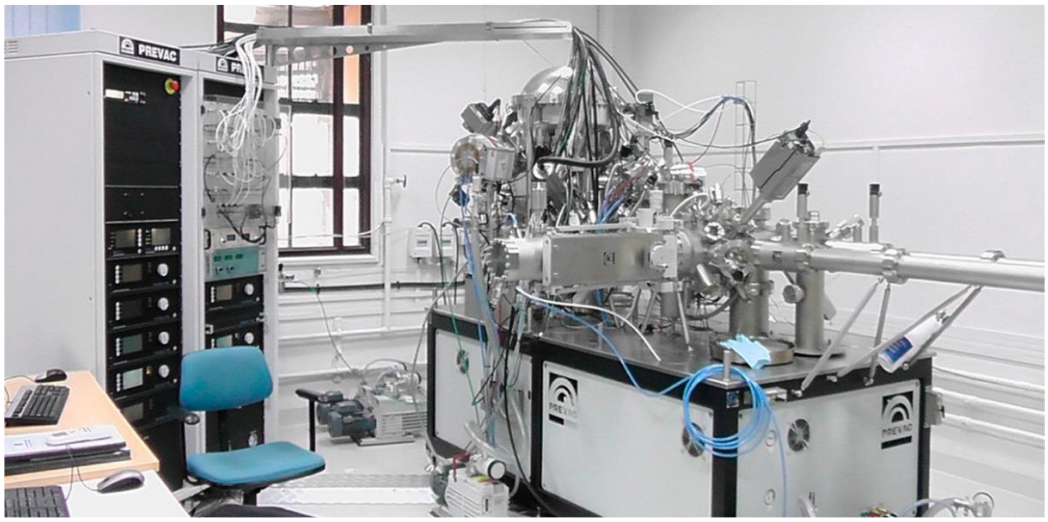

Figure 2.10 Photograph of the custom-built Lab-NAPPES setup at CSIR-NCL, Pune. Figure reproduced from **Ref. [28]**, Copyright permission obtained from ACS.

to the load-lock chamber, a turbo molecular (TMP) in conjunction with rotary pumps is employed to achieve UHV conditions within the preparation chamber. Within the preparation chamber, an Ar-ion sputter gun is installed to enable atomic-level cleaning of sample surface. This cleaning process operates at a maximum power of 5kW at an Arpressure of 5×10^{-6} mbar. Additionally, a quadrupolemass spectrometer (QMS also called as residual gas analyser or RGA) from SRS RGA200 is employed to detect gaseous products generated during *in-situ* experiments. QMS lined to the analysis chamber is either directly or via the output of the first turbo-molecular pump, which in turn is connected to the electrostatic lens column. Furthermore, a four-axis manipulator is integrated, providing the capability to heat samples up to a temperature of 1023 K. The preparation chamber also features a sample storage assembly capable of accommodating up to 10 samples holders. This system primarily serves to store metallic foil samples, preventing contaminations from external air and allowing for more thorough and time-consuming cleaning procedure.

2.8.3 High-pressure reactor chamber:

The instrument setup also allows for treatments or reactions to be carried out under pressures of up to 1 bar. This chamber, referred to as the high-pressure reactor, is directly connected to the preparation chamber.

2.8.4 Analysis (AN) Chamber:

The analysis chamber serves as the core of the instrument, responsible for conducting spectral measurements under near-ambient pressure (NAP) conditions ($P\leq1$ mbar) and high temperatures. It utilizes an open reactor design, as depicted in **Figure 2.11**. Notably, the

NAPPES system incorporates several significant advancements in comparison to conventional PES, and these innovations are of paramount importance for *in-situ* experiments conducted under NAP conditions. The fundamental objective in designing this specific chamber is to minimise the loss of photoelectrons, which occurs due to their inelastic collisions with gases present in the reaction atmosphere. This involves reducing their IMFP. To achieve this goal, three key aspects demand consideration: the minimization of inelastic scattering among ejected photoelectrons, the prevention of electron path divergence, and the optimization of the sample-to-cone distance. A detailed explanation of the distinctive features of the NAPPES system is provided below:

2.8.4 (i) An Advanced ELR:

PES instrument typically operate under UHV conditions with an open cone system to maximise the collection of photoelectrons. However, in NAPPES system, the interaction of photoelectrons with gas molecules present in the environment, along with electron divergence, leads to a reduction in the number of photoelectrons reaching the detector. This ultimately results in a poor signal-to-noise (S/N) ratio. To address this challenge, NAPPES incorporate an advanced ELR configuration with a small-diameter cone positioned at the entrance of the ELR. Compared to the conventional PES, this set up collects a less number of photoelectrons due to reduced diameter of collection cone. The gap between the sample surface and the cone aperture is a crucial consideration, and an ideal distance of 0.5 to 2 mm is maintained to optimize electron collection, minimize electron loss due to inelastic collision with gas molecules, and restrict the diffusion of gas molecule inside the cone. Preserving the ejected electron that enter the cone and travel through the ELR to reach the analyzer is imperative. Two primary factors contribute to obtaining high-quality spectra; an efficient three-stage differential pumping system and electron convergence within the ELR. The differential pumping setup within the ELR includes three stages, enhancing the vacuum and creating a pressure gradient where the sample surface experience 0.1 mbar pressure while the analyzer remains under UHV conditions.Through the implementation of differential pumping, vacuumlevels of 5×10^{-3}, 10^{-6} to 10^{-7}, and 10^{-9} mbar can be attained in the first and second stages of differential pumping within the ELR, and in the third stage of differential pumping within the analyzer, respectively. This is achieved through the use of a combination of powerful TMPs coupled with rotary pumps. Consequently, as the evacuation process progresses from the ELR to analyzer, the efficiency of evacuation increases stepwise, resulting in a significant reduction in inelastic collision of electrons due to the higher vacuum levels achieved.

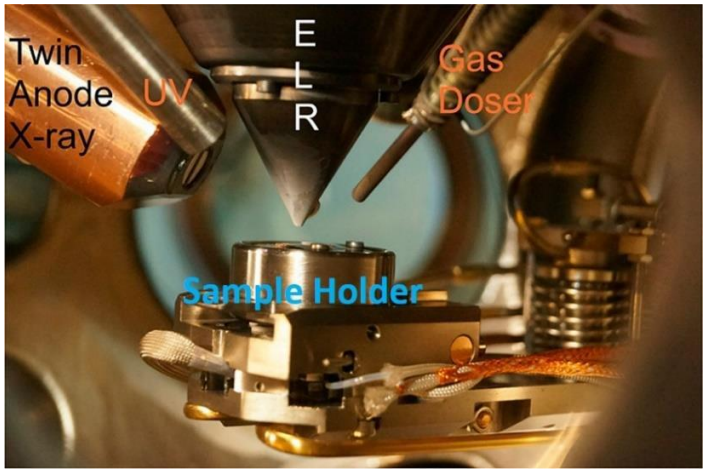

Figure 2.11 Photograph depicting the open-reactor design implemented in the lab-NAPPES facility. The illustrated sample holder is capable of being relocated to the cone affixed to the Electrostatic Lens Regime (ELR). A dosing apparatus is incorporated to elevate the temperature of the input gas mixture, thereby reducing temperature differentials between the spectral measurements and gas temperatures. Figure reproduced from Ref. **[29]** and copyright permission obtained from ACS publisher.

Moreover, an innovatively designed dual-front cone pumping system improves vacuum efficiency across a short span, as depicted in **Figure 2.12**. This advancement allows for swift pressure reduction with a sharp transition from the lower part of the cone to the analyzer, effectively reducing inelastic collision within the ELR under high-pressure conditions. Furthermore, electron convergence within the ELR is crucial for preserving collected photoelectrons, ensuring that a maximum number of electrons enter the analyzer for detection. The advanced design of the analyzer enables angle-resolved XPS investigation and rapid spectral recording under NAP conditions. Alongside the R3000HP analyzer, the NAPPES instrument system incorporates several unique features designed to enhance the experimentation process. These distinctive attributes will be elaborated upon in subsequent sections.

2.8.4 (ii) An Exchangeable Analyser Cone:

The primary functions of the analyzer cone are twofold: First to collect the photoelectrons generated from the surface subjected to (X-ray or UV) irradiation, and second to act as a barrier separating the ELR from high-pressure environment within the analysis chamber. The analyzer cone can be equipped with interchangeable cones featuring a range of aperture diameters, typically varying from 0.3 to 5 mm, in accordance with specific experimental requirements. A spectral resolution of approximately 0.42 ± 0.02 eV was achieved using the operating conditions comprising 50 eV pass energy, a 0.2 mm slit width, and an 0.8 mm cone diameter.

This resolution aligns closely with findings from prior studies conducted with a similar analyzer, as documented. **[30]**

2.8.4 (iii) Photon sources: The instrumentation features two distinct X-ray excitation sources designed for XPS analysis. One of these sources is a conventional dual anode, which includes Al Kα and Mg Kα, capable of reaching peak powers of 600 and 400 W, respectively. The alternative X-ray photon excitation source utilizes an aluminum Kα monochromator (MX 650) from VG Scienta. This X-ray system operates at an acceleration voltage of up to 15 KV and delivers a maximum output power of 650 W. To isolate the X-ray monochromator from the analysis chamber, a thin aluminum window, measuring 5 μm in thickness, is securely attached within a ring structure and is positioned within the dividing port.

The aluminum window, which separates the analysis chamber from the monochromator, is accessed through a 150CF axis port, ensuring an airtight seal that allows for stable X-ray emission during NAP experiments. It's worth noting that, even under typical operational conditions, the X-ray monochromator maintains a vacuum level of 10^{-6} mbar, even when the analysis chamber is subjected to a pressure of 1 mbar. Recent reports have also suggested the effectiveness of Silicon Nitride (Si_3N_4) **[31]** as an alternative material for X-ray transmission in high-pressure environments. Furthermore, the analysis chamber is equipped with anultraviolet (UV) photon source capable of generating stable He-I and He-II UV radiation. This feature enables the investigation of UVPES under both UHV and 1 mbar conditions. The water-cooled UV source is attached to a CF40 flange and can deliver emission currents of up to 100 mA for He-I and 200 mA for He-II.

The analysis chamber is also furnished with an electron flood source that can function at energy levels of up to 50 eV. This flood source plays a vital role in compensating for charges during PES experiments. It not only facilitates PES analysis of insulating or semiconducting materials within the scope of XPS but also operates effectively under 1 mbar conditions. It's important to note that, in NAP conditions, any potential charge build-up due to static charge accumulation is promptly compensated for by gas-phase molecules. For a clearer understanding of the setup, you can refer to **Figure 2.13**, which provides an overview of the analysis chamber mbar conditions. It is noteworthy that, under NAP conditions, static charge accumulation is averted due to the prompt compensation of any potential charge build-up by gas-phasemolecules. A bird's eye view of AN chamber is provided in Figure 2.13 for more understanding of the present unit.

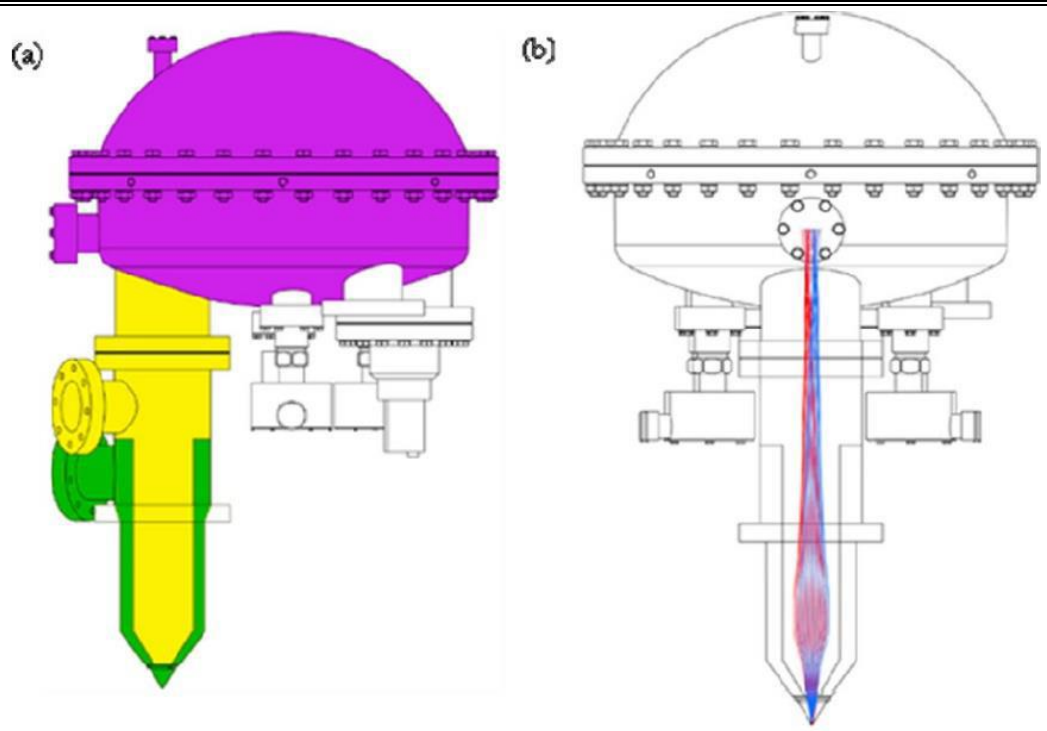

Figure 2.12A double front cone pumping configuration (depicted in green and yellow hues) significantly enhances differential pumping, thereby minimizing inelastic scattering within the ELR and reducing data collection time dring high-pressure conditions. The region corresponding to the electron energy analyzer is highlighted in purple. (b) A schematic representation of the aperture-free ELR and the electron trajectory designed for expedited data acquisition. Figure reproduced from Ref. **[28]** and copyright spermission obtained from ACS publisher.

2.8.4 (IV) Gas Mixing Chamber: A gas mixing chamber is connected through AN chamber through an extremely narrow capillary tube, permitting the controlled release of gases into the AN chamber via precision leak valves. This arrangement enables the performance of PES measurements under NAP conditions, typically within the mbar range. The mixing chamber is equipped with an appropriate number of mass flow controllers (MFCs) for precisely mixing of different types of gases, achieving the desired gas composition tailored to specific reactions. The pre-mixed gases can be introduced into the analysis chamber using a gas doser, which utilizes a z-axis manipulator that can be brought close to the sample surface. This manipulator has the capability to reach temperatures as high as 873 K, mitigating temperature differentials between the sample and the incoming gases. Accurate measurement of sample pressure constitutes a critical facet of *in-situ* experiments. To address this, a cold cathode Gauge (CTR gauge) is strategically situated in close proximity to the sample surface. This gauge plays a pivotal role in precisely ascertaining sample pressure, ensuring the provision of precise pressure values and enhancing data reproducibility.

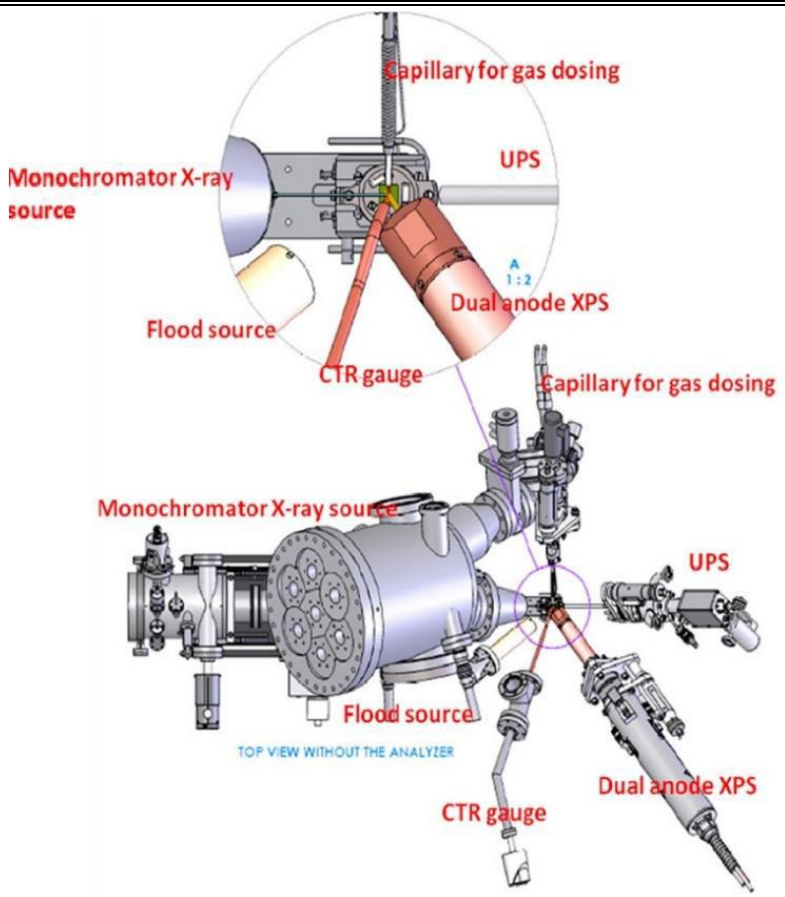

Figure 2.13A Bird's eye view of the main chamber, observed from the analysis chamber side and without the analyzer. The inset offers an enlarged depiction of the analysis location, providing insights into the pressure assessment utilizing a CTR guageand the apparatus for gas introduction. Figure reproduced from **Ref. [28]** and permission obtained from ACS publisher.

2.8.4 (v) Quadrupole mass spectrometer (QMS): The NAPPES measurement can be enhanced by simultaneous QMS measurements conducted within the preparation chamber. The integrated QMS allows for the real-time monitoring of reaction kinetics. A thin leak capillary, connecting the analysis chamber directly to the QMS, serves a dual purpose: analyzing reaction products and comparing the data with the mass spectral information obtained from the first differential pumping stage. Alternatively, a bellows arrangement, equipped with a leak valve, connects the first differential pumping stage of the analyzer to the preparation chamber. This configuration enables the simultaneous collection of spectral and kinetic data, eliminating any time discrepancies between the two measurements. **[32-33**.]

2.8.5 Sample Holders: Specially designed sample holders, capable of resistive heating and withstanding high temperatures at 1 mbar pressure, are commonly used for high-pressure measurements. The system also has the capacity to heat samples up to 2273 K using resistive electron bombardment under vacuum conditions.

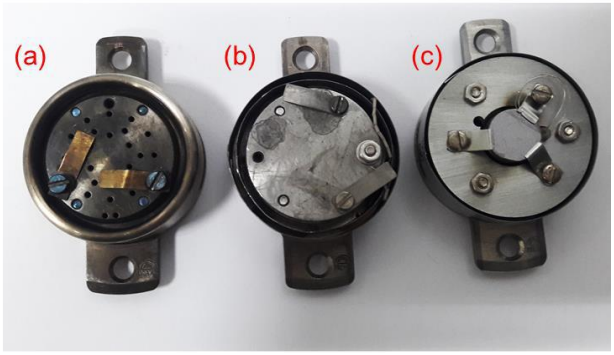

Figure 2.14 Sample holders used for NAPPES measurements (a) High pressure reactor (PT750), (b) UHV heating sample holder (PTS 1000) (c) electron beam heating sample holder.

2.8.6 Data acquisition: During PES experiments, the acquisition of spectral data was carried out using the SES (Spectroscopic Experimental Suite) software, which works in conjunction with the NAPPES unit. The SES software plays a crucial role in overseeing and controlling various parameters of the analyzer. It offers the capability to adjust several iteration parameters to meet specific analysis requirements. These parameters encompass pass energy, analysis type, iteration duration, frame size, photon energy utilization and more.

2.8.7 Data processing:

Computer-aided surface analysis for XPS (CASA XPS) is specialised software designed for the comprehensive processing of PES data. It facilitates the conversion of raw data, typically stored in an unprocessed format such as .pxt (in our case) to the standardized VAMAS format. CASA XPS offers powerful tools for both quantitative and qualitative analysis through data deconvolution, specifically peak fitting. In the context of PES data analysis, accurate peak fitting plays a pivotal role in determining the composition of surface elements, and CASA software streamlines this process, ensuring reliability and ease of use. Moreover, if any charge shifts are observed in the acquired PES data, CASA provides the functionality to calibrate and rectify these shifts post-acquisition. For the present study, data processing was performed using CASA 2.3.24.

2.9 Conclusion: Current chapter comprehensively explores various synthesis methodologies employed in the synthesis of nanocatalysts intended for catalysis applications. The technique employed for characterization these meticulously prepared catalyst is also discussed. Furthermore, these nanocatalysts, find utility in addressing the challenges posed by industrial catalytic reaction condition, bridging the pressure and material gaps. In addition, they play a vital role in surface science investigations. The latter part of this chapter offers a detailed exploration of the technical complexities related to the specially designed laboratory-based

NAPPES system implemented at CSIR-NCL, Pune. The NAPPES systems have distinctive features, including a double front cone pumping arrangement, and multiple stages of differential pumping. These features are instrumental in maintaining a high vacuum environment within the ELR, thereby enabling the acquisition of high-quality data using photon sources under reaction conditions, even at pressure of up to 1 mbar. This innovative facility extends the capability to replicate the conditions of heterogeneous catalysis reactions on catalyst surfaces, all while achieving temperatures as high as 1073 K and maintaining pressure of P≤1 mbar.

2.10 References:

1. Gnanakumar, E. S.; Naik, J. M.; Manikandan, M.; Raja, T.; Gopinath, C. S.*ChemCatChem.* **2014**,*6,* 3116.
2. Mathew, T.; Shiju, N. R.; Sreekumar, K.; Rao, B. S.; Gopinath, C. S.*J. Catal.***2002**,*210,* 405.
3. Patra, K. K.; Gopinath, C. S.*ChemCatChem.* **2016**,*8,* 3294.
4. Vysakh, A. B.; Jain, R.; Chinnakonda, G. S.; Prabhakaran, V.*Catal. Sci. Technol.***2017**,*7*, 4489- 4498
5. Dubey, A.; Kolekar, S. K.; Gnanakumar, E. S.; Roy, K.; Vinod, C. P.; Gopinath, C. S.*Catal. Struct. React.***2016**,*2,* 1–12.
6. Imbihl, R.; Behm, R. J.; Schlögl, R.*Phys. Chem. Chem. Phys.***2007**,*9,* 3459–3459.
7. Park, J. Y.; Somorjai, G. A.*Current Trends of Surface Science and Catalysis.* **2014**, 3–17.
8. Nagarajan, S.; Gopinath, C. S.*J. Indian Inst. Sci.***2010**,*90,* 245–260.
9. Gopinath, C. S.; Roy, K.; Nagarajan, S.*ChemCatChem***2015**,*7,* 588–594.
10. Nagarajan, S.; Thirunavukkarasu, K.; Gopinath, C. S.*J. Phys. Chem. C***2009**,*113,* 7385–7397.
11. Gopinath, C. S.; Thirunavukkarasu, K.; Nagarajan, S.*Asian J. Chem.***2008**,*4,* 74-80.
12. Tao, F.; Salmeron, M.*Science*,**2011**,*7,* 171–174.
13. Makhlouf, M.T.; Abu-Zied, B.M.; Mansoure, T.H.*Met. Mater. Int.***2013**,*19,* 489–495.
14. Post, B.*X-Ray Spectrometry*,**1975**,*4,* A17-A22.
15. "X-ray diffraction".*Encyclopedia Britannica*, 31 Mar. **2023**, https://www.britannica.com/science/X-ray-diffraction.
16. "TPR - Wikipedia."https://en.wikipedia.org/wiki/TPR.
17. Pirola, C.; Galli, F.; Patience, G. S.*Can. J. Chem. Eng.***2018**,*96,* 2317–2320.
18. Inkson, B. J.*In Materials Characterization Using Nondestructive Evaluation (NDE) Methods*,**2016**, 17-43.
19. Transmission Electron Microscope (TEM)- Definition, Principle, Images.https://microbenotes.com/transmission-electron-microscope-tem/#principle-oftransmission-electron-microscope-tem.
20. Hilal, N., Ismail, A. F., Matsuura, T., Oatley-Radcliffe, D., Eds.*Membrane Characterization.;* Elsevier,**2017**, 161.

21. Frank Ogletree, D.; Bluhm, H.; Hebenstreit, E. D.; Salmeron, M.*Nucl. Instr. Meth. Phys. Res.A* **2009**,*601*, 151.
22. Kondoh, H.*Compendium of Surface and Interface Analysis.*Springer, Singapore, **2018**.
23. Gelius, U.; Siegbahn, K.*Faraday Discus. Chem. Soc.***1972**,*54*, 257-268.
24. Axnanda, S.; Scheele, M.; Crumlin, E.; Mao, B.; Chang, R.; Rani, S.; Faiz, M.; Wang, S.; Alivisatos, A. P.; Liu, Z.*Nano Lett.***2013**,*13*, 6176-6182.
25. Rabalais, J. W.*Principles of ultraviolet photoelectron spectroscopy;*Wiley, New York, **1977**.
26. Reddy, K. P; Jain, R; Ghosalya, M. K.; Gopinath, C. S.*J. Phys. Chem. C* **2017**,*121*, 21472−2148.
27. Ghosalya, M. K.; Jain, R.; Reddy, K. P.; Gopinath, C. S.*J. Phys. Chem. C*,**2018**,*122*, 4331-4338.
28. Roy, K.; Vinod, C. P.; Gopinath, C. S.*J. Phy. Chem. C* **2013**,*117*, 4717-4726.
29. Roy, K.; S. Gopinath, C.*Anal. Chem.* **2014**, *86*, 3683–3687.
30. Mangolini, F.; Åhlund, J.; Wabiszewski, G. E.; Adiga, V. P.; Egberts, P.; Streller, F.; Backlund, K.; Karlsson, P. sG.; Wannberg, B.; Carpick, R. W.*Rev. Sci. Instrum.***2012**, *83*, 093112.
31. Zheng, F.; Alayoglu, S.; Guo, J.; Pushkarev, V.; Li, Y.; Glans, P.-A.; Chen, J.-l.; Somorjai, G.*Nano Lett.***2011**,*11*, 847.
32. Jain, R.; Gnanakumar, E. S.; Gopinath, C. S.*ACS Omega*,**2017**,*2*, 828.
33. Jain, R.; Reddy, K. P.; Ghosalya, M. K.; Gopinath, C. S. *J. Phys. Chem.***2017**, 20296.

Chapter 3

Electronic Structure EvolutionFrom Metallic Vanadium to Metallic V_xO_y: A NAPPES Study for O_2 + V Gas-Solid Interaction

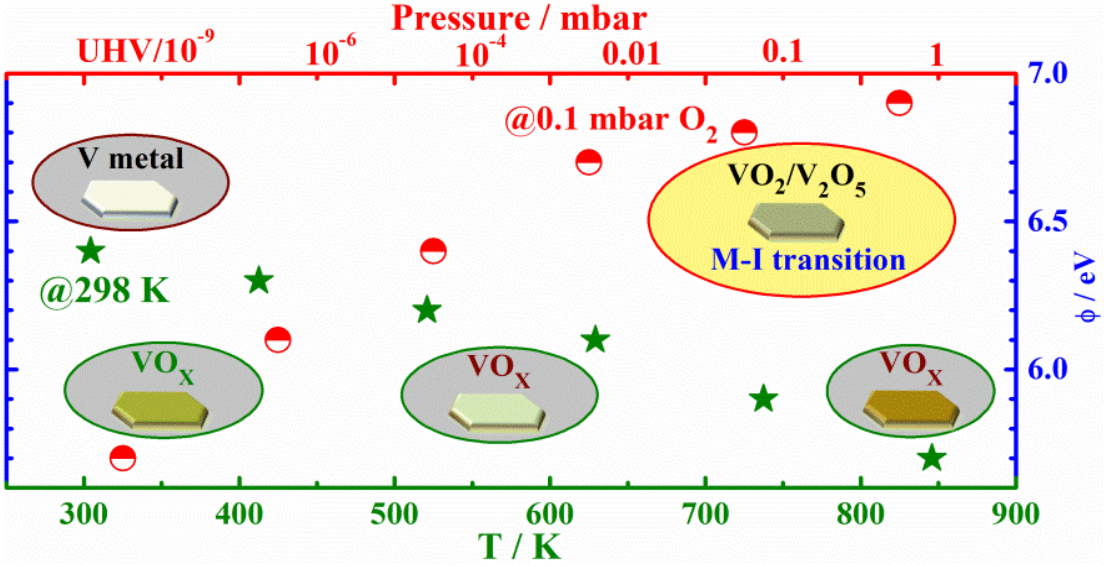

A part of the work presented in chapter 3 has been published, and the publication detail is: -

Ranjan, R.; Mhamane, N. B.; Kolekar, S. K.; Gopinath, C. S. Electronic Structure Evolution from Metallic Vanadium to Metallic VxOy: A NAPPES Study for O_2 + V Gas−Solid Interaction, *J. Phys. Chem. C.***2022,***126*, 19136−19146.

3.1 Introduction

Vanadium is a fascinating element exhibiting an electronic configuration of $[Ar]3d^3 4s^2$, with abilities to be employed in ceramics to catalyst to superconducting magnets.The diverse and extensive chemistry of vanadium is attributed to its ability to exist in numerous accessible oxidation states and its redox properties. Vanadium pentoxide is a renowned catalyst for the production of sulfuric acid. Vanadium compounds are stable in different oxidation states and hence variety of oxides are possible, such as, VO, VO_2, V_2O_3, V_6O_{13}, and V_2O_5**[1-2]**. Properties of vanadium and vanadium oxides attracted interest of researchers across various fields, such as catalysis **[3-4],** electrochemistry **[5]**, and opto-electronic applications **[6]**. Partially filled 3d-orbitals of vanadium are important in electron exchange mechanism and ferromagnetic properties of defective VO_2**[7]**. Vanadium forms a large no of oxides, which are also stable over a certain range of pressure and temperature conditions **[8]**. The phase transition between vanadium to V_2O_5 has been speculated to be due to the insertion of oxygen in the vicinity of vanadium surface, but no systematic studies are available. Indeed, from catalysis point of view, monomeric vanadium, mixed valence and/or redox nature of vanadium has been demonstrated to show high activity and selectivity in number of heterogeneous catalysis reactions **[9]**. Catalysis is indeed a surface phenomenon, and catalyst surface should undergo reversible changes easily for sustainable catalytic activity. There are number of elementary steps/reactions occurs over the catalyst surface, such as adsorption of reactant(s), dissociation, diffusion of various species and reaction among them, followed by desorption of product(s); diffusion of small atoms (H, C, O) into the catalyst subsurface is also possible **[10]**. These steps involve bond making or breaking, which depends on the electronic nature of the catalyst surfaces. ϕof a catalyst (or any solid material) issurface sensitive property, and the same is required to understand the relative E_F and carrier concentration near E_F. ϕcan be defined asenergy required to removean electron from E_F into vacuum. ϕ affects chemical, magnetic, optical, structural characteristics of the surface **[11-12]**. ϕ is readily influenced bymany common factors, such as adsorbed layers of molecules, surface contamination, oxide formation. Measuring ϕ reliably for a specific material under technically relevant conditions is imperative because ϕ strongly depends on the surface properties.

It has been documented those materials such as MoOx, WOx, and V_2O_5 can exhibit significant changes in ϕ, with values reaching up to 6.7 eV. These high ϕ materials are particularly effective as hole-injecting electrodes in organic semiconductor devices **[13-14]**. On the contrary, TiO_2, and ZnO are better electron-injector materials, and it has excellent

applications in photocatalysis **[15-16]**. The change in ϕ and hence change in physicochemical properties of the vanadium oxides can be tuned by oxygen vacancy with changing stoichiometry of the oxide **[17]**. Vanadium dioxide (VO_2) show some unique properties, such as it exhibits first-order metal-insulator (MI) transition from an insulating phase (below 340 K) with monoclinic structure to a metallic phase with a tetragonal rutile structure ≥340K **[18]**. The conductivity is five orders of magnitude below the transition temperature, with an energy gap in the insulating phase is typically 0.6eV **[19]**. Due to this factor, the monoclinic VO_2 is considered as a semiconductor, and it has interesting application in dilute magnetic semiconductor (DMS). Further, The density of charge carriers can be precisely adjusted by introducing ionic doping or through the diffusion of small atomic species like hydrogen within the subsurface, oxygen, sulphur etc **[20]**. The phase transition temperature can be altered over a wide range of doping and external strain of the VO_{2-x}; due to these extra-ordinary features of VO_{2-x}, it has manypotential applications, such as electrodes in electrochemistry **[21]**. The ϕ of un-doped VO_2 is ≥6eV at room temperature mainly due to structural electronic rearrangement on the surface VO_x. Thus, the un-doped VO_2 is not considered as a suitable hole injecting metal oxide in devices. In case of VO_2, it has been reported that by doping with W^{6+}-ion, thenumber of oxygen vacancies can be altered and hence the ϕ of $VO_2$and MI transition temperature can be decreased to 323 K; indeed, there is an oxygen vacancy handle to tune the MI temperature significantly **[22]**.

VB photoelectron spectroscopy using low-energy photons is a crucial technique for investigating surface-specific electronic alterations within the top 2 nm. NAP-UPS is particularly valuable for studying the interaction between oxygen and vanadium in gas-solid systems. NAP-UPS allows us to examine how the 3d band structure evolves and observe the effects of V3d–O2p hybridization during the transition from V-metal to VOx oxides. Additionally, XPS and UPS are highly effective methods for characterizing surface properties, which provide information about oxidation state and electronic structure, VBaspects, ϕ change and density of state (DOS). Our group has contributed to this area of research with NAP-UPS and NAP-XPS with many metals and metal oxides under relevant redox conditions and interesting findings has been reported. **[23-29]**.

In this study, we have illustrated the evolution of the electronic structure from metallic vanadium to V_2O_5 as it transitions through various VOx phases, with changes dependent on the partial pressure of oxygen and temperature. Specifically, changes in the ϕ between 5.5 and 7 eV with changing stoichiometry of the vanadium oxides (VO_x), and metal-insulator transition

of VO_2 at 0.1 mbar O_2 pressure and ≥725K are shown. Oxidation of V-surface is highly limited to few atomic layers at room temperature, while oxidation progress into somewhat deeper layers at high temperatures (but, within the XPS probing depth) demonstrates the thermodynamic dependence.

3.2 Cleaning procedure of V metal foils

A 1M HNO_3 acid-etched vanadium (V) metal foil underwent a thorough preparation procedure within the NAPPES unit. The V foil was meticulously cleaned through multiple cycles of Ar+ sputtering at a pressure of 5.5 $\times 10^{-6}$ mbar, using 4 kV and 7 mA at 550 K. Following this, annealing was conducted in an oxygen environment (1×10^{-6} mbar) at 600 K for 15 minutes, followed by vacuum annealing at 1000 K for 30 minutes. This sputter cleaning process was repeated until XPS analysis revealed no peaks other than those characteristics of V metal. This method effectively removed carbon impurities in the form of CO_2, and subsequent vacuum annealing helped eliminate any remaining surface oxygen from the previous annealing steps. Impurities such as sulfur, silicon, and phosphorus were either not detected or present at concentrations below the detection limits of the R3000 analyzer. The PES experiments were performed across a pressure range that extended from UHV conditions at 1×10^{-10} mbar up to 0.1 mbar, and at temperatures ranging from 295 to 873 K. These investigations were conducted utilizing a specially designed laboratory-based NAPPES facility, as detailed earlier.

3.3 Result and Discussion

3.3.1Clean V-surface Features

A vanadium foil sample have been sputtered and annealed extensively, and then the XPS and UPS spectra have been recorded at UHV condition at RT and the results are shown in **Figure 3.1.** The clean vanadium foil shows typical $V2p_{3/2}$ and $2p_{1/2}$ at RT at 512.3 eV and 519.8 eV, respectively. The observed BE for metallic vanadium and oxidized vanadium species is in good agreement with the literature reports **[33-34]**. There is no carbon and oxygen core level feature appear on the surface which has been confirmed by XPS spectra (Fig. 3.1c and d); no other impurities, such as chlorine, phosphorous were observed. As the vanadium foil is extensively sputtered, some surface defects are possible, such as nanoclustering or nanostructuring of vanadium, surface inhomogeneity, and this feature could appear at high BE **[35]**. A minor broadening observed on the higher BE side of V 2p feature (~513 eV) is due to sub-surface/bulk layers of vanadium (Fig. 3.3a). A marginal amount of surface oxide as surface contamination, due to the residual oxygen present in NAPPES unit, cannot be ruled out. Indeed, initially sputtering was carried out till the V surface does not show any O and C impurities. UPS is

considerably more surface-sensitive than XPS and offers insights into the top 2 nm of the surface under UHV conditions. Surface oxide(s) was removed during the sputtering and annealing process, which was also confirmed by the UPS. It shows high density of state (DOS) near $E_F$which is characteristics of a metal; indeed, this is the critical characteristic of metallic vanadium surface, and supports the surface is devoid of any other foreign elements. UPS spectrum of clean foil, recorded with He-I photons, is shown in **Figure 3.1b**. It is to be noted that due to extensive sputtering employed to clean the V-surface could introduce some solid-state defects and the same cannot be ruled out. Broadening observed on the high BE side (~513 eV) of V $2p_{3/2}$ and a broad peak observed around 6 eV in UPS (**Figure3.1b**) is attributed primarily due to such defects, and they are within the probing depth of XPS. Another broad feature centred at 11-12 eV in **Figure3.1b** is attributed to secondary electrons. As the photoelectrons are ejected out of the solid surface, part of kinetic energy is lost due to inelastic scattering within the solid surface layers and those electrons appear at higher BE. Indeed, this is bit more severe and changes significantly as the O_2 partial pressure increases.

3.3.2 Pressure dependent oxidation V+O_2 interaction – NAPPES study

Oxidation aspects of the vanadium metal surface were evaluated in detail as a function of O_2 partial pressure, temperature, and O_2 exposure duration at 1 mbar pressure. Initially, V 2p and O 1s core level data were collected while varying the oxygen partial pressure from UHV ($10^{-6)}$ to 1 mbar on the vanadium foil at 298 K, as illustrated in **Figure 3.2.** Up on exposure to O_2, high BE features evolve and the metallic V 2p features are also retained up to 1 mbar pressure. Indeed, first-row 3d transition metals are known to be pyrophoric **[23-25]** and the observation of metallic V in Fig.3.3a is indeed interesting. At low partial pressure the new features observed are attributed to V^{2+} (blue peak) at 513.7 eV **[33]**. With increasing O_2 partial pressure from 10^{-6} to 1 mbar, the extent of severity of surface oxidation increases; however, observation of metallic V even at 1 mbar O_2 partial pressure, suggests the oxidation is limited to surface layers even within the XPS probing depth of 10 nm, rather than deeper into subsurface/deeper layers of vanadium. Curve fitting was carried out to resolve the various V-species present and the curve fitting parameters were adopted as that of Biesinger *et.al.* **[33]** with some marginal changes. Initially complete metallic vanadium was observed under UHV conditions; these changes gradually to 41.1 % at 1 mbar due to oxygen exposure and oxygen diffusion on the top few surface layers of vanadium. This indicates a predominant lateral oxygen diffusion and oxidation of subsurface layers are limited at measurement conditions, especially at 298 K. At 10^{-6} mbar O_2 partial pressure and among the oxidized V-species, V^{3+} (pink) oxidation state was

observed predominantly at 515.3 eV, along with V^{2+} (blue) at 513.7 eV with corresponding satellite peak at 521 eV. On increasing O_2 partial pressure to 10^{-4} mbar, V^{4+} (green) and V^{5+} (dark yellow) at 515.8 and 517.2 eV with corresponding satellite peak at 523.4 eV and 524.6, respectively, oxidation states were observed, at the cost of V^{2+} and V^{3+}. Only 14.4 % of V^{5+} state was observedat 1mbar conditionindicating the onset of the severe oxidation requires more harsh condition, such as high temperature. However, an increasing partial pressure of O_2up to 1 mbar at RTexhibits the multiple oxidation states from V^{2+} to V^{5+}.Although molecular oxygen was available under experimental conditions, observation of multiple oxidation states concurrently demonstrates the heterogeneity of the surface, possibly due to oxide islands, surface defects etc. Observation of 41.1% metallic V at 1 mbar pressure also indicates the surface oxide layers might be acting as a protective layer and hindering the oxidation of sub-surface and deeper layers of V foil, which requiresvertical oxygen diffusion and more energy. Indeed, similar observation was reported for silicon oxidation **[27]**.

No oxygen feature was observed on the clean V foil, which highlights the purity of the surface **Figure 3.2b** (bottom spectra). As the oxygen partial pressure increased from UHV to 10^{-6} mbar, a broad O1s signal was detected with a notable signal-to-noise (S/N) ratio. The deconvoluted result is displayed in the following figure. **Figure 3.2b**. The high intensity peak at 529.6±0.1 eV(red trace) and the peak at 530.2±0.1 eV (green trace) are attributed to the lattice oxygen of VO_x with short range and long-range ordering, respectively.This suggests a possibility of VO_x islands formation under the present experimental conditions for the results shown in **Figure3.2**. Another peak at 531.2±0.1 eV (blue trace in Fig. 3.3b) presents in all O 1s spectra recorded indicating the formation of hydroxyl features are on the surface, which is likely due to background level hydrogen present in the UHV chamber. Indeed, this is supported from the observation of some back-streaming of hydrogen into the analysis chamber is shown in Fig. 3.2 in the mass spectrum recorded, while all other air components remain observed at the background level. Even at 0.1 mbar, the oxygen peaks appear at the same BE, as that of 10^{-6} mbar, at 529.6 eV, 530.2 eV and 531.2 eV. In pressure dependent condition the O1s peak intensity at 530.2 eV increases gradually till 0.1 mbar and it becomes comparable to that of 529.6 eV feature during 1 mbar O_2 treatment.

The NAP-UPS VB spectra of vanadium metal surfaces were acquired while varying the oxygen partial pressure, and the outcomes are depicted in Figure 3.3. This investigation aims to elucidate the changes in the electronic structure of vanadium oxide(s) in response to different

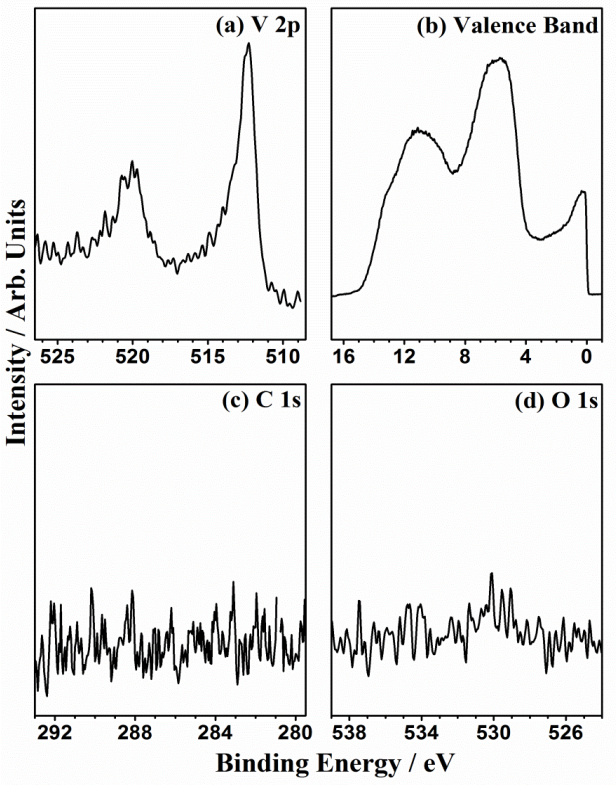

Figure 3.1 XPS and UPS spectra recorded at UHV and 298 K after several sputter-anneal cycles on vanadium foil; (a) V2p, (b) VB spectra recorded usingUPS, (c) C1s and, (d) O1s levels. Y-axis counts for panel c and d has been multiplied 5 times, to show that there is no contamination on the clean surface.

O_2 partial pressures at 298 K. It is also to be noted that while XPS explores up to 10 nm depths, UPS explores hardly top 2 nm layers, and hence they are likely to provide complementary information. There are three electrons in the metallic V 3d band and two electrons in the V 4s band. High density of states (DOS) observed at E_F indicates the complete metallic nature of the surface; also, the amount of residual air components (particularly oxygen) present in the UHV chamber is not sufficient to oxidize the surface layers of vanadium at 298 K. Critically, the high DOS feature observed at E_F on metallic V surface under UHV decreases drastically, but not disappeared completely, upon introduction of gas-phase oxygen at 10^{-6} mbar. Similar reduction in E_F intensity was observed on Co **[25]** and Cu surface,**[31]** this observation confirms the highly pyrophoric and oxidising nature of the metallic vanadium surface. While **Figure 3.3a** exhibits 41.1 % metallic V 2p features in NAP-XPS even at 1 mbar O_2partial pressure, drastic reduction of E_F features even at 10^{-6} mbar (and above) partial pressure in **Figure 3.4a** is due to the low probing depth (≤2nm) in NAP-UPS. In addition to the E_F changes, V 3d band at 10^{-6} mbar O_2 partial pressure exhibits two features. One centred on 1.3-1.5 eV and a second feature around ~ 0.4 eV; these features are attributed to V^{3+} and V^{2+} species,

respectively. This is further supported by the disappearance of V^{3+} and another low BE species on oxygen annealing of VO_2 (with oxygen vacancies), in a study by Wang *et. al.* **[35]**. We also want to underscore the time required for average experiment, as it helps other researches to reproduce the data. Time taken to record each set of spectra (XPS and UPS), at a given pressure, took about 25 min. and randomly in few cases we repeated measurements to make sure that there are no further changes in the recorded spectra for BE position as well as counts. We have not observed any significant change in spectral results, even if it is prolonged to 60 min. and hence the results represent steady state oxidation at 298 K. However, we recorded a set of spectra at a given high pressure/temperature also in 25 min. and no significant changes are observed within this time frame, and up to 30 min.; however significant changes are observed beyond 30 min at and above 673 K and at 0.1 mbar and above.

The oxygen partial pressure was then systematically raised from 10^{-6} to 1 mbar at room temperature (RT), and the spectra were captured. Several noteworthy observations merit highlighting: **(a)** E_F intensity gradually decreases and completely disappears at≥0.1 mbar O_2 partial pressure (Fig. 3.4b). **(b)** A careful look at the photoelectron emission offset around 15 eV shows the decrease in ϕ up to 0.1 mbar, followed by a minor reversal in increase in the ϕ at 1 mbar. **(c)** ϕ changes reflect in the oxygen vibrational features too, which is given in detail in the next paragraph. **(d)** A broad feature observed around 6 eV feature (on metallic V) was further broadened, particularly on the lower BE side towards 3-4 eV. This broadened feature is attributed to the O 2p features of V 3d – O 2p hybridized band. **(e)** A new broad and low intensityfeature appeared around 1 eV correspond to V3d – O2p interaction. As the O_2 partial pressure is elevated from 10^{-4} mbar to 1 mbar at 298 K, there is a noticeable decrease in the V^{2+} feature and a corresponding increase in the intensity of V^{3+}. This indicates surface oxidation leading to the presence of V^{3+}. The first feature around 1.3 eV is attributed to [Ar] $3d^2$- O2p or [Ar] $3d^3$-O2p correspond to V_2O_3 or VO, respectively, indicates the charge transfer from V to O **[34]**. Similar type of features was observed and attributed to charge transfer from metal to oxygen with oxidation of metals, such as Cu, Mo, Co, and Pd **[23,25,31,36]**. Continuing to raise the O_2 partial pressure to 1 mbar at 298 K, no major changes were observed, except for O_2-gas phase features, which is different at 1 mbar; this indicates further minor modification of VO_x composition at 1 mbar, possibly due to the onset of severe oxidation. NAP-UPS spectra also shows the vibrational features of molecular oxygen and the same appear at different BE with increasing pressure underscores the interaction of molecular oxygen with solid surface. Molecular oxygen by itself exhibits distinct features at approximately 8.0, 12.0,

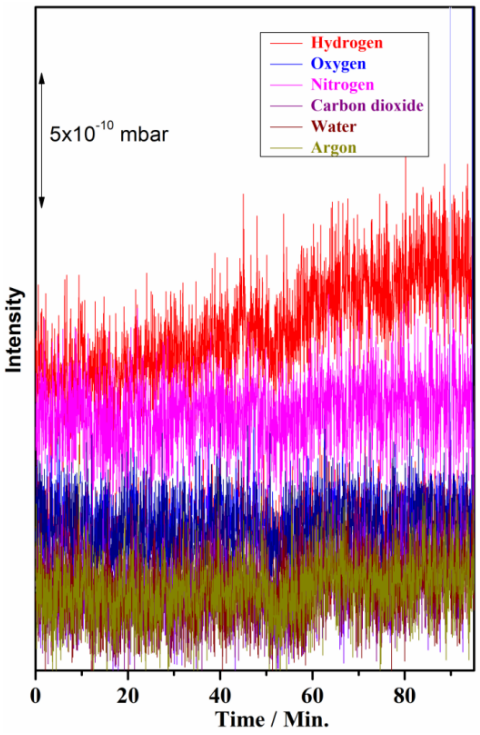

Figure 3.2 Mass spectrum recorded from the analysis chamber indicates a back-streaming of hydrogen slowly. This hydrogen is considered as a possible source for hydroxyl species formation during the *in-situ* oxidation experiments carried out between 298 and 623 K.

and 14.0 eV, corresponding to molecular vibrations of oxygen in the gas phase, stemming from the photoexcitation of an electron from the $2p\pi^*$ orbital $2p_\pi$, and $2p_\sigma$ valence orbitals of oxygen, respectively **[25, 27]**. These features are not observed up to 0.01 mbar in **Figure 3.4b** due to low partial pressure (concentration) of O_2; nonetheless, there is a huge shift in the BE of O_2 features was observed towards low BE by 1 eV, In comparisonto pure gas-phase O_2, the displacement of the vibrational characteristics may result from several factors, including adsorption and/or dissociation of the adsorbed molecules on the surface. This process could potentially alter the surface ϕ due to the creation of surface VOx layers. Such phenomena have been observed in various fields, including catalysis, electrochemistry, and sensing. In contrast to the sharp and clearly defined O_2 features observed for pure O_2, these changes are notable. (Black trace), a broad and not-so-well resolved features are observed on vanadium surface at 0.1 mbar and above indicates a possible heterogeneous nature of the surface with more than one type of VO_x species are present. Indeed, this is in good correspondence with the V 2p and O 1s core level results observed in **Figure3.3**. It is also to be noted that broadening and shift in O_2 vibrational features underscores its high sensitivity to detect the surface changes in a precise manner. Very low intensity, but narrow, bands are observed in pure O_2 spectrum around 6.1

eV. These bands originate due to He I β (23.09 eV; 1.5% intensity) satellite photons, compared to He I α (21.2 eV; 100%) photons. Satellite features appears at 1.9 eV below the main O_2 bands confirms this fact.

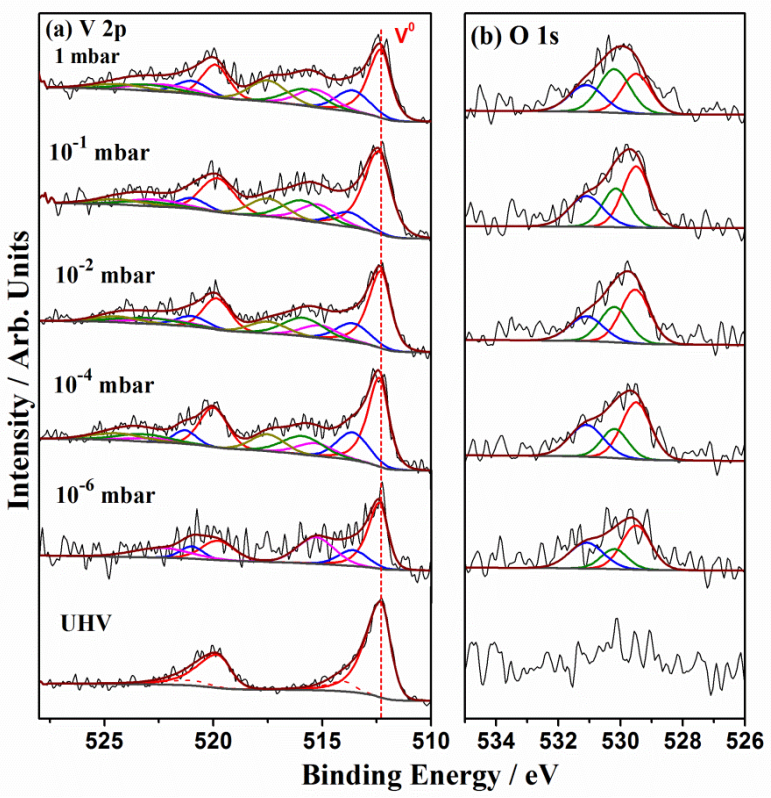

Figure3.3 NAP-XPS of **(a)** V 2p, and **(b)** O 1s core levels recorded as a function of O_2 partial pressure between 10^{-6} to 1 mbar at 298 K. Clean surface features recorded is shown as the bottom for comparison. (Red dashed line) shown in panel a is to denote the metallic vanadium feature. Y-axis intensity counts for panel b have been multiplied 2.5 times.

3.3.3 Temperature dependent V+O_2 interaction at 0.1 mbar O_2 partial pressure – NAPPES study

After conducting the V + O_2 interaction studies at 298 K, the next step involved exposing the re-sputtered and cleaned V foil to a constant O_2 partial pressure of 0.1 mbar while gradually increasing the temperature from 298 to 825 K. Spectra of V2p and O1s were recorded at various temperatures, and the outcomes are presented in **Figure 3.5**. In contrast to the observation of V-oxidation restricted to top surface layers in **Figure 3.3a**, severe change in oxidation towards higher oxidation state of $V^{4+}$and V^{5+} was observed as seen in **Figure 3.5**. a Number of interesting changes observed and the following points are worth highlighting: **(a)** Metallic V feature decreases gradually in intensity up to 625 K, and thereafter it disappears completely, indicating the vertical progression of oxidation into the bulk VO_x layers occurs at high

temperatures. **(b)** From 325 to 625 K, severity of the oxidation increases and V^{3+} increases in content, before it starts further oxidizing to V^{4+}at 625 K and above.

Also, V^{2+}oxidation state was observed only up to 425 K **(c)** 3+, 4+ and 5+ oxidation states of V is observed between 725-825 K; nearly V^{3+} (15.3 %), V^{4+} (36.0 %) and V^{5+} (41.3 %) oxidation states, along with minor V^{2+}, are observed under the most severe condition employed (825 K; 0.1 mbar) in **Figure 3.5**. Indeed, higher oxidation states of V forms at the expense of lower valence states, as the temperature increases. **(d)** Comparable amount of V^{4+} and V^{5+} oxidation states are observed from 425 K and above underscore the feasibility of oxidation to highest states, but within the limited layers of thickness. However, thickness of such oxidized layers increases with increasing temperature, at the cost of lower valence V oxidation states. **(e)** These observations demonstrate the requirement of thermal energy for oxygen diffusion into sub-surface and bulk layers of V. Indeed, progressive oxidation from lower to higher oxidation states of V and from surface to deeper layers occurs with increasing temperature at 0.1 mbar O_2 pressure and demonstrates a predominant thermodynamic control of oxidation. It may also be noted that prolonging the oxygen exposure for longer time could lead to more stable oxides at a given temperature. Hence some amount of kinetic control also is present. Nonetheless, within the same set of experimental conditions employed in the present studies, predominant thermodynamiccontrol is evident. V 2p features are shiftedtowards higher BE indicating that at high temperatures the rate of diffusion of oxygen is higher and revealing the changes in the oxidation state. One final observation is indicated by grey color trace fitted at 520 eV for 725 and 825 K spectral lines. When V-metal is predominantly observed at low temperatures, 520 eV feature (red color trace) is attributed to metallic vanadium (V $2p_{1/2}$). However, when the surface layers are predominantly oxidized, satellite feature of O 1s appears at 520 eV (due to secondary radiations of Al K α3 (6.4% intensity) and α4 (3.2 % intensity), with 9.8 and 11.8 eV higher than parent AlKα 1486.6 eV), which is indicated by grey color.

Spectra of the O 1s core level was also acquired, and the findings are displayed in Figure 3.5b. A distinct increase in S/N ratio at 525 K and above is observed for O 1s core level, compared to the results shown up to 425 K and in **Figure 3.3b**.This single observation underscores the previously drawn conclusion that oxygen permeates into subsurface and bulk layers at elevated temperatures, indicating the thermodynamic control nature of VOx formation.The Entire thickness of top 8-10 nm is explored under the present measurements conditions and observation of oxides of V^{4+} and V^{5+} supports the same. The intensity of the O 1s feature corresponding to long-range ordered species (530.3 eV) is also enhanced, underscoring the sign

of progression of oxide formation into deeper layers, at the cost of metallic vanadium layers. While the surface layers undergo oxidation, it's worth noting that the conditions of 0.1 mbar O_2 pressure and 825 K temperature are insufficient to fully oxidize vanadium into V_2O_5, even within the NAP-XPS probing depth of 8-10 nm. This stands in contrast to the complete oxidation of cobalt, which reaches Co_2O_3 even within the temperature range of 400 to 500 K at 0.1 mbar O_2 partial pressure. **[25]**.A comparative analysis and overall view of O 1s spectra presented in Figs. 3.3 and 3.5 suggests an interesting point. While it is expected that hydroxide would remain stable at ambient temperatures, the same is not true at

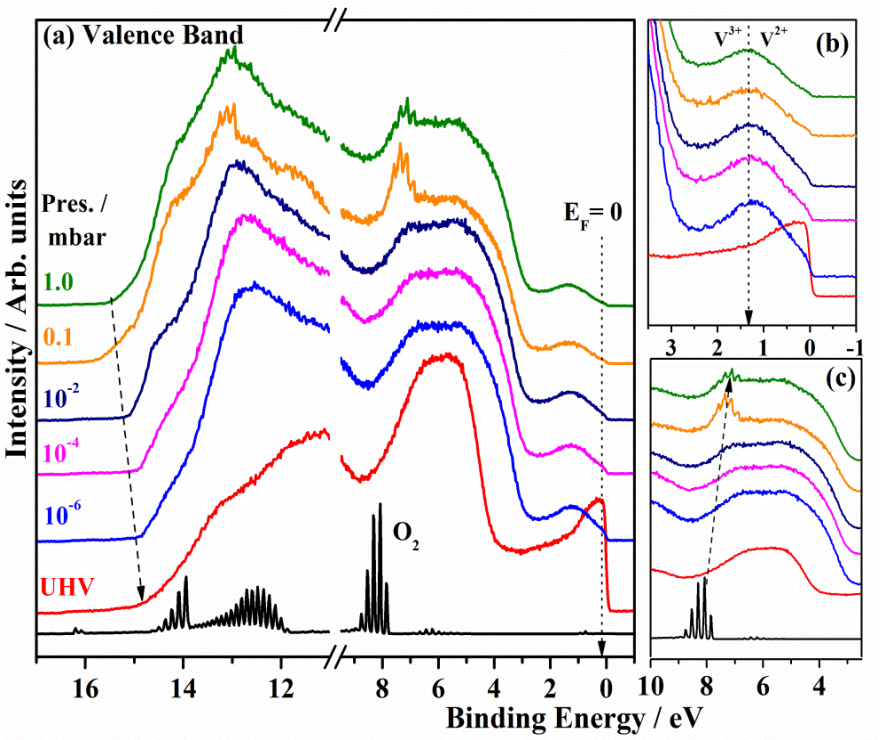

Figure 3.4 (a) NAP-UPS results recorded during V metal oxidation to VO_xin presence of gradually increasing O_2 partial pressure up to 1 mbar at 298 K. (b) $E_F$feature is shown in enlarged scale; the spectra shown for 10^{-6} to 1 mbar has been multiplied by a factor of 3.E_F feature is observed even at an O_2 partial pressure of 0.01 mbar. (c) O_2 gas-phase vibrational featuresand mainVB are shown on an enlarged scale. A shift towards low BEfor vibrational features and broadening of main VB is observed, as the O_2 partial pressureincreases.

high temperatures and hydroxide would decompose in thepredominant O_2atmosphere. However, the possibility of finding oxygen vacancies is significant, especially when the oxide layers are growing deeper into several layers at high temperatures at 0.1 mbar O_2 partial pressure. Indeed, the observation of gradual oxidation from low to high oxidation states at increasing temperature fully supports this. It is known that those oxide ions in the vicinity of

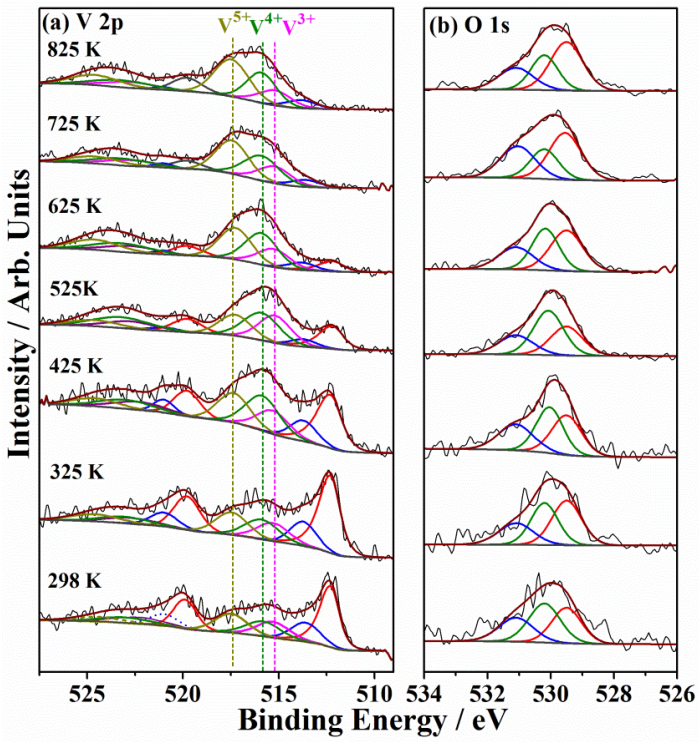

Figure3.5NAP-XPS of V 2p and O 1s region as a function of temperature at 0.1 mbar O_2 partial pressure. (a) V 2p XPS spectra, (b) O 1s XPS. Note the absence of metallic V feature above 625 K. Y-axis counts for panel b has been multiplied 2.5 times for 298, 325 and 425 K spectra.

oxygen vacancies (O_v) appear between 531-532 eV, and it is well documented in the literature, **[17, 23, 35, 37]**. In view of this factor, we attribute the 531.5 eV feature ≤425 K to hydroxide, and a combination of OH^- and oxygen in the neighbourhood of O_v between 425 and 625 K; above 625 K it is attributed only to oxides species that are closer to O_v.

VB spectra under NAP-UPS conditions were also captured while varying the temperature from 298 to 825 K at a 0.1 mbar O2 partial pressure, and these outcomes are depicted in **Figure 3.6.** While the features observed around 1 eV is attributed to V 3d features, main VB (between 3-7 eV) is due to strongly hybridized V 3d – O2p orbitals. Six important and complementary observations (to NAP-XPS results shown in Fig. 3.5) in **Figure 3.6** are worth highlighting, and they are the following: **(1)** A gradual change was noted in the O_2 gas phase features, with a shift towards lower binding energies at elevated temperatures. Notably, a significant shift of 0.65 evin the O_2 features was observed when the temperature was raised from 325 to 425K under a 0.1 mbar O_2 partial pressure. **(2)** In addition to the shift of vibrational features, an enormous broadening was also observed at high temperatures and the enlarged vibrational features are shown in **Figure3.5b**. This suggests the formation of different oxides on the surface, which makes the surface highly heterogeneous in nature. It is well known that molecular vibrations are sensitive to detect the homogeneous or heterogeneous nature of the

surface **[38]**. **(3)** with careful analysis of the spectra recorded between 325 and 625K reveal a low intensity broad hump at 1 eV, and this is attributed to V^{3+} feature. While 1 eV feature shows no changes, main VB picks up more area and becomes a square feature ≥425 K, compared to that of at 298-325 K. **(4)** Very interestingly, on increasing the temperature a sharp metallic feature started appearing at ≥725K near E_F. It is worth mentioning that at similar conditions, NAP-XPS (**Figure 3.5**) shows predominantly 4+ and 5+ oxidation states of V. It is known that the large V 3d – O 2p hybridization occurs in VO_2 and V_2O_5, with an appearance of $3d^1L$ feature of VO_2 at E_F **[18]**. **(5)** A significant broadening of the VB occurs, shifting by 0.6 eV towards lower binding energies when the temperature is increased from 625 K and above. Concurrently metallic E_F feature appears and the 1 eV feature remains observed. **(6)** **Figure3.6c** demonstrates an increase in ϕ from 5.7 to 6.8 eV between 298 to 725-825 K, respectively. This is in good agreement with the ϕ ~ 6.7 eV reported by Kim *et. al.* for VO_2**[21]**. Critically, VO_2 shows MI phase transition at various temperatures depending on the particle size of the vanadium oxide. It is also to be noted that significantly wide range of ϕ values is reported for VO_2 as well as metallic V, and it is partly due to various methods employed for ϕ measurements, particle size. ϕ of VO_2 is shown to change from 5.15 to 5.30 eV between 300 and 375 K **[17]**.

Sudden appearance of $E_F$feature observed at 0 eV supports the metallic nature of VO_2. The changes observed in the E_F is caused by the increased oxygen diffusion in polycrystalline V-metal foil in the form of VO_2 as a result of heating to high temperatures. An increased rate of oxygen diffusion in polycrystalline metal foil is related to the presence of more number of dangling bonds. Such phenomenon exists at lower temperature in amorphous film and nano-particles, and it depends on oxidation current, anodic oxidation time, and sample sizes **[39]**. The rate of oxygen diffusion is reported to be 5-7 timeslower with amorphous vanadium film compared to polycrystalline V-foil. We speculate the atomic oxygen diffusion into the polycrystalline vanadium foil and mixed VO_x observation leads to the explanation for observed MI phase transition at high temperature (725K) in comparison to the previously reported low temperature MI transition at 340 K with VO_2 nanodomain **[21]**. Fast switchable/reversible MI transition makes VO_2 widely employed in applications, such as, electronic devices, energy efficient switches, and ultrafast switches. Furthermore, the charge carrier concentration and dielectric constant of VO_2 in the normal insulating state at ambient temperatures makes it applicable to Hall effect devices, due to low electron mobility and sensitive temperature dependence of the carrier concentration in VO_2. VO_2 is also used for making heterostructure

devices, by deposition of high-quality thin film of VO_2 on high mobility semiconductors, such as, heavily doped Ge, TiO_2, Al_2O_3.**[1]**

3.3.4 Time dependent Study of V+O_2 interaction – NAPPES study

The core level NAP-XPS and NAP-UPS spectra were obtained at various time intervals during the protracted oxidation process, and the findings are reported in **Figure 3.7** and **3.8**, respectively. In time dependent study, the V-foil was exposed to molecular oxygen at 875 K for up to 18 h and spectra were recorded periodically with significantly long interval. Oxidation from metallic vanadium to a mixture of V_2O_3, VO_2 and $V_2O_5$was observed in the earlier results (**Figures 3.3-3.6**). After exposure to 0.1 mbar O_2 partial pressure at 825K, the V foil underwent oxidation, resulting in the formation of V^{4+} (36.0%) and V^{5+} (41.3%) species (Figure 3.5a). By heating the sputter cleaned vanadium metal foil at 1 mbar O_2 at 875 K, a minor decrease in the V^{4+} content was observed to 27-35%, from 36.0% at 0.1mbar O_2 at 825 K. Continuous oxygen exposures at 1 mbar for up to 18h, no significant change in the ratio of V^{4+}:V^{5+} was observed. The intensity of V^{4+} and $V^{5+}$was almost the same and it is observed within 5% error limit. V^{5+} was the dominant (42-55.9%) followed by V^{4+} 27-35%) and V^{3+} (17-20%).The oxidation of VO_2 to V_2O_5 is kinetically a slow process and it requires concurrent high temperature as well as high pressures (>1 mbar). Nonetheless, observation of V^{3+} and V^{4+}, even after prolonged exposure of O_2suggests the oxygen diffusion into the sub-surface and bulk layers might be rate determining factor towards oxidation to V_2O_5.

Periodic NAP-UPS spectra were collected to investigate the progression of electronic structure and interface alterations, with the aim of assessing changes in ϕ. The obtained results are depicted in **Figure 3.8a-c**. Following each 2-hour interval of oxygen treatment at 875 K and 1 mbar O_2 partial pressure, a spectrum was acquired at 0.1 mbar O_2 pressure and compared in **Figure 3.8**. NAP-UPS recorded at 875 K show high E_F intensity, and this corresponds to metallic nature of VO_2 and dominant over the surface. This set of spectra is similar to that of spectrum given in green/purple color in **Figure 3.6a**. Enlarged E_F features are shown in **Figure 3.8b** as a function of O_2 treatment at 875 K; however, results show very similar E_F pattern hinting the stability of VO_2 under the measurement conditions. A minor decrease in E_F intensity is observed, as the time of O_2 exposure increases. Nonetheless, no change in the photoelectron emission offset was observed (**Figure 3.8 c**) also supports the robust nature of VO_2 on the surface. Indeed, it is surprising that VO_2 does not undergo further oxidation, despite prolonged heating; we speculate that the metallic character of VO_2 might hinder further oxidation, until the oxidation condition becomes more severe. It is also to be noticed that on returning to 298

K under UHV, metallic feature remains to be seen (dark purple trace). However, a shift in main VB to higher BE suggests a significant change in the nature ofsurface oxide. A careful look at the O_2 gas-phase vibrational feature shifts to high BE at t = 18 h, likely hinting a possibility of onset of further oxidation. Curve fitting parameters of XPS spectra in pressure, Temperature and time dependent study and the quantification of various V-species are shown in Table 3.1, 3.2 and 3.3.

3.3.5 The Relationship between Surface Composition and Work Function

The changes in the ϕ of the VO_x can be tuned by changing the stoichiometry of the surface **[35, 40-41]**. The ϕ of VOx at various oxidation stages, determined from the offset value of NAP-UPS spectra, is graphed in**Figure 3.9**, as a function of (a) partial pressure of O_2, (b) temperature at 0.1 mbar O_2 pressure, and (c) time of exposure to O_2 at 1 mbar at 875 K. The change in the ϕ indicated that surface dipole changes with exposure to O_2. At UHV and

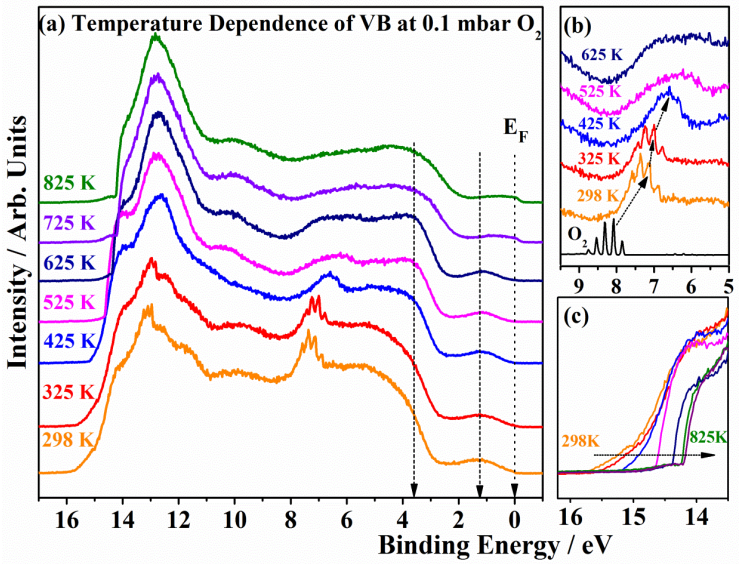

Figure 3.6 (a) Temperature dependent NAP-UPS results recorded for V-metal oxidation in presence of 0.1 mbar O_2 partial pressure. (b) Molecular O_2 vibrational features, and (c) changes in the work-function, through photoelectron emission offset, are shown on an enlarged scale. Features in panel b is multiplied for clarity; 298 and 325 K spectra are multiplied by a factor of 3, and 425 to 625 K spectra are multiplied with a factor of 5.

Table 3.1: Relative % of various Vanadium oxidation state on the surface for results shown in Fig. 3.3a:

Pressure / mbar	V(0)	V(2+)	V(3+)	V(4+)	V(5+)
10^{-9}	88.4	0	0	0	
10^{-6}	49.9	16	34.1	0	
10^{-4}	45.2	17.8	9.7	15.5	11.6
10^{-2}	44.3	15	11.4	18.3	12
10^{-1}	44.3	10.3	14	17.4	14.1
1	41.1	11.5	15.5	17.5	14.4

Table 3.2: Relative % of various Vanadium oxidation state on the surface for results shown in Fig. 3.5a:

T /K	V(0)	V(2+)	V(3+)	V(4+)	V(5+)
325	38.1	14.2	13.3	15	16.4
425	29.8	11.3	15.4	23.9	19.4
525	18.6	5.7	26.2	29.1	20.2
625	9	6.7	18.7	32.6	32.8
725	0	7.5	20.2	35.5	36.5
825	0	6.4	15.3	36	41.3

Table 3.3: Relative % of various Vanadium oxidation state on the surface for results shown in Fig. 3.7a:

Time (h)	V(0)	V(2+)	V(3+)	V(4+)	V(5+)
1	0	6	14.5	35	36.5
3	0	0	20.4	36.1	43.5
5	0	0	20.5	34.9	44.6
7	0	0	18.6	32.6	48.8
9	0	0	18	30.5	51.2
13	0	0	17.5	28.8	53.7
18	0	0	17	27.1	55.9

298K, the ϕ of metallic V was observed to be 6.4 eV; however, it varies between 5.9 to 6.8 eV for VO_x. The change in ϕ depends on variousfactors, such as stoichiometry of VO_x, size of VO_x particles/islands or growth of VO_x layers and surrounding environment. With increase in the O_2 partial pressure from metallic vanadium under UHV conditions to 1 mbar partial pressure of O_2 at ambient temperature (**Figure 3.9a**), a decrease in the ϕ by 0.5±0.05 eV was observed. Nonetheless, when the VOx depicted in **Figure 3.9a** is subjected to 0.1 mbar O_2 partial pressure at elevated temperatures, the ϕ rises from 5.9 eV at 298 K to 6.9 eV at 825 K (**Figure 3.9b**). However, in the time dependent study (**Figure 3.9c**), the ϕ shows a marginal change of 0.1 eV. It is evident from the above data that the ϕ increases linearly withtemperature, and decreases linearly with O_2 partial pressure. While the temperature depend-dence at 0.1 mbar shows an increase in ϕ, metallic VO_2 observed at high temperatures is an unusual phenomenon with transition metal oxides.

Indeed, VO_2 is an exceptional case; at least we are unaware that any other metal oxide turns metallic at such high temperatures (≥725 K). Further, it is known in the literature that metallic behaviour is due to rutile phase of VO_2 with contribution from V t_{2g} and O 2p orbitals. Infact, the interesting observation is the MI transition observed at high temperatures, but at 0.1 mbar O_2 partial pressure, while all the literature reports are carried out at ambient pressure with bulk/nano VO_2 materials. It is also to be reemphasized that the thickness of VO_2 in the present

experiments cannot be more than 10 nm, which is the probing depth of NAPXPS, and observed along with significantly larger amount of V_2O_5. Hence it is very likely that VO_2 is present in the nano-domains with interweaving V_2O_5, under the present experimental conditions. Metallic $E_F$feature observed at 298 K in Fig. 3.9a (dark purple trace)could be possibly due to this, which is in contrast to the insulating behaviour of bulk

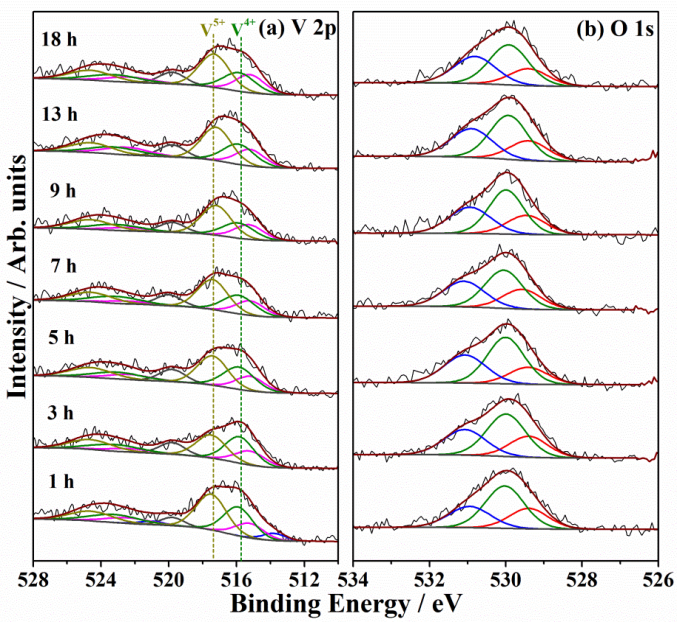

Figure 3.7. In situ NAP-XPS studies of (a) V2p and (b) O1s core level spectra recorded on vanadium as a function of oxygen exposure time at 0.1 mbar partial pressure of O_2at 875 K.

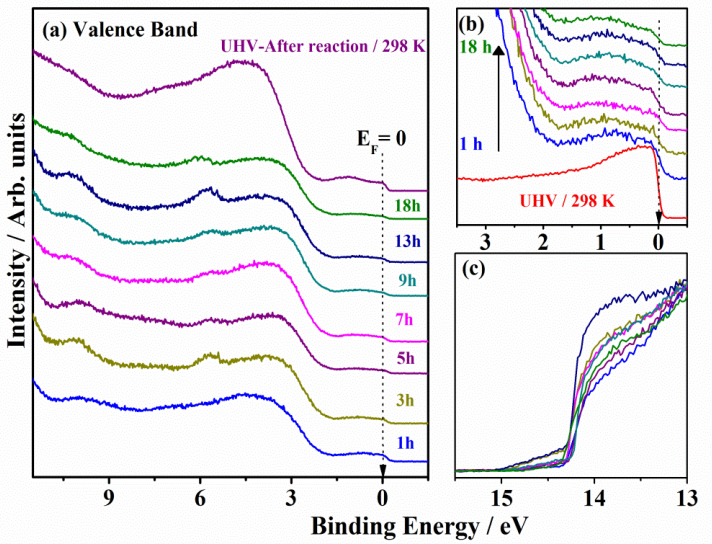

Figure 3.8. (a) Time dependent evolution of V oxidation from V metal to a mixture of VO_2 and V_2O_5 at 1 mbar / 875 K; however, NAP-UPS spectra were recorded at 0.1 mbar / 875 K, (b) Fermi energy level, and (c) spectral offset features are shown at an enlarged scale.

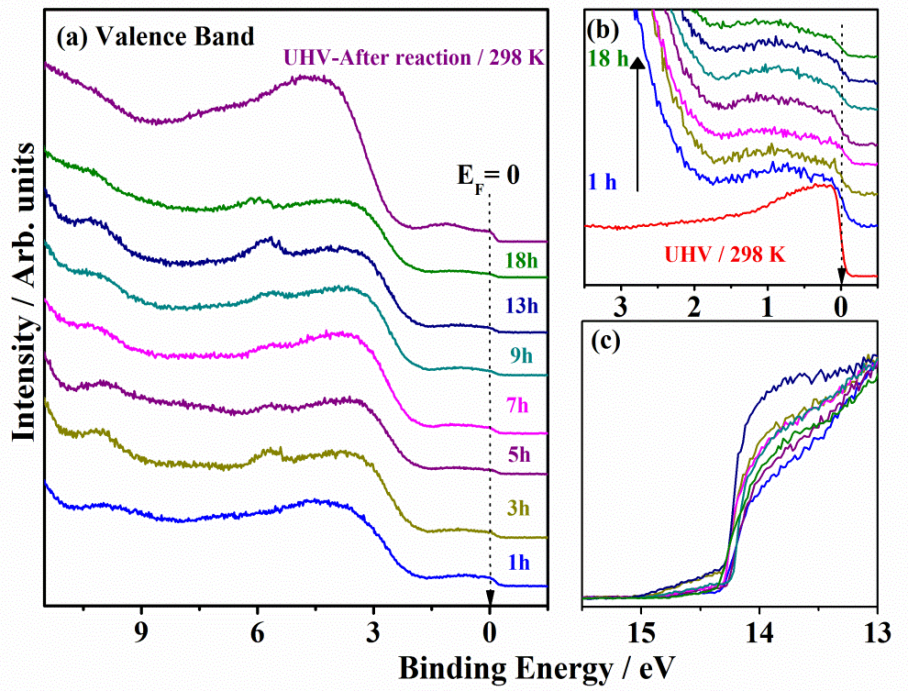

Figure 3.9. (a) Time dependent evolution of V oxidation from V metal to a mixture of $VO_2$and V_2O_5 at 1 mbar/ 875 K; however, NAP-UPS spectra were recorded at 0.1 mbar / 875 K,(b) Fermi energy level, and (c) spectral offset features are shown at an enlarged scale.

VO_2 below 340 K. Another interesting observation is the decrease in ϕ due to increasing O_2 partial pressure, but at 298 K, while ϕincreases with temperature at 0.1 mbar O_2 partial pressure. While multiple oxidation states of vanadium is observed in both scenarios, the thickness of oxidation was really limited to 3-5 nm at 298 K with underlying metallic vanadium, and oxidized layers.

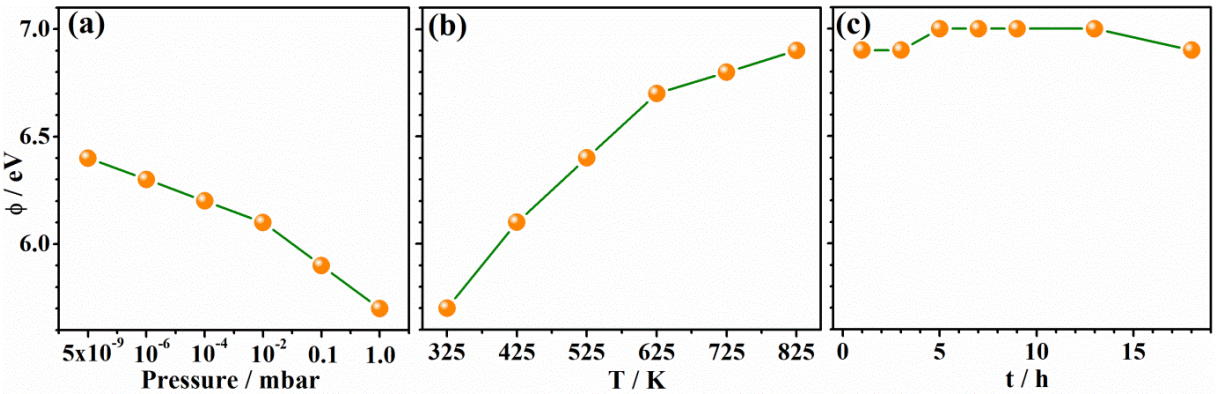

Figure 3.10 Changes in the ϕof VO_x layers during the oxidation of metallic V to VO_x as a function of, (a) O_2 partial pressure at 298 K, (b) temperature at 0.1 mbar O_2 partial pressure, and (c) exposure time to 1 mbar O_2 partial pressure at 875 K.

A bird's eye view for the changes in oxidation states of vanadium as a function of all measurement conditions are shown in **Figure 3.11**. Changes in V^0, V^{2+}, V^{3+}, V^{4+} and V^{5+} content, which is measured from deconvolution of NAP-XPS results, as a function of (a) O_2

partial pressure at 298 K, (b) temperature at 0.1 mbar O_2partial pressure, and (c) O_2 exposure time at 1 mbar and 875 K is shown. Irrespective of the O_2 pressure, metallic vanadium content dominates the surface at 298 K, while all other oxidation states contribute to a comparable extent. This trend completely changes, when the temperture increases at 0.1 mbar O_2 pressure; metallic vanadium and V^{5+} oxidation state decreases and increases, respectively, when the reaction conditions applied become severe. The metallic feature disappears completely above 625 K. V^{2+} and V^{3+} content increases initially from 298 to 525 K, and thereafter it decreases for further increase in temperature. This underscores that the oxidation of vanadium occurs sequentially from lower to higher oxidation states. Predominant presence of V^{5+} followed by V^{4+} states, along with minor amount of lower valence oxidation states, even after 18 h O_2 treatment at 875 K at 1 mbar, reiterates that oxygen diffusion into bulk layers requires more severe conditions towards complete oxidation to V_2O_5. In the lab-based NAPPES system employed for the present measurements, exposure to higher pressure is not possible due to operation limitations.

3.4 Conclusion

In conclusion, we have examined oxide formation of V foil. The surface layers of V metal are methodically transformed into a blend of different oxides, including VO, V_2O_3, VO_2, and V_2O_5, utilizing NAPPES techniques through controlled oxidation of the V foil under near-ambient pressures (0.1 mbar) and temperatures (up to 875 K). V metal gradually oxidises to VO and then slowly it started evolving to V_2O_3 and VO_2; approximately 55.9 % V metaloxidises to higher oxidation states (VO_x). Complete oxidation is not evident at 0.1 mbar O_2 pressure and 298 K. However, when exposed to 0.1 mbar O_2 pressure and temperatures above 625 K, the metallic feature vanishes entirely, and there is a systematic development of VO_2. Further, the transition of V_2O_3 to VO_2 is observed at high temperature (>725 K) along with MI transition. Although the MI transition was first observed at high temperatures, it is stable even at ambient temperatures, which is worth investigating further. Thepresent investigations reveal not only the formation of VO_x with various stoichiometries, but also the diffusion of atomic oxygen into the layers of the V surface. Therate of oxygen diffusion increases at high temperatures and decreases at high pressure, likely because of the presence of oxide layers that inhibit further oxidation. The formation of VOx is also substantiated by the change in the ϕ of the surface.

The diffusion of oxygen and VO_x formation is identified through V 3d – O 2p interaction in NAP-UPS. Changes in the width of oxygen vibration features characterize the formation of heterogeneous natures due to the formation of mixture of VO_x.**[26]** ϕ is a critical

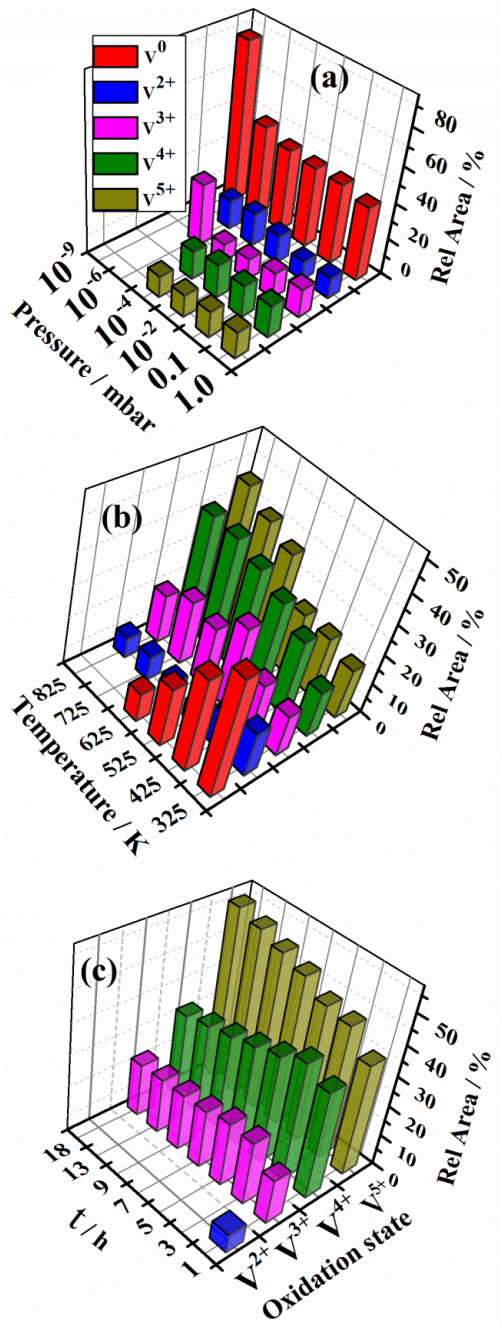

Figure 3.11. 3D plots of relative area percentage and various oxidation states of vanadium as a function of (a) particle pressure of O_2, (b) temperature, and (c) time.

electronic property of a surface that is primarily influenced by its structure and electronic characteristics, and it is assessed under realistic or near-realistic conditions. Moreover, at temperatures exceeding 625 K, metallic vanadium undergoes predominant oxidation, resulting in a mixture of V^{3+}, V^{4+}, and V^{5+} oxidation states at a partial O_2 pressure of 0.1 mbar. The alterations in the density of states (DOS) near the E_F above 723 K and at 0.1 mbar O_2 partial pressure indicate the emergence of metallic behaviour, attributed to the formation of VO_2. Although other VO_x are present, metallic feature characterizes the dominance of VO_2, even

with the presence of nano-domains of other VO_x. Critically, metallic nature preserved even at ambient temperature is worth investigating further with other methods, particularly for conductivity and microscopy studies. Indeed, thin film form of VO_2 with other VO_x could still be a potential solution for many applications. The NAPPES study clearly demonstrates its ability to investigate the evolution of electronic structure under varying reaction conditions, emphasizing its significance in fields such as heterogeneous catalysis and sensing.

3.5 Reference:

1. Griffiths, C. H.; Eastwood, H. K. *J. Appl. Phys.***1974,***45*, 2201–2206.

2. Whittaker, L.; Zhang, H.; Banerjee, S.*J. Mater. Chem.***2009,***19*, 2968–2974.

3. Sivaranjani, K.; Verma, A.*Green Chem.***2012,***14*, 461–471.

4. Shiju, N. R.; AnilKumar, M.; Mirajkar, S.P.; Gopinath, C. S.; Roa, B. S.; Satyanarayana, C.V.*J. Catal.***2005,***230*, 484–492.

5. Talledo, A.; Granqvist, C. G. *J. Appl. Phys.***1995,***77*, 4655–4666.

6. Devaraji, P.; Sathu, N. K.; Gopinath, C. S;*ACS Catal.***2014**, *4*, 2844-2853.

7. Herman, I. P. Electrical and Magnetic Properties. Springer, Cham, Switzerland,**2016**; pp 819–871.

8. Suga.S.; Taniguchi, M.; Kanzaki, H.*Phys. Rev. B***1990,***41*, 4993-5009.

9.Langeslay, R. R.; Kaphan, D. M.; Marshall, C. L.; Stair, P. C.; Sattelberger, A. P.; Delferro, M.*Chem. Rev.* **2019,***119*, 2128−2191.

10. Gopinath, C. S.; Roy, K.; Nagarajan, S.*ChemCatChem***2015,***7*, 588–594.

11. Klein, A.; Körber, C.; Wachau, A.; Säuberlich, F.; Gassenbauer, Y.; Harvey, S. P.; Proffit, D. E.; Mason, T. O.*Materials* **2010,***3*, 4892–4914.

12. Walsh, A.; Catlow, C. R. A.*J. Mater. Chem.***2010,***20*, 10438–10444.

13. Son, M. J.; Kim, S.; Kwon, S.; Kim, J. W.*Org. Electron.***2009,***10*, 637–642.

14. Meyer, J.; Khalandovsky, R.; Görrn, P.; Kahn, A.*Adv. Mater.***2011,***23*, 70–73.

15. Gopinath, C. S.; Nalajala, N.*J. Mater. Chem. A.***2021,***9*, 1353-1371.

16. Raja Ambal, S.; Sivaranjani, K.; Gopinath, C. S.*J. Chem. Sci.***2015,***127*, 33-47.

17. Ko, C.; Yang, Z.; Ramanathan, S.*ACS Appl. Mater. Interfaces.***2011,***3*, 3396–3401.

18. Shao, Z.; Cao, X.; Luo, H.; Jin, P.*NPG Asia Mater.***2018**, *10*, 581–605.

19. Goodenough, J. B. The.*J. Solid State Chem.***1971**, *3*, 490–500.

20. Shibuya, K.; Kawasaki, M.; Tokura, Y. *Appl. Phys. Lett.***2010**, *96*, 022102.

21. Kim, C. Y.; Slusar, T.; Cho, J.; Kim, H. T.*ACS Appl. Electron. Mater.***2021**, *3*, 605–610.

22. Morin, F. J.*Phys. Rev. Lett.***1959,***3*, 34-36.

23. Reddy, K. P.; Mhamane, N. B.; Ghosalya, M. K.; Gopinath, C. S.*J. Phys. Chem. C.***2018,***122*, 23034–23044.

24. Jain, R.; Reddy, K. P.; Ghosalya, M. K.; Gopinath, C. S.*J. Phys. Chem. C***2017,***121**, 20296–20305.

25. Reddy, K. P.; Jain, R.; Ghosalya, M. K.; Gopinath, C. S.*J. Phys. Chem. C***2017,***121**, 21472–21481.

26. Ghosalya, M. K.; Prabhakar Reddy, K.; Mhamane, N. B.; Ranjan, R.; Gopinath, C. S.*Phys. Chem. Chem. Phys.***2020,***22**, 15528–15540.

27. Ghosalya, M. K.; Jain, R.; Reddy, K. P.; Gopinath, C. S.*J. Phys. Chem. C.***2018,***122**, 4331–4338.

28. Kolekar, S. K.; Dubey, A.; Date, K. S.; Datar, S.; Gopinath, C. S.*Phys. Chem. Chem. Phys.***2016,***18**, 27594–27602.

29. Ghosalya, M. K.; Reddy, K. P.; Jain, R.; Roy, K.; Gopinath, C. S.*J. Chem. Sci.***2018**, *130*, 30.

30. Roy, K.; Vinod, C. P.; Gopinath, C. S.*J. Phys. Chem. C***2013,***117**, 4717–4726.

31. Roy, K.; Gopinath, C. S.*Anal. Chem.***2014,***86**, 3683–3687.

32. Fairley, N.; Fernandez, V.; Richard-Plouet, M.; Guillot-Deudon, C.; Walton, J.; Smith, E.; Flahaut, D.; Greiner, M.; Biesinger, M.; Tougaard, S.; Morgan, D.; Baltrusaitis, J. *Appl. Surf. Sci. Adv.***2021**, 5,100112

33. Biesinger, M. C.; Payne, B. P.; Grosvenor, A. P.; Lau, L. W. M.; Gerson, A. R.; Smart, R. S. C.*Appl. Surf. Sci.***2011,***257**, 2717–2730.

34. Sawatzky, G.; Post, A. D.*Phys. Rev. B***1979**, *20*, 1546-1555.

35. Wang, R.; Katase, T.; Fu, K. K.; Zhai, T.; Yang, J.; Wang, Q.; Ohta, H.; Koch, N.; Duhm, S.*Adv. Mater. Interfaces***2018,***5**, 1–7.

36. Roy, K.; Jain, R.; Gopinath, C. S.*ACS Catal*. **2014**, *4*, 1801−1811.

37.Mhamane, N. B.; Chetry, S.; Ranjan, R.; Raja, T.; Gopinath, C.S.*ACS Sustainable Chem. Eng.***2022**, 10, 3521−3531.

38. Jain, R.; Reddy, K. P.;Ghosalya, M. K.;Gopinath, C. S.*J. Phys. Chem. C***2017,***121**, 20296-20305.

39. Ilinski. A.; Silva-Andrade. F,; Shadrin. E,; Klimov. V.*J. Non-Cryst. Solids***2004**, *338–340*, 266–268**.**

40.Wu, Q. H.; Thissen, A.; Jaegermann, W.; Liu, M.*Appl. Surf. Sci.***2004,***236**, 473–478.

41. Greiner, M. T.; Lu, Z. H.*NPG Asia Mater.***2013,***5**, 1–16.

Chapter -4

$Cu – Cu_2O – CuO – Cu_2O – Cu$ – Roundtrip Electronic Structure Evolution by near ambient pressure valence band photoelectron spectral studies

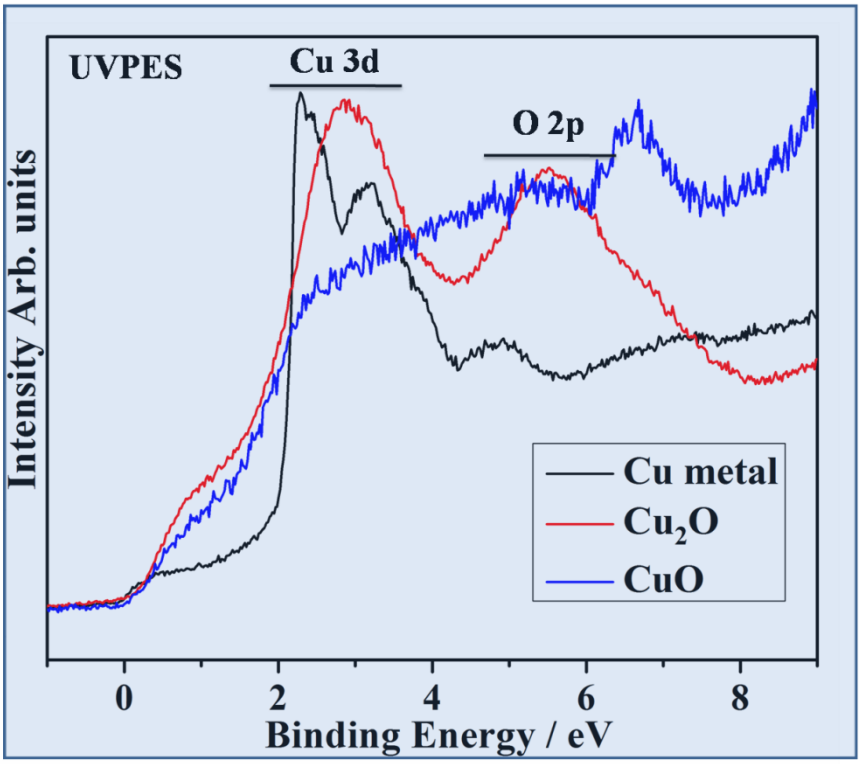

4.1 Introduction

The investigation of copper (Cu) oxidation and copper oxide reduction is driven by both fundamental and applied considerations. Primarily, there is a significant interest in comprehending the unique structural and electronic properties exhibited by oxides. Additionally, the extensive utilization of copper and its oxide in electronic and catalytic applications further motivates this study **[1, 2]**. During catalysis operation or activation, the exposure of copper to oxidizing or reducing environments can induce modifications in its electronic structure. Reduction processes are attributed to the consumption of lattice oxygen, which facilitates the removal of oxide and ionsfrom the surface and the bulk. Numerous studies have been conducted to comprehend the behavior of copper oxidation and reduction, employing surface science techniques. These studies have utilized single crystals, polycrystalline materials **[3]**, and powder form **[4]** of Cu, CuOx and Cu-containing catalysts. **[5-7]** Within many of these investigations, an intriguing characteristic of the Cu and CuO_x system is observed, wherein the surface composition can be readily modified, leading to relatively facile oxidation and reduction processes.

Copper could exist in metallic, 1+, 2+ 3+ oxidation states **[8]** and a possible combination of few of them in a single material. Notably, CuO and Cu_2O are widely recognized as p-type and anti-ferromagnetic semiconductors, with reported band gaps ranging from 1.3 eV to 2.1 eV for CuO and from 2.1 eV to 2.6 eV for Cu_2O **[9,10]**. CuO possesses a band gap of approximately 1.4 eV **[11]**, It offers a stepwise progression in the alteration of the oxidation state, starting from 2+ to 0 and proceeding through 1.5+ and 1+ ($CuO \rightarrow Cu_4O_3 \rightarrow Cu_2O \rightarrow Cu$). These sub-oxides, Cu_4O_3 and Cu_2O, known for their distinct band structures and phase stability, have been thoroughly investigated by Heinemann *et. al.* **[12]**. The interfaces between CuO/Cu_4O_3, Cu_4O_3/Cu_2O, and Cu_2O/Cu play a crucial role in catalysis and the microelectronic industry. The use of hydrogen for reducing copper oxide is a commonly utilized technique to create catalysts and electronic devices with enhanced activity. Often pre-treatment or activation involves reduction in hydrogen atmosphere with many oxide catalysts. However, the atomic or molecular-level understanding of the reduction behavior of Cu remains limited.At a fundamental level, it is crucial to understand how hydrogen dissociation, the removal of oxygen (leading to the creation of oxygen vacancies), and the stability of sub-oxides interact with each other. The study of the redox behavior of copper oxides (CuOx) holds significant importance in the field of catalysis. CuO_x is among the most extensively employed for many different

applications in catalysis, electrochemistry, metallurgy and corrosion science. Since numerous industrial components are composed of copper, comprehending the redox behavior of copper is of paramount importance. Enhancing our comprehension of oxide catalysts empowers researchers to exert more precise control over the chemical reactions they facilitate, offering potential solutions for clean energy applications. Copper and its oxides play a catalytically important role in various chemical reactions involving hydrogen as both a reactant and product, such as methanol synthesis from CO_2 or CO **[13]**, water-gas, and reverse water-gas shift reactions **[14,15]**, methanol steam reforming **[16]**, oxidative methanol reforming **[17]**, and NO reduction **[18]**, leading to valuable fuels. Therefore, achieving precise control over the amount of oxygen/hydrogen and the oxidation or electronic state of copper is a crucial step toward efficient chemical reactions.

The reduction of copper at the bulk level was investigated through the utilization of temperature programmed reduction (TPR), which revealed a three-step reduction process for CuO**[19]**. X-ray absorption near edge structure (XANES) spectroscopy offered evidence supporting the presence of transient Cu^{1+} species during the reduction process from Cu^{2+} to Cu(0) **[20]**. Additionally, *in-situ* X-ray diffraction (XRD) allowed for the real-time observation of the CuO to Cu transformation across various temperature and pressure conditions. **[21]**. However, the electronic state changes and variations in the ϕ during the bulk reduction of copper have not been studied. While the systematic oxidation of Cu metal to CuO has been explored in previous publications by our research group **[22, 23, 24]**, the reverse of the same or the reduction process and its kinetics have not been adequately understood. Consequently, we have conducted an extensive study to explore variations in ϕ during the oxidation process in the presence of oxygen and the subsequent reverse process of reduction in the presence of hydrogen. Aim of the current work is to gain insights into the reversibility of the entire process and how difficult or easy to achieve the same under the NAPPES conditions.

UVPES offers higher sensitivity compared to XPS, making it particularly effective in detecting surface contamination and surface-specific electronic alterations occurring within the top 2 nm. In this study, NAP-UPS was employed to investigate the modifications in the VB, electronic structure, and ϕ changes during the oxidation of Cu to CuO and the subsequent reverse of reduction of CuO surfaces to Cu, under oxidizing (O_2) and reducing (H_2) atmospheres, respectively, at pressures around sub-millibar range and elevated temperatures. From a practical standpoint, it is crucial to comprehend the kinetics and thermodynamic

parameters that govern the formation of interface and surface species. While our research group has examined the systematic oxidation of Cu metal to cupric oxide (CuO), the reduction process from CuO to Cu metal has not been investigated. In this study, we address various stages of the oxidation of Cu metal to CuO, including the formation of Cu_2O, and investigate the kinetics of the transitions from CuO to Cu_2O and from Cu_2O to Cu metal. Significant shifts in the energy levels of Cu 3d and O 2p were observed during these processes.

4.2 Cleaning procedure of Cu metal foil

A 1M HNO_3 acid-etched copper (Cu) metal foil underwent a thorough cleaning process within the NAPPES unit. The Cu foil was meticulously cleaned through repeated cycles of Ar+ sputtering under a pressure of 5.5 $\times 10^{-6}$ mbar, using 4 kV and 7 mA at 550 K. Following this, annealing was performed in an O_2 environment (1×10^{-6} mbar) at 600 K for 15 minutes, followed by vacuum annealing at 1000 K for 30 minutes. This sputter cleaning procedure was repeated until XPS analysis revealed no peaks other than those of Cu metal. This process effectively eliminated carbon impurities in the form of CO_2, Following the vacuum annealing, any residual surface oxygen from the previous annealing steps was effectively removed. Additionally, impurities such as sulfur, silicon, and phosphorus were either not detected or were present at concentrations below the detection limits of the R3000 analyzer. The PES experiments covered a pressure range from UHV conditions at 1×10^{-10} mbar to 0.1 mbar and temperatures ranging from 295 to 873 K. These experiments were conducted utilizing a custom-designed laboratory-based NAPPES facility, as explained in detail in Chapter 2.

4.3 Result and discussion

4.3.1 Oxidation of Cu metal to CuO

It is well-known that 3d transition metals are pyrophoric in nature, and surface layers of those metals get oxidized even at ambient temperatures and pressure. Part of the current investigation focuses on the modulation of VB characteristics of the Cu surface in response to variations in O_2 partial pressure and temperature. The experimental findings, as illustrated in **Figure 4.1**, reveal that the pristine Cu surface displays typical 3d VB attributes within the BE range of 1.5 to 4.5eV, accompanied by a distinct feature corresponding to the E_F. The identification of clean Cu-surface motifs is consistent with earlier reports and this was observed after repeated surface cleaning and annealing processes. Clean Cu-metal temperature was increased initially to 600 K, and subsequently the O_2 partial pressure was increased gradually; the spectra were recorded

as a function of O_2 partial pressure at 600 K. Representative set of spectra are shown in Fig.4.1. Introduction of gas-phase oxygen at $2x10^{-7}$ mbar at 600 K induces many changes on the Cu-surface, which is well above simple chemisorption. Elevated partial pressures induce a broadening of the CuO_x VB feature at $2x10^{-7}$ mbar, causing the disappearance of the Cu metallic characteristic and its transformation directly into Cu_2O. This surface chemical transition is marked by the emergence of a broad single Cu 3d feature spanning 2-4 eV, along with a low intensity feature around 1 eV. Although Cu_2O is an oxide, due to the fully filled nature of Cu 3d orbitals ($3d^{10}$), there cannot be any hybridization between Cu 3d and O 2p orbitals. Indeed, second broad feature observed between 4-7 eV is attributed to the O 2p feature of Cu_2O. A deep valley observed between Cu 3d and O 2p features testifies that there is no hybridization among them, and both Cu 3d and O 2p bands are sufficiently energy separated.

Complete oxidation of surface layers of Cu to Cu_2O, as evident from the appearance of a characteristic feature at 1.3 eV, suggest very low partial pressure is sufficient to form Cu_2O at 600 K. Figure 4.1 (bottom spectra) shows a reference molecular oxygen gas-phase spectrum taken at 0.1 mbar at 298 K. The gas-phase photoelectron spectrum of O_2 arises as a consequence of the emission of electrons from distinct electronic states of O_2. The excitation of electrons with He-I photons leads to the emergence of photoelectron bands exhibiting vibrational characteristics features centered at binding energies of 8, 12.5, and 13.5 eV, as observed for oxygen.Three set of bands observed are due to $2p_\pi$* (anti-bonding), $2p_\pi$, (bonding-π) and $2p_\sigma$ (bonding-σ) orbitals at 8, 11.5 and 13.5 eV, respectively **[25]** However, no significant oxygen vibrational features are observed at a partial pressure of $2x10^{-7}$ mbar, which is very low to observe any meaningful features.Nonetheless, our research group haveinvestigated the preliminary aspects of oxidation of Cu metal, and similar transformations have been observed during the oxidation process leading to the formation of CuO**[22]**.

On increasing the O_2 partial pressure from $2x10^{-7}$to $5x10^{-3}$ mbar facilitated a dramatic change in the VB features, and it is attributed to significant oxidation of Cu_2O to CuO. While Cu 3d feature around 3 eV remains observed at the same BE, as that of Cu_2O, the O 2p feature shifted to lower BE by 0.6-0.8 eV. This transition was accompanied by the broadening of the Cu 3d feature and the elimination of the valley around 4.5 eV, which is typical for Cu_2O. These variations are due to substantial hybridization between the Cu 3d and O 2p bands, which is also compatible with the observed surface alterations around 0.6 eV. A set of minor features was observed around 7 eV, even at $5x10^{-3}$mbar.On increasing the O_2 partial pressure to $7x10^{-2}$ mbar,

a clear set of features observed around 7 eV is attributed to the vibrational features of molecular oxygen. Indeed, this set of features shift rigidly with further increase in pressure alongwith the complete oxidation ofsurface layers to CuO. A significant shift in Cu 3d feature was also observed to lower BE, as the O_2 partial pressure

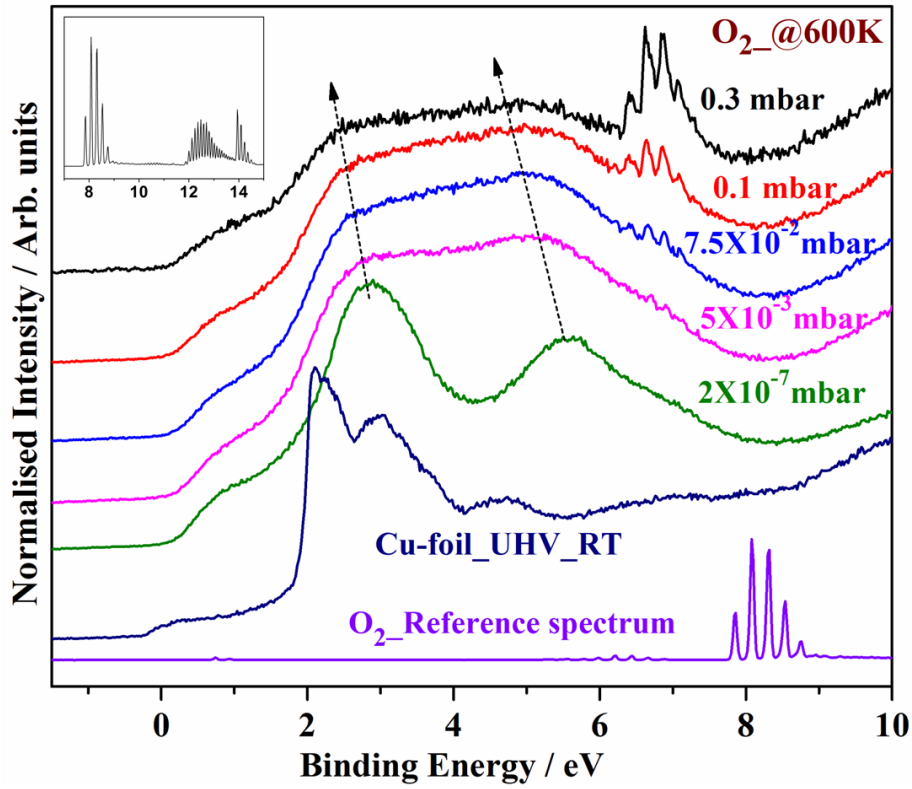

Figure 4.1.VB photoelectron spectra were acquired from a Cu-metal surface as the partial pressure of O_2 was systematically increased, ranging from UHV at 298 K to 0.3 mbar at 600 K. The uppermost spectra, depicted in black, was obtained at 600 K and 0.3 mbar O_2 pressure. However, before capturing the VB measurements, the top spectra (0.3 mbar) were oxidized at 600 K and 1 mbar O_2. Solid and dashed arrows indicate the shift in Cu 3d and O 2p bands, as the oxidation progresses from Cu_2O to CuO. Reference gas-phase O_2 spectrum is given in purple colourfor comparison. Full O_2 spectrum is given in inset.

increased; this possibly indicates the progression of CuO formation to deeper layers. It is well known that CuO (1.4-1.6 eV) and Cu_2O (2.2-2.6 eV) exhibits different band-gap energy, and the same reflects in the rigid shift in vibration features. The relationship between oxidation state and satellite in Cu has been extensively documented, and it is due to charge transfer from O 2p to Cu 3d in the final state of photoelectron emission spectrum. This charge transfer is possible with partially filled Cu 3d orbitals due to Cu $3d^9$ configuration, and hence a strong satellite is observed for Cu^{2+} oxidation state, and not for $3d^{10}$ configuration (with Cu^0 and Cu^{1+})

[26]. The results of 1 mbar high-pressure O_2 dosing, as well as the VB spectra collected at 0.3 mbar O_2 pressure and 600 K. Although the systematic oxidation of Cu metal to Cu_2O has been well-documented in the literature, the reversibility of cupric oxide to copper metal remains inadequately explored using UVPES. **[22]**

4.3.2 Reduction of CuO to Cu metal

Following the complete oxidation of a Cu foil, we conducted a comprehensive investigation into the reverse of (or reduction process) CuO was converted to Cu metal by progressively raising the temperature under 0.1 mbar H_2 pressure, as illustrated in Fig. 4.2. Cu-surface oxidised to CuO was used for this purpose. CuO spectrum taken at 0.1 mbar O_2. partial pressure and 700 K are also shown for reference. CuO spectrum observed at ambient to 400 K remains unchanged indicating that there is no significant change due to CuO-H_2 interaction; indeed, it is well-known in the literature that generally Cu^{2+} reduction occurs above 450 K. The VB spectra recorded at 450 K/0.1 mbar H_2 partial pressure exhibited an unusually different spectrum; it is neither CuO nor Cu_2O. While the broad VB is still observed between 2 and 7 eV at 450 K and similar to CuO, an emergence of additional intensity was observed between 4 and 6 eV. Nonetheless, when the temperature is raised to 550 K/0.1 mbar H_2, characteristic features of onset of CuO to Cu_2O reduction are observed; indeed they are evident from the small valley observed between Cu 3d and O 2p features; however, O 2p feature was observed around 5.5 eV indicating the surface contains a mixture of predominant CuO along with Cu_2O.TheCu 3d – O 2p valley further deepens on heating to 650 K/0.1 mbar H_2 along with O 2p feature shifting to 6 eVsupportingthe full conversion of CuO surface layers to Cu_2O, at least within the probing depth of NAPUPS of 2 nm. Simultaneously characteristic feature of Cu_2O appears at 1 eV, compared to the 450-550 K spectra. The broad Cu 3d-O 2p hybridization gradually diminished at 650 K, along with the satellite feature. It is to be noted that $2x10^{-7}$ mbar O_2 partial pressure at 600 K on metallic Cu oxidized the surface to Cu_2O (green trace in Fig. 4.1). At 600 K, Cu_2O is also converted to CuO by increasing the O_2 partial pressure from $2x10^{-7}$ to 10^{-3}-10^{-2}mbar (**Figure 4.1**), while the reduction required more severe conditions (650 K and 0.1 mbar H_2 partial pressure). Additional intensity observed at 450 K also suggests a possibility of CuO to Cu_2O reduction involves an intermediate step, such as interpenetrating CuO-Cu_2O interface or Cu_4O_3, which will be explored in the subsequent section. Above observation suggests that the oxidation and reduction processes follow a significantly different pathway between CuOand Cu_2O.

At temperatures above 650 K, the intensity of Cu_2O gradually decreased, and the evolution from Cu_2O to Cu metal became evident from the following observations. Observation of onset of metallic Cu 3d doublet bands, with clear first band appearing at 2 eV, decreased intensity of O 2p feature at 6 eV, and the disappearance of the satellite peakaround 1 eV.The onset of transition from Cu_2O to Cu metal initially becomes evident at around 700 K, with significant amount of Cu_2O features still observed. Within the temperature range of 650-700 K, a co-existence of Cu_2O and Cu metal is observed. However, when the temperature is raised to 750 K, metallic Cu 3d doublet is observed, and also without any significant Cu_2O features, such as no O 2p feature at 6 eV; however, no E_F feature was observed for the formation of metallic Cu. On prolonged heating at 750 K for 2h, no significant changes in the VB were observed; nonetheless a weak E_F feature was observed on prolonged heating. It should also be mentioned that the metallic Cu 3d doublet features observed is different from the spectrum recorded on freshly cleaned Cu-foil (**Figure 4.1**), and this aspect to be discussed in detail in the next section. The gas phase vibrational features of H_2, presented in **Figure 4.2 (b)**, exhibited an interesting trend with broadened or narrowed intensity pattern under different experimental conditions. Upon evacuation of H_2 and decreasing the temperature to 400 K, spectral quality improved and the same can be ascertained through higher Cu 3d intensity with Cu 3d pattern evolving towards metallic Cu andan improved E_F feature; increase in intensity is partly due to evacuation, which decreases the scattering.

Gas-phase H_2 and H_2 on CuO at 450 K appears at the same BE range; however, a significant broadening isnoticed on the latter. On bringing the temperature up to 550 K, H_2 vibrational features changed to a lower BE by about 0.8 eV and broadened further, indicating a drastic change in the nature of the surface. From the main VB, it has been deduced that there is a transition from CuO to Cu_2O begun in this temperature range, with a possible intermediate. It is well-known that the band gap of CuO and Cu_2O is different by about 0.8-1 eV, and the shift observed above supports the change in nature of surface from CuO to Cu_2O. Large broadening with diminished intensity ofthe observed vibration properties are related to the surface's very heterogeneous nature, due to the presence of CuO, Cu_2O along with Cu_4O_3 intermediate. The VB gas phase spectra of H_2 displayed lower BE due to alterations in the surface dipole with increasing temperature. Similar observations have been previously reported by our research group in studies on the oxidation and reduction of Co, Mo, V, and Ag **[25, 27, 28, 29]**. As the temperature increases, the vibrational features of H_2 gradually becomes sharper, and the bands

become more distinct. This is due to a decrease in surface area heterogeneity and subsequent increase in Cu metal content on the surface.

To investigate the evolutionary process of CuO to Cu_2O, a prolonged heating at 550 K and 0.1 mbar partial pressure of H_2 was carried out and NAP-UPS measurements were made periodically. The results obtained are shown in **Figure 4.3**. Initially, a freshly cleaned Cu foil was oxidized to CuO, as shown in Fig. 1. CuO layers generated on Cu-foil was subjected to a H_2 pressure of 0.1 mbar at 550 K for 240 minutes, and the spectra were systematically recorded. NAPUPS spectra were acquired for every 30 minutes while H_2 dosing at 550 K. Interestingly, a systematic change observed from CuO to Cu_2O, through Cu_4O_3 intermediate formation. Following points are worth highlighting: **(a)** As the H_2 exposure time increases, a decrease in CuO intensity was observed, indicating the slow kineticsof reduction. **(b)** The spectra represented by red and pink colors for 15 and 60 mins., exhibit the initial transition of CuO to Cu_4O_3, where the characteristic valley for Cu_2O between 2-4 eV was not discernible. Rather a feature less very broad band was observed with intensity peaking at the centre of the wide feature. This region could potentially serve as the rate-determining step for the transition from CuO to Cu_2O. **(c)** After 120 minutes of exposure time, a distinct characteristic valley within the broad spectrum, ranging from 2-7 eV, emerged, indicating the onset of transition from Cu $3d^9$ to Cu $3d^{10}$. **(d)** With further increase in heating time, the valley formed by Cu 3d and O 2p features deepens and Cu_2O features emerges strongly. Characteristic feature at 0.75 eV also observed, which is observed at 1.2 eV for CuO (Figs. 4.1and 4.3c). Additionally, a shift of 0.9eV in the gas-phase H_2 vibrational feature was observed (compared to reference H_2 spectrum), and the same is attributed to the change in band gap due to the transition from CuO to Cu_2O. However, just by prolonging the H_2 exposure for the next 3 hours did not induce further electronic evolution from Cu_2O to Cu metal at 550 K, suggesting that more severe conditions would be required for further reduction to Cu metal.

To investigate further, a time-dependent reduction experiment was conducted by increasing the temperature to 600 K. NAPUPS spectra were obtained on a regular basis and the result is shown in **Fig. 4.4a**; however, only minimal changes in the electronic state of $Cu_2O$was observed. Prolonged heating induced a minor change with a shoulder feature observed around 2 eV, corresponding to an onset of reduction. Nonetheless, complete transition fromCu_2O to Cu metaldid not occur even after prolonged heating at 600 K, indicating that a further higher temperature and/or H_2 pressure is required for the transition.

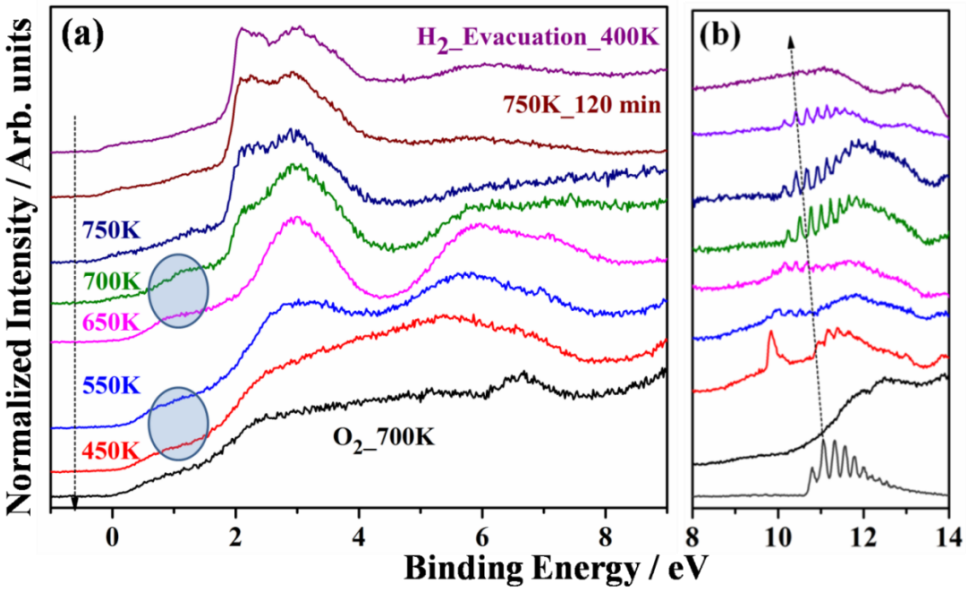

Figure 4.2 VBphotoelectron spectra were acquired using He I photons on a Cu surface, capturing the following observations **(a)** The spectra were recorded during the reduction process of CuO to Cu, performed under a H_2 pressure of 0.1 mbar. **(b)** An enlarged view of the spectra revealed molecular H_2 vibrational features.

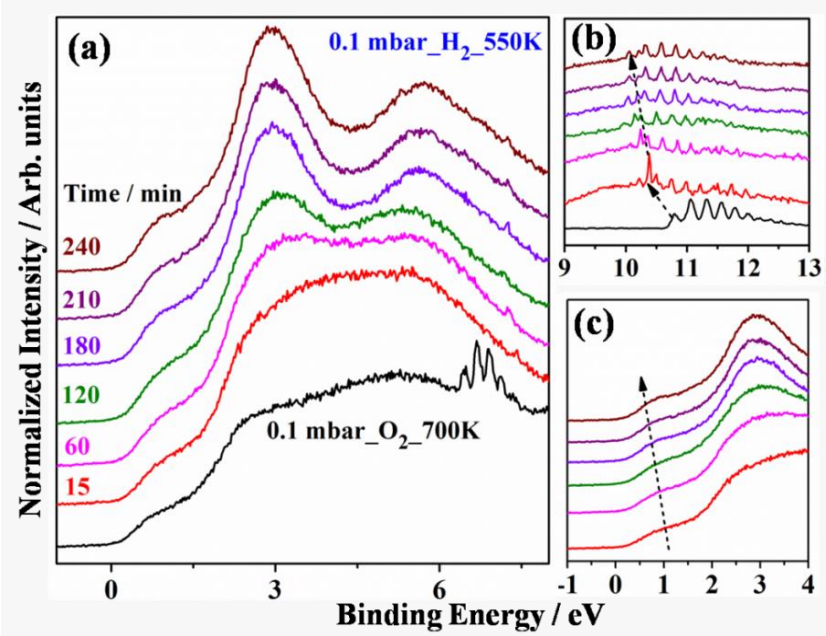

Figure 4.3.**(a)** VB photoelectron spectra were recorded over time during the reduction process of CuO to Cu_2O under a H_2 pressure of 1 mbar and a temperature of 550 K. **(b)**Molecular H_2 gas vibrational features were examined, focusing on their characteristics within the VB spectra. **(c)** The changes in the E_F level were investigated to understand the variations in electronic structure and energy distribution during the reduction of CuO to Cu_2O.

Similar to the results shown in Fig. 4.4a was completed, at 750 K and 0.1 mbar H_2 partial pressure. This is mainly to observe the kinetics of reduction of Cu_2O to Cu. a definite

signature of E_F for reduction to Cu-metal was observed on heating to 750 K at 0.1 mbar; ramping time from 600 to 750 K in 0.1 mbar H_2 partial pressure was sufficient to induce the above transition. This underscores the requirements of somewhat harsh conditions for the reduction of Cu_2O to metallic Cu. Gradual reduction of the Cu_2O surface to Cu metal state occurred at 750 K, as shown in the sharp Cu 3d doublet bandsobservedbetween 2-4 eV in **Figure 4.4(b)**. Temperatures between 600 and 700 K were discovered to represent the rate-determining step for the transition from Cu_2O to Cu metal at 0.1 mbar H_2 partial pressure.

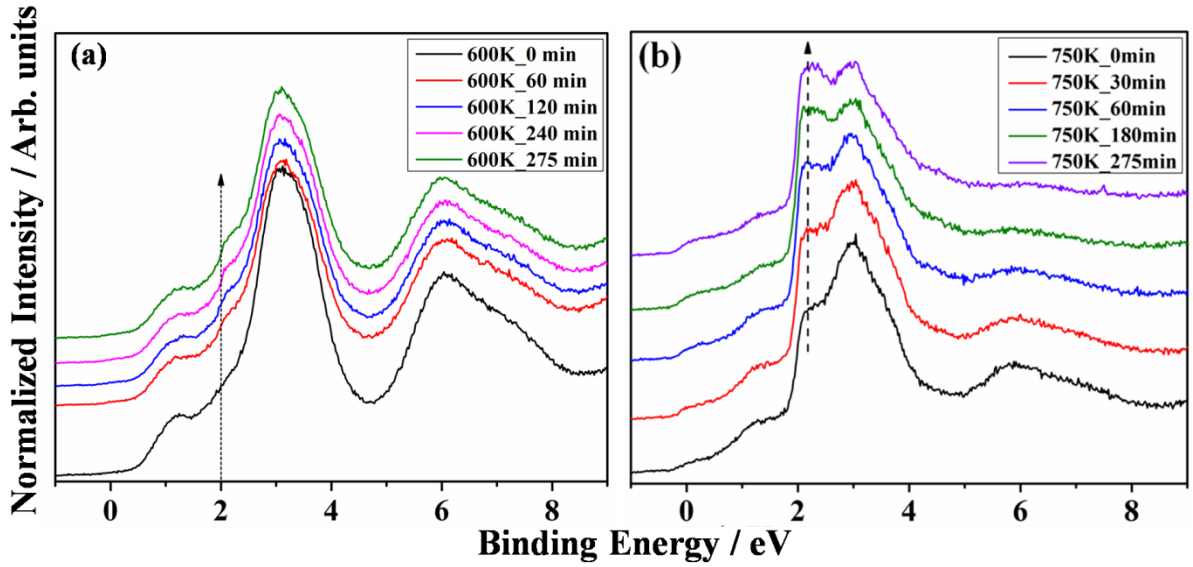

Figure 4.4 (a) VB photoelectron spectra were recorded as a function of time to investigate the time-dependent behavior during the reduction process under a constant H_2 pressure of 0.1 mbar and a temperature of 600 K. **(b)**Time dependent evolution of VB photoelectron spectra obtained at a constant temperature (750 K) and H_2 pressure (0.1 mbar) to examine the effects of temperature on the reduction process.

Similar transition patterns to Cu metal were observed in a clean Cu polycrystalline foil after multiple sputtering and annealing, as shown in the bottom spectra of **Figure4.4**, which is consistent with the reduced spectra in **Figure 4.4(b)** at the top. It is also to be mentioned that the prolonged heating made the Cu 3d doublet to be equal in intensity; it is not the same as that of virgin Cu-surface observed on Cu-foil (Fig. 4.1). A significant intensity of Cu_2O at 1.2 and 6 eV is observed indicating significant amountof oxide layers are present in the sub-surfaces; although these features decreased in intensity, but did not disappear completely. It is likely that the hydrogen diffusion into subsurface layers may be slow and/or hindered, which prevents a complete reduction under the experimental conditions studied.

4.3.3 Correlation between surface changes and ϕ

The ϕ is a critical parameter representing the energy needed to eject an electron from a solid material's E_F. Variations in the ϕ offer valuable insights into the electronic structure and surface characteristics of the copper foil during both oxidation and reduction processes. In the oxidation process at 600 K, the ϕ of the CuOx was expected to increase due to the formation of an oxide layer from metallic Cu surface layers. During reduction, as thetemperature increased from 450 to 750 K, the ϕ of the CuOx layers was anticipated to decrease towards Cu-metal, indicating a decrease in the energy required to remove electrons and suggesting the transition from the oxide to the metallic state. The ϕ is an inherent characteristic property of any material, and its changes can be modulated by altering the surface CuOx stoichiometry **[25]**. In **Figure 4.5**, the calculated ϕ values of CuOx at different oxidation andshown in **Figure 4.1**, where electronic changes of the clean Cu surface were monitored reduction phases are plotted, which are obtained from the offset values from NAP-UPS spectra. **Figure 4.5(a)** represents the ϕ values observed during a systematic oxidation studyat 600 K under O_2pressure-dependent conditions. The initial ϕ of the clean Cu foil was measured to be 5.1 eV, which increased to 5.9 eV after dosing O_2 at a pressure of $2x10^{-7}$ mbar. This observed increase in ϕ can be attributed to a significant alteration in the Columbic potential of the Cu surface upon exposure to oxygen atmosphere. As the pressure was further elevated, surface oxidation progressed from monolayer to multilayer stages, resulting in the gradual and vertical oxidation of the deep-down Cu surface layers. Notably, the change in ϕ clearly indicates a transition from metal to semiconductor behavior at higher pressures at 600 K, where ϕ decreases from 5.9 to 5.5 eV as oxygen diffuses into the system.

The change in ϕ during the reduction process is presented in **Figure 4.5(b)**, and the calculated values are plotted against the reduction conditions with increasing temperature in Fig 4.6b. These changes in ϕ suggest variations in the surface dipole upon exposure to O_2 and H_2. At UHV and 298 K, the ϕ of polycrystalline Cu metal foil was determined to be 5.1 eV, albeit varying between 4.7 and 5.1 eV for different forms of Cu metal foil. [**30, 31**] **Figure 4.6(a)** illustrates the calculated ϕ values plotted against the oxidation conditions with increasing oxygen partial pressure at 600 K. The Cu samples were exposed to varying O_2 pressures, and the resulting ϕ values were measuredand shown in **Figure 4.6a**. It was observed that as the O_2 partial pressure increased, the sudden increase in ϕof the CuOx layer observed. This correlation suggests that the surface potential and electronic structure of the CuOx layer are influenced by

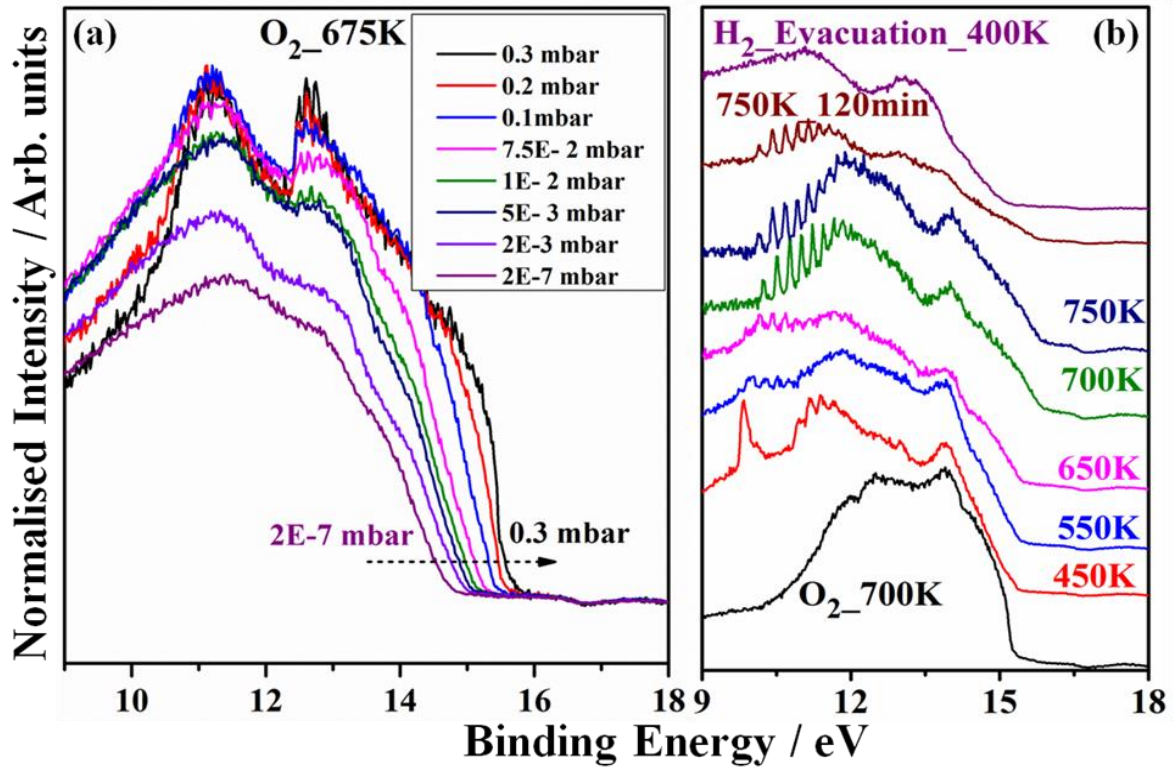

Figure 4.5.Changes in the ϕ wasinvestigated during systematic (a) Cu oxidation to CuOat 675 K and (b) reduction of CuOtoCufrom 450 to 750 K.

the presence of O_2. The changes in ϕ reflect the transformation of Cu to CuO, indicating the formation of a semiconductor-like surface. The observed changes in ϕ depend on various factors, including the level of cleanliness, size, formation of Cu metal clusters/islands, and the surrounding environment. Furthermore, an rise in the reduction temperature from 450 to 750 K resulted a fall in the ϕ, from 5.5 eV to 4.9 eV, at 0.1 mbar H_2 partial pressure. Secondly, the changes in ϕ during the reduction process of CuO to Cu metal were studied at constant partial pressure 0.1 mbar H_2 examined as a function of temperature and time (**Figure 4.6b**). After complete oxidation, the chamber was evacuated, and the surface was utilized for reduction experiments. The CuO samples were subjected to increasing temperatures, and the ϕ values were measured at different time intervals. It was found that as the temperature increased the ϕof the CuOx layer decreased gradually. This reduction in ϕ indicates the transition from a semiconductor-like surface to a metallic state as CuO transforms into Cu metal. The evolution of ϕ over time provides insights into the kinetics of the reduction process and the thermodynamic stability of the CuOx layer. These findings demonstrate the tunability of the ϕ of the CuOx layer during both oxidation and reduction processes, highlighting the role of external factors such as O_2 partial pressure, temperature, and time. The modification in ϕ reflect

the electrical structure and surface properties of the CuOx layer, providing valuable information for understanding the oxidation and reduction mechanisms of copper-based materials.

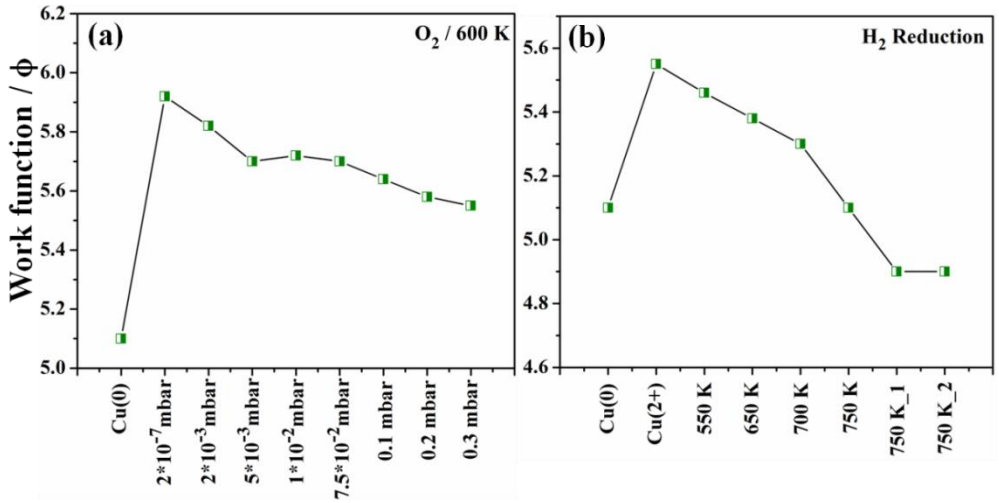

Figure 4.6 Changes in the ϕ of CuOx layer during **(a)** Oxidation of Cu to CuO as function of O_2 partial pressure **(b)** reduction of CuO to Cu metal as function of temperature and time at 0.1 mbar Hydrogen partial pressure.

Additionally, alterations in the surface properties are detected with changes in the ϕ, shifting from metallic Cu to semiconducting Cu_2O. The outcomes of this study indicate that the gas-phase attributes of the O_2or H_2 feature are strongly influenced by variations in the ϕ of the Cu surface, which aligns with previous observations made during the oxidation of other transition metal oxides **[25, 28, 29].**

4.4 Conclusion

In summary, exploration of the oxidation and reduction reactions involving molecular O_2 and H_2 was conducted on polycrystalline copper (Cu) metal foil using NAP-UPS. We have examined the Cu/Cu_2O, Cu_2O/CuO interfaces along with Cu_4O_3 intermediate by using NAPUPS method by controlled oxidation and reduction of Cu-polycrystalline foil at close to near atmospheric pressure (0.1 mbar) and temperature (750K). Upon raising the temperature, the foil undergoes systematic oxidation as the chamber O_2 partial pressure is increased from $2x10^{-7}$ mbar to 0.3 mbar. Under low-pressure conditions, Cu oxidation follows a sequential pathway, as observed under NAP-UPS ($CuO \rightarrow Cu_4O_3 \rightarrow Cu_2O \rightarrow Cu$). To promote the generation of intermediates in catalytic reactions, one can restrict the oxygen partial pressure or oxidation temperature. This contrasts with the behaviour observed during Cu oxidation, where Cu_2O acts as a stable intermediate observed.

To address the kinetic issue, we conducted a time-dependent study, revealing that the reduction of CuO is a kinetically slow process, and 550 K is the rate-determining zone for the transformation from CuO to Cu_2O. Furthermore, harsh conditions are required for the subsequent transformation from Cu_2O to metallic Cu, which can be achieved within the temperature range of 700-750 K. While NAP-UPS provides information about the initiation of H_2 diffusion around 300 K and the phase transition around 450 K from CuO to Cu_4O_3 or the formation of a CuO/Cu_2O interface, CuO is completely converted to Cu_2O with distinct features appearing around 2-4 eV corresponding to Cu_2O as the temperature increases to approximately 650 K. For complete reduction, high temperatures are required, and further reduction of Cu_2O to metallic Cu is only possible above 700 K on the surface of Cu polycrystals. The oxidation and reduction behaviors, as well as the thermal stability, of surface CuO and Cu_2O exhibit notable deviations compared to those reported for CuO thin films, single crystals, and powder samples. This discrepancy can be attributed to the reliance on lattice oxygen mobility, which demonstrates significant variability among distinct materials and also within individual samples. The diffusion of oxygen is discerned through the Cu 2d –O2p interaction in NAP-UPS, and alterations in the ϕ also serve as indications of the oxidation of the Cu surface. Furthermore, the reverse reduction process follows a similar pathway, accompanied by observed changes in the $\phi$from 5.5 to 4.9 eV, thus supporting the evidence of oxidation.

It is also to be stated that some of the industrially important reactions, like oxidative steam reforming of alcohols, involves oxygen as a reactant and the same reaction generates H_2 as a product, in a complex environmental condition. Indeed, it would be interesting to study such experimental conditions to explore the status of Cu or any metal-based catalysts. Although NAPPES operating pressure could be low, otherwise experimental conditions can be simulated. We believe our work may be extended to such complex reaction conditions.

4.5 References

1. Grioni, M.; van Acker, J. F.; Czyzyk, M. T.; Fuggle, J. C.*Phys. Rev. B***1992**,*45,* 3309.
2. Ghijsen, J.; Tjeng, L. H.; Eskes, H.; Sawatzky, G. A.; Johnson, R. L.*Phys. Rev. B***1990**,*42,* 2268.
3. Platzman, I.; Brener, R.; Haick, H.; Tannenbaum, R.*J. Phys. Chem. C***2008**,*112,* 1101-1108.
4. Rodriguez, J. A.; Kim, J. Y.; Hanson, J. C.; Perez, M.; Frenkel, A. I.*Catal. Lett.***2003**,*85,* Nos. 3–4.

5. Mathew, T.; Rao, B. S.; Gopinath, C. S.*J. Catal.***2004**,*222,* 107-116.
6. Velu, S.; Suzuki, K.; Vijayaraj, M.; Barman, S.; Gopinath, C. S.*Appl. Catal. B: – Environ.***2005**,*55,* 287-299.
7. Vijayaraj, M.; Gopinath, C. S.*J. Catal.***2006**,*241,* 83-95.
8. Gopinath, C. S.*Faraday Trans.***1996**,*92,*3605-3610.
9. Chen, A.; Long, H.; Li, X.; Li, Y.; Yang, G.; Lu, P.Volume 83, Issue 6, 12 February**2009**, Pages 927-930.
10. Papadimitropoulos, G.; Vourdas, N.; Vamvakas, V. E.; Davazoglou, D.Volume 515, Issue 4, 5 December**2006**, 2428-2432.
11. Henrich, V. E.; Cox, P. A.*Cambridge University Press: Cambridge, U.K.*, ***1994***.
12. Heinemann, M.; Eifert, B.; Heiliger, C.*Phys. Rev. B***2013**,*87,* 115111.
13. Zhu, J.; Su, Y.; Chai, J.; Muravev, V.; Kosinov, N.; Hensen, E. J. M.*ACS Catal.***2020**,*10,* 11532−11544.
14. Zhang, Z.; Chen, X.; Kang, J., et al.*Nat Commun* **2021**,12, 4331.
15. Mhamane, N. B.; Chetry, S.; Ranjan, R.; Raja, T.; Gopinath, C. S.*ACS Sus. Chem. Eng.***2022**,*10,* 3521−3531.
16. Velu, S.; Suzuki, K.; Gopinath, C. S.*J. Phys Chem. B***2002**,*106,* 12737-12746.
17. Velu, S.; Satoh, N.; Gopinath, C. S.; Suzuki, K.*CatalLett***2002**,*82,* 145-152.
18. Bera, P.; Aruna, S. T.; Patil, K. C.; Hegde, M. S.*J. Catal.***1999**,*186,* 36-44.
19. Dow, W.-P.; Wang, Y.-P.; Huang, T.-J.*Appl. Catal. A: Gen.***2000**,*190,* 25–34.
20. Wang, X.; Hanson, J. C.; Frenkel, A. I.; Kim, J. Y.; Rodriguez, J. A.*J. Phys. Chem. B***2004**,*108,* 13667-13673.
21. Rodriguez, J. A.; Kim, J. Y.; Hanson, J. C.; Perez, M.; Frenkel, A. I.*Catal. Lett.***2003**,*85,* 247–254.
22. Roy, K.; Gopinath, C. S.*Anal. Chem.***2014**,*86,* 3683−3687.
23. Kowalskaa, J.; Gopinath, C. S.*Acta Phys. Pol.* A. **2014**, *125*, 1065 – 1066.
24. Roy, K.; Vinod, C. P.; Gopinath, C. S.*J. Phys. Chem. C***2013**,*117,* 4717−4726.
25. Reddy, K. P.; Jain, R.; Ghosalya, M. K.; Gopinath, C. S.*J. Phys. Chem. C***2017**,*121,* 21472−21481.
26. Evans, S.*Edward Davies Chemical Laboratories, University College of Wales, Aberystwyth, Dyfed SY23 1 NE*Received 19th August, 1974.
27. Ghosalya, M. K.; Reddy, K. P.; Jain, R.; Roy, K.; Gopinath, C. S.*J. Chem. Sci.***2018**,*130, 30.*
28. Ranjan, R.; Mhamane, N. B.; Kolekar, S. K.; Gopinath, C. S.*J. Phys. Chem. C***2022**,*126,* 19136−19146.
29. Reddy, K. P.; Mhamane, N. B.; Ghosalya, M. K.; Gopinath, C. S.*J. Phys. Chem. C***2018**,*122,* 23034−23044.
30. Michaelson, H. B.*J. Appl. Phys.***1977**,*48,* 4729.
31. Fall, C.*Ab Initio Study of the Work Functions of Elemental Metal Crystals, Thesis,* **1999**.

Chapter 5a

Co_3O_4 for sustainable CO_2 reduction and possible fine-tuning towards selective COproduction

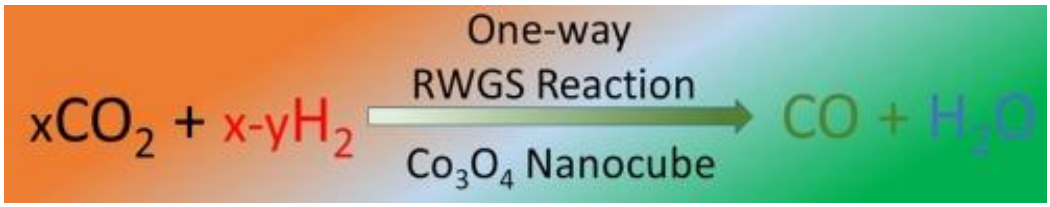

A part of the work presented in chapter 5a has been published, and the publication details:-

Ranjan, R.; Tekawadia, J.; Jain, R.; Mhamane, N. B.; Raja, T.; Gopinath, C. S.Co_3O_4 for sustainable CO_2 reduction and possible fine-tuning towards selective CO production.*Chem. Eng. J.***2023,***471*,144459.

5.1 Introduction

Carbon dioxide (CO_2) is a colorless and odorless greenhouse gas responsible for ocean acidification and climate change **[1]**. The burning of fossil fuels in various industries and automobiles has resulted in the massive emission of greenhouse gases, leading to an alarming increase in the concentration of CO_2 in the environment; and critically it continues to increase due to increasing consumption of various commodities and increasing population. **[2-5]**. To address this concern, various methods are being investigated to manage the CO_2 concentration in the atmosphere, such as carbon capture and storage (CCS) and carbon capture and utilization (CCU). Present work is a part of CCU and focusing only on CO_2utilization.CCU involves the conversion of CO_2 into valuable chemicalsand fuels by various methods. Among these, a promising and scalable route for the conversion of CO_2 to C1-oxygenates, such as CO, methanol, has been widely investigated in recycling technology. While the conversion of CO_2 to methane is also possible, it is not preferred due to the added cost and energy required for compression and transportation. Liquid products, like methanol, are preferred due to their high volumetric energy density. CO is also an important building block molecule, and along with hydrogen, it can be used to produce many liquid chemicals and fuels through Fischer-Tropsch (FT) synthesis **[6-8]**. Transition metal-based catalysts have been found to be a promising approach for the catalytic conversion of CO_2 to achieve high conversion and product selectivity and low cost compared to precious metal catalyst**[9][10]**.However, there are challenges associated with CO_2 conversion. The CO_2 molecule is symmetric and linear, with a high heat of formation (-395 kJ/mol), and the strong O=C bonds (O=C=O) make it very stable. The enthalpy required to break the O=C bond into CO and O is very high (+293 kJ/mol), making CO_2activation difficult **[11]**.

The reverse water gas shift (RWGS) reaction is a familiar process for converting CO_2 into CO and water through hydrogenation. However, achieving high CO_2 conversion with high selectivity towards CO is a major challenge due to possible methane formation. This issue can be addressed by decreasing the H_2 content and increasing the CO_2 content to suppress the formation of methane and water; indeed, adsorbed ratio of reactants is more important than the input feed ratio of reactants. In addition, employing lower than stoichiometric amount of hydrogen would be cost-effective, from an industrial viewpoint. The present work focuses precisely on addressing this challenge, resulting in a significantly large CO_2 conversion to CO with a 1:1 and 3:2 ratio of CO_2:H_2. Furthermore, using less than stoichiometric amounts of H_2

decreasesthe methane selectivity. Since shale gas reserves are widely available, low volumetric energy density and transportation issues associated with methane may be avoided. Therefore, the catalyst should also possess oxygen storage with redox capability; making Co_3O_4 an ideal catalyst for CO_2 reduction. The process of CO_2 reduction involves three main reactions: CO_2 methanation, RWGS, and methanol formation, as shown in equations (1), (2), and (3), respectively. However, the most desirable

$CO_2 + 4H_2 \rightarrow CH_4 + 2H_2O$ $\quad \Delta H^0_{298K} = -165\ kJ/mol$ (5.1)

$CO_2 + H_2 \rightleftharpoons CO + H_2O$ $\quad \Delta H^0_{298K} = 41.2 kJ/mol$ (5.2)

$CO_2 + 3H_2 \rightarrow CH_3OH + H_2O$ $\quad \Delta H^0_{298K} = -50\ kJ/mol$ (5.3)

pathway is the conversion of CO_2 to CO, which is a key feedstock molecule for the FT process. It is worth noting that even if the current global demand for CH_3OH could be met by CO_2, it would only reduce global CO_2 emissions by 0.1%. Additionally, methanation requires a large amount of H_2, while RWGS requires the least. Therefore, achieving high selectivity towards CO by using the minimum required H_2 would be prudent.

One of the main challenges of RWGS is to ensure the catalyst remains active over a prolonged period. Recent research on active catalysts for CO_2 reduction has focused on optimizing their properties by altering the composition, particle size, and oxidation state **[12-13]**. For instance, Co-based catalysts with an average particle size of 10 nm exhibited three times higher turnover frequency than those with a 3 nm particle size **[14-15]** However, in some recent studies, surface structure and properties have been overlooked, despite the fact that the top few atomic layers of the catalyst surface actively participate in the catalytic reaction**[16-17]**.Understanding the evolution of surface changes under different reaction conditions is crucial. For example, metallic Co on SiO_2 support is four times more active than oxidized cobalt catalyst for CO_2 reduction**[13][18-19]**. On the other hand, metallic Co on TiO_2 support has shown to be five times less active than oxidized Co on the same support due to metal-support interaction. The activity of metallic Co on different supports varies, and it may be worthwhile to explore these differences further. Transition metal-based catalysts, such as nickel, cobalt, and ruthenium, have been found to be economical and efficient for CO_2 reduction. While other catalysts, like Cu/ZnO, can partially reduce CO_2 to methanol**[16][20]**,the electronic and geometric structure, caused by a specific morphology of the catalyst, such as Cu/ZnOnanoplates or Cu-Ni/CeO_2 nanotubes, can fine-tune the selectivity of CO_2 reduction[21-22].

Spinel cobalt oxide ($Co^{2+}Co_2^{3+}O_4$), particularly, is a promising active material with tunable redox properties and high potential for catalytic activity in CO_2 reduction. Spinel Co_3O_4 is known to consist tetrahedrally (T_d) coordinated Co^{2+} sites and octahedrally (O_h) coordinated Co^{3+} sites, which exhibit interesting chemistry at the nanoscale. This effects in a high degree of heterogeneity on the catalytically relevant surface structure due to changes in different facets **[23-25]**, point defects**[26]**, and particle size**[14]**. Recent studies have also shown that the oxide support can significantly influence the product selectivity of CO_2 reduction. For instance, PtCo bimetal supported on TiO_2 (CeO_2 and ZrO_2) exhibits high (low) selectivity to CO (CH_4)**[27]**.Therefore, *in-situ* spectral studies of a heterogeneous catalyst under relevant conditions or closer to those conditions are important for fundamental understanding of surface chemistry and its correlation to catalytic performance. It is essential to identify the catalyst's active state under reaction conditions to enhance its activity and selectivity further.

An overall view of literature results [**13,14,23,24**,**28,29**], especially based on Co-based catalysts, suggest the following: Generally, CO_2 reduction has been carried out with H_2-rich CO_2:H_2 (1:x, x≥3) feed. In general, metallic Co as an active phase lead to methanation of CO_2 with H_2-rich CO_2:H_2 (1:x, x≥3) feed; this is due to facile activation of H_2 and CO_2. However, cobalt oxides lead to variety of products and it depends on the nature of the support, reaction conditions, due to strong (weak) CO_2 (H_2) activation on Co-oxides; for example, methanol and C_{2+} alcohols are reported on Co-oxides. Other Co-containing catalysts, such as carbides, lead to light olefins. Generally, H_2-rich CO_2 feed on metallic Co or mixed valent cobalt oxide has been employed and no studies are available on stoichiometric or lower than stoichiometric CO_2:H_2 feed ratios. By employing H_2-lean CO_2-feed, maintaining the mixed valent character of cobalt oxide is possible, which can show sustainable CO_2 activation. In addition, high selectivity of a product might be possible by maintaining a singletype of crystallographic facet, which is not reported so far; often mixed products formation observed with cobalt oxides makes the products separation inevitable. Indeed, NC morphology is very apt for this, as it exposes only (100) facets on all six sides of NC particles. By employing NC morphology of Co_3O_4 with H_2-lean feeds, highlyselective CO production is observed in the present work; this also emphasize the need to explore more with H_2-lean feeds. In the current study, we studied the possibility of Co_3O_4 NC catalyst for CO_2 reduction under realistic conditions using a fixed bed reactor. Current analysis includes studying the influence of factors such as CO_2:H_2 ratio, temperature, and time on stream (ToS) on the reaction. Reaction results indicate that the highest

CO selectivity is achieved at temperatures between 673 and 823 K, particularly when the feed mixture has a H_2:CO_2≤1. Additionally, we investigated the alterations in the catalyst's nature when a 1:3 CO_2:H_2 feed ratio was employed by utilizing NAPPES at 0.1 mbar pressures up to 675 K. We also assessed the reactivity of the catalyst after reducing Co_3O_4 to CoO and Co metal through *in-situ* reduction in the presence of hydrogen. NAPPES results reveal a significant alteration in the oxidation state of Co and the surface ϕ of Co_3O_4 NC under realistic conditions, which correlates well with catalysis results. Present findings demonstrate the active state of the catalyst under working conditions as well as bridging the pressure gap between surface science and real-world catalysis.

5.2 Results and Discussion

5.2.1Texture Characterization of Co_3O_4 NC

Figure 5.1 depicts the XRD characterization of both the fresh and spent catalysts; the spent catalyst was recovered after a 12-hour reaction at 723 K with a 3:2 CO_2:H_2 ratio. The XRD pattern of the fresh catalyst, as shown in Figure 5.1a, exhibits characteristic features at 2θ = 19.3, 31.5, 37, 38.8, 45, 55.8, 59.5, and 65.4°, corresponding to the (111), (220), (311), (222), (400), (422), (511), and (400) facets of cubic Co_3O_4, respectively. These findning are consistent with the literature values (JCPDS 65-3103), showing that the catalyst has a cubic spinel structure. However, after the reaction at 723 K, new facets have emerged, along with an intense (400) feature, as shown in Figure 5.1b. The intensity of the (400) facet is the highest and appears as the parent peak, and peaks at 2θ = 47.91° and 52.08° correspond to CoO phase, while the peak at 2θ =47.91°and 52.08° correspond to CoO phase, and peak at 2θ =76.3 correspond to (533) phase of Co_3O_4crystalfacets were observed in Figure. 5.1b.

Indeed, this observation suggests a restructuring of the surface and high intensity (400) facet suggests a surface with step like structure on thesurface. NC exposes (100) facet on all six sides of the cube and observation of (400) is not unusual; however, disappearance of all other peaks and appearance of CoO features needed more investigation. The particle size and morphology of the fresh and spent Co_3O_4 NC catalysts were examined by TEM, and the resultsare presented in Figure 5.2a-c and 5.2d-e, respectively. TEM results indicate that the fresh Co_3O_4 material has a cubic morphology, and the high magnification image of a single cube (Figure 5.2a) reveals a size of 30-35 nm, indicating that the NC catalysts are faceted (100) orientation. The particle size was found to be in the range of 20-50 nm, with a predominant size of 30 ± 5

nm.The preferentially exposed plane in Co_3O_4 NC, according to XRD study, is (311). Based on energy considerations, the Co_3O_4 morphology should preferentially reveal the (100) facet, and the lattice fringe confirms the presence of the (100) facet. Indeed, this is a novel aspect of the catalyst, which exposes predominantly (100) facet with single set of activity sites; this aspect helps to achieve high selectivity of CO. The TEM image in Figure 5.2d and e shows the mostly cubic morphology of the spent catalyst after reaction with 3:2 ratio of CO_2:H_2 at 723 K, with an average particle size ~ 30 nm, similar to the fresh Co_3O_4, but with a marginal agglomeration. The TEM image shows the NC with inter-planar distances of 0.23 nm, corresponding to (222) facet, as shown in Figure5.2.

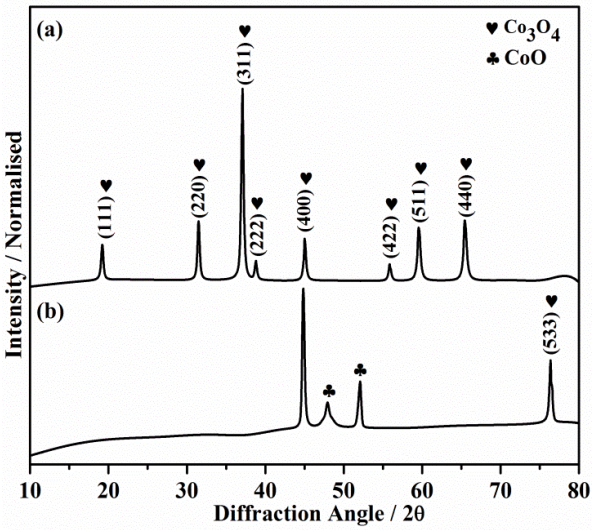

Figure. 5.1 The X-ray diffraction (XRD) patterns of the Co_3O_4 catalyst are presented, with (a) representing the fresh catalyst and (b) representing the spent catalyst. The spent catalyst was obtained after conducting the CO_2 reduction reaction with a feed ratio of 3:2 of CO_2:H_2 at 723 K for 12 hours.

5.2.2 H_2-TPR analysis

The reducibility of spinel Co_3O_4 NC was evaluated by conducting H_2-TPR analysis, and the result is shown in Figure 5.3. Two distinct reduction features were observed in the temperature range of 450-750 K. A sharp peak at 545 K and a broad reduction feature between 600 and 700 K were observed, with an area ratio of 1:3. No further reduction or hydrogen uptake was observed beyond 723 K, indicating complete reduction of Co_3O_4 to metal. The TPR results suggest a two-step reduction mechanism, where Co_3O_4 is initially reduced to CoO (peak at 545 K), followed by final reduction to metallic Co (between 600 and 700 K) **[30-31]**. It is worth investigating thepossibility of two or more micro reduction steps in a narrow temperature range using careful spectral and structural methods, as indicated by the broad reduction features. First

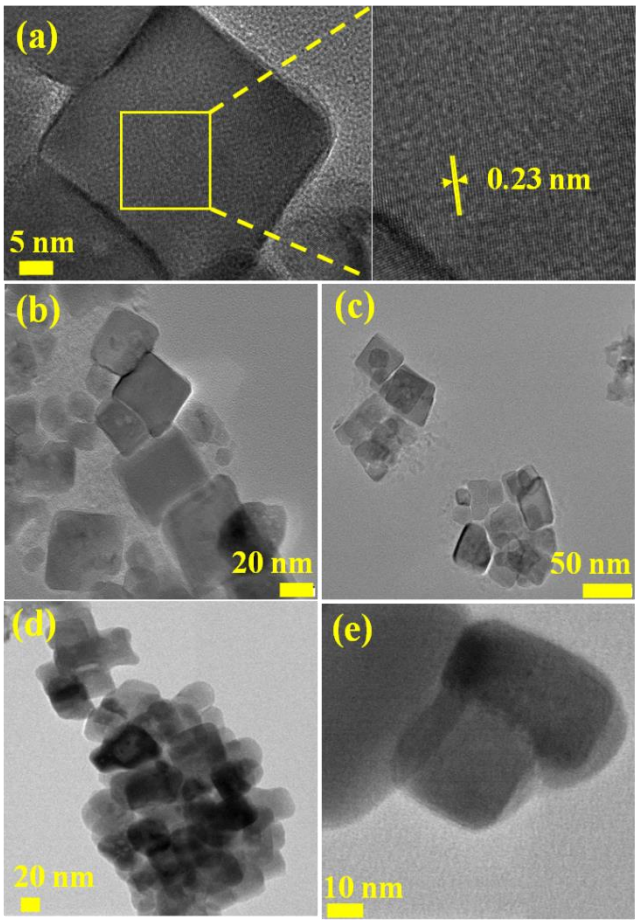

Figure 5.2.TEM analysis performed on both the fresh and spent Co_3O_4 NC. **(a)**HR-TEM image of the fresh Co_3O_4 is shown, which displays a cubic morphology with an average particle size of 35 nm. Panels **(b)** and **(c)** show TEM images of the fresh catalyst, revealing particle sizes ranging from 20 to 50 nm, with a predominant size of 30±5 nm. **(**d and e**)** TEM image of the spent catalyst obtained after the CO_2 reduction reaction, performed at 723 K with a 3:2 ratio of CO_2:H_2 feed for 12 h at GHSV 19200 h^{-1}, is presented. The lattice fringes observed in this image correspond to the interplanar distance of (222) facet (d_{222} = 0.23 nm).

reduction to CoO at ambient pressure, NAPPES measurements are made at 0.1 mbar, and hence the pressure dependency to be taken into account while interpreting the results. hints the possibility of at least partial reduction of Co_3O_4 to CoO under the present reaction conditions, since H_2 would be available at ambient pressure. It is to be reiterated that while TPR measurements are made 5.4c). This finding indicates that metallic Co cannot activate CO_2 below 675 K and is therefore unlikely to be an active phase in the present findings. It should also be noted that metallic cobalt is expected to undergo oxidation due to interaction with CO_2 and hence a change in surface nature. As such, the results observed in the mass spectra (Figure. 5.4) can be considered qualitative. The mass spectra show that CO and H_2O formation occurred

at temperatures ≥475 K (Figure5.4b). This observation indicates that the CoO activates CO_2 at a relatively lower temperature than the spinel Co_3O_4 (Figure 5.4a).

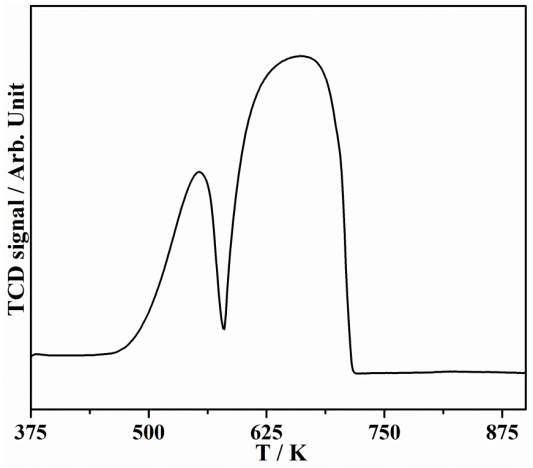

Figure 5.3 H_2-TPR profile for Co_3O_4 NC catalyst.

5.2.3 In-situ catalytic activity measurement in NAPPES

A quadrupole mass spectrometer (QMS) in the experiment was used to investigate the partial pressures of reactants and products in the NAPPES unit were utilized to record mass spectra. The CO_2 reduction reaction was conducted using CO_2:H_2= 1:3 between 325 and 675 K at 0.1 mbar pressure. The reactions were performed using fresh Co_3O_4 NC, *in-situ* reduced CoO (prepared from Co_3O_4 by *in-situ* H_2 reduction treatment at 523 K for 3 h), and Co metal (prepared from Co_3O_4 by *in-situ* H_2 reduction treatment at 673 K for 5 h) QMS was used to observe product evolution, and the results are depicted in Figure 5.4. The opening of a leak valve to maintain a pressure of 0.1 mbar caused a minor oscillation in all mass species, with the overall pressure being maintained within 10% of 0.1 mbar. Between 375 and 675K under dynamic dosing conditions at a total pressure of 0.1mbar. For simplicity and convenience, the two surfaces will be referred to as CoO and Co, respectively. The While the reaction was taking place in the main chamber, the QMS was retained in the preparation chamber. The output of the first turbo molecular pump in the electrostatic lensregime was directed to the QMS through a leak valve, which may result in diffusion of different components. Given these experimental challenges, any changes observed in QMS results should be considered qualitative. Despite the difficulty of observing CO (which is also a fragment of CO_2 in QMS) in the presence of CO_2, a significant change in spectral data was observed due to CO_2 dissociation on the catalyst surface. Figure 5.4 depicts the evolution of important masses as a function of reaction temperature as a result of CO_2 reduction. Fig. 5.4a shows a distinctly different evolution

pattern, compared to reactants, and confirms the formation of CO and H_2O from 575 K and above due to CO_2 activation on the Co_3O_4 NC catalyst. The same evolution pattern was observed for CO_2 and amu 16, indicating that the latter is due to atomic oxygen fragment from CO_2 dissociation, rather than methane formation on any catalyst; amu15 results recorded (not shown) did not show any change and supports the above point. The same reaction was performed on *in-situ* prepared CoO and Co metal from spinel Co_3O_4through H_2reduction, as shown in Figure 5.4b and 5.4c, respectively. The result in Figure 5.4b indicates that CoO activates CO_2 from around 525 K, while Co activates CO_2 at 675 K (Figure5c).

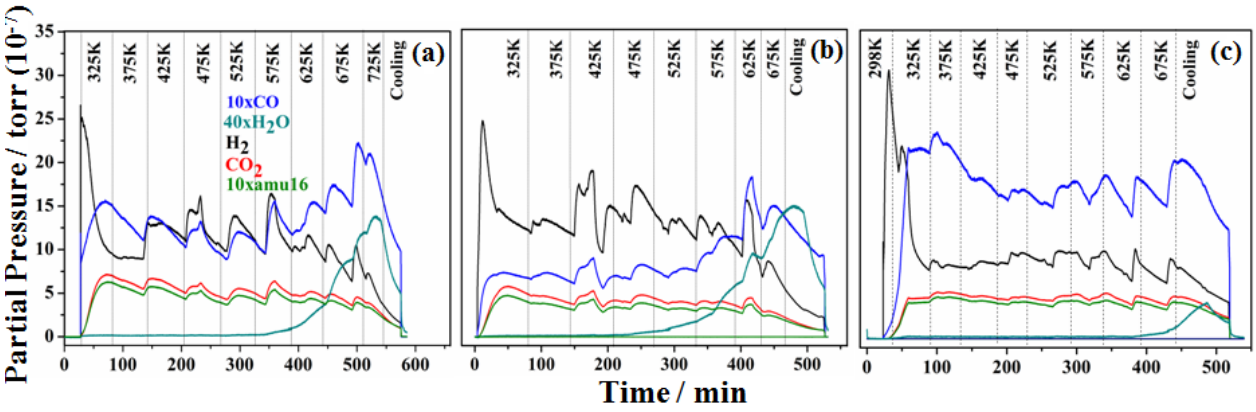

Figure 5.4. The mass spectral analysis of the CO_2 reduction reaction was conducted at 0.1 mbar with a 1:3 CO_2:H_2 ratio over the temperature range of 325 to 725 K using **(a)** Co_3O_4 NC catalyst, **(b)** Co_3O_4 reduced to CoO, and **(c)** Co_3O_4 reduced to Co. The partial pressure of CO, H_2O, H_2, CO_2, and amu 16 (O) were represented by blue, cyan, black, red, and olive colors, respectively. To enhance clarity, the partial pressures of CO, amu 16, and H_2O were multiplied by factors of 10, 10, and 40, respectively. The total pressure of the system was maintained at 0.1 mbar.

5.2.4 In situ NAP-XPS study under Reaction condition

To investigate the surface electronic structure of Co_3O_4 NC under catalytic reaction conditions, NAPPES experiments were conducted at a pressure of 0.1 mbar with a CO_2:H_2 ratio of 1:3 and at temperatures ranging from 325 to 675 K. Despite the use of low pressure, the results obtained from the NAPPES measurements provided relevant information about surface changes and their correlation to the active state under reaction conditions. Although kinetic changes occur more rapidly at higher pressures, such as 1 bar, the surface chemistry/changes remained the same and were observed in the present measurements. Under the same reaction circumstances, NAP-XPS and NAP-UPS measurements were carried out systematically, and the results are depicted in Figures 5.5-5.6, 5.8-5.9, and 5.11 respectively. Co $2p_{3/2}$ spectra obtained from

Co_3O_4 NC, CoO, and fully reduced Co metal surfaces are demonstrated in Figures 5.5a, 5.5b, and 5.5c, respectively **[32]**. The (100) facet of Co_3O_4 is known to exhibit Co^{2+} ions on the surface, whereas Co^{3+} is found in the underlying layers, suggesting that the activity could be predominantly determined by the former ions. However, CoO also exhibits a Co^{2+}-terminated surface that is similar to that of Co_3O_4 and has no Co^{3+} in the layers beneath. In all spectra, Co $2p_{3/2}$ core-level spectra exhibited features at 778.1 eV (red trace) and 780.1 eV (blue trace) corresponding to Co^{3+} (O_h coordination) and Co^{2+} (Td coordination) oxidation states, respectively **[33][34]**. The UHV spectra recorded at 298 K are shown at the bottom of all panels of Figure 5.5, revealing the expected Co^{3+}, Co^{2+}, and weak satellite features, along with a feature at 782.1 eV (olive), which is attributed to Co at defect sites. Marginal changes were observed in the $Co2p_{3/2}$ spectrum up to 475 K at 0.1 mbar pressure, which was comparable to the UHV spectrum. This suggests that the surface remained relatively unaffected and appeared to be comparable to that of the surface at 298 K conditions. However, an increase in Co^{2+} and Co near defect sites content was observed at 575 and 675 K, underscoring reaction-induced changes.

The surface electronic structure of CoO was investigated using the same experimental techniques as for Co_3O_4 NC, and the results are presented in Figure 5.5b. The spectrum obtained after reduction of Co_3O_4 to CoO is shown as the second spectrum from the bottom in Figure 5b and denoted as "after reduction". An increase in the intensity of Co^{2+} at 780.1 eV and a high intensity satellite peak at 786.4 eV confirms the reduction of Co_3O_4 to CoO**[35]**. The NAP-XPS measurements were carried out on the CoO surface at 0.1 mbar pressure and temperatures ranging from of 375 to 675 K. Intrestingly, a considerable increase in intensity Co^{3+} was seen at the expense of the Co^{2+} intensity at temperatures ≥475 K. The formation of CO and H_2O starts at 475 K, which is 100 K lower than for the spinel Co_3O_4 sample, as observed in Fig. 5.4b. The ratio of the +2/+3 oxidation states changes from 2:1 at 475 K to 6:5 at 675 K. The relative percentage area of various cobalt species, obtained after decoupling the NAP-XPS data, is plotted in Figure 5.7. It is noteworthy that the satellite intensity islargely maintained up to 675 K, indicating the equally important role of both Co^{3+} and Co^{2+}; However, a shift in the satellite feature by 0.6 eV to lower BE is observed at temperatures ≥475 K, indicating some electronic changes. It is to be emphasized the necessity of both 2+ and 3+ oxidation states of Co for the CO_2 activation on the catalyst surface, rather than any one of them. Although some CoO is observed in XRD result (Figure 5.1b), Figure 5.5b emphasizes

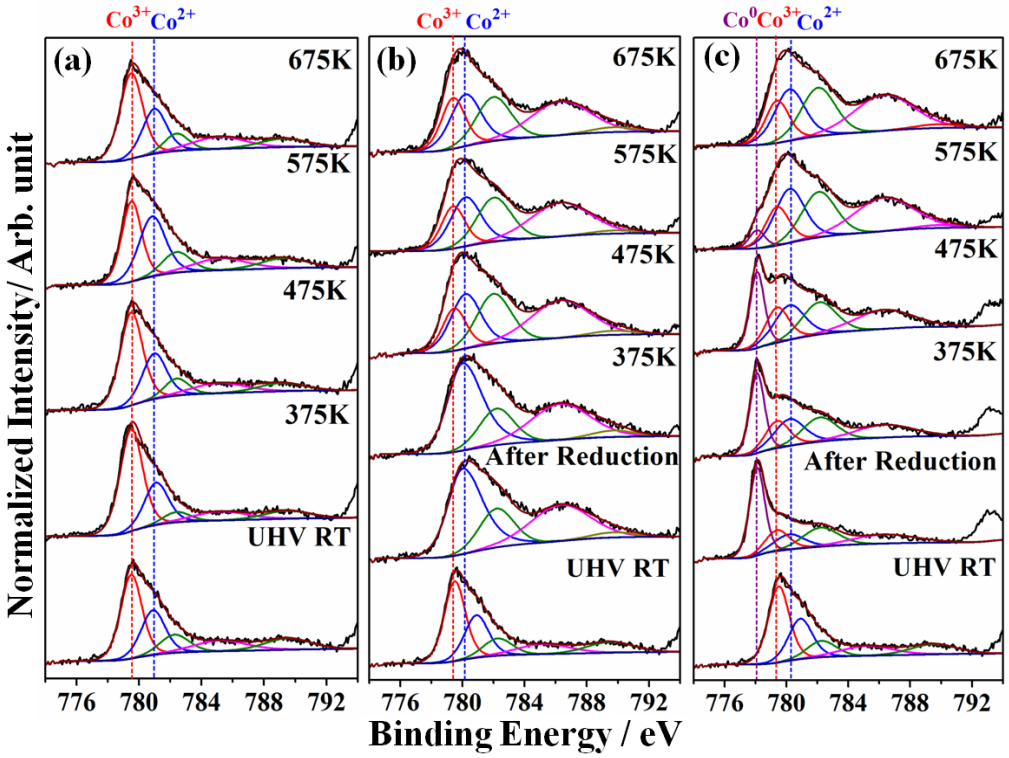

Figure 5.5 Deconvoluted Co $2p_{3/2}$ spectra recorded under reaction conditions of 0.1mbar pressure (CO_2:H_2 = 1:3) and temperature range between 375and 675K (a) on Co_3O_4NC,(b) on In-situ prepared CoO from Co_3O_4,(c) on in-situ prepared Co metal from Co_3O_4.

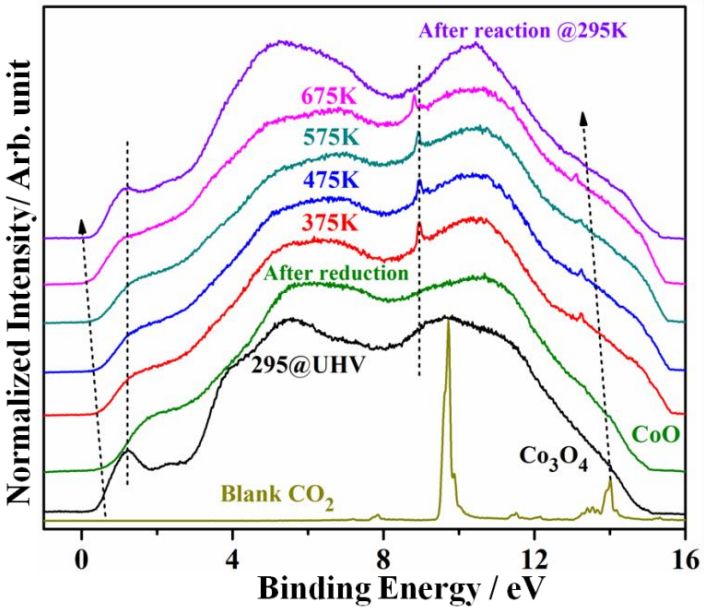

Figure. 5.6 Ultraviolet photoelectron spectral measurements recorded to observe the changes in VB of partially reducedcatalyst (Co_3O_4 to CoO phase).Thereafter NAPUPS was recorded under reaction conditions with CO_2/H_2= 1:3ratio at 0.1 mbar between 375and 675K.

the mixed oxidation states on the surface under the reaction conditions. This observation is further supported by the NAP-UPS results (Figure 5.6). Figure. 5.6 shows only Co^{2+} features

measured under the experimental conditions with increasing temperature, where the VB of Co 3d slowly evolve in the mixed oxidation states of Co^{2+} and Co^{3+}. The UPS outcome shown in Figure 5.6 is in agreement with the XPS result (Figure 5.5b).

Figure 5.5c shows the Co $2p_{3/2}$ spectrum obtained after the reduction of Co_3O_4 to metallic Co, and data acquired under reaction conditions. The conversion of spinel Co_3O_4 NCs to metallic cobalt was also confirmed by the NAP-UPS spectrum shown latter (in **Figure 5.11b** (wine red)) with a high $E_F$intensity. The small amount of Co^{2+} and Co^{3+} features observed are attributed to their presence beneath metallic layers. When measurements were made in thepresence of CO_2:H_2 (1:3) at 375 K and above, there was a gradual increase in Co^{2+} and Co^{3+} content at the cost of metallic. Co, and metallic Co almost disappeared at 675 K. The oxidation of Co indicates that the oxygen atoms available from CO_2 dissociation are used for surface oxidation, with the extent of surface oxidation gradually increasing with temperature and metallic Co disappearing at 675 K. However, metallic Co is preferentially oxidized to Co^{3+} up to 475 K with low intensity satellite, and then Co^{2+} increases, which is supported by the increase in satellite intensity. It is likely that H_2 from the reactant mixture is playing a role in the reduction of Co^{3+} to Co^{2+} at higher temperatures. It is also worth noting that effective CO_2 reduction starts ≥ 625 K, and the chances of metallic Co-formation under reaction conditions and its effect on CO_2 activation are remote. O1s spectrawere recorded under the same conditionsas illustrated in Figure 5.5, with the results displayed in Figure 5.8. The features appearing at 529.9 eV (red), 530.5 eV (blue), and 532 eV (olive) belong to lattice oxygen, oxygen near defect sites, and OH, respectively (**Figure 5.8a-c**). Co_3O_4 NCs (**Figure 5.8a**) and CoO (**Figure 5.8b**) show very similar features, indicating that the changes are similar. The O1s spectrum recorded for metallic cobalt (second spectrum from bottom in **Figure 5.8c**) shows some interesting changes. Firstly, the low signal-to-noise ratio of the O1s peak observed after reduction indicates that the complete reduction to Co-metal occurs only on the surface, even lower than the XPS probing depth of 10 nm. This is supported by the high intensity E_F feature observed in NAPUPS (**Figure 5.11b**), indicating that the underlying layers are not fully reduced, and the 0.1 mbar pressure may not be sufficient to achieve complete reduction. Secondly, after reduction, the hydroxyl peak rises sharply, indicating an increase in defect sites, with an increase in defect sites, which could be due to the interaction with hydrogen. As the reaction proceeds to higher temperatures, the intensity of the hydroxyl features decreases, and the O1s spectrum resembles to that of recorded at 675 K on Co_3O_4 NC or CoO. This is in

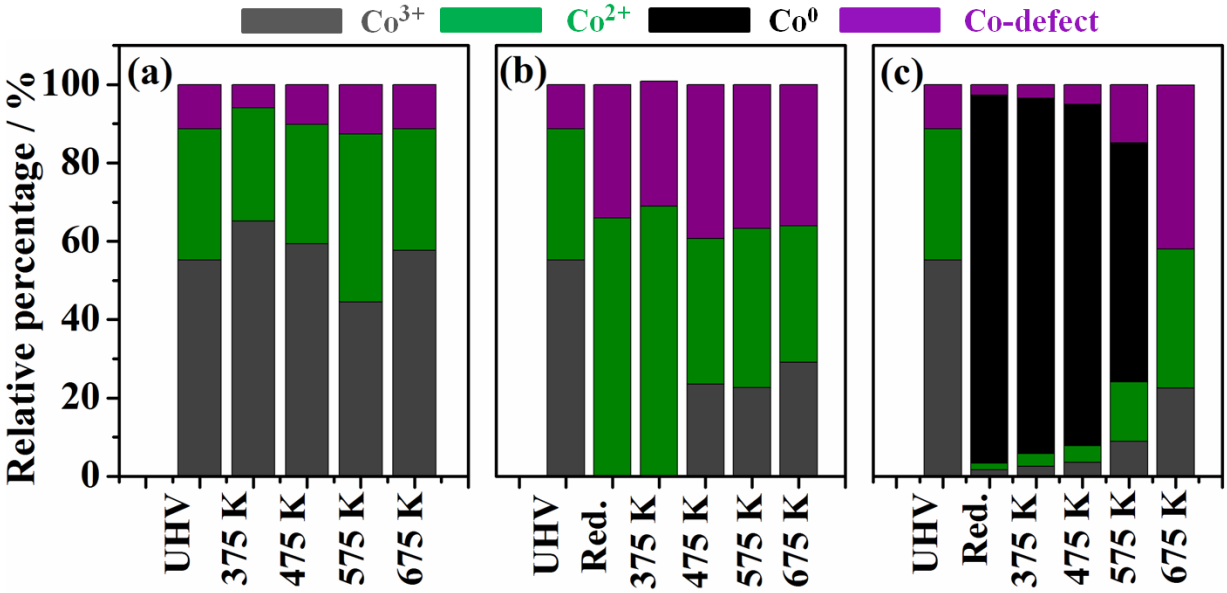

Figure. 5.7 Relative percentage change of cobalt species during *in-situ* CO_2 reduction reaction with ratio 1:3 of CO_2:H_2 during by using NAP-XPS **(a)** on spinel Co_3O_4 NCs **(b)** on reduced Co_3O_4 to CoO, and **(c)** on reduced Co_3O_4 to Co metal.

agreement with changes observed with C 1s spectra recorded under same conditions (**Figure 5.9**).

C1s spectra were collected on Co_3O_4 (CO_2:H_2 = 1:3 at 0.1 mbar pressure and temperatures ranging from 375 to 675K), in situ reduced to CoO and in situ reduced to Co-metal,were deconvoluted in order to comprehend the nature of the surface and reaction intermediate species involved in the CO_2 reduction reaction. A systematic deconvolution of C1s (Figure. 5.9a-c) core level was carried out. C1s spectra were deconvoluted into four main features appearing at 284.8 (red trace), 286.2 (dark cyan trace), 287.4 (magenta trace) and289.2 (dark yellow trace) correspond to adventitious carbon, adsorbed CO or C-OH species, $HCOO^-$, and HCO_3^- respectively. The bicarbonate, formateand CO peak intensityincreasesat high temperatures. Indeed, this is sustained throughout the temperature range studied, withsignificant increase in the intensity at 673 K. It is speculated that HCO_3^- is likely to be the reaction intermediate, which also helps towards CO and water formation at high temperatures. There could be a possibility of formation of methanol or higher hydrocarbonproduct, if high pressure/temperature condition can be provided. Under the reaction conditions, this

observation confirms the creation of a stable intermediate. The similar thing happens when CoO (Figure 5.9b) and metallic Co (Figure 5.9c).

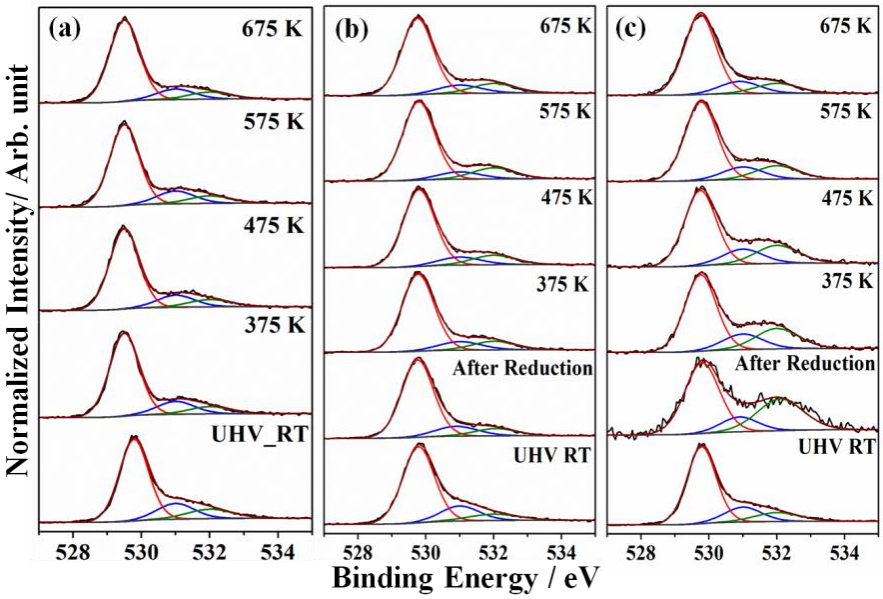

Figure 5.8. Shows the O1s spectra recorded under reaction conditions, with a total pressure of 0.1 mbar and temperatures ranging from 375 K to 675 K, on **(a)** Co_3O_4 NC catalyst, **(b)** *in-situ* prepared CoO catalyst, and **(c)** in situ prepared metallic Co catalyst by H_2 reduction. It is worth noting that the low signal-to-noise ratio observed in panel c, after reduction to Co-metal, is attributed to partially reduced or unreduced oxide layers beneath the metal.

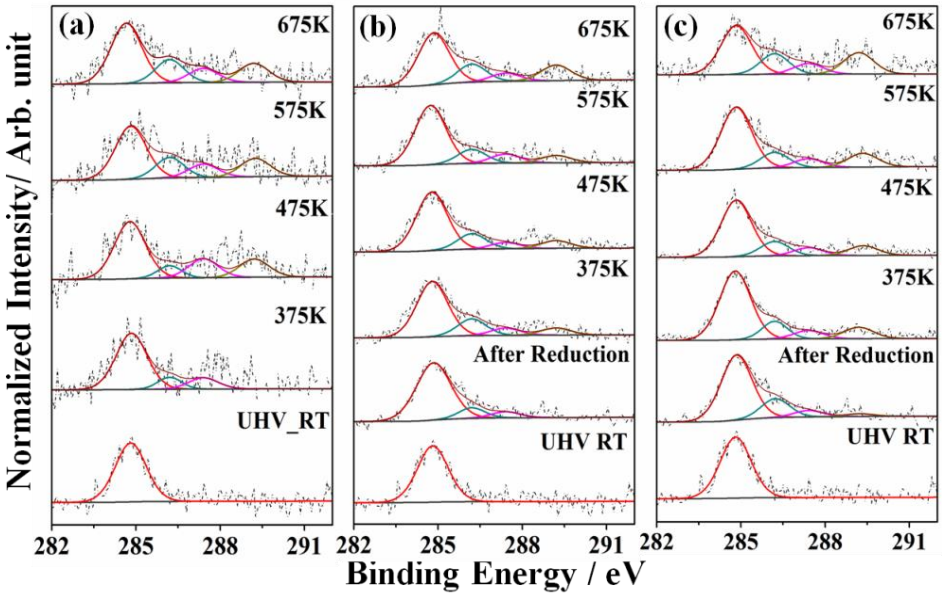

Figure 5.9 C1s NAP-XPSspectra recorded during CO_2 reduction on Co_3O_4 NC catalyst under reaction condition at 0.1 mbar pressure (CO_2:H_2 = 1:3) and between 375and 675K on **(a)**Co_3O_4 NC catalyst, **(b)** In situ prepared CoO catalyst by reducing Co_3O_4, and **(c)**In-situ prepared metallic Co catalystby H_2 reduction.

5.2.5 In situ NAP-UPS Study under reaction condition

The nature of the catalyst, particularly the VB, under reaction conditions with CO_2:H_2 = 1:3 between 375 and 675 K at a total pressure of 0.1 mbar was explored using NAP-UPS analysis. Figure 5.10a and 5.10b shows the NAP-UPS spectral data recorded on Co_3O_4 NCs and Co_3O_4 reduced to metallic Co, respectively. The UPS result obtained at UHV@295 K demonstrates an onset of VB at 0.37 eV, and a typical O_h Co^{3+} feature was observed at 1.22 eV[**36**], which is consistent with similar spectral results reported in the literature for Co_3O_4. From the NAP-UPS measurements carried out on Co_3O_4 up to 675 K (Figure 5.10a), four critical observations are worth highlighting. First, very similar VB results under reaction conditions were observed compared to those under UHV-RT conditions. Second, a gradual and rigid shift of the entire spectrum to lower BE) was observed up to 0.35eV from UHV-RT to 675 K. For example, Oh Co^{3+} shifted from 1.22 eV under UHV-RT to 0.88 eV at 675 K at 0.1 mbar. Third, an increase in the FWHM of the CO_2 vibrational feature was observed with increasing reaction temperature from 160 meV at 375 K to 300 meV at 675 K (Figure 5.11). Notably, the drastic change in BE and FWHM is directly evident when the temperature increases from 475 to 575 K, which also coincides with the onset of CO_2 reduction activity. Fourth, these observations indicate that the Co_3O_4 surface remains in the same state but with a gradually decreasing ϕ under the reaction conditions at high temperatures. Furthermore, the increasing FWHM observed at high temperatures for the CO_2 vibrational feature is attributed to an increasing heterogeneity of the surface. It is worth reiterating that NAP-UPS probes a maximum of the top 2 nm layers, while NAP-XPS probes up to 10 nm. Hence it is surprising to observe no major change in the VB pattern, except for the aforementioned points.

Figure 5.10b displays similar measurements conducted on Co metal surfaces. The ultraviolet photoelectron spectroscopy (UPS) VB spectrum recorded at room temperature under ultra-high vacuum (UHV-RT) conditions for freshly reduced Co metal is presented as the second spectral trace in Figure 5.10b; a sharp E_F feature observed is characteristic of metallic nature **[36]**. Under the conditions of NAP-UPS measurements, the surface nature of the Co-catalyst gradually transformed from metallic to the oxide phase, and fully supported by the disappearance of E_F intensity and the transformation of the broad VB feature of metallic Co to the evolution of typical O 2p VB. Notably, the typical Oh Co^{3+} began evolving from 575 K and above, indicating the gradual oxidation of the metallic surface to oxide **[37]**. However,

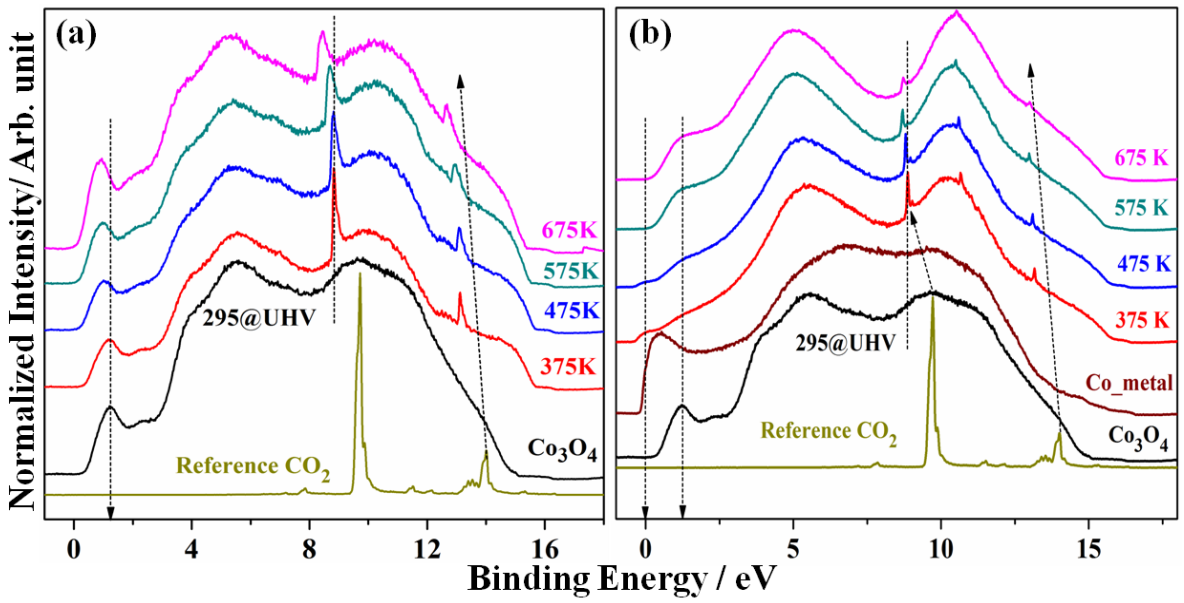

Figure. 5.10 Ultraviolet photoelectron VB spectra recorded under measurement conditions of 1:3 CO_2/H_2 ratio at 0.1 mbar between 375 and 675K.NAP-UPS VB features recorded with **(a)**Co_3O_4 NCs, and **(b)**Co_3O_4 reduced to Co metal. The intensity of CO_2 has decreased and broadening in the spectra observed because of formation of CO at high temperature. UVPES recorded for pure gas-phase CO_2, Co_3O_4 and Co_3O_4 reduced to metal are also shown for comparison and as reference.

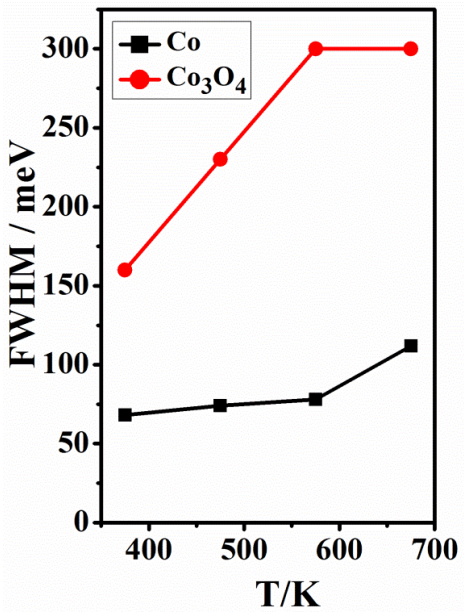

Figure.5.11 Temperature dependent FWHM observed for the CO_2 vibrations feature at 9.7 eV with 1:3 CO_2:H_2 ratio reactant gasmixture on Co_3O_4 (red) and Co(*in-situ* reduced from Co_3O_4). Higher FWHM is observed on $Co_3O_4$is attributed to the heterogeneity of the surface. It is also to be noted that reference CO_2 spectrum recorded exhibits FWHM of 210meV.

unlike the changes in BE and FWHM of CO_2 vibrational features on Co_3O_4 (**Figure 5.10a**), only a marginal shift in BE (0.16 eV) of CO_2 vibrational feature was observed, with a small

change in FWHM (Figure 5.11). These observations indicate the relatively passive nature of the metallic Co-surface to CO_2 activation, compared to Co_3O_4 NC, at least under the present experimental conditions. Therefore, in light of these observations, catalytic activity measurements were carried out on Co_3O_4 NC under relevant condition at ambient pressure.

5.2.6 Catalytic Activity Measurements

The CO_2 reduction was carried out in a fixed bed catalytic reactor under atmospheric pressure in the temperatures range from 523 to 823 K, with various CO_2:H_2 ratios (1:3, 1:2, 1:1, and 3:2), and at a GHSV of 19200 h^{-1}. CO_2 activation was observed to be insignificant below 473 K, and thus, the measurements were limited to 523 to 823 K and Figure 5.12 shows the outcomes. Only products detected were methane, CO, and water. The following results are worth highlighting:

(a) CO_2 conversion increased with rising reaction temperature up to 723K for all CO_2:H_2 ratios, after which it decreased marginally. In contrast, H_2 conversion remained nearly constant for a given CO_2:H_2 ratio between 523 and 623 K, after which it decreased rapidly with further increase in temperature.

(b) At low temperatures, methane is the preferred product, whereas CO is produced predominantly at high temperatures, regardless of the reactants ratio. A CO_2rich reactant ratio (CO_2:H_2 = 1:1, 3:2) showed 100% selectivity towards CO.Novelty of the present work partly lies in employing lower content of hydrogen, and still achieving 100 % CO selectivity.

(c) Methanation occurred preferentially with hydrogen-rich feed and at low temperatures, whereas CO was selectively produced with CO_2-rich feed and at relatively high temperatures. For example, a 1:3 ratio of CO_2:H_2 led predominantly to methane, with maximum CO_2 and H_2 conversion of 49.5% and 76.3% at 723 K and 573 K, respectively. In contrast, 3:2 CO_2:H_2 ratio resulted in the maximum CO_2 conversion of 26.2% at 723 K and the maximum H_2conversion of 64.7% at 623 K, with over 90% CO selectivity and less than 10% methane selectivity.

(d)A decrease in H_2 conversion observed at high temperatures for all CO_2:H_2 ratios support the notion that surface coverage decreased with temperature, thereby enhancing CO production and minimizing methanation. It is likely that hydrogen was used predominantly to remove oxygen dissociated from CO_2 in the form of water under high-temperature conditions. Hence, the ratio of adsorbed surface reactants was likely close to unity. While methane is a thermodynamically stable product, CO is the preferred product, and the current catalyst

maximizes its production under the given experimental conditions. As one mole of methane (and two moles of water) formation requires four moles of hydrogen for CO_2 reduction (Eq. 5.1), it is anexpensive process. In addition, there is a possibility that large H_2 conversion conditions might lead to dynamic oxygen vacancy generation on the catalyst surface, which can influence the activity/selectivity.

In Figure 5.12a, the catalytic conversion of CO_2 is presented and the results offer additional insights. Below 523 K, there was no substantial CO_2 conversion, which is in consitent with the TPR results depicted in Figure 5.3 and confirms that the reaction is initiated by H_2 adsorption and consumption. The maximum CO_2 conversion is observed at 723 K, regardless of the reactant ratio; however, a slight decrease of 3-4% in CO_2 conversion was observed beyond this temperature. Surprisingly, significant CO_2 (with large H_2) conversion was observed with a less than stoichiometric CO_2:H_2 ratio (3:2), highlighting the preference of hydrogen adsorption on the catalyst sites over CO_2 adsorption at low temperatures. Thecontact time of high CO_2 (low H_2) with 3:2 and 1:1 ratio assists in achieving high CO yield at 673 K and 823 K, respectively.

Figure 5.12b presents the H_2 conversion data, and it shows an opposite trend to that observed in Figure 5.12a for CO_2 data. The H_2 conversion decreases for all feed compositions as the reaction temperature increases. The maximum H_2 conversion (75.6%) was observed with CO_2:H_2 =1:3 at 573 K, which leads to high methane selectivity. Generally, an increase in H_2 content leads to an increase in CO_2 conversion but a decrease in H_2 conversion. The increase in CO_2 conversion can be attributed to the generation of equal or nearly equal amounts of $Co^{2+}$and Co^{3+} on the CoO surface, which activate CO_2at relatively low temperature (473 K, **Figure5.4b**), as observed in QMS. A similar trend is also observed for partially reducedCo_3O_4 catalyst, which shows less CO selectivity compared to CH_4 at high temperature in afixed-bed reactor study at atmospheric pressure, and it is discussed later.

The results presented in Fig. 5.12 are displayed in terms of the rate of reactant conversion and product formation. The corresponding plot is shown in Fig. 5.13, which enables direct comparison with previously published results and complements the findings from Fig. 5.12. It is observed that CO_2 and H_2 conversions exhibit the same trend, asillustrated in Fig. 5.12. The highest rate of CO formation is obtained with a 1:3 CO_2:H_2 feed, whilealso producing methane at 823 K. Exclusive CO (CH_4) production at the lowest

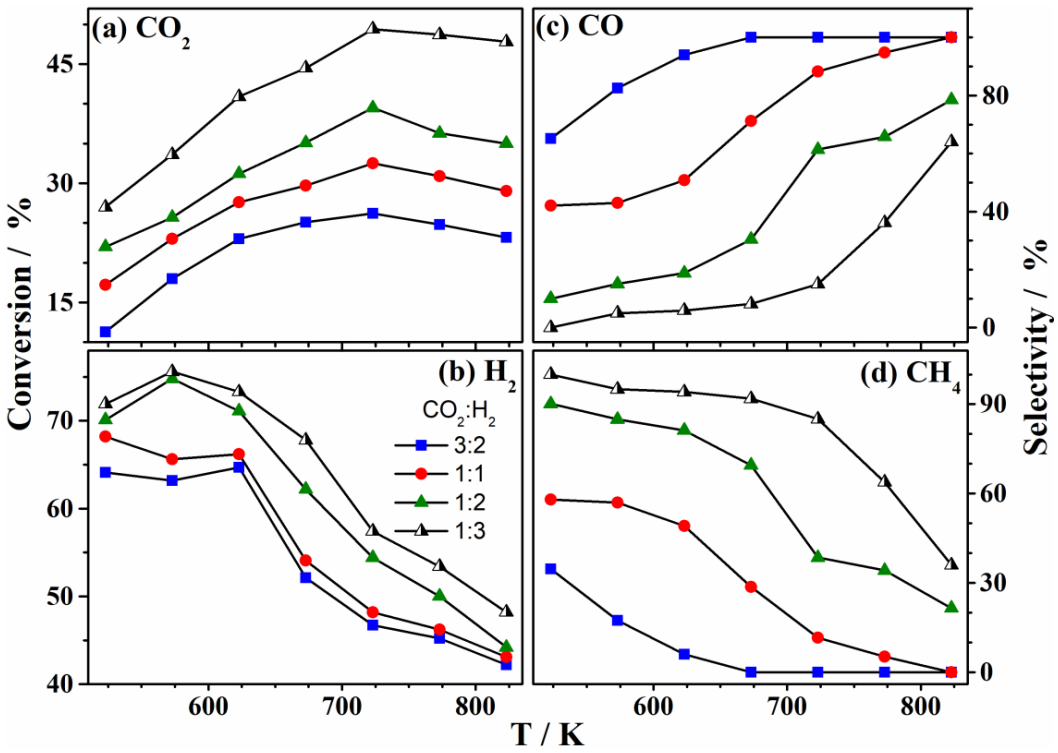

Figure 5.12 Presents the results for (a) CO_2 conversion, (b) H_2 conversion, (c) CO selectivity, and (d) CH_4 selectivity under the following reaction conditions: reaction temperature range of 523 K to 823 K, atmospheric pressure, gas flow of 320 ml/min, and GHSV of 19200h^{-1} for varying CO_2:H_2 ratios of 1:3, 1:2, 1:1, and 3:2.

temperature of 673 K (523 K) was observed with 3:2 (1:3) CO_2:H_2. The rate of CO formation nearly plateaus between 100-120 mmol/h.g_{cat} for the other three CO_2:H_2 feeds between 723 and 823 K. Although no methane production was observed, a minor decreasing trend in the rate of CO production with CO_2:H_2 3:2 above 723 K indicates that the hydrogen-deprived surface is likely to change further. Hydrogen deprived surface is likely to decrease the CO_2conversion too, especially at 773-823 K.It may be noted that same CO yield (120 mmol/h.g, with a decreasing methane yield from 20 to 0 mmol/h.g) is observed with 1:1 CO_2:H_2 feed between 723-823 K; while a marginal decrease in CO yield (with no methane yield) with temperature is observed with 3:2 CO_2:H_2 underscores the hydrogen deprived surface decreases the CO_2conversion.These observations underscore the necessity of maintaining the redox nature of the surface for sustainability, especially in terms of a combination of the availability of both Co^{2+} and Co^{3+} oxidation states under reaction conditions. It is also highly probable that dynamic changes occur on the catalyst surface, which is worth studying with in situ spectral methods, such as IR.

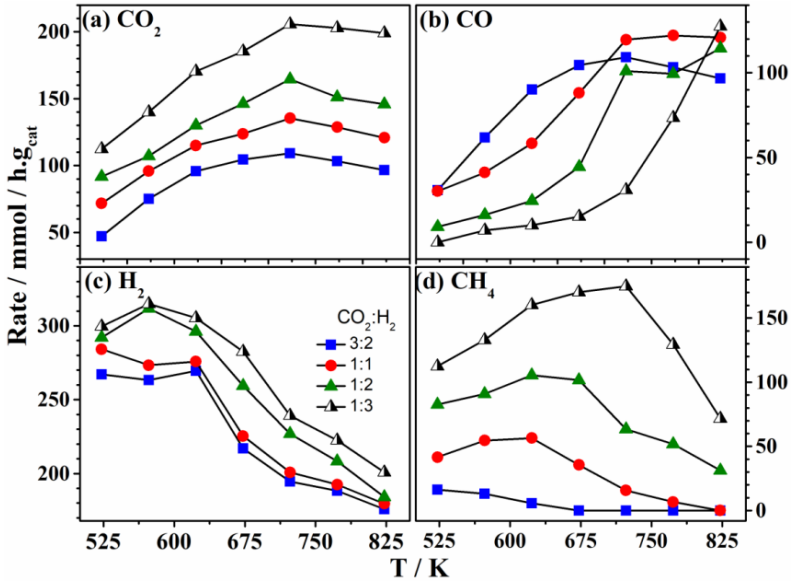

Figure 5.13. Rate of CO_2 reduction with H_2 and products formation is shown as a function of temperature for various CO_2:H_2ratios. Conversion of (a) CO_2 and (b) H_2, as well as the formation of products (c) CO and (d) CH_4 are separately plotted.

Catalytic CO_2 reduction reaction was also carried out on pre-reduced catalysts, namely, CoO and metallic Co, with CO_2:H_2 = 3:2 to understand the role of different oxidation states of Co. Same reduction conditions were applied, as given in sec. 5.2.4, but at H_2 flow rate of 25 ml/min, which reduces the Co_3O_4 catalyst. The reaction results obtained with Co-metal and CoO are compared with that of Co_3O_4 (NC) and shown in Figure 5.14. Expectedly, the initial activity of CoO (Figure 5.14b) and metallic Co (Figure 5.14c) is very different at temperatures ≤673 K, compared to Co_3O_4 NC (Figure 5.14a). Metallic Co exhibitscomparable CO_2 conversion as that of Co_3O_4, even at 523-573 K, but with high methane selectivity, which is in accordance with the literature reports [**13,23**]; while Co_3O_4 (NC) exhibits high CO selectivity. Interestingly, low H_2-conversion observed, in spite of high methane selectivity, underscores the oxygen stripped from CO_2 oxidizes the metallic Co to higher oxidation states. This suggests the changes that occur on the catalyst surfaces under H_2-lean conditions. Nonetheless, as the temperature increases, CO selectivity increases at the cost of methane selectivity, indicating the change in the nature of the metallic Co-catalyst. It is also known that H_2-rich feed composition, (1:4 in ref. **23**) exhibits high methane selectivity even at high temperatures with metallic Co, while the present results with H_2-lean feed shows high CO selectivity. While exclusive methane selectivity was observed below 673 K with CoO, CO selectivity increases with temperature. Surprisingly, CO_2 conversion observed to be the lowest (8-10 %), along with low H_2 conversion with CoO. Nonetheless, CO (CH_4) selectivity increases (decreases) linearly

with temperature, again underscoring the nature of the catalyst surfaces gradually changes under reaction conditions.

Present set of results given in Figure 5.14 suggests the following: (a) In contrast to the literature reports, which employed generally H_2-rich feed compositions (CO_2:H_2 = 1:x; x≥2), present H_2-lean reactants feed changes the nature of the catalysts (especially Co-metal) gradually towards higher oxidation state(s). This in turn influences the reactants conversion and products selectivity. (b) While the CO_2 conversion remains observed between 20-25 % on Co_3O_4 and Co, it decreased to ~5-10 % with CoO. (c) Increase in CO selectivity at the cost of methane with CoO and with Co at high temperature indicates the progressive oxidation of the surface towards Co_xO_y; this aspect is confirmed from the XRD pattern recorded with the spent catalyst, collected after the reaction carried out, and discussed later. (d) Nanocube morphology is present only for Co_3O_4, while it changes to random morphology with agglomeration (Figure 5.15) on reduction to CoO or metallic Co, which also a major reason for changes in the activity observed in Figure 5.14b and c panels. This point underscores the importance of NC morphology for 100 % CO selectivity with Co_3O_4. It is also to be pointed out that under NAPPES conditions, reduction was carried out at 0.1 mbar H_2 pressure, which reduces the surface layersandhence it retains the nanocube morphology. Hence upon reaction at the same pressure, the surface gets oxidized.

XRD results shown in **Figure 5.1** is also included for comparison in Figure. 5.16. Inset shows the enlarged region around 44-45 degree. First of all it is evident that (400) facet of metallic Co and Co_3O_4 appears at a difference of 0.4 degree, and hence they could be easily distinguished. While fresh and spent Co_3O_4 catalysts exhibits (400) facet at 44.9 deg., reduced Co shows the (400) facet at 44.4 deg., which is typical for metallic Co [**23**,**38**]. More interestingly, after CO_2 reduction reaction was carried out with Co-metal with CO_2:H_2 = 3:2 (Figure 5.14c), all diffraction features corresponding to Co_3O_4 and CoO are observed; this is in addition to the metallic Co-features. Very similar XRD pattern was observed with spent CoO catalyst also (not shown). This observation reiterates that under the present experimental conditions with H_2-lean feed, metallic Co-surface undergoes oxidation towards Co_3O_4 along with CoO. Indeed, NAPPES studies have earlier shown the evolution of Co-metal and CoO surfaces towards Co_3O_4 under in-situ measurement conditions (**Figure 5.5**). Another aspect is the presence of many different crystallographic facets on the spent catalyst, after the reaction. Upon reduction of Co_3O_4 to Co, nanocube morphology disappears and TEM analysis indicates

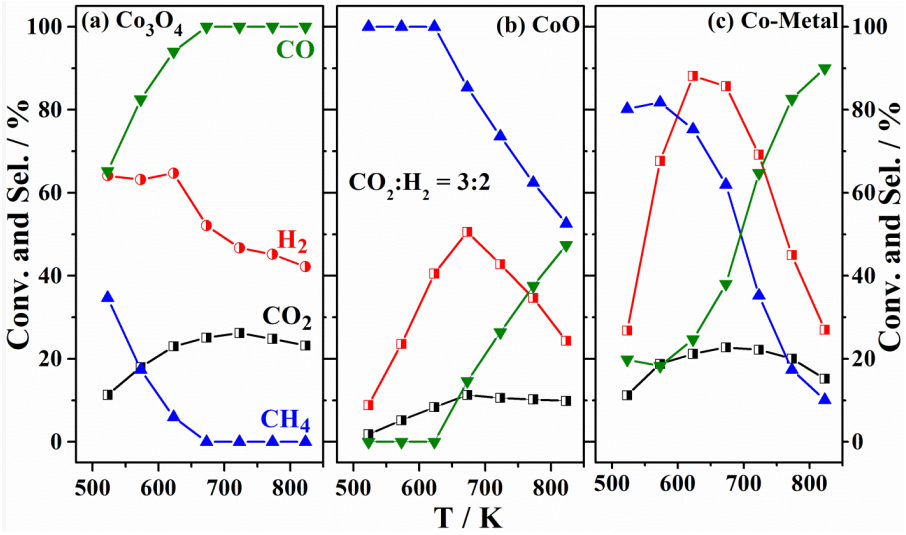

Figure 5.14 Comparison of temperature dependent CO_2 reduction activity and selectivity for (a) Co_3O_4, (b) CoO, and (c) Co-metal. Later two were generated by reducing Co_3O_4 in H_2 at 250 and 400 °C for 3 and 5h, respectively. Note a significant decrease in CO_2 conversion with CoO.

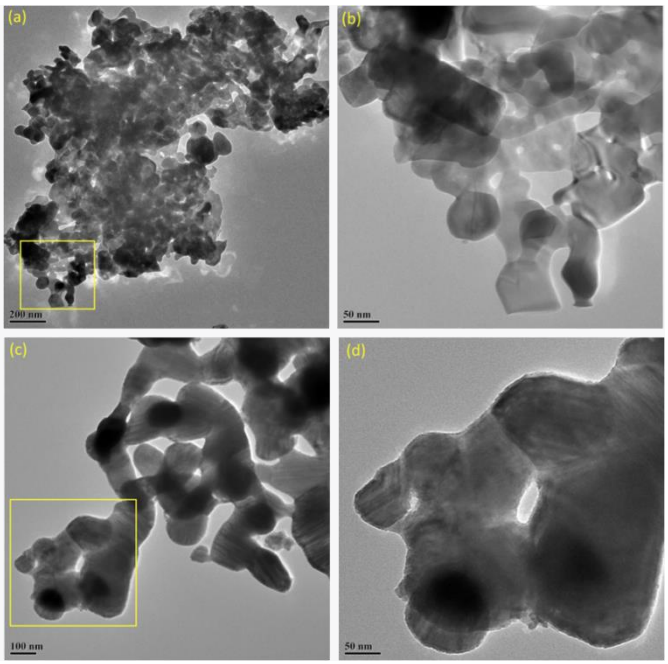

Figure 5.15 TEM images recorded for Co_3O_4 reduced freshly to (a and b) CoO, and (c and d) Co-metal. Yellow square drawn in (a) and (c) are shown at enlarged scale in (b) and (d), respectively.

a random morphology with Co or CoO (**Figure 5.15**). Chain growth of particle (or agglomeration) observed with random morphology in TEM results (Fig. 5.15), and different crystallographic facets observed in Fig. 5.16 underscores the activity observed in Fig. 5.14b and c is due to an averaging effect of different crystallographic sites, which may be considered

as comparable to conventionally synthesized Co_3O_4. Although by continuing the reaction for longer time on stream (Fig. 5.14b and c) catalyst could be fully converted to long-range ordered Co_3O_4; however, NC morphology cannot be restored by simply continuing the reaction. Entirely different activity/selectivity observed in Fig. 5.14b and c, compared to Fig. 5.14a attests this conclusion. Indeed, selective CO production observed was due to exclusive (1 0 0) facets present on NC morphology. This fact also supports the high conversion and exclusive CO selectivity with Co_3O_4 is due to NC morphology with (1 0 0) facets, which promotes CO formation. Metallic Co in nanorod and nanoparticle forms was evaluated for CO_2 hydrogenation with CO_2:H_2 = 1:4 **[23]**. Though both are metallic Co, completely different activity was reported; Co-nanorod exhibits 100 % methane selectivity, while Co-nanoparticles exhibit a reactivity similar to the results shown in Fig. 5.14c (with high methane selectivity at low temperature, while high CO selectivity a high temperatures). Observations like this along with our present results underscores the importance of adopting suitable nanoscience would lead to the desired results.

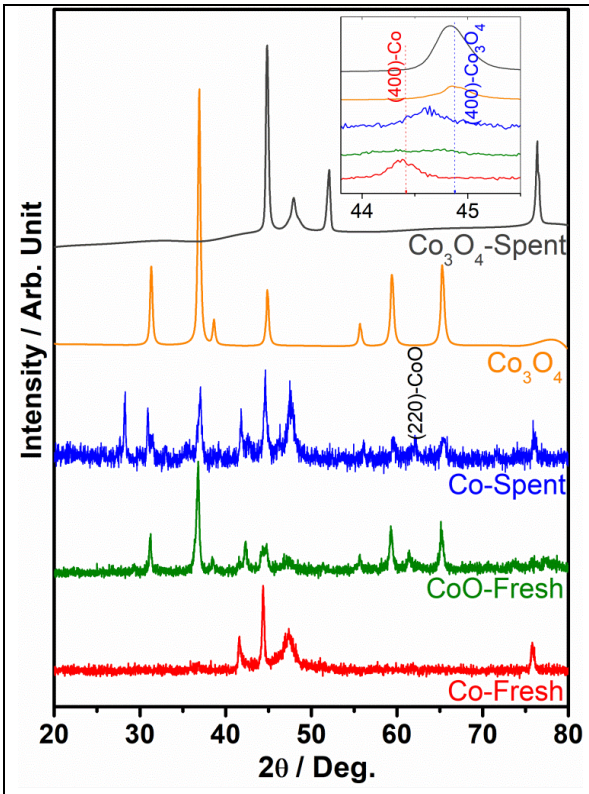

Figure 5.16 XRD pattern recorded after Co_3O_4 was reduced to Co, CoO and compared with the fresh Co_3O_4 and spent Co_3O_4 catalysts. Spent Co catalyst, obtained after the reaction results shown in Figure 5.14c, XRD pattern was also carried out and compared. Evolution of Co-metal to cobalt oxides is directly evident from the results, due to CO_2-reduction with H_2-lean feed. Inset shows the enlarged pattern around 44-45 deg. to distinguish the (400) facet of metallic Co and Co_3O_4.

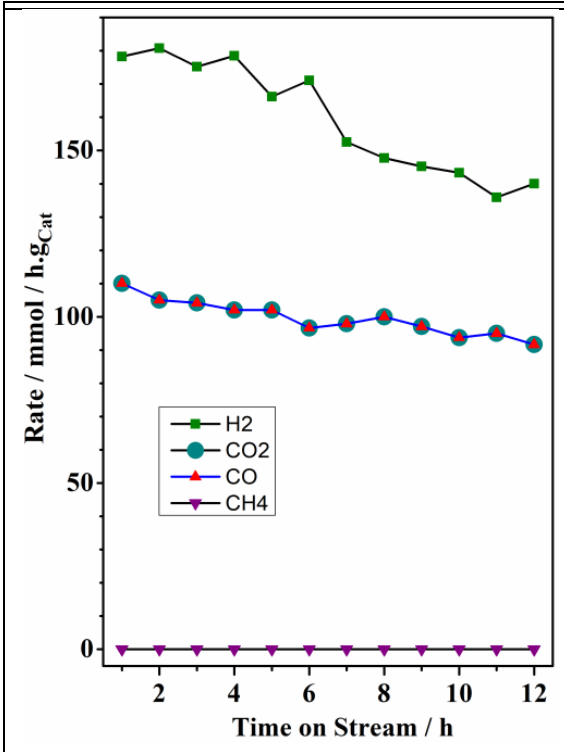

Figure 5.17. Time on stream (ToS) studies were conducted to investigate the reactant conversion of CO_2 (represented by the color cyan) and H_2 (represented by the color olive) on Co_3O_4 NC, with the resulting products of CO (represented by the color red) and CH_4 (represented by the color purple), at 723 K and a CO_2:H_2 ratio of 3:2, at a pressure of 1 bar, a flow rate of 320 ml/min, and a gas hourly space velocity (GHSV) of 19200 h^{-1}. The ToS study demonstrated sustainable activity of the catalyst throughout the experimental period.

5.2.7 Time on Stream

In order to evaluate the feasibility of the Co_3O_4 NC spinel catalyst, a time-on-stream (ToS) study was conducted for the CO_2 reduction reaction with CO_2:H_2=3:2 at 723 K for 12 hours, and the results are shown in **Figure 5.17**. The Co_3O_4 NC catalyst exhibited a remarkable catalytic activity for the CO_2 reduction to CO, without the formation of methane, and this presents a more cost-effective approach to producing a single product that can be utilized in various applications. The stable CO_2 and H_2 conversion rates were observed to be 98±10 and 160±15 mmol/h.g_{cat} at 723 K within the experimental error limit of 10%, while the CO and CH_4 production rates were 98±5% and 0 mmol/h.g_{cat} at 723 K, respectively. The CO production was maintained at 100% for the entire duration of the study at 723 K with minimal variation, which falls within the acceptablerange of error. The catalyst demonstrated sustainable activity and selectivity throughout the entire reaction period at both temperatures. A decrease in H_2 consumption observed between 4 and 7th hour, while constant rate of CO production demonstrates a dynamic change on the surface. Same numbers observed for CO_2 conversion and CO production fully supports the above conclusion. The ToS study shows that the Co_3O_4 NC catalyst exhibits high activity and stability under the CO_2 reduction reaction condition, with no significant change in activity observed.

Moreover, the results suggest that an optimal concentration of cobalt (+2/+3) oxidation state is maintained throughout the reaction, which could be the key to catalytic stability. Furthermore, higher H_2 and CO_2 conversions were observed at CO_2:H_2=3:2, along with high CO selectivity. Under H_2-rich conditions, the amount of Co^{2+} concentration on the catalyst surface was higher compared to Co^{3+}, while the opposite trend was observed under CO_2-rich conditions.The CO_2 acted as an oxidizing agent and maintained the optimal concentration of Co^{3+} on the surface, resulting in selective CO production at a relatively lower temperaturethan under CO_2-lean conditions.Table 1 lists the catalyst activityand selectivity for some of the topperforming catalysts for CO_2 reduction reaction from the literature. A preliminary analysis of the results demonstrates that the present results for Co_3O_4 NC exhibit a better performance compared to other reported systems. Previous work by our group on Mo_2C reported 44% conversion with 34% CO selectivity with reactant ratio 1: 3 CO_2:H_2 at 623K **[39]**; this isonly the second report on CO_2 reduction under H_2 lean conditions; another report on In_2O_3 reported 24% CO_2 conversion with 98% CO selectivity at873 K. However, in the present work, the maximum 26% CO_2 conversion along with 100% CO selectivity observed at 723 K, which is 100 K lower than the previous work reported under comparable conditions **[40]**. At optimum conditions, Co_3O_4 NC demonstrates the potential to produce exclusively CO, which reduces the separation cost of methane and makes the process more economically viable and sustainable. On the other hand, Ni-CeO_2 catalystshows 40% CO_2 conversion with 1:1 CO_2:H_2 ratio with 100% CO selectivity but lacks sustainability **[41]**. A significant number of systems show 5-85% CH_4 selectivity, which is not preferred in the RWGS reaction.

5.3. Conclusion

In this study, we investigated the surface chemistry and catalysis aspects of Co_3O_4NC for CO_2 reduction, using relevant methods, such as NAP-XPS, UPS, RGA and fixed bed reactor. The results show that the Co_3O_4 spinel phase is sustainable at least up to 773 K under reaction conditions. Under near-ambient pressure and temperature conditions, Co metal surfaces oxidize to CoO and Co_3O_4 during the reaction, underscoring the dynamic changes. Indeed, a direct correlation was observed between the findings of NAPPES at 0.1 mbar pressures and catalysis at 1 bar along with XRD/TEM characterization. Especially the disappearance of metallic nature of Co and appearance of oxides of cobalt was observed in NAPPES as well as under ambient pressure reaction conditions and further confirmed by XRD.The activation of CO_2 starts at 575 K on freshly prepared Co_3O_4 at 0.1 mbar pressures. The metallic phase of

cobalt prepared by H_2 reduction activates CO_2 at 473 K, the oxygen from CO_2 dissociation oxidizes the Co metal surface, resulting in a higher oxidation state at higher temperatures as the reaction proceeds. The oxidation of the Co-metal catalyst surface was characterized by NAP-XPS and NAP-UPS spectra, and XRD. Several interesting results are observed with CO_2 reduction on various oxidation states of cobalt and ex-situ reactor study at 1 bar pressure with varying reactant ratios.

(1) Contrary to some of the reports suggesting that Co metal is active for CO_2 activation and selective towards CO formation, our studies with NAP-XPS and NAP-UPS indicate that a combination of 2+ and 3+ oxidation states of Co activate CO_2 at lower temperatures and exhibits high selectivity to CO production. **(2)** A 1:1 and 3:2 CO_2:H_2 ratio exhibits the best and sustainable performance between 623 and 723 K with 100% CO selectivity at 723 K. The highest CO selectivity was observed at the cost of methanation, and this was observed by employing lower than stoichiometric amounts of H_2 and at moderate temperatures. This point underscores the unique and inherent catalytic activity and selectivity of Co_3O_4-NC. **(3)** There is a dynamic redox interaction between Co^{2+} and Co^{3+} states, which seems to help for high CO selectivity **[48] (4)** Increases in broadening of CO_2 vibrational features support the formation of CO, which is overlapping with the CO_2 features. Finally, by optimizing the reaction conditions, especially with contact time and fine-tuning the CO_2:H_2 ratio, highly sustainable activity can be achieved around 700 K. By optimizing the pressure to significantly higher levels, it is possible to obtain value-added liquid products as well. Indeed, Co_3O_4 catalyst has already direct conversion of CO_2 to methanol, C2 and C3 products has been recorded, but at high pressures (20 bar and above) **[49]**. We believe the information provided in this manuscript could be helpful for carbon-neutral economy or carbon-recycling aspects, and more work is desired in that direction. Highly selective CO formation, with or without H_2, could be utilized in the steel industry for steelmaking and to minimize emissions. It is also worth exploring the structure dependent activity of Co_3O_4, especially with different crystallographic facet(s), since there is a possibility to selectively produce one or fewer products.

Table 5.1. Comparison of Activity and Sustainability Reported for CO_2 Reduction with different Catalyst Systems

Catalyst	T /K	Pressure (bar), GHSV/WHSV/Feed Flow	CO_2:H_2#	CO_2conv. (%)	CO Sel. (%)	CH_4Sel .(%)	Sustainability aspects	Ref.
β-Mo_2C	723	1 bar,GHSV: 20000 /h	1:3	56	61	5-9	Stable activity for 12 h	42
In_2O_3	873	1 bar, GHSV:15000 h^{-1}	1:3 3:2	49 24	85 98	15 2	Stable performance for 12 h	43
Ni-CeO_2	973	1 bar, flow:100 mL min^{-1}	1:1	40	100	0	TOS: N/A	44
$BaCe_{0.2}Zr_{0.6}Y_{0.16}Zn_{0.04}O_3$	873	1 bar, Flow: 20 mL/ min	1:1	36.3	94	~5	Stable performance for 5 h	45
Pt- SiO_2 Pt-TiO_2	573	1 bar, WHSV: 119.7 h^{-1} WHSV: 24.7 h^{-1}	1:2	3.38 4.51	100 99	0 1	TOS: N/A	46
Cu/SiO_2 Cu/CeO_2	573	1 bar, WHSV: 4.32 h^{-1} and 1.08 h^{-1}	1:3	6 18	98 100	~2 0	Marginal decrease in activity in 2h	47
$La_{0.75}Sr_{0.25}FeO_3$	823	1 bar.50 sccm (10% H_2 10% CO_2 v/v)	1:1 Bal. He	15.5	95	~3	TOS: 2.5 h. Stable activity for 2.5 h	48
Ni_3-Fe_3/ZrO_2	673	1 bar,40 ml/ min,	1:2 Bal. Ar	38.8	12.9	87	Marginal decrease in activity in 14 h	49
In_2O_3 Ga_2O_3	873	1 bar, 40 mL/ min	1:1	29.63 19.08	N/A	N/A	TOS: N/A	50
Co_3O_4 NC	723	1 bar, GHSV:19200 h^{-1}	1:3 3:2	49.4 26.2	15 100	85 0	Stable performance for 12 h	Present work

Balance by N_2/He/Ar

5.4 References

1. Arakawa, H.; Aresta, M.; Armor, J. N.; Barteau, M. A.; Beckman, E. J.; Bell, A. T.; Bercaw, J. E.; Creutz, C.; Dinjus, E.; Dixon, D. A.; Domen, K.; DuBois, D. L.; Eckert, J.; Fujita, E.; Gibson, D. H.; Goddard, W. A.; Goodman, D. W.; Keller, J.; Kubas, G. J.; Kung, H. H.; Lyons, J. E.; Manzer, L. E.; Marks, T. J.; Morokuma, K.; Nicholas, K. M.; Periana, R.; Que, L.; Rostrup-Nielson, J.; Sachtler, W. M. H.; Schmidt, L. D.; Sen, A.; Somorjai, G. A.; Stair, P. C.; Stults, B. R.; Tumas, W.*Chem. Rev.***2001**,*101*, 953-996.
2. Lewis, N. S.; Nocera, D. G.*PNAS.***2006**,*103*, 15729-15735.
3. Aresta, M.; Dibenedetto, A.*Dalton Trans.***2007**,*28*, 2975-2992.
4. Appel, A. M.; Bercaw, J. E.; Bocarsly, A. B.; Dobbek, H.; DuBois, D. L.; Dupuis, M.; Ferry, J. G.; Fujita, E.; Hille, R.; Kenis, P. J. A.; Kerfeld, C. A.; Morris, R. H.; Peden, C. H. F.; Portis, A. R.; Ragsdale, S. W.; Rauchfuss, T. B.; Reek, J. N. H.; Seefeldt, L. C.; Thauer, R. K.; Waldrop, G. L.*Chem. Rev.***2013**,*113*, 6621-6658.
5. Aresta, M.; Dibenedetto, A.; Angelini, A.*Chem. Rev.***2014**,*114*, 1709-1742.
6. Wang, W.; Wang, S.; Ma, X.; Gong, J.*Chem. Soc. Rev.***2011**,*40*, 3703-3727.
7. Ohya, H.; Fun, J.; Kawamura, H.; Itoh, K.; Ohashi, H.; Aihara, M.; Tanisho, S.; Negishi, Y.*J. Membr. Sci.***1997**,*131*, 237-247.
8. Kim, D.; Resasco, J.; Yu, Y.; Asiri, A. M.; Yang, P.*Nature Commun.*2014,*5*, 4948.
9. Wang, W.-H.; Himeda, Y.; Muckerman, J. T.; Manbeck, G. F.; Fujita, E.*Chem. Rev.***2015**,*115*, 12936-12973.
10. Nitopi, S.; Bertheussen, E.; Scott, S. B.; Liu, X.; Engstfeld, A. K.; Horch, S.; Seger, B.; Stephens, I. E. L.; Chan, K.; Hahn, C.; Nørskov, J. K.; Jaramillo, T. F.; Chorkendorff, I.*Chem. Rev.***2019**,*119(12)*, 7610-7672.
11. Bradford, M. C. J.; Vannice, M. A.*Catal. Rev.***1999**,*41*, 1-42.
12. An, K.; Somorjai, G. A.*Catal. Lett.***2015**,*145*, 233-248.
13. Melaet, G.; Ralston, W. T.; Li, C.-S.; Alayoglu, S.; An, K.; Musselwhite, N.; Kalkan, B.; Somorjai, G. A.*J. Am. Chem. Soc.***2014**,*136*, 2260-2263.
14. Iablokov, V.; Beaumont, S. K.; Alayoglu, S.; Pushkarev, V. V.; Specht, C.; Gao, J.; Alivisatos, A. P.; Kruse, N.; Somorjai, G. A.*Nano Lett.***2012**,*12*, 3091-3096.
15. Den Breejen, J. P.; Radstake, P. B.; Bezemer, G. L.; Bitter, J. H.; Frøseth, V.; Holmen, A.; de Jong, K. P.*J. Am. Chem. Soc.***2009**,*131*, 7197-7203.
16. Zhu, Y.; Zhang, S.; Ye, Y.; Zhang, X.; Wang, L.; Zhu, W.; Cheng, F.; Tao, F.*ACS Catal.***2012**,*2*, 2403-2408.
17. Enache, D. I.; Rebours, B.; Roy-Auberger, M.; Revel, R.*J. Catal.***2002**,*205*, 346-353.
18. Jozwiak, W. K.; Szubiakiewicz, E.; Góralski, J.; Klonkowski, A.; Paryjczak, T.*Kinet. Catal.***2004**,*45*, 247-255.
19. Lahtinen, J.; Anraku, T.; Somorjai, G. A.*Catal. Lett.***1994**,*25*, 241-255.
20. Weatherbee, G. D.; Bartholomew, C. H.*J. Catal.***1982**,*77*, 460-472.
21. Velu, S.; Suzuki, K.; Gopinath, C. S.; Yoshida, H.; Hattori, T.*Phys. Chem. Chem. Phys.***2002**,*4*, 1990-1999.

22. Duyar, M. S.; Tsai, C.; Snider, J. L.; Singh, J. A.; Gallo, A.; Yoo, J. S.; Medford, A. J.; Abild-Pedersen, F.; Studt, F.; Kibsgaard, J.; Bent, S. F.; Nørskov, J. K.; Jaramillo, T. F.*Angew. Chem. Int. Ed.***2018**,*57,* 15045-15050.
23. Jimenez, J. D.; Wen, C.; Lauterbach, J. *Catal. Sci. Tech.***2019**,*9,* 1970-1978.
24. Jimenez, J.; Bird, A.; Santos Santiago, M.; Wen, C.; Lauterbach, J.*Energy Tech.***2017**,*5,* 884-891.
25. Kim, I. H.; Seo, H. O.; Park, E. J.; Han, S. W.; Kim, Y. D.*Sci. Rep.***2017**,*7,* 40497.
26. Wu, J.; Wen, C.; Zou, X.; Jimenez, J.; Sun, J.; Xia, Y.; Fonseca Rodrigues, M.-T.; Vinod, S.; Zhong, J.; Chopra, N.; Odeh, I. N.; Ding, G.; Lauterbach, J.; Ajayan, P. M.*ACS Catal.***2017**,*7,* 4497-4503.
27. Kattel, S.; Liu, P.; Chen, J. G.*J. Am. Chem. Soc.***2017**,*139,* 9739-9754.
28. Fan, T.; Liu, H.; Shao, S.; Gong, Y.; Li, G.; Tang, Z.*J. Phys. Chem. Lett.***2021**,*12,* 10486-10496.
29. Navarro-Jaen, S.; Virginie, M.; Bonin, I.; Robert, M.; Wojcieszak, R.; Khodakov, A. Y.*Nature Chem.***2021**,*5,* 564-579.
30. Zhou, G.; Wu, T.; Xie, H.; Zheng, X.*Int. J. Hydrogen Energy***2013**,*38,* 10012-10018.
31. Sexton, B. A.; Hughes, A. E.; Turney, T. W.*J. Catal.***1986**,*97,* 390-406.
32. Shi, R.; Chen, G.; Ma, W.; Zhang, D.; Qiu, G.; Liu, X.*Dalton Trans.***2012**,*41,* 5981-5987.
33. Liotta, L. F.; Di Carlo, G.; Pantaleo, G.; Venezia, A. M.; Deganello, G.*Appl. Catal. B: Environ.***2006**,*66,* 217-227.
34. Biesinger, M. C.; Payne, B. P.; Grosvenor, A. P.; Lau, L. W. M.; Gerson, A. R.; Smart, R. S. C.*Appl. Surf. Sci.***2011**,*257(7),* 2717-2730.
35. Mathew, T.; Shiju, N. R.; Sreekumar, K.; Rao, B. S.; Gopinath, C. S.*J. Catal.***2002**,*210,* 405-417.
36. Dubey, A.; Reddy, K. P.; Gopinath, C. S.*ChemSel***2017**,*2,* 533-536.
37. Reddy, K. P.; Jain, R.; Ghosalya, M. K.; Gopinath, C. S.*J. Phys. Chem. C***2017**,*121,* 21472-21481.
38. Barakat, N. A. M.; Khil, M. S.; Sheikh, F. A.; Kim, H. Y.*J. Phys. Chem. C***2008**,*112,* 12225-12233.
39. Reddy, K. P.; Dama, S.; Mhamane, N. B.; Ghosalya, M. K.; Raja, T.; Satyanarayana, C. V.; Gopinath, C. S.*Dalton Trans.***2019**,*48,* 12199-12209.
40. Mhamane, N. B.; Chetry, S.; Ranjan, R.; Raja, T.; Gopinath, C. S.*ACS Sus. Chem. Engn.***2022**,*10,* 3521-3531.
41. Wang, L.; Liu, H.; Liu, Y.; Chen, Y.; Yang, S.*J. Rare Earths***2013**,*31,* 969-974.
42. Kim, D. H.; Park, J. L.; Park, E. J.; Kim, Y. D.; Uhm, S.*ACS Catal.***2014**,*4,* 3117-3122.
43. Kattel, S.; Yan, B.; Chen, J. G.; Liu, P.*J. Catal.***2016**,*343,* 115-126.
44. Yang, S.-C.; Pang, S. H.; Sulmonetti, T. P.; Su, W.-N.; Lee, J.-F.; Hwang, B.-J.; Jones, C. W.*ACS Catal.***2018**,*8,* 12056-12066.
45. Daza, Y. A.; Kuhn, J. N.*RSC Adv.***2016**,*6,* 49675-49691.
46. Yan, B.; Zhao, B.; Kattel, S.; Wu, Q.; Yao, S.; Su, D.; Chen, J. G.*J. Catal.***2019**,*374,* 60-71.

47. Sun, Q.; Ye, J.; Liu, C.-j.; Ge, Q.*Greenhouse Gases: Sci. Tech.***2014**,*4*, 140-144.
48. Jain, R.; Gopinath, C. S.*ACS Appl. Mater. Interfaces***2018**,10*, 41268-41278.
49. Have, I. C. t.; Kromwijk, J. J. G.; Monai, M.; Ferri, D.; Sterk, E. B.; Meirer, F.; Weckhuysen, B. M.*Nature Commun.***2022**,*13*, 324.

Chapter 5b

Exploration of Ni@Co Core-shell Nanoparticles for CO_2 Hydrogenation under NAPPES Conditions

5.5 Introduction

Over the past century, the swift industrialization and surging energy demands of our society have caused significant addition to the carbon content in the atmosphere, primarily due to the relentless increase in the greenhouse gas emissions. Despite the intensification of renewable energy production through photovoltaics, wind energy etc, it is not sufficient to offset the adverse impacts on our planet's climate and ecosystems. Due to growth in global population, energy demand is constantly increasing and hence the total energy produced and consumed also increasing, which is mainly produced from fossil fuels. **[1-2]** Concerns have grown regarding the levels of carbon dioxide (CO_2) in the atmosphere, which have now reached approximately 420 ppm. **[3-4]** This has compelled the establishment of political objectives and scientific/technological endeavours aimed at curbing CO_2 emissions and capturing and storing CO_2 within porous rock formations. **[5-6]** Another vital approach involves the conversion of CO_2as a valuable feedstock and to convert into chemicals and fuels, a strategy that not only serves to eliminate CO_2 from the atmosphere but also reduces our reliance on petrochemicals, as well as it recycles the carbon.

While the process of CO_2 hydrogenation is demanding due to the high stability of CO_2, resulting in limited conversion rates significant strides have been made towards the conversion of CO_2 into single-carbon (C1) products. This comprises molecules such as formic acid, carbon monoxide (CO), methane, and methanol, which are produced in water via direct hydrogen reduction or hydrothermal-chemical and photocatalytic reduction **[7-8].** Efficient CO_2 hydrogenation, particularly for the production of methanol, is a critical aspect of carbon capture and utilization (CCU), in view of more emphasis on methanol economy. This entails the conversion of CO_2 into valuable chemicals and fuels using various methods. Among these methods, a promising and scalable approach for converting CO_2 into C1-oxygenates, such as CO and methanol, has garnered widespread attention in carbon recycling technology. Although it is feasible to convert CO_2 into methane, it is not the preferred choice due to the additional costs and energy required for compression and transportation. Liquid products like methanol are favoured due to their high volumetric energy density and the availability of established infrastructure for transportation and dispensation. Furthermore, CO serves as a fundamental building block molecule, and when combined with hydrogen, it can be employed to produce a wide range of liquid chemicals and fuels through Fischer-Tropsch (FT) synthesis, offering the potential for clean synthetic fuels and various chemicals, including Cx-oxygenates (x = 1-5). **[9-10]**

Effortlessly achieving thermocatalytic hydrogenation of CO_2 to methane is possible under atmospheric pressure and high gas hourly space velocity (GHSV), demonstrating CO_2 conversion and CH_4 selectivity that closely approach theoretical equilibrium values. **[11]**
Previous research endeavours have focused on the development of catalysts based on copper (Cu) and nickel (Ni), each offering distinct advantages and drawbacks **[12]**. Although Cu-based catalysts have shown promise in selectively producing carbon monoxide (CO) and methanol (CH_3OH), they have fallen short of expectations in converting carbon dioxide (CO_2) **[13].** Conversely, Ni-based catalysts have demonstrated decent catalytic activity under mild conditions, favoring methane (CH_4) production over CO and CH_3OH **[14-15]**. However, CO, a crucial building block for synthetic fuels and oxygenates through Fischer–Tropsch or methanol synthesis reactions, remains the more desirable product **[16]**. Therefore, the current challenge is to enhance the selectivity of Ni-based catalysts for CO and formic acid (HCOOH) without compromising their CO_2 conversion efficiency.

Bimetallic catalysts have recently gained significant attention due to their distinct reactivity patterns, which often differ from those observed in monometallic counterparts **[17]**. These unique patterns result from geometric and electronic effects that lead to notable changes in the electron density of the metals' d-band, subsequently influencing their catalytic performance **[18]**. The impact of bimetallic synergies on catalytic activity has been evident in various studies. For example, in a study by Ruchi Jain *et. al.*, bimetallic Pd@Co core-shell nanoparticle (NPs) catalysts demonstrated exceptional activity and selectivity in olefin hydrogenation and styrene oxidation reactions **[19]**. Similarly, research by Yao *et.al.* revealed that copper–nickel (Cu–Ni) bimetallic catalysts exhibited enhanced catalytic activity in the selective hydrogenation of nitrocyclohexane to cyclohexanoneoxime **[20]**. These findings highlight the fundamental principle that introducing an additional active metal alongside Ni can modify its electronic properties, ultimately leading to improvements in adjusting the Ni valence state for catalytic processes. Bimetallic structures containing Ni have also been investigated for their potential to alter the selectivity of CO_2 hydrogenation. To achieve this, there is a need to promote CO insertion reactions over CO_2 and CO dissociation **[21]**. Bimetallic nanoparticles (NPs), such as CoCu, CoPd, and CoPt supported on oxide substrates, have been employed for this purpose **[22-23]**. The core−shell architecture, characterized by the arrangement where one element (A) forms a shell encapsulating a core composed of another element (B), often referred to as B@A core−shell, is one of the extensively studied bimetallic

nanoalloys. The high cost associated with noble metals has renewed interest in exploring the potential of more cost-effective first-row transition metals like Fe, Co, and Ni, despite the challenges in preparing nanoparticles (NPs) with these metals due to their more negative redox potential and susceptibility to surface oxidation. Creating customized nanoalloys with a core−shell structure presents an economical approach to catalyst production. This approach involves using the less expensive 3d transition metal in the core while incorporating the pricier yet highly active metal catalyst on the shell. Additionally, core−shell NPs based on transition metals have revealed unique physical properties that approach those of noble metals. **[24-25]**

The potential for improved catalytic activity and selectivity in core−shell nanoparticles (NPs) compared to monometallic NPs is a strong motivation for investigating core−shell configurations in bimetallic NPs. The catalytic behavior exhibited by these core−shell structures results from the interplay between strain and ligand effects, which arise from the heterometallic bonding interaction between the core and shell. This interaction can either cooperate or compete, depending on the specific configuration. By precisely adjusting factors such as chemical composition, surface oxidation, structure, morphology, and dimensions of the core and/or shell, the catalytic properties of the NP can be finely tuned. **[26]** In some cases, outstanding catalytic properties have been linked to the resulting core−shell structure after subjecting initially bimetallic mixed nanoalloys to processes like thermal annealing and oxidation−reduction cycles **[27]**. Therefore, it becomes essential to conduct experiments starting with core−shell NPs to confirm, understand, and harness their catalytic properties for practical use in industrial applications. Additionally, it's crucial to examine the structural stability of these materials under high-temperature conditions encountered during normal operations, as these nanostructures may display instability at temperatures considerably lower than the bulk materials' melting point and/or under specific reaction conditions. In the realm of cobalt-based catalysts, the utilization of CO_2 as a feedstock, instead of CO, has been shown to generate intermediates that eventually lead to alkane formation **[28]**. Conversely, nickel catalysts predominantly yield methane as the primary product **[29]**. Notably, recent research by Yu *et. al.* has demonstrated that NiCo nanoparticles (NPs) produce mixtures of alkanes with a significant methane component **[30]**. These findings underscore the shift of interest from single-metal to bimetallic NPs, highlighting the remarkable potential of NiCo NPs for selectively reducing CO_2. Additionally, CO_2, beyond its significance as a C1-feedstock, serves the purpose of preventing the undesired leaching of nickel species in the form of $Ni(CO)_4$**[31]**.

However, it is essential to recognize that bimetallic NPs, unlike single-component NPs, are susceptible to structural alterations when exposed to reactive environments, such as H_2, O_2, CO, H_2O, or CO_2. For example, in a prior study, it has been demonstrated that core–shell CuCo NPs undergo partial dealloying when subjected to CO and H_2, even at low-pressure conditions **[32]**.

In the current investigations, a novel synthesis approach is introduced for core–shell Ni@Co bimetallic NPs within a catalytic system. These NPs are of particular interest due to their intriguing catalytic activity in producing CO and formic acid. The electronic changes and segregation phenomena within the core-shell nanoparticle are closely examined using NAPPES. Subsequent activation cycles involving oxidation and reduction steps are implemented to eliminate surface contamination. Additionally, the NAPPES chamber is exposed to a mixture of CO_2 and H_2, with the temperature gradually increasing. The formation of products is closely monitored using a residual gas analyzer (RGA) connect to the chamber, operating within a low-pressure regime.

5.6 Result and discussion

5.6.1 Characterization of the catalyst

Synthesis details of Ni@Co core shell nanomaterial is given in sec. 2.3. The XRD analysis of the synthesized Ni@Co (2:1) core-shell catalyst is shown in Fig. 5.18. The XRD pattern of the as prepared catalyst exhibits characteristic features at $2\theta = 44.5°$, 51.84°, 76.37° respectively (JCPDS No. 04–0850), which could be assigned to (111), (200), (220) of face centered cubic (fcc) Ni. No signal for Nickel hydroxide or NiOx were observed. The XRD pattern of Co also had three peaks at 44.3°, 51.57°, and 75.89 ° corresponding to (111), (200) and (220) facets of fcc of cobalt. The XRD pattern of Ni also had three peaks at 44.47°, 51.85°, and 76.34 ° corresponding to (111), (200) or (220) of fcc of Ni. The NiCo XRD peak occurred at 44.5°, 51.84°, 76.37°, similar to those of fcc Ni **[33]**. Nonetheless, the broadened (200) and (220) features suggest the possibility of some form of NiCo bimetal/alloy formation.

5.6.2 Transmission Electron Microscopy Analysis

The results of the TEM analysis of Ni@Co nanoparticles with a 2:1 Ni/Co ratio is presented in Fig. 5.19. The synthesized Ni@Co core-shell nanoparticles were dispersed in isopropanol through sonication and then drop-cast onto a copper grid to facilitate HR-TEM analysis. The

freshly prepared sample was examined using HR-TEM to determine particle size and shape, as shown in Fig. 5.19a-c. Elemental mapping results are also depicted in Fig. 5.19d-e. The ligand-

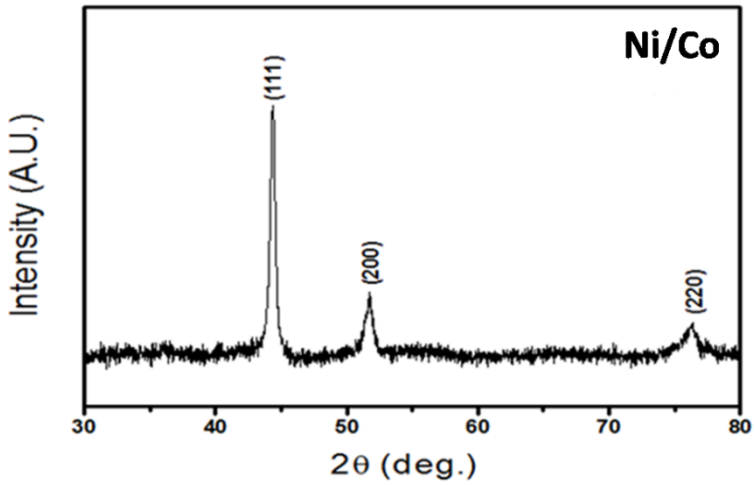

Figure 5.18. X-ray diffraction (XRD) pattern of the Ni@Cocore-shellNPscatalyst

free synthesis process yields an elongated network-like nanostructure, as evident from the TEM image provided in Fig. 5.19. This structure displayed a chain-like appearance with continuous multi-stranded branches. TEM analysis results indicated that the NiCo nanoparticles with a 2:1 Ni:Co ratio exhibited a core-shell morphology with a uniform Co-thin layer on the Ni-core. The width of this nanochain structure, as measured in Fig 5.19a, fell within the range of 100-150 nm, with an average size of 120±10 nm. This finding supports that the formation of nanochains commenced after the individual core-shell nanoparticles were initially formed up to a certain threshold particle size. This indicates that there is scope to minimize the chain growth by optimizing the synthesis conditions, especially at the early stage of particle growth. A systematic time-dependent synthesis is expected to give the details of optimized particle size and without or minimum chain growth. The ferromagnetic properties of Ni and Co guided the nanoparticles to assemble in a chain-like fashion. The HR-TEM image from one of the strands within the nanochain is displayed in Fig 5.19, and elemental mapping in Fig 5.19d-f highlights the inner core (yellow) and outer shell (red) regions distinctly, confirming the core-shell morphology within the nanochains. In Fig 5.19d, Co is represented in red, while Fig 5.19e represents Ni in yellow. An overlapping image of both elements, as determined by EDX analysis in Fig 5.19f, illustrates the elemental distribution. The elemental mapping indicates the presence of hollow or vacant spaces in Fig 5.19d, where Ni exhibits contrast over the entire

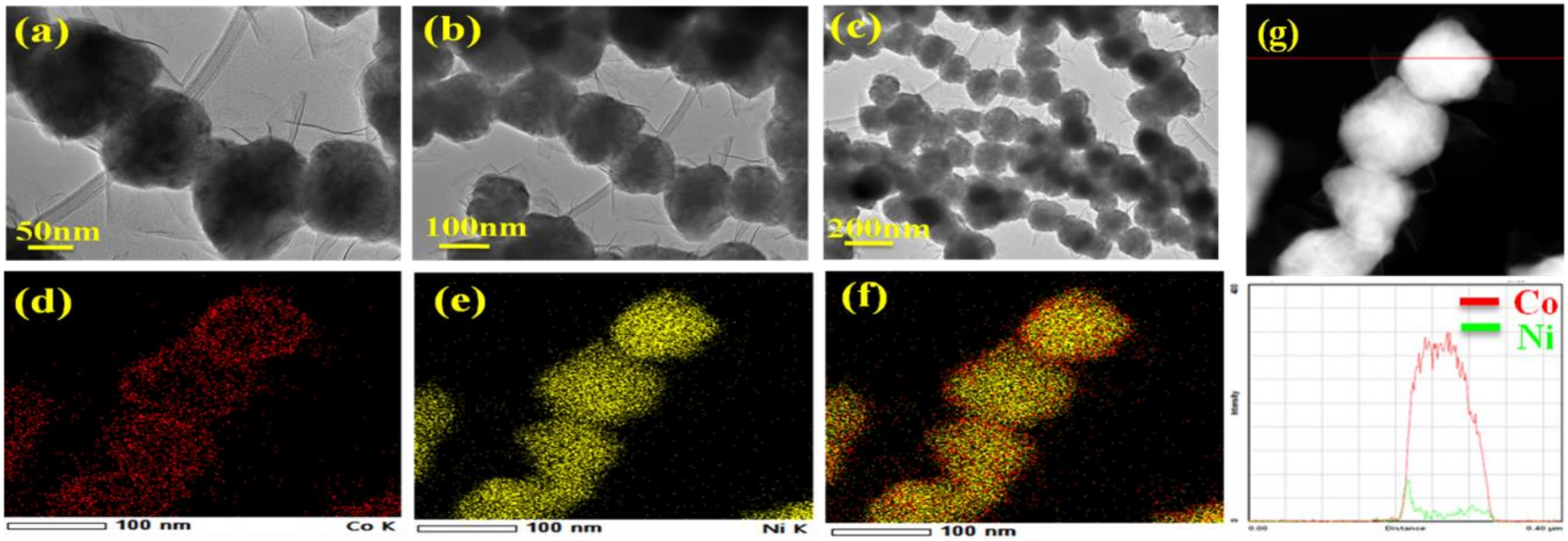

Figure5.19. TEM analysis performed on the fresh or as prepared sample. Panel (a), (b) and (c) show the TEM image at 50, 100 and 200 nm scale. Panel (d), (e), and (f) shows the elemental mapping of Co, Ni and NiCo. Panel (g) shows EDX line profile mapping over the single particle of Ni@Co NP. Panel d-e displays the core-shell morphology with thick Ni-core and possibly somewhat porous Co shell on the surface. This is likely to help the diffusion of Ni onto the surface.

.

area, panel d-e displays the core-shell morphology with thick Ni-core and possibly somewhat porous Co shell on the surface. This is believed to aid Ni diffusion onto the surface. Furthermore, EDX line scanning was performed across the diameter of a single nanoparticle, as shown in Fig 5.19g. which presents the line scanning profile, revealing that Co dominates the surface, with the highest intensity represented in red, while Ni is relatively less abundant compared to Co, indicated by the green line. This observation confirms the core-shell behavior of the Ni@Co bimetal with a 2:1 Ni/Co ratio.

5.6.3 In-situ catalytic activity measurement in NAPPES

To investigate the reactants consumption and products evolution during the *in-situ* experiment, RGA within the NAPPES unit was employed to record the mass spectra. The CO_2 reduction reaction was carried out with a reactant stoichiometry of CO_2:H_2 = 1:3 and the reaction took place throughout a temperature range from 325 to 825 K at a total partial pressure of 0.1 mbar. The reactions were conducted utilizing pristine Ni@Co core-shell nanoparticles, *in-situ* reduced Ni@Co core-shell catalyst (prepared via the oxidation of Ni@Co at 500 K in the presence of oxygen to remove surface pollutants, followed by an *in-situ* H_2 reduction treatmentat 625 K for 2 hours), and Ni@Co bimetal oxides (prepared through oxidation-reduction-oxidation (ORO condition) in the presence of oxygen of Ni@Co at 500 K for 2 hours, reduction at 625 K for 2h and further oxidation at 500 K for 2h under dynamic dosing conditions at a total pressure of 0.1 mbar within the temperature range of 375 to 825 K. For brevity and convenience, we shall henceforth refer to these two surfaces as Ni@Coalloy and Ni@Co bimetal oxides, respectively. The RGA findings are displayed in Fig 5.20. A slight oscillation in all mass species was detected as a result of periodic opening a leak valve to keep total pressure at 0.1 mbar, with the overall pressure being kept within 10% of the target value. The QMS was stationed in the preparation chamber, while the reaction occurred in the primary chamber. The output from the turbo molecular pump attached to the first differential pumping stage, operating in the electrostatic lens regime, was directed to the QMS through a leak valve, potentially leading to diffusion of reactants and products. In light of these experimental complexities, especially the different diffusion rates of gas-phase components, any changes observed in the QMS data should be regarded as qualitative. Despite the challenges associated with detecting CO (which is also a fragment of CO_2 in the QMS) in the presence of CO_2, a substantial shift in spectral data was noted due to the dissociation of CO_2 on the catalyst surface.

The evolution of important mass species as a function of reaction temperature during CO_2 reduction is depicted in Fig 5.20. Figure 5.20a

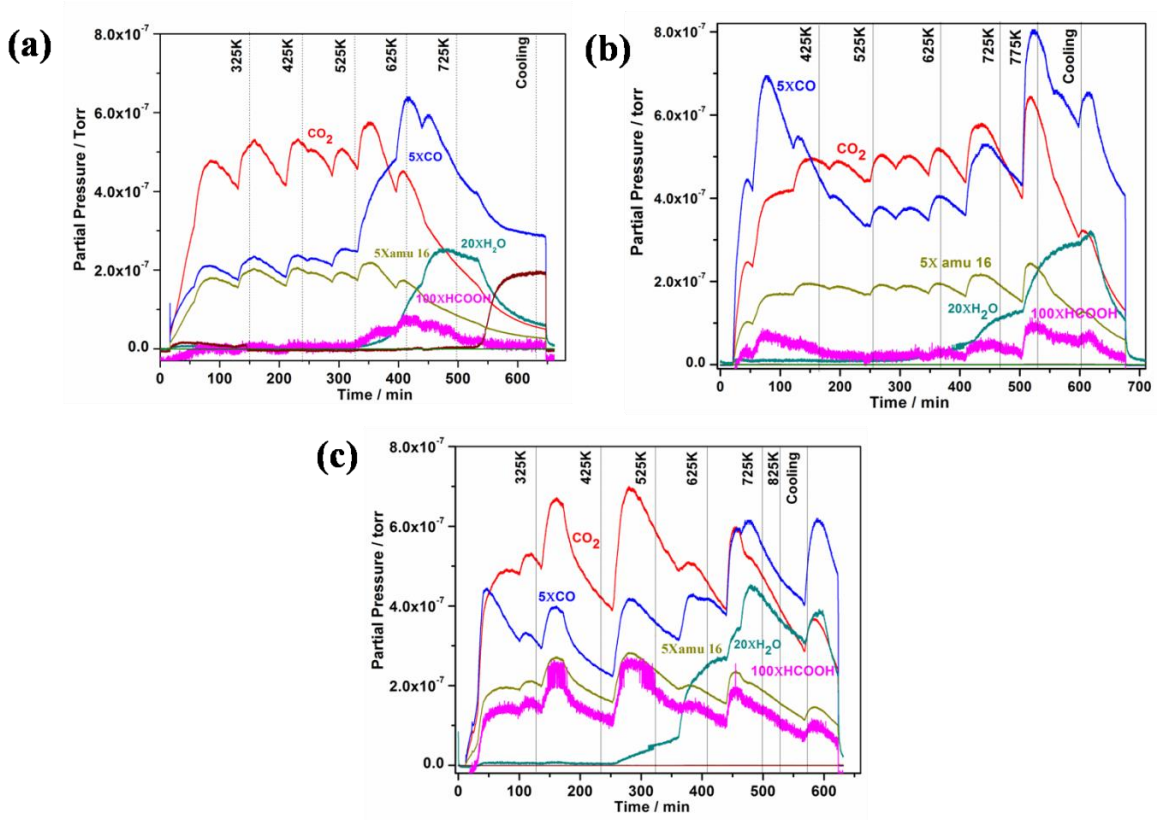

Figure 5.20 The mass spectral analysis of the CO_2 reduction reaction is shown, which was conducted under controlled conditions at 0.1 mbar pressure, using a 1:3 ratio of CO_2 to H_2 over a temperature range spanning from 325 to 825 K. The analysis was carried out employing (a) Ni@Co NPs in their as-prepared state, (b) Ni@Co NPs after reduction, and (c) Ni@Co NPs post-oxidation. In this depiction, the partial pressures of various gases, including CO, H_2O, amu16 (confirmed to be atomic oxygen fraction, rather than methane), CO_2, and HCOOH, are visually represented by distinct colors, namely blue, cyan, yellow, red, and magenta, respectively. For the sake of clarity and improved visualization, the partial pressures of CO, amu 16 , H_2O, and HCOOH have been multiplied by specific factors—5, 5, 20, and 100, respectively. It is noteworthy that the total pressure within the experimental system was meticulously maintained at a constant value of 0.1 mbar throughout the analysis.

depicts adistinct evolution pattern compared to the reactants, confirming the formation of CO and H_2O at temperatures of 625 K and above, as a result of CO_2 activation on the as-prepared NiCo bimetallic core-shell catalyst. The same evolution pattern was observed for CO_2 and mass unit 16, suggesting that the latter originates from the atomic oxygen fragment produced by CO_2 dissociation, rather than methane formation on any catalyst; results recorded at mass unit 15 (not shown) exhibited no variation, corroborating the aforementioned point.The same reaction

was conducted on the *in-situ* prepared reduced and oxidized Ni@Co catalysts via an oxidation-reduction and oxidation process, as depicted in Figs 5.20b and 5.20c, respectively. The results in Fig 5.20b indicate that the reduced Ni@Co catalyst activates CO_2 at temperatures around 725 K, while the oxidized Ni@Co catalyst activates CO_2 at 525 K (Fig 5.20c). This observation suggests that the reduced Ni@Co catalyst is incapable of activating CO_2 below 725 K, and thus, it is improbable that this phase is active under the current experimental conditions. It should be noted that Ni@Co is expected to undergo oxidation upon interaction with CO_2, leading to a change in surface properties. Consequently, the findings obtained from the mass spectra (Fig. 5.20) should be regarded as qualitative. The mass spectra reveal the formation of CO and H_2O at temperatures ≥ 725 K (Fig 5.20b). This observation signifies that the reduced Ni@Co catalyst activates CO_2 at a relatively higher temperature than the as-prepared catalyst (Fig 5.20a) and theNi@Co bimetal oxides catalyst. Along with the CO we have also observe the formation of HCOOH through QMS in all the condition. Due to relatively low partial pressure compare, we have multiplied with 100 to show the formation of HCOOH. It is also to be noted that the formic acid formation was observed from the beginning of the experiment at 325 K and above on oxidized Ni@Co, underscoring the conversion of CO_2 directly to formic acid. Nonetheless CO_2 activation to CO occurs at 625 K, which is supported from the concurrent observation of CO and water formation. Assuming the diffusion rate/coefficient of all components are similar under all three experimental conditions shown in Fig. 5.20, it may be indicated that oxide surfaces promotes formic acid formation at low temperatures. However, this needs to be verified by performing in a typical catalytic reactor at atmospheric pressure conditions, which is worth exploring.

5.6.4 In situ NAP-XPS study under reaction condition

In order to analyse the evolution of surface electronic structure and the oxidation state of Co and Ni, Ni@Co nanoparticle was drop-casted as a thin film on a gold foil. This thin film was employed and a set of NAPPES experiments were conducted at a pressure of 0.1 mbar with CO_2:H_2 = 1:3 in the temperature range 325 and 725 K. Despite the use of high pressure (0.1 mbar in NAPPES), the results obtained from the NAPPES measurements provided relevant information about surface changes and their correlation to the active state under reaction conditions. Although kinetic changes occur more rapidly at higher pressures, such as 1 mbar, the surface chemistry changes remained the same and were observed in the present measurements.The NAP-XPS and NAP-UPS measurements were carried out in a systematic

manner under the identical reaction circumstances, and the findings are shown in **Figs. 5.21**, **5.22**, and **5.23**. Ni@Co thin film was exposed to the mixture of CO_2+H_2 under systematic heating; simultaneously Co and Ni core level XPS was recorded and the results are shown in **Fig. 5.21**. The Ni and Co 2p spectra were collected using a twin anode photon source energy = 1486.6 eV, anode X-ray source (Al k). The bottom-most spectra in Fig. 5.21 correspond to the spectrum recorded for the Ni@CoNPs under UHV conditions recorded at 298 K. Cobalt could be observed in an oxidized form along with small amount of metallic Co around 777.5 eV; CoOx observed with at a BE of 780.1 eV with decent satellite intensity is mostly attributed to Co^{2+} oxidation state;**[34]** while there was no meaningful Ni 2p spectrum could be observed, except for some broad Ni 2p signal at noise level. It is well known that the XPS probing depth is up to 10 nm, and no meaningful Ni 2p feature was observed indicates that the Ni- content in the top-10 nm is very low and negligible. Initially the signal-to-noise (S/N)

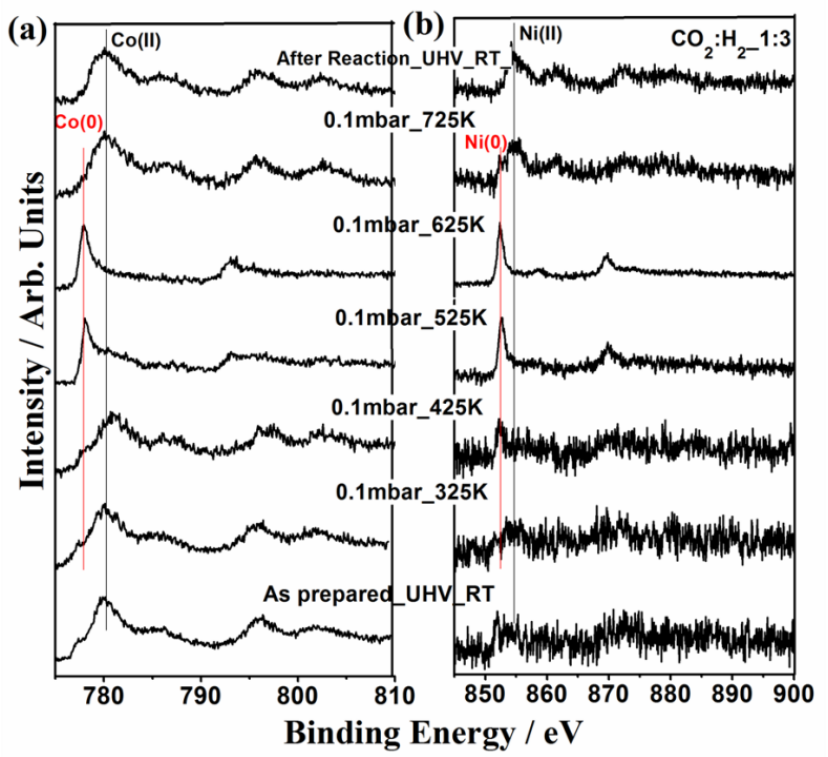

Figure 5.21XPS spectra that were acquired under a partial pressure of 0.1 mbar, with CO_2 to H_2 ratio of 1:3, while progressively elevating the reaction temperature from 325 to 725 K. These spectra were obtained using the as-prepared Ni@Co NPs catalyst. Panel (a) of the figure presents the Co 2p XPS spectra, while panel (b) illustrates the Ni 2p XPS spectra.

ratio was fairly low due to the presence of oxide and possibly carbon contamination on the surface of the NPs. Up on heating to high temperatures under reaction atmosphere (H_2+ CO_2, at 0.1 mbar total reactants pressure), many significant to drastic changes were observed. Up to

425 K marginal changes were observed in Co 2p spectra with features from metal and oxides of Co (Fig 5.21a) and they are comparable to UHV spectrum. This suggests that the surface remained relatively unaffected and appeared to be comparable to that of the surface at 298 K conditions. However, the transition from CoOx to predominant Co metal transition was observed at 525 K with some amount of CoOx; almost a complete transition to Co-metal was observed with negligible CoOx on the surface. This suggests that under the experimental conditions, Ni@Co gets reduced in the presence of CO_2 and H_2 and remain in the metallic state till 625 K. Nonetheless, at 725 K, CoOx reappears fully at the cost of Co-metal; high satellite intensity indicating the nature of oxide to be CoO.

Surface electronic structure evolution of Ni 2p is shown in Fig 5.21b, which is recorded under the similar conditions, as that of Co 2p spectra. Up to 425 K, the marginal intensity of Ni spectrum was observed, which is similar to that of observed at 298 K and UHV conditions. However, characteristic metallic Ni peak at 852.6 eV, but with low intensity, was observed at 425 K. As the temperature rises to 525 and 625 K, a large change in S/N ratio was observed alongwith the emergence of narrow metallic Ni 2p feature. With no Ni feature on the surface at low temperatures to characteristic Ni-metal feature observed between 425-625 K underscores the segregation of Ni on the surface of the Ni@Co; even though Ni is in the core, emergence of Ni as well as Co-metals, between 525 and 625 K, hints the competition among the Ni and Co is very high to be on the surface. It is very likely that the porous Co-shell also helps for the diffusion/segregation of Ni from the core. It is to be noted that large Co-intensity with hardly any Ni could be seen in the line profile analysis of EDX result (Fig. 5.19g). All these observations also indicate the reaction environment induced changes in the surface composition and electronic state occurs with Ni@Co. RGA spectra, shown in Fig. 5.20a, indicate that the CO_2 activation started at 625 K, where both the metals arein metallic state. At 725 K, Ni metal converts to NiOx, and it is likely to form NiCo bimetal oxide, which is confirmed from the observation of satellite peak of Ni and Co. It is also to be noted that the S/N ratio decreased significantly on oxidation of Ni to NiOx at 725 K, underscoring the decrease in the Ni-content on the surface. upon cooling to 298 K under reaction environment conditions, oxide features of both metals are retained. Although the XPS studies revealed the structural changes along with Ni segregation on the surface of the NPs, more detailed studies are carried out to understand the nature of pre-treated Ni@Co material.

To understand the segregation behaviour of Ni from Ni@Co core-shell nanoparticle, the catalyst was pre-treated in the presence of O_2 at 500 K for 2 h. This treatment is mainly to

remove the impurities due to contact with air components, present on the surface like H_2O, CO_2, as well as to understand the interaction of Ni@Co with oxygen. After the pre-treatment, Co 2p and Ni 2p spectra were recorded and the results are shown in Fig 5.22. Surprisingly, there were no notable changes noticed with O_2 pre-treated Ni@Co catalyst, compared to the as-prepared catalyst. Unlike the changes observed in Fig. 5.21 under heating in reaction environment (CO_2:H_2 = 1:3 at 425 and 525 K), no changes observed hints the nature of interaction is different. Only CoOx was observed without any trace of Ni features. Subsequently, the O_2 pre-treated catalyst was reduced at 625 K in presence of H_2 for 2h. The reductive environment is known to reduce the oxide to metal and possibly with segregation of core metal. As see in Fig 5.22a and Fig 5.22b Co 2p and Ni 2p XPS spectra shows narrow metallic features at 778.1 and 852.6 eV, respectively, (and without any satellite feature, typical for oxidized species) after reduction at 625 K (3rd spectra from bottom; spectra recorded at 298 K). Metallic Ni present on the surface again reiterates the diffusion/segregation from the inner core to the surface, through the porous Co-shell layer. The NAP-XPS measurementswere carried out on the reduced surface of Ni@Coat 0.1 mbar total pressure of reactants (CO_2:H_2 = 1:3) and within the temperature range of 325 and 725 K. Interestingly, Ni retains its metallic nature under CO_2+H_2 exposure conditionsup to 625 K, predominant metallic Co with increasing CoOx was observed with increasing temperature. This underscores the tolerance of metallic Ni and the vulnerability of Co to oxidation under the reaction environment up to 625 K. On increasing the temperature to 725 K, only CoOx was observed, while a mixture of metallic Ni with NiOx was observed. It is also to be noted the poor S/N for Ni, compared to Co, underscoring the surface enrichment with Co-species. Nonetheless, reduction enhances the segregation of Ni towards surface layers and indicating the formation of NiCo bimetal/alloy system on the surface under reaction conditions. Sophie *et. al.* has shown a similar kind of oxidation and reduction study of the NiCo nanoparticle, where similar segregation behaviour was studied by cycles of oxidation and reduction by using APXPS and TEM measurements.**[35]** Ni and Co 2p region (Fig 5.22) shows the changes in oxidation states of both metals during CO_2 activation over surface. This also indicates the formation of NiCo bimetal oxide formation above 625 K; availability of both oxide components in close proximity could be a reason for efficient RWGS. RGA spectra (Fig 5.20b) correspond to this experiment shows the formation of CO and H_2O at and above 625 K, which is 100 degree higher than the as prepared catalyst used in previous experiment (Fig.5.21). It is very likely that the initial CO_2 activation on metallic components leads to its oxidation to CoOx and NiOx, while CO and H_2O

evolution occurs. It is to be emphasized the necessity of oxides of Ni and Co for CO_2 activation rather than metallic phase. It is also well-known that both Ni and Co are highly pyrophoric and interacts with oxygen atoms, splintered from CO_2. In case of as prepared catalyst the oxide phase of the Ni@Co core-shell NPs observed in XRD, and this activate the CO_2 comparatively lower temperature than reduce catalyst.

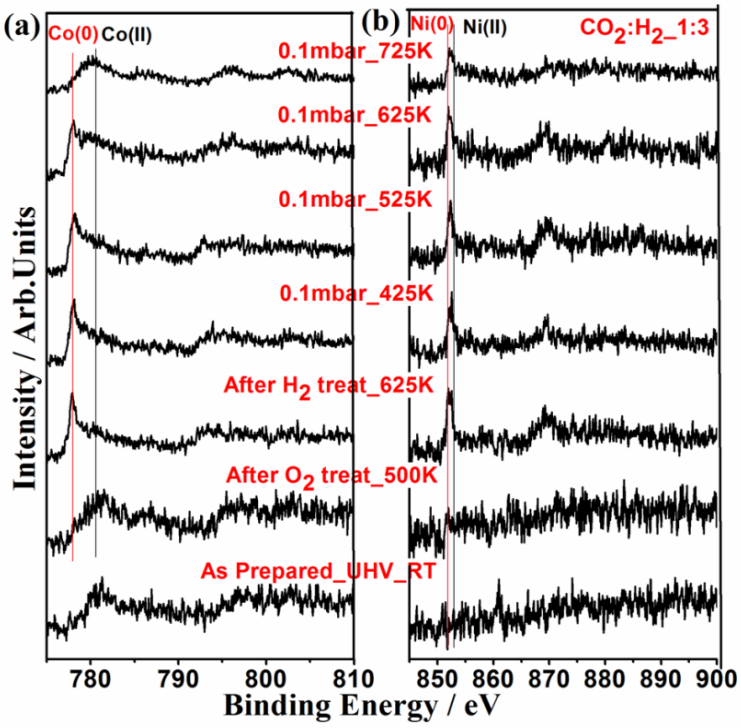

Figure 5.22 XPS spectra that were acquired under a partial pressure of 0.1 mbar, with a CO_2 to H_2 ratio of 1:3, while progressively elevating the reaction temperature from 325 K to 725 K. These spectra were obtained using the oxidation-reduction pre-treated Ni@Co NPs catalyst. Panel (a) of the figure presents the Co 2p XPS spectra, while panel (b) illustrates the Ni 2p XPS spectra. spectra labelled as after O_2 treatment at 500 K and after H_2 treatment at 625 K spectra were recorded at 298 K.

Fig 5.23 shows Co and Ni 2p XPS spectra obtained after cycles of oxidation (500 K for 2h) – reduction (625 K for 2h)-oxidation (500 K for 2 h) (ORO pre-treatment) after first oxidation followed by reduction, the Ni-metal get segregated from the core to surface; this surface is further oxidized at 500 K for 2 h. The bottom spectrum in both panels of Fig. 5.23 shows the XPS spectra of as prepared catalyst. The second set of XPS spectra recorded after the second oxidation cycle resulted in the formation of nearly complete Ni@Co oxides, and both metals, particularly Ni, showsan increase in the XPS peak intensity. ORO pre-treatment cycle transformed the Ni@Co catalyst from inhomogeneous to homogeneous metal-dispersion; critically, the ORO treatment resulted in the migration of nickel from the core to the shell and

it is consistent with the XPS observation. XPS spectra show good intensity of Ni 2p along with a mix of Co^{2+} and Co^{3+}oxidation states observed in Co 2p XPS. When NAPPES measurements were made in the presence of CO_2:H_2 (1:3) between 325 and 525 K, Co and Ni 2p core levels appeared very similar, with no significant changes in either set of spectra. Un-affected. At 625 K, the surface of Ni@Co gets partially reducedto Ni metal along with NiOx; on further increase in temperature to 725 K, NiOx content increase at the expense of metallic Ni. However, under the same conditions between 625 and 725 K, the Co 2p shows an

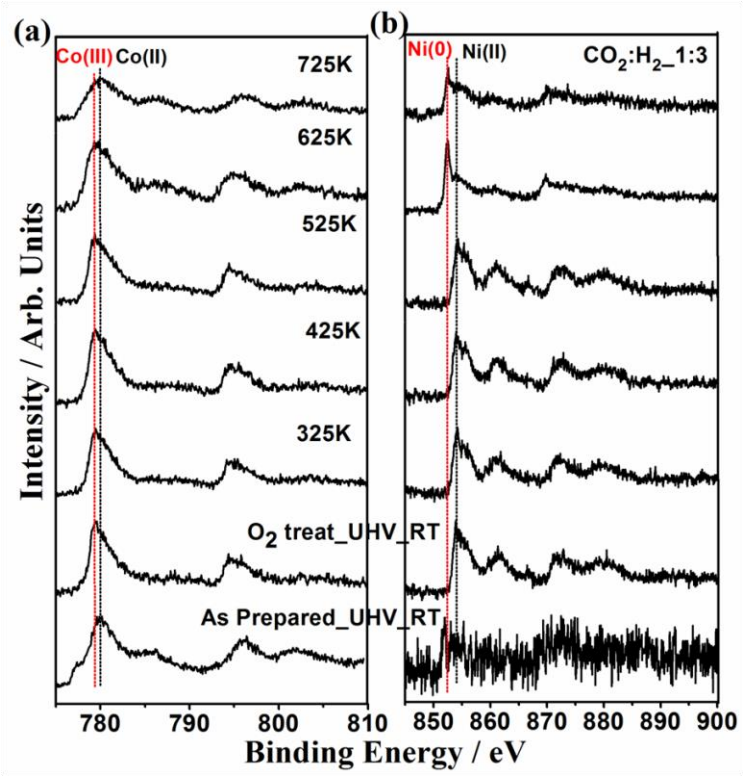

Figure 5.23 XPS spectra that were acquired at a partial pressure of 0.1 mbar, with CO_2:H_2= 1:3, while progressively elevating the reaction temperature from 325 to 725 K. These spectra were obtained using the repeated oxidation-reduction-oxidation (ORO) pre-treated Ni@Co NPs catalyst. Panel a and b presents the Co 2p and Ni 2p XPS spectra.

increase in the satellite intensity and underscoring the formation of CoO, which is likely due to the partial reduction of Co^{3+} to Co^{2+}. It is likely that the H_2 from the reactant mixture is playing a role in the reduction of Ni@Co oxide to partially reduced Ni@Co. It is worth noting that effective CO_2 reduction starts above 525 K, almost 100 K less than the reaction initiation on as prepared Ni@Co (Fig. 5.21) and 200 K lower than the reaction performedonreducedNi@Co catalyst, employed in Fig. 5.22. Irrespective of any pre-treatment or on fresh catalyst, metallic Ni also appears at 625 K under reaction conditions, highlighting

a strong influence of reaction conditions on Ni-segregation and porous Co-shell helps for Ni-diffusion.

5.6.5 In situ NAP-UPS study under reaction condition

The electronic state of catalyst, particularly the VB features, under reaction conditions with CO_2:H_2 = 1:3 between 325 and 725 K at a total pressure of 0.1 mbar, was explored using NAP-UPS analysis. Fig. 5.24 shows the NAP-UPS spectral data recorded on as prepared Ni@Co NPs as well under *in-situ* reaction conditions. The bottom-most UPS was recorded at 298 K under UHV conditionwith freshly prepared Ni@Co catalyst. Under the NAP-UPS measurement conditions, the main VB features of Ni@Co NPs remains observed to be similar up to 425 K, except for some broadening of the VB feature at 6 eV. However, a change in ϕ is evident from the shift in the photoelectron emission offset from around 13.5 eV (for fresh Ni@Co) to 14.5 eV (at 325 K under *in-situ* conditions, pink trace). It is to be remembered that NAPUPS explores a maximum of 2 nm depth, and indicates the onset of interaction between the catalyst and the reactants, the offset moves further to 1.5 eV at 425 K. Many changes observed when temperature raised to 525 K in the VB spectrum. The presence of a sharp E_F signature is indicative of metallic character. Similar type of characteristics has been observed over reduced Co_3O_4 NC. **[36]** Along with E_F, another feature observed at ~1.4eV corresponds to the oxide feature of metals, possibly CoO and/or NiO, and this feature grows in intensity at the cost of E_F feature at high temperatures. Both features of VB merges into one broad feature along with broadening to low BE. The gas-phase vibrational characteristics of CO_2 is attributed to a sharp feature found between 9 and 10 eV.; broadening of this feature can be attributed to the surface's heterogeneous nature, which results from the presence of both metallic and oxide features in Ni@Co. Indeed gas-phase CO_2 senses and broadened; whilesimple CO_2 alone shows a sharp feature, broadening is attributed to the presence of different species on the surface. On further increase in the temperature to 625 K, catalyst nature transformed from metallic to the oxide phase, and fully supported by the disappearance of E_F feature. In addition, broadened VB feature at 525 K become narrow at 625 K and indicating the emergence of CoOx phase, while metallic Ni is retained but with low intensity. This is fully supported by the XPS results. These observations indicate the relatively active nature of the Ni@Co oxide to CO_2 activation, compared to Ni@Co catalyst, at least under the present experimental conditions. When the temperature is increased to 725 K, two unique VB characteristics are noticed CoOx (5 eV) and mixed CoNiOx (7.5 eV). A significant change in photoemission offset indicates the

complete oxidation of surface layers and the effective onset of CO_2 activation reaction. Very interesting changes observed from 298 to 725 K under *in-situ* reaction conditions highlights the efficacy of NAP-UPS to observe the electronic, chemical and hybridization changes and it provides plenty of information about the state of catalyst.

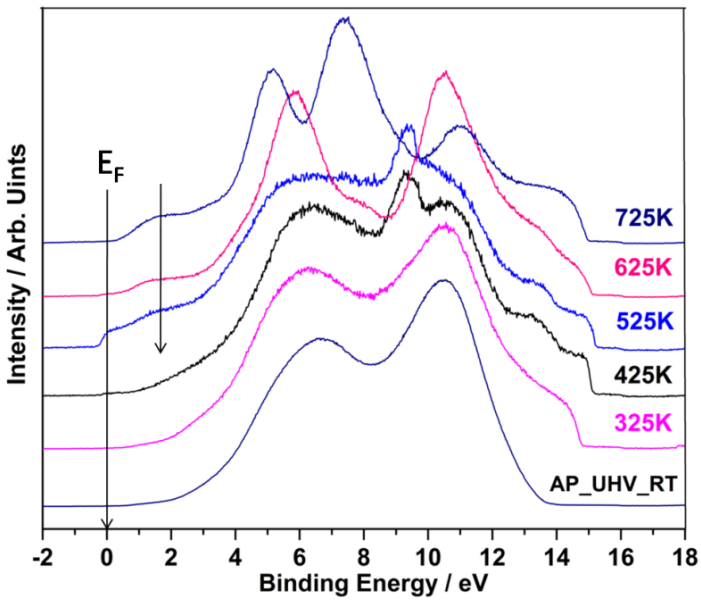

Figure 5.24 Ultraviolet photoelectron VB spectra recorded under measurement conditions of 1:3 CO_2/H_2 ratio at 0.1 mbar between 325 and 725 K. NAP-UPS VB features recorded with using the as-prepared Ni@Co NPs catalyst.

5.7 Conclusion

The unique combination of NAP-XPS, NAP-UPS, and RGA (for products identification) facilitates the comprehensive delineation of the behavioural characteristics exhibited by Ni@Co core-shell nanoparticles (NPs) when exposed to a CO_2:H_2 gas ratio of 1:3, both during oxidation and reduction cycles. Present findings furnish an exhaustive portrayal of the Ni@Co core-shell configuration in the as-synthesized NPs, wherein a crystalline metallic core, rich in Ni, occupies approximately two-thirds of the core, while a shell predominantly comprised of CoOx surrounds it. Subjecting the Ni@CoNPs to oxidation and reduction treatments demonstrate the eliminationof contaminants followed by reduction to the metallic state, yielding profound alterations in structure and surface composition. During the reduction process, a unique mixed alloy of Ni@Co is formed, with Ni segregating from the core to the shell, and achieving homogeneity at 625 K under a CO_2+H_2 atmosphere, and the segregation pattern was further corroborated by both XPS and UPS spectra. It is very likely that between 525 and 625 K, thermal diffusion of hydrogen promotes considerable mass transport, leading

to Ni-segregation towards the surface under CO_2:H_2 =1:3 conditions leading to mixed NiCo in the form of bimetal or alloy. The core-shell morphology with thick Ni-core and porous Co shell on the surface helpsfor the diffusion of Ni onto the surface.

Remarkably, the Co-rich shell and Ni-rich metallic core of the NPs remain largely unaffected by the oxidation process, as evidenced by their chemical and structural stability. The NPs surface exhibits mechanical robustness, possibly attributed to volume expansion during oxidation. Partial bimetal/alloy formation of the surface layer is likely to be an irreversible phenomenon; however more experiments are needed to confirm this aspect. NAP-XPS and NAP-UPS analyses confirm that the Ni@Co NPs are in an active state as bimetallic oxide phases during CO_2 hydrogenation, especially at and above 625 K, which is active for CO_2 reduction to CO. Generation of CO and HCOOH was observed through RGA at mbar pressure levels, which suggest further exploration through fixed-bed reactor experiments to optimize reaction conditions and comprehend product formation.

Our study underscores the substantial structural modifications that emergeswhen the NPs undergo activation treatments, especially under mixed CO_2 and H_2 reactants. This underscores that the final structure of the operational catalyst can diverge significantly from its initial state, thus necessitating further exploration through techniques such as environmental transmission electron microscopy (TEM) and operando techniques.

The conclusions drawn in the current study pertain specifically to the Ni@Co system, which has been relatively underexplored despite its relevance in various technological applications, benefiting from the abundance and affordability of both metals. Moreover, this work bears relevance in fields beyond catalysis, extending to metallurgy, magnetism, and others, whereasnanoparticle stability in operational conditions is crucial for technological viability and long-term durability.

5.8 References

1. Mardani, A.; Štreimikien˙ E, D.; Cavallaro, F.; Loganathan, N.; Khoshnoudi, M. *Sci. Total. Environ.***2019,***649,* 31–49.
2. Gielen, D.; Boshell, F.; Saygin, D.; Bazilian, M. D.; Wagner, N.; Gorini, R. *Energy Strategy Rev.***2019,***24,* 38–50.
3. Mauna Loa Observatory, Hawaii. http://co2now.org , **2014.**
4. Tollefson, J. *Nature***2009,***462,* 966–967.
5. Dzubak, A. L.; Li-chiang, Lin; Jiham. Kim.; Joseph A. Swisher; Roberta. Poloni; Sergey, N. Maximoff.; Smith, B.; Gagliardi, L. *Nat. Chem.***2012,***4,* 810–816.

6. Lin, L.-C.; Li-Chiang Lin; Adam H. Berger; Richard L. Martin; Jihan Kim; Joseph A. Swisher; Kuldeep Jariwala; Chris H. Rycroft; Abhoyjit S. Bhown; Michael W. Deem; Maciej Haranczyk; Berend Smit. *Nat. Mater.***2012,***11,* 633–641.
7. Yufan Sun; Hanjun Hu; Yutian Wang; Jia Gao; Yang Tang; Pingyu Wan; Qing Hu; Jianjun Lv; Tianshu Zhang; Xiao Jin Yang. *Chem. Eng. Technol.***2019,***42,* 1223–1231.
8. Salgaonkar, K. N.; Bajpai, H.; Mhamane, N. B.; Nalajala, N.; Chauhan, I.; Thakkar, K.; Joshi, K.; Gopinath, C. S. *J. Mater. Chem. A***2023,***11,* 15168.
9. Wang, W.; Wang, S.; Ma, X.; Gong, J. *Chem. Soc. Rev.***2011,***40,* 3703–3727.
10. Ohya, H.; Fun, J.; Kawamura, H.; Itoh, K.; Ohashi, H.; Aihara, M.; Tanisho, S.; Negishi, Y. *J. Membr. Sci.***1997,***131,* 237–247.
11. Yan, Y.; Dai, Y. H.; He, H.; Yu, Y. B.; Yang, Y. H. *Appl. Catal. B Environ.***2016,***196,* 108–116.
12. Szanyi, J.; Goodman, D. W. *Catal. Lett.***1991,***10,* 383–390.
13. Zhao, H.; Yu, R.; Ma, S.; Xu, K.; Chen, Y.; Jiang, K.; Fang, Y.; Zhu, C.; Liu, X.; Tang, Y. *Nat. Catal.***2022,***5,* 818–831.
14. Li, C-F.; Guo, R-T.; Zhang, Z-R.; Wu, T.; Pan, W-G. *Small***2023,***19,* 2207875.
15. Spennati, E.; Riani, P.; Garbarino, G. *Catal. Today***2023,***418,* 114131.
16. Chen, M.; Li, B.; Wang, F.; Fang, J.; Li, K.; Zhang, C. **2023,***6,* 5826–5834.
17. Rommens, K.T.; Saeys, M. *Chem. Rev.***2023,***123,* 5798–5858.
18. Liu, L.; Corma, A. *Chem. Rev.***2023,***123,* 4855–4933.
19. Hong, X.; Zhu, H.; Du, D.; Zhang, Q.; Li, Y. *Catalysts***2023,***13,* 376.
20. Jain, R.; Gopinath, C. S. *ACS Appl. Mater. Interfaces***2018,***10,* 41268–41278.
21. Tuxen, A.; Carenco, S.; Chintapalli, M.; Chuang, C.-H.; Escudero, C.; Pach, E.; Jiang, P.; Borondics, F.; Beberwyck, B. J.; Alivisatos, A. P.; Thornton, G.; Pong, W.-F.; Guo, J.; Perez, R.; Besenbacher, F.; Salmeron, M. *J. Am. Chem. Soc.***2013,***135,* 2273.
22. Schweicher, J.; Bundhoo, A.; Frennet, A.; Kruse, N.; Daly, H.; Meunier, F. C. *J. Phys. Chem. C***2010,***114,* 2248.
23. Kumar, N.; Smith, M. L.; Spivey, J. J. *Catal.***2012,***289,* 218.
24. Yamauchi, T.; Tsukahara, Y.; Yamada, K.; Sakata, T.; Wada, Y. *Chem. Mater.***2011,***23,* 75−84.
25. Carenco, S.; Tuxen, A.; Chintapalli, M.; Pach, E.; Escudero, C.; Ewers, T. D.; Jiang, P.; Borondics, F.; Thornton, G.; Alivisatos, A. P.; Bluhm, H.; Guo, J. H.; Salmeron, M. *J. Phys. Chem. C***2013,***117,* 6259−6266.
26. Mandal, S.; Krishnan, K. M. *J. Mater. Chem.***2007,***17,* 372−376.
27. Zheng, X.; Liu, S.; Chen, X.; Cheng, J.; Qing, Y.; Pan, Z.; Marcelli, A.; Chu, W.; Wu, Z. *J. Phys.: Conf. Ser.***2013,***430,* 012038.
28. Iablokov, V.; Beaumont, S. K.; Alayoglu, S.; Pushkarev, V. V.; Specht, C.; Gao, J.; Alivisatos, A. P.; Kruse, N.; Somorjai, G. A. *Nano Lett.***2012,***12,* 3091.
29. Sanchez-Escribano, V.; Larrubia Vargas, M. A.; Finocchio, E.; Busca, G. *Appl. Catal. A***2007,***316,* 68.
30. Yu, Y.; Jin, G.; Wang, Y.; Guo, X. *Catal. Commun.***2013,***31,* 5.
31. Mihaylov, M.; Hadjiivanov, K.; Knözinger, H. *Catal. Lett.***2001,***76,* 59.

32. Carenco, S.; Tuxen, A.; Chintapalli, M.; Pach, E.; Escudero, C.; Ewers, T. D.; Jiang, P.; Borondics, F.; Thornton, G.; Alivisatos, A. P.; Bluhm, H.; Guo, J.; Salmeron, M. *J. Phys., Chem. C***2013,***117*, 6259.
33. Wang, H.; Li, X.; Lan, X.; Wan, T. *ACS Catal.***2018,***8*, 2121−2128.
34. Biesinger, M. C.; Payne, B. P.; Grosvenor, A. P.; Lau, L. W. M.; Gerson, A. R.; Smart, R. S. C. *Appl. Surf. Sci.***2011,***257*, 2717–2730.
35. Sophie Carenco, Cheng-Hao Wu, Andrey Shavorskiy, Selim Alayoglu, Gabor A. Somorjai, Hendrik Bluhm, and Miquel Salmeron. *Small***2015,***11*, No. 25, 3045–3053.
36. Ranjan, R.; Tekawadia, J.; Jain, R.; Mhamane, N. B.; Raja, T.; Gopinath, C. S. *Chem. Eng. J.* **2023,***471*, 144459.

Chapter 6

Conclusions

and

Future Prospects

Surface science methodologies enable the monitoring of alterations transpiring on the catalyst surface under catalytic reaction circumstances. This monitoring provides valuable insights into the catalyst's functionality under operational conditions, encompassing surface electronic structural attributes. These insights can subsequently be correlated with the catalytic performance, thereby aiding in the development of more efficient, selective, and environmentally sustainable catalysts. Among the myriad surface science techniques available, NAPPES emerges as a state-of-the-art, surface-sensitive instrument capable of investigating sample surfaces under catalytically pertinent conditions, such as near ambient pressure (NAP) and elevated temperatures. The current thesis has attempted to investigate surfaces at near-ambient pressure levels across a wide range of temperature regimes using the NAPPES technique. This exploration aims to elucidate the "gas-solid" interaction phenomenon, which constitutes a fundamental aspect with profound implications in various research domains, including catalysis, nanomaterials, corrosion, sensors, electrochemistry etc. Our focus has been on elucidating changes in surface ϕand the active state of surfaces under near-ambient conditions. We have diligently examined the utility of this information in unravelling the processes occurring under genuine operational conditions, particularly in terms of the electrical structure of the VB.

The first working chapter (**Chapter 3**) delves into the intricate evolution of the electronic structure of metallic vanadium as it transforms into metallic vanadium oxides. The study systematically traces the progression from a pristine V metal surface to a complex mixture of various oxides, including VO, V_2O_3, VO_2, and V_2O_5. This evolution is achieved using NAPPES methods, which entail controlled oxidation of the V foil under near-ambient pressures (0.1 mbar) and elevated temperatures (up to 875 K). Through a meticulous control of oxidation conditions, the study demonstrates the transition of the vanadium surface to VO and V_2O_3 with increasing O_2pressure and temperature. At higher temperatures (>725 K), a transition from V_2O_3 to VO_2 is observed, accompanied by a Metal-Insulator (MI) transition. Intriguingly, the MI transition, initially observed at high temperatures, persists even at ambient temperatures.while bulk VO_2 is metallic above 340 K, present findings of metallic nature in an ensemble of VOx along with VO_2 at ambient temperatures is interesting, and it certainly deserves further investigationsThe research not only unveils the formation of various stoichiometric forms of VOx but also reveals the infiltration of atomic oxygen into the layers of the V surface. It is noteworthy that metallic vanadium displays robustness, and sub-surface oxidation necessitates elevated temperatures. Above 625 K, under 0.1 mbar partial pressure of

O_2, metallic V oxidises primarily into a blend of oxides having V^{3+}, V^{4+}, and V^{5+} oxidation states. Alterations in the DOS near the E_F become evident above 723 K at 0.1 mbar O_2 partial pressure, indicative of the metallic nature due to VO_2 formation. Despite the presence of other VOx species, the dominance of VO_2 underscores its metallic character. These findings underscore the significance of NAPPES in probing surface-related phenomena and suggest the potential for future investigations into reversible changes in the ϕ of vanadium during oxidation and reduction studies.

Modulating the surface energy, particularly the ϕ of a material, holds considerable significance across a broad spectrum of surface and interface-driven devices and applications. Copper (Cu) and its oxides, renowned for their unique properties; find extensive utility in electronics and catalysis. In **Chapter 4**, we embarked on an exploration of oxidation and reduction reactions involving molecular oxygen (O_2) and hydrogen (H_2) on polycrystalline copper (Cu) metal foil using NAP-UPS. The study involved a meticulous examination of the Cu/Cu_2O and Cu_2O/CuO interfaces, along with the intermediacy of Cu_4O_3, achieved through controlled oxidation and reduction of Cu-polycrystalline foil under near-ambient pressure (0.1 mbar) and temperature conditions (750K). As the temperature is raised, the foil undergoes a systematic oxidation process with the increase in chamber O2 partial pressure from $2x10^{-7}$ mbar to 0.3 mbar. Under low-pressure conditions, Cu oxidation proceeds sequentially, as observed through NAP-UPS ($CuO \rightarrow Cu_4O_3 \rightarrow Cu_2O \rightarrow Cu$). To encourage the generation of intermediates in catalytic reactions, it is possible to restrict the oxygen partial pressure or modify the oxidation temperature. This stands in contrast to Cu oxidation behavior, where Cu_2O serves as a stable intermediate.We also conducted a time-dependent study, revealing that the reduction of CuO is a slow kinetic process, with 550 K identified as the rate-determining zone for the transformation from CuO to Cu_2O. Harsh conditions are subsequently required for the transformation from Cu_2O to metallic Cu, which can be achieved within the temperature range of 700-750 K.Remarkably, the oxidation and reduction behaviors, as well as the thermal stability of surface CuO and Cu_2O, exhibit noteworthy variations compared to those reported for CuO oxide thin films, single crystals, and powder samples. These disparities can be attributed to differences in lattice oxygen mobility, which exhibit substantial variations among distinct materials and even within individual samples. The diffusion of oxygen is discerned through the Cu 3d –O2p interaction in NAP-UPS, and alterations in the ϕ serve as additional indicators of Cu surface oxidation. Indeed, investigating such experimental conditions to assess

the performance of catalysts like Cu or other metal-based catalysts is intriguing. While the operating pressure of NAPPES may be low, it can be adjusted to simulate the experimental conditions. We believe that our research could be extended to encompass these complex reaction conditions.

CO_2 is a greenhouse gas that needs to be transformed into valuable feedstocks such as carbon monoxide, formic acid, and methanol. In the quest for active, selective, and cost-effective catalysts, mono-metallic and bimetallic catalysts based on transition metals, particularly Co and Ni-based catalysts, have garnered special attention due to their high CO_2 conversion rates and product selectivity. **Chapter 5** explains how CO_2 can be reduced using H_2 as a reducing agent via the reverse water gas shift (RWGS) reaction utilising a low-cost spinel Co_3O_4 nano-cube catalyst and a Ni@Co bimetal core-shell catalyst. In **chapter 5a,** a direct correlation is observed between the findings from NAPPES conducted at 0.1 mbar pressure and catalytic experiments performed at 1 bar, substantiated by XRD/TEM characterization. The NAP-XPS and NAP-UPS analyses suggest that a combination of 2+ and 3+ oxidation states of Co activate CO_2 at lower temperatures and exhibits high selectivity for CO production. A CO_2 to H_2 ratio of 1:1 and 3:2 demonstrates optimal and sustainable performance between 623 and 723 K, achieving 100% CO selectivity at 723 K. A dynamic redox interaction between Co^{2+} and Co^{3+} states appear to contribute to the high selectivity for CO. Our findings have implications for achieving a carbon-neutral economy and carbon recycling, and further research in this direction is warranted. Highly selective CO formation, with or without H_2, could find application in the steel industry for steelmaking and emissions reduction. Exploring the structure-dependent activity of Co_3O_4, particularly concerning different crystallographic facets, holds potential for selectively producing one or fewer products.

In **Chapter 5b**, elucidate the behavioral characteristics exhibited by Ni@Co core-shell nanoparticles (NPs) when exposed to a CO_2:H_2 gas ratio of 1:3 as well as during both oxidation and reduction pre-treatment cycles. The nanoparticles possess a Ni-rich core and a Co-rich shell, and their restructuring behavior under oxidation and reduction conditions is investigated. During the reduction process, a distinctive Ni@Co mixed alloy is formed, with a segregation of Ni from the core to the shell, achieving homogeneity at 625 K (under a CO_2+H_2 atmosphere). It is likely that between 525 and 625 K, thermal diffusion of hydrogen promotes significant mass transport, leading to Ni-segregation towards the surface under CO_2:H_2 = 1:3 conditions, resulting in mixed NiCo in the form of a bimetal or alloy. The core-shell morphology,

characterized by a thick Ni-core and porous Co shell on the surface, facilitates the diffusion of Ni onto the surface. Partial bimetal/alloy formation of the surface layer is likely to be an irreversible phenomenon, although further experiments are required to confirm this aspect. NAP-XPS and NAP-UPS analyses confirm that the Ni@Co nanoparticles are in an active state as bimetallic oxide phases during CO_2 hydrogenation, particularly at and above 625 K, making them active for the reduction of CO_2 to CO. The generation of CO and HCOOH is observed through RGA at millibar pressure levels, suggesting the need for further exploration through fixed-bed reactor experiments to optimize reaction conditions and understand product formation.Our study underscores the substantial structural modifications that occur when the nanoparticles undergo activation treatments, especially in the presence of mixed CO_2 and H_2 reactants. This highlights that the final structure of the catalyst in operation can diverge significantly from its initial state, necessitating further investigation using techniques such as environmental transmission electron microscopy (TEM) and operando techniques. The conclusions drawn in this study are specifically applicable to the Ni@Co system, which has been relatively underexplored despite its relevance in various technological applications, benefitting from the abundance and affordability of both metals. Moreover, this work holds relevance beyond catalysis, extending into fields such as metallurgy, magnetism, and others, where operational nanoparticle stability is crucial for technological viability and long-term durability.

The preceding discussion emphasizes that enables the direct investigation of fundamental aspects of heterogeneous catalysis, including phenomena like gas-solid interactions, ϕ variations, and alterations in electronic structure, all under catalysis conditions. This capability has the potential to pinpoint the "true active phase" of a catalyst during its operational state. This holistic approach has injected fresh vitality into the field of catalysis,especially at a time when energy efficiency and green chemistry are societal goals. In this trajectory, further advancements are in progress, promising an intricate understanding of molecular-level mechanisms with details. This newfound insight is anticipated to facilitate the development of superior and more active materials for a multitude of applications. Theexhaustive exploration of demanding reactions, such as water splitting, $N_2/CO_2/CH_4$ activation, becomes a viable prospect within this framework.

ABSTRACT

Name of the Student: Ravi Ranjan **Registration No.:** 10CC17A26022

Faculty of Study: Chemical Science **Year of Submission:** 2023

CSIR Lab: NCL, Pune **Name of the Supervisor:** Dr. C.S. Gopinath

Title of the Thesis: Gas-Soild interactions and its influence in electronic structure evolution and heterogeneous catalysis.

The current thesis has a primary focus on the utilization of Near Ambient Photoelectron Spectroscopy (NAPPES) to elucidate the surface chemistry of underlying chemical conversions, reaction mechanisms, active oxidation states, and the evolution of oxidation states of catalyst under operational conditions. It commences with a broad introduction to catalysis, followed by an in-depth exploration of heterogeneous catalysis from a surface science perspective. The importance of bridging the pressure and material gaps through surface science tools and employing real-world catalysts is also discussed. Detailed information is provided regarding the synthesis and characterization methods employed in this study. Additionally, the technical specifications of the NAPPES system at CSIR NCL and its significant relevance to catalytic systems are thoroughly examined. The study delves into the gas-solid interactions between molecular oxygen and metallic vanadium surfaces, systematically exploring the evolution in the electronic structure of vanadium oxide (VOx) surfaces using NAPPES. Specifically, the chapter investigates the transformation of various vanadium oxides concerning partial oxygen pressure (ranging from UHV to 1 mbar), temperature (from 298 K to 875 K), and exposure time to oxygen (up to 18 hours). VB and core-level spectral measurements are recorded using UV (He-I = 21.2 eV) and Al Kα (1486.6 eV) photons, respectively. In chapter 4, NAP-UPS is employed to investigate modifications in VB, electronic structure, and ϕchanges during the oxidation of Cu to CuO and the subsequent reduction of CuO surfaces to Cu, under both oxidizing (O_2) and reducing (H_2) atmospheres, at pressures around the sub-millibar range and elevated temperatures. Understanding the kinetics and thermodynamic parameters governing the formation of interface and surface species is crucial from a practical standpoint. While the Cu oxidation to cupric oxide (CuO) could be observed easily, the reverse process, i.e., reduction from CuO to Cu metal, could be observed predominantly; however complete reduction requires more harsh conditions. For chapter 5A, Co_3O_4 spinel catalyst was used for CO_2 reduction, showing predominant CO selectivity at temperatures ≥ 673 K under atmospheric pressure. CO_2 conversion initiates at temperatures ≥ 523 K, with 100% CO selectivity achieved at temperatures ≥ 673 K using a CO_2 to H_2 ratio of 3:2. Current work demonstrates sustainable catalytic CO_2 conversion with Co_3O_4nanocube, where an increase in CO selectivity and yield is observed at the expense of methane with reduced H_2 quantities. A CO_2 to H_2 ratio of 1:1 and 3:2 results in 88–100% CO selectivity with 24–32.5% CO_2 conversion between 623 and 823 K. Near ambient pressure photoelectron spectroscopy reveals surface electronic state changes, suggesting that Co_3O_4(200) is the active phase facilitating selective CO_2 reduction to CO. Furthermore, the next work introduces a novel synthesis approach for core-shell Ni@Co bimetallic nanoparticles exhibiting a remarkable catalytic activity in the production of CO and formic acid. Electronic changes and segregation phenomena within the core-shell nanoparticles are extensively examined using NAPPES. Additionally, the NAPPES chamber is exposed to a mixture of CO_2 and H_2, with temperature incrementally rising, and the product formation is closely monitored using a residual gas analyzer (RGA) attached to the chamber, operating under low-pressure conditions.

List of Research Publications

List of Publication(s) in SCI Journal(s) Emanating from the Thesis Work

1.**Ravi Ranjan**, Nitin B. Mhamane, Sadhu K. Kolekar, and Chinnakonda S. Gopinath., Electronic Structure Evolution from Metallic Vanadium to Metallic V_xO_y: A NAPPES Study for O_2+ V Gas–Solid Interaction**,** *J. Phys. Chem. C.***2022**, 126, 45, 19136-19146.

2. **Ravi Ranjan**, Jyoti Tekawadia, Ruchi Jain, Nitin B. Mhamane, Thirumalaiswamy Raja and Chinnakonda S. Gopinath, Co_3O_4 for sustainable CO_2 reduction and possible fine-tuning towards selective CO production, *Chem. Eng. J.***2023**, 471,144459.

3. Exploration of Ni@Co Core-shell Nanoparticles for CO_2 Hydrogenation under NAPPES Conditions (Under Preparation)

List of Publication(s) in SCI Journal(s) Out of the Thesis Work

4. Bindu Antil ,**Ravi Ranjan** , Chinnakonda S. Gopinath and Sasanka Deka.,Directed holey and ordered g-$C_3N_{4.5}$ nanosheets by a hard template nanocasting approach for sustainable visible-light hydrogen evolution with prominent quantum efficiency, *J. Mater. Chem. A*, **2020**, 8, 13328–13339.

5. Himanshu Bajpai, Kshirodra K. Patra, **Ravi Ranjan**, Naresh Nalajala, Kasala Prabhakar Reddy, and Chinnakonda S. Gopinath., Can Half-a-Monolayer of Pt Simulate Activity Like That of Bulk Pt? Solar Hydrogen Activity Demonstration with Quasi-artificial Leaf Device, *ACS Appl. Mater. Interfaces*, **2020**, 12, 30420−30430.

6. Manoj Kumar Ghosalya, Kasala Prabhakar Reddy, Nitin B. Mhamane, **Ravi Ranjan** and Chinnakonda S. Gopinath., Gas–solid interactions with reactive and inert gas molecules by NAPUPS: can work function be a better descriptor of chemical reactivity?, *Phys. Chem. Chem. Phys*., **2020**, 22, 15528.

7. Bindu Antil, LakshyaKumar, **Ravi Ranjan**, S. Shenoy, Kartick Tarafder,C. S. Gopinath, and Sasanka Deka, One-Dimensional Multichannel g-$C_3N_{4.7}$ Nanostructure Realizing an Efficient Photocatalytic Hydrogen Evolution Reaction and Its Theoretical Investigations *ACS Appl. Energy Mater*, **2021**, 4, 3118−3129.

8. Shubhadeep Adak, Jabor Rabeah, **Ravi Ranjan**, Tuhin Suvra Khan, Mukesh Kumar Poddar, Rishi Kumar Gupta, Takehiko Sasaki, Sagar Kumar, Ankur Bordoloi, Chinnakonda S. Gopinath, Angelika Brückner, Rajaram Bal., In-situ experimental and computational approach to investigate the nature of active site in low-temperature CO-PROX over CuO_x-CeO_2 catalyst, *Appl. Catal. A: Gen.*, 624, **2021** 118305.

9. Nitin B. Mhamane, Sibo Chetry, **Ravi Ranjan**, Thirumalaiswamy Raja, and Chinnakonda S. Gopinath., Sustainable CO_2 Reduction on In_2O_3 with Exclusive CO Selectivity: Catalysis and In Situ Valence Band Photoelectron Spectral Investigations *ACS Sustainable Chem. Eng.*, **2022**, 10, 3521−3531.

10. Nitin B. Mhamane, Suresh Panchal, Sadhu K. Kolekar, **Ravi Ranjan**, Kranti N. Salgaonkar, Anand S. Burange, Naresh Nalajala Suwarna Datar, and Chinnakonda S.

Gopinath., Possible handle for broadening the catalysis regime towards low temperatures: proof of concept and mechanistic studies with CO oxidation on surface modified Pd–TiO_2, *Phys. Chem. Chem. Phys.*, **2023**, 25, 22040.

THE JOURNAL OF PHYSICAL CHEMISTRY C
A JOURNAL OF THE AMERICAN CHEMICAL SOCIETY

pubs.acs.org/JPCC

Article

Electronic Structure Evolution from Metallic Vanadium to Metallic V_xO_y: A NAPPES Study for O_2 + V Gas−Solid Interaction

Ravi Ranjan, Nitin B. Mhamane, Sadhu K. Kolekar, and Chinnakonda S. Gopinath*

Cite This: *J. Phys. Chem. C* 2022, 126, 19136−19146

Read Online

ACCESS | Metrics & More | Article Recommendations | Supporting Information

ABSTRACT: Gas−solid interactions between molecular oxygen and metallic vanadium surfaces and the systematic evolution in the electronic structure of vanadium oxide (VO_x) surfaces have been explored in the present work by near-ambient pressure photoelectron spectroscopy (NAPPES). The current article studies the evolution of various oxides of vanadium as a function of partial pressure of O_2 (ultrahigh vacuum to 1 mbar), temperature (298−875 K), and the exposure time to oxygen (up to 18 h). Valence-band (VB) and core-level spectral measurements recorded with UV (He−I = 21.2 eV) and Al Kα (1486.6 eV) photons, respectively, show interesting changes. (1) Oxidation is limited to the top layers of vanadium at 298 K and up to a partial pressure of 1 mbar O_2. About 50% of vanadium gets oxidized, and the remaining amount exists as metal within the top 10 nm. (2) Metallic vanadium disappears above 625 K, and it is predominantly oxidized to a mixture of V^{4+} and V^{5+} oxidation states at a 0.1 mbar partial pressure of O_2. Points 1 and 2 suggest the predominantly thermodynamically controlled nature of vanadium oxidation through oxygen diffusion into the subsurface and bulk layers. (3) The Fermi-level (E_F) feature observed first at ≥725 K at a 0.1 mbar O_2 pressure demonstrates the formation of metallic VO_2; however, its metallic nature is preserved even at ambient temperature due to interweaving nanodomains of VO_x with VO_2. (4) Only partial conversion of surface layers to V^{5+} (V_2O_5) along with VO_2 and V_2O_3 (within the probing depth of 8−10 nm by near-ambient pressure X-ray photoelectron spectroscopy (NAP-XPS)) was observed even after prolonged heating (18 h) in 1 mbar O_2 pressure. (5) The nature of the surface changes between metal and semiconducting/insulator oxides is substantiated by the observation of changes in work function (ϕ) and E_F features. Typical VB features and Fermi intensity of V-metal and vanadium oxides were observed, and the results were corroborated with core-level and VB spectra. The present results extend the capabilities of NAPPES to explore the electronic structure evolution as a function of reaction conditions and underscore its relevance to areas such as heterogeneous catalysis and sensing.

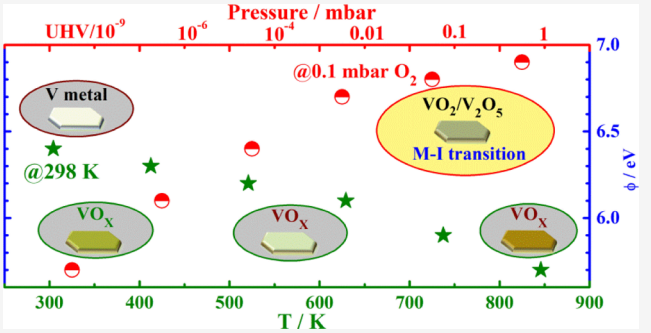

INTRODUCTION

Vanadium is a fascinating element exhibiting an electronic configuration of $[Ar]3d^34s^2$, with abilities to be employed in ceramics as the catalyst for superconducting magnets. The rich and varied chemistry of vanadium has been recognized to be due to the variety of easily accessible oxidation states as well as the redox nature of vanadium. Vanadium pentoxide is a well-known catalyst for sulfuric acid production. Vanadium compounds are stable in different oxidation states and hence a variety of oxides are possible, such as VO, VO_2, V_2O_3, V_6O_{13}, and V_2O_5.[1,2] Properties of vanadium and vanadium oxides attracted the interest of researchers across various fields, such as catalysis,[3,4] electrochemistry,[5] and optoelectronic applications.[6] Partially filled 3d-orbitals of vanadium are important in the electron exchange mechanism and ferromagnetic properties of defective VO_2.[7] Vanadium forms a large number of oxides, which are also stable over a certain range of pressure and temperature conditions.[8] The phase transition between vanadium to V_2O_5 has been speculated to be due to the insertion of oxygen in the vicinity of the vanadium surface, but no systematic studies are available. Indeed, from a catalysis point of view, monomeric vanadium, mixed valence, and/or redox nature of vanadium have been demonstrated to show high activity and selectivity in a number of heterogeneous catalysis reactions.[9] Catalysis is indeed a surface phenomenon, and the catalyst surface should undergo reversible changes easily for sustainable catalytic activity. There are a number of elementary steps/reactions that occur over the catalyst surface, such as adsorption of reactant(s), dissociation, diffusion of various species and reaction among them, followed by desorption of product(s); diffusion of small atoms (H, C, and O) into the catalyst subsurface is also possible.[10] These

Received: July 23, 2022
Revised: October 16, 2022
Published: November 3, 2022

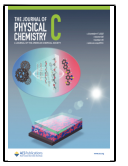

https://doi.org/10.1021/acs.jpcc.2c05212
J. Phys. Chem. C 2022, 126, 19136−19146

steps involve bond making or breaking, which depends on the electronic nature of the catalyst surfaces. The work function (ϕ) of a catalyst (or any solid material) is a surface-sensitive property, and the same is required to understand the relative Fermi energy (E_F) and carrier concentration near E_F. ϕ can be defined as the energy required to remove an electron from E_F into the vacuum. ϕ affects the chemical, magnetic, optical, and structural characteristics of the surface.[11,12] ϕ is readily influenced by many common factors, such as adsorbed layers of molecules, surface contamination, and oxide formation. Due to the significant dependence of ϕ on the surface nature, it is necessary to measure the same reliably for any particular material under technically relevant conditions.

It has been reported that ϕ change reaches up to 6.7 eV for materials such as MoO_x, WO_x, and V_2O_5; indeed, the high-ϕ materials are excellent hole-injecting electrodes in organic semiconductor devices.[13,14] On the contrary, TiO_2 and ZnO are better electron-injecting materials, and it has excellent applications in photocatalysis.[15,16] The change in ϕ and hence the change in physicochemical properties of the vanadium oxides can be tuned by oxygen vacancy (O_v) by changing the stoichiometry of the oxide.[17] Vanadium dioxide (VO_2) shows some unique properties, such as it exhibits first-order metal−insulator (MI) transition from an insulating phase (below 340 K) with a monoclinic structure to a metallic phase with a tetragonal rutile structure ≥340 K.[18] The conductivity is 5 orders of magnitude below the transition temperature, with the energy gap in the insulating phase being typically 0.6 eV.[19] Due to this factor, the monoclinic VO_2 is considered as a semiconductor, and it has interesting applications in dilute magnetic semiconductors. Furthermore, the charge carrier density can be fine-tuned by ionic doping and/or subsurface diffusion of small atomic species such as hydrogen, oxygen, sulfur, and so forth.[20] The phase-transition temperature can be altered over a wide range of doping and external strain of VO_{2-x}; due to these extraordinary features of VO_{2-x}, it has many potential applications, such as electrodes in electrochemistry.[21] The ϕ of undoped VO_2 is ≥6 eV at room temperature (RT) mainly due to structural electronic rearrangement on the surface VO_x. Thus, the undoped VO_2 is not considered as a suitable hole-injecting metal oxide in devices. In case of VO_2, it has been reported that by doping with the W^{6+}-ion, the number of O_v can be altered, and hence, the ϕ of VO_2 and MI transition temperature can be decreased to 323 K; indeed, there is an O_v handle to tune the MI temperature significantly.[22]

Valence-band (VB) photoelectron spectroscopy with low-energy photons is an important tool to explore the surface-specific electronic changes that occur within the top 2 nm. Indeed, near-ambient pressure ultraviolet photoelectron spectroscopy (NAP-UPS) is fully relevant to explore oxygen−vanadium gas−solid interaction. NAP-UPS helps to explore the evolution of the 3d band structure and V 3d−O 2p hybridization effects, while the transition happens from V-metal to VO_x oxides. X-ray photoelectron spectroscopy (XPS) and UPS are very powerful surface characterization techniques which provide information about the oxidation state and electronic structure, VB aspects, ϕ change, and density of state (DOS). Our group has contributed to this area of research with NAP-UPS and NAP-XPS with many metals and metal oxides under relevant redox conditions, and interesting findings have been reported.[23−29]

In the present work, the electronic structure evolution of metallic vanadium to V_2O_5 through different VO_x was demonstrated as a function of partial pressure of oxygen and temperature. Specifically, changes in the ϕ between 5.5 and 7 eV upon changing the stoichiometry of the vanadium oxides (VO_x) and metal−insulator transition of VO_2 at 0.1 mbar O_2 pressure and ≥725 K are shown. Oxidation of the V-surface is highly limited to a few atomic layers at RT, while oxidation progress into somewhat deeper layers at high temperatures (but within the XPS probing depth) demonstrates the thermodynamic dependence.

2. EXPERIMENTAL SECTION

VB and core-level PES experiments were performed using a custom-built lab-based near-ambient pressure photoelectron spectrometer (NAPPES) available at the CSIR—National Chemical Laboratory, Pune (India).[30,31] NAP-XPS (NAP-UPS) experiments can be performed up to a 1 mbar (0.3 mbar) pressure and a 1000 K temperature. The instrument is equipped with a differentially pumped electron energy analyzer R3000 HP (VG Scienta). In contrast to many such systems employed with closed high-pressure cells, the system employed for the present studies involves an open reactor design.[31] A high-pressure gas-doser extends right up to the solid surface, and in situ pressure measurements made very close to the surface ensure that the pressure values reported are reliable. A gas doser can be heated up to 873 K, which increases the temperature of gas molecules and helps to minimize the temperature fluctuations on the surface of the sample while doing NAPPES measurements. More information about NAPPES is described in refs 30 and 31.

A high-purity polycrystalline metal foil of vanadium (99.99%) procured from Otto Chemie Pvt. Ltd was employed for the present studies. Vanadium metal was initially acid-etched with 1 M HNO_3 acid to remove the inevitably oxidized thick layers of VO_x. Subsequently, a vanadium metal foil was introduced into the NAPPES unit. XPS spectra were recorded with Al Kα (1486.6 eV), and UPS spectra were recorded using a He I photon source ($h\nu$ = 21.2 eV) from a He discharge lamp. Photoelectron spectroscopy is highly sensitive to the surface, and any adsorbate-induced changes can be identified more precisely than any other technique due to the limited probing path of UPS (up to 2 nm) and XPS (8−10 nm). A V-metal foil was sputter-cleaned repeatedly by several cycles of Ar^+ sputtering by applying a potential (3.5 keV and 6 mA) to the sputter gun at a pressure of 5.5×10^{-6} mbar at 700 K followed by vacuum annealing at 1000 K for 30 min. This process was repeated multiple times until no peak other than the V-metal was detected on the surface and was free from oxygen and carbon, as confirmed by XPS. No other impurities such as sulfur, phosphorous, and silicon were detected. All high-pressure experiments were performed in the range of ultrahigh vacuum (UHV) to 1 mbar O_2 (99.99%) from 298 to 875 K. Although 1 mbar partial pressure experiments were carried out at the same pressure, the spectra were recorded at 0.1 mbar pressure since the scattering is too high at 1 mbar. Furthermore, above a 0.3 mbar pressure, no meaningful spectra could be recorded in NAP-UPS.[31] While 1 mbar treatment was carried out at the same pressure, while recording the spectra, the pressure was decreased to a 0.1 mbar O_2 partial pressure, and the spectra (NAP-UPS and NAP-XPS) were recorded. CasaXPS software was used for curve fitting,[32] and the goodness of the fitting was ensured with a chi-square value of

https://doi.org/10.1021/acs.jpcc.2c05212
J. Phys. Chem. C 2022, 126, 19136−19146

0.1−0.2. All spectra are calibrated with respect to the E_F of a clean gold foil and normalized against RT measurement data. All spectra were deconvoluted after subtracting the Shirley-type background.

3. RESULTS AND DISCUSSION

3.1. Clean V-Surface Features. A vanadium foil sample has been sputtered and annealed extensively, and then the XPS and UPS spectra have been recorded under a UHV condition at RT, and the results are shown in Figure 1. The clean

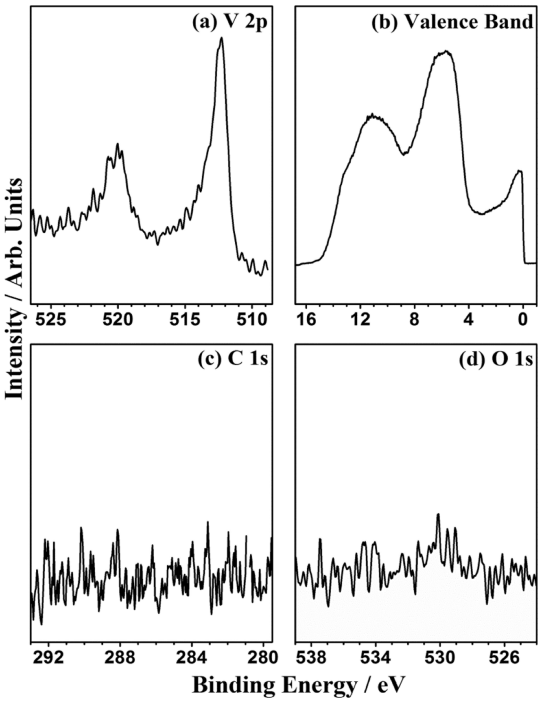

Figure 1. XPS and UPS spectra recorded at UHV and 298 K after several sputter−anneal cycles on the vanadium foil; (a) V 2p, (b) VB spectra recorded using UPS, (c) C 1s, and (d) O 1s levels. The *Y*-axis counts for (c,d) have been multiplied 5 times to show that there is no contamination on the clean surface.

vanadium foil shows typical V $2p_{3/2}$ and $2p_{1/2}$ at RT at 512.3 and 519.8 eV, respectively. The observed binding energy (BE) for metallic vanadium and oxidized vanadium species is in good agreement with the literature reports.[33,34] There is no carbon and oxygen core-level feature that appears on the surface, which has been confirmed by XPS spectra (Figure 1c,d); no other impurities, such as chlorine and phosphorous were observed. As the vanadium foil is extensively sputtered, some surface defects are possible, such as nanoclustering or nanostructuring of vanadium and surface inhomogeneity, and this feature could appear at a high BE.[35] A minor broadening observed on the higher BE side of the V 2p feature (~513 eV) is due to subsurface/bulk layers of vanadium (Figure 2a). A marginal amount of surface oxide as surface contamination, due to the residual oxygen present in the NAPPES unit, cannot be ruled out. Indeed, initially, sputtering was carried out until the V-surface did not show any O and C impurities. UPS is much more surface-sensitive than XPS, and it explores and provides information about the top 2 nm of the surface under UHV conditions. Surface oxide(s) was removed during the sputtering and annealing process, which was also confirmed by UPS. It shows high DOS near E_F which is a characteristic of a

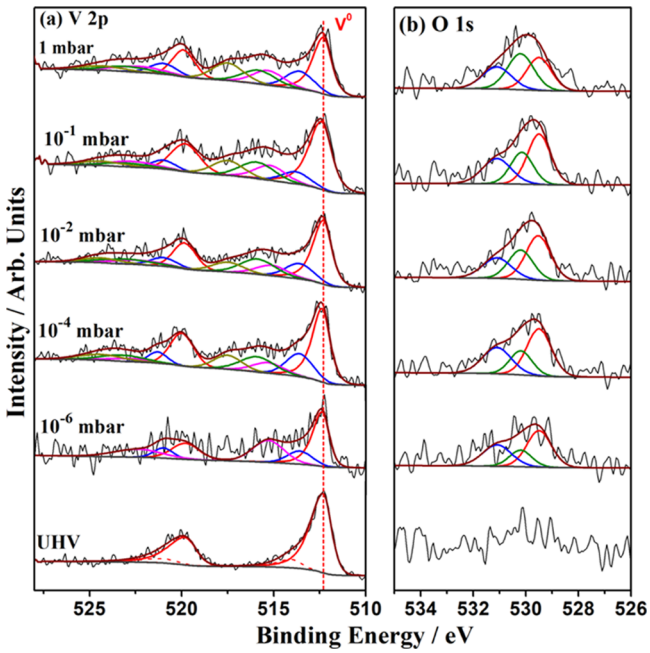

Figure 2. NAP-XPS of (a) V 2p and (b) O 1s core levels recorded as a function of O_2 partial pressure between 10^{-6} to 1 mbar at 298 K. The clean surface feature recorded is shown at the bottom for comparison. The red dashed line shown in (a) is to denote the metallic vanadium feature. *Y*-axis intensity counts for (b) have been multiplied 2.5 times.

metal; indeed, this is the critical characteristic of the metallic vanadium surface and supports the fact that the surface is devoid of any other foreign elements. The UPS spectrum of a clean foil, recorded with He−I photons, is shown in Figure 1b. It is to be noted that the extensive sputtering employed to clean the V-surface could introduce some solid-state defects, and the same cannot be ruled out. Broadening observed on the high BE side (~513 eV) of V $2p_{3/2}$ and a broad peak observed around 6 eV in UPS (Figure 1b) is attributed primarily to such defects, and they are within the probing depth of XPS. Another broad feature centered at 11−12 eV in Figure 1b is attributed to secondary electrons. As the photoelectrons are ejected out of the solid surface, part of the kinetic energy is lost due to inelastic scattering within the solid surface layers, and these electrons appear at higher BEs. Indeed, this is a bit more severe and changes significantly as the O_2 partial pressure increases.

3.2. Pressure-Dependent Oxidation V + O_2 Interaction−NAPPES Study. Oxidation aspects of the vanadium metal surface were evaluated in detail as a function of O_2 partial pressure, temperature, and O_2 exposure time at 1 mbar pressure. In the first step, V 2p and O 1s core-level results were recorded as a function of increasing oxygen partial pressure from UHV, 10^{-6} to 1 mbar on the vanadium foil at 298 K, and the results are shown in Figure 2. Upon exposure to O_2, high-BE features evolve and the metallic V 2p features are also retained up to a 1 mbar pressure. Indeed, first-row 3d transition metals are known to be pyrophoric[23,25] and the observation of metallic V in Figure 2a is indeed interesting. At low partial pressure, the new features observed are attributed to V^{2+} (blue peak) at 513.7 eV.[33] With increasing O_2 partial pressure from 10^{-6} to 1 mbar, the extent of severity of surface oxidation increases; however, the observation of metallic V even at a 1 mbar O_2 partial pressure suggests that the oxidation is limited to surface layers even within the XPS probing depth

https://doi.org/10.1021/acs.jpcc.2c05212
J. Phys. Chem. C 2022, 126, 19136−19146

of 10 nm, rather than deeper into subsurface/deeper layers of vanadium. Curve fitting was carried out to resolve the various V-species present, and the curve fitting parameters were adopted as that of Biesinger et al.[33] with some modifications. The curve fitting parameters employed are given in Table S1 and S2, and the quantification of various V-species is given in Table S3 (see Supporting Information S1). Initially complete metallic vanadium was observed under UHV conditions; this changes gradually to 41.1% at 1 mbar due to oxygen exposure and oxygen diffusion on the top few surface layers of vanadium. This indicates that a predominant lateral oxygen diffusion and oxidation of subsurface layers are limited under the measurement conditions, especially at 298 K. At 10^{-6} mbar O_2 partial pressure and among the oxidized V-species, a V^{3+} (pink) oxidation state was observed predominantly at 515.3 eV along with V^{2+} (blue) at 513.7 eV with the corresponding satellite peak at 521 eV. On increasing the O_2 partial pressure to 10^{-4} mbar, with V^{4+} (green) and V^{5+} (dark yellow) at 515.8 and 517.2 eV with corresponding satellite peaks at 523.4 eV and 524.6, respectively, oxidation states were observed at the cost of V^{2+} and V^{3+}. Only 14.4% of the V^{5+} state was observed at the 1 mbar condition, indicating that the onset of the severe oxidation requires more harsh conditions, such as high temperature. However, the increasing partial pressure of O_2 up to 1 mbar at RT exhibits multiple oxidation states from V^{2+} to V^{5+}. Although molecular oxygen was available under experimental conditions, the observation of multiple oxidation states concurrently demonstrates the heterogeneity of the surface, possibly due to oxide islands, surface defects, and so forth. The observation of 47.4% metallic V at 1 mbar pressure also indicates that the surface oxide layers might be acting as a protective layer and hindering the oxidation of the subsurface and deeper layers of the V-foil, which requires vertical oxygen diffusion and more energy. Indeed, a similar observation was reported for silicon oxidation.[27]

No oxygen feature was observed on the clean V-foil, which highlights the purity of the surface Figure 2b (bottom spectra). When the oxygen partial pressure increased from UHV to 10^{-6} mbar, a broad O 1s envelope was observed with a significant signal-to-noise (S/N) ratio, and the result is shown after deconvolution in Figure 2b. The high-intensity peak at 529.6 ± 0.1 eV (red trace) and the peak at 530.2 ± 0.1 eV (green trace) are attributed to the lattice oxygen of VO_x with short-range and long-range ordering, respectively. This suggests a possibility of VO_x island formation under the present experimental conditions for the results shown in Figure 2. Another peak at 531.2 ± 0.1 eV (blue trace in Figure 2b) appears in all O 1s spectra recorded, indicating the formation of hydroxyl features on the surface, which is likely due to background-level hydrogen present in the UHV chamber. Indeed, this is supported by the observation of the back-streaming of hydrogen into the analysis chamber in the mass spectrum recorded (S2 in the Supporting Information), while all other air components remain observed at the background level. Even at a 0.1 mbar, the oxygen peaks appear at the same BE, as that of 10^{-6} mbar, at 529.6, 530.2, and 531.2 eV. In pressure-dependent conditions, the O 1s peak intensity at 530.2 eV increases gradually up to 0.1 mbar, and it becomes comparable to that of the 529.6 eV feature during 1 mbar O_2 treatment.

The NAP-UPS VB spectra of V-metal surfaces were recorded as a function of oxygen partial pressure, and the results are shown in Figure 3. This is to explore the electronic

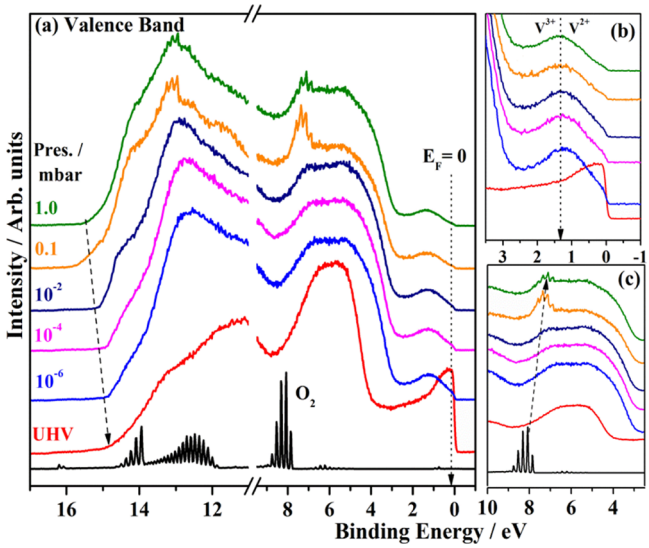

Figure 3. (a) NAP-UPS results recorded during V-metal oxidation to VO_x in the presence of gradually increasing O_2 partial pressure up to 1 mbar at 298 K. The (b) E_F feature is shown in an enlarged scale; the spectra shown for 10^{-6} to 1 mbar have been multiplied by a factor of 3. The E_F feature is observed even at an O_2 partial pressure of 0.01 mbar. (c) O_2 gas-phase vibrational features and the main VB are shown in an enlarged scale. A shift toward a low BE for vibrational features and broadening of the main VB is observed as the O_2 partial pressure increases.

structure evolution of vanadium oxide(s) as a function of O_2 partial pressure at 298 K. It is also to be noted that while XPS explores up to 10 nm depths, UPS hardly explores the top 2 nm layers, and hence, they are likely to provide complementary information. There are three electrons in the metallic V 3d band and two electrons in the V 4s band. The high DOS observed at E_F indicates the complete metallic nature of the surface; also, the amount of residual air components (particularly oxygen) present in the UHV chamber is not sufficient to oxidize the surface layers of vanadium at 298 K. Critically, the high DOS feature observed at E_F on the metallic V-surface under UHV decreases drastically but does not disappear completely upon the introduction of gas-phase oxygen at 10^{-6} mbar. A similar reduction in E_F intensity was observed on Co[25] and Cu surfaces;[31] this observation confirms the highly pyrophoric and oxidizing nature of the metallic vanadium surface. While Figure 2a exhibits 41.1% metallic V 2p features in NAP-XPS even at 1 mbar O_2 partial pressure, the drastic reduction of E_F features even at 10^{-6} mbar (and above) partial pressure in Figure 3a is due to the low probing depth (≤2 nm) in NAP-UPS. In addition to the E_F changes, the V 3d band at 10^{-6} mbar O_2 partial pressure exhibits two features: one centered around 1.3−1.5 eV and a second feature around ∼0.4 eV; these features are attributed to V^{3+} and V^{2+} species, respectively. This is further supported by the disappearance of V^{3+} and another low-BE species upon oxygen annealing of VO_2 (with O_v) in a study by Wang et al.[35] We also want to underscore the time required for the average experiment as it helps other researchers to reproduce the data. The time taken to record each set of spectra (XPS and UPS), at a given pressure, was about 25 min, and randomly, in few cases, we repeated measurements to make sure that there are no further changes in the recorded spectra for the BE position as well as counts. We did not observe any significant change in spectral

https://doi.org/10.1021/acs.jpcc.2c05212
J. Phys. Chem. C 2022, 126, 19136−19146

results, even if it was prolonged to 60 min, and hence, the results represent steady-state oxidation at 298 K. However, we recorded a set of spectra at a given high pressure/temperature also in 25 min, and no significant changes were observed within this time frame and up to 30 min; however, significant changes were observed beyond 30 min at and above 673 K and at 0.1 mbar and above.

The oxygen partial pressure was further increased gradually from 10^{-6} to 1 mbar at RT, and the spectra were recorded. Few interesting observations worth underscoring are as follows: (a) E_F intensity gradually decreases and completely disappears at ≥0.1 mbar O_2 partial pressure (Figure 3b). (b) A careful look at the photoelectron emission offset around 15 eV shows a decrease in ϕ up to 0.1 mbar, followed by a minor reversal in the increase in ϕ at 1 mbar. (c) ϕ changes are reflected in the oxygen vibrational features too, which is given in detail in the next paragraph. (d) A broad feature observed around 6 eV (on metallic V) was further broadened, particularly on the lower BE side toward 3−4 eV. This broadened feature is attributed to the O 2p features of the V 3d−O 2p hybridized band. (e) A new broad and low-intensity feature appeared around 1 eV corresponding to V 3d−O 2p interaction. Upon increasing the O_2 partial pressure from 10^{-4} mbar up to 1 mbar at 298 K, the V^{2+} feature is suppressed and V^{3+} increases in intensity, suggesting the oxidation to V^{3+} on the surface. The first feature around 1.3 eV is attributed to [Ar] $3d^2$−O2p or [Ar] $3d^3$−O 2p, corresponding to V_2O_3 or VO, respectively, and indicating the charge transfer from V to O.[34] Similar types of features were observed and attributed to charge transfer from metal to oxygen with oxidation of metals, such as Cu, Mo, Co, and Pd.[23,25,31,36] Upon further increasing the O_2 partial pressure up to 1 mbar at 298 K, no major changes were observed, except for O_2-gas-phase features, which is different at 1 mbar; this indicates further minor modification of VO_x composition at 1 mbar, possibly due to the onset of severe oxidation. The NAP-UPS spectra also show the vibrational features of molecular oxygen, and the same appear at different BEs with increasing pressure, underscoring the interaction of molecular oxygen with a solid surface. Pure molecular oxygen alone shows a set of features around 8.0, 12.0, and 14.0 eV for molecular vibrations of oxygen in the gas phase due to photoexcitation of an electron from $2p_{\pi^*}$, $2p_{\pi}$, and $2p_{\sigma}$ valence orbitals of oxygen, respectively.[25−27] These features are not observed up to 0.01 mbar in Figure 3b due to low partial pressure (concentration) of O_2; nonetheless, a huge shift in the BE of O_2 features was observed toward a low BE by 1 eV, compared to pure gas-phase O_2. The shift in the vibration features can be due to many reasons, such as simple adsorption and/or dissociation of the adsorbed molecule on the surface; this leads to a possible change in the surface ϕ due to the formation of surface VO_x layers. Such phenomenon is observed in various fields such as catalysis, electrochemistry, and sensing. In contrast to the sharp and well-resolved O_2 features observed for pure O_2 (black trace), broad and not-so-well-resolved features are observed on the vanadium surface at 0.1 mbar and above, indicating a possible heterogeneous nature of the surface with more than one type of VO_x species present. Indeed, this is in good correspondence with the V 2p and O 1s core-level results observed in Figure 2. It is also to be noted that broadening and shift in O_2 vibrational features underscore its high sensitivity to detect surface changes in a precise manner. Very low-intensity but narrow bands are observed in the pure O_2 spectrum around 6.1 eV. These bands originate due to He−I β (23.09 eV; 1.5% intensity) satellite photons compared to He−I α (21.2 eV; 100%) photons. Satellite features appear at 1.9 eV below the main O_2 bands, confirming this fact.

3.3. Temperature-Dependent V + O_2 Interaction at a 0.1 mbar O_2 Partial Pressure−NAPPES Study. After measuring the V + O_2 interaction studies at 298 K, in the second step, the resputtered and cleaned V-foil was exposed to a constant 0.1 mbar O_2 partial pressure while increasing the temperature from 298 to 825 K. V 2p and O 1s spectra have been recorded at several temperatures, and the results are shown in Figure 4. In contrast to the observation of V-

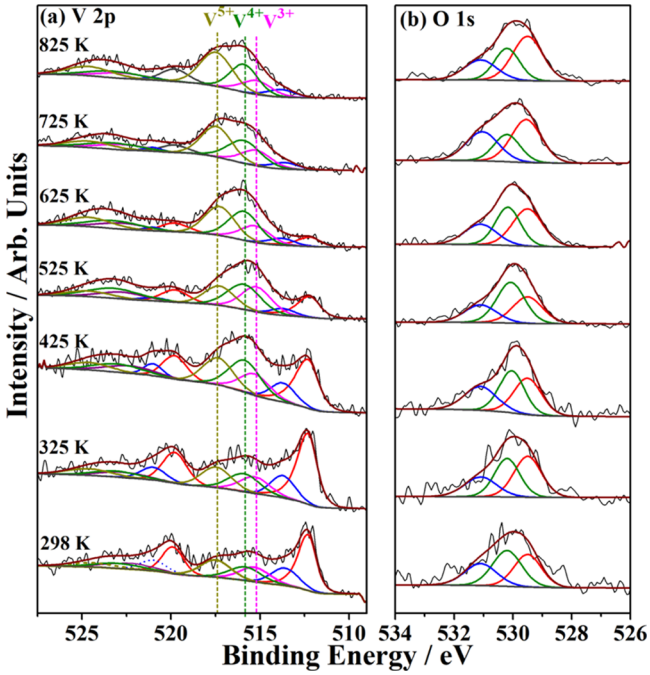

Figure 4. NAP-XPS of V 2p and O 1s regions as a function of temperature at a 0.1 mbar O_2 partial pressure. (a) V 2p XPS spectra and (b) O 1s XPS. Note the absence of the metallic V feature above 625 K. *Y*-axis counts for panel b have been multiplied 2.5 times for the 298, 325, and 425 K spectra.

oxidation restricted to the top surface layers in Figure 2a, a severe change in oxidation toward higher oxidation states of V^{4+} and V^{5+} was observed as seen in Figure 4. A number of interesting changes were observed, and the following points are worth highlighting: (a) the metallic V feature decreases gradually in intensity up to 625 K, and thereafter, it disappears completely, indicating that the vertical progression of oxidation into the bulk VO_x layers occurs at high temperatures. (b) From 325 to 625 K, the severity of the oxidation increases, and V^{3+} increases in content, before it starts further oxidizing to V^{4+} at 625 K and above.

Also, the V^{2+} oxidation state was observed only up to 425 K. (c) 3+, 4+, and 5+ oxidation states of V are observed between 725 and 825 K; nearly V^{3+} (15.3%), V^{4+} (36.0%), and V^{5+} (41.3%) oxidation states, along with minor V^{2+}, are observed under the most severe condition employed (825 K; 0.1 mbar) in Figure 4. Indeed, higher oxidation states of V form at the expense of lower valence states as the temperature increases. (d) Comparable V^{4+} and V^{5+} oxidation states are observed from 425 K and above, underscoring the feasibility of oxidation to the highest states but within the limited layers of thickness.

https://doi.org/10.1021/acs.jpcc.2c05212
J. Phys. Chem. C 2022, 126, 19136−19146

However, the thickness of such oxidized layers increases with increasing temperature at the cost of lower-valence V-oxidation states. (e) These observations demonstrate the requirement of thermal energy for oxygen diffusion into the subsurface and bulk layers of V. Indeed, progressive oxidation from lower to higher oxidation states of V and from surface to deeper layers occurs with increasing temperature at 0.1 mbar O_2 pressure and demonstrates a predominant thermodynamic control of oxidation. It may also be noted that prolonging the oxygen exposure for a longer time could lead to more stable oxides at a given temperature. Hence, some amount of kinetic control also is present. Nonetheless, within the same set of experimental conditions employed in the present studies, predominant thermodynamic control is evident. V 2p features are shifted toward higher BEs, indicating that at high temperatures, the rate of diffusion of oxygen is higher and revealing the changes in the oxidation state. One final observation is indicated by a gray-color trace fitted at 520 eV for 725 and 825 K spectral lines. When V-metal is predominantly observed at low temperatures, the 520 eV feature (red color trace) is attributed to metallic vanadium (V $2p_{1/2}$). However, when the surface layers are predominantly oxidized, the satellite feature of O 1s appears at 520 eV (due to secondary radiations of Al K α3 (6.4% intensity) and α4 (3.2% intensity), with 9.8 and 11.8 eV higher than parent Al Kα 1486.6 eV), which is indicated by gray color.

O 1s core-level spectra were also recorded, and the results are shown in Figure 4b. A distinct increase in the S/N ratio at 525 K and above is observed for the O 1s core level, compared to the results shown up to 425 K and in Figure 2b. This single observation reiterates the earlier conclusion of oxygen diffusion into the subsurface and bulk layers at high temperatures and the thermodynamic control nature of VO_x formation. The entire thickness of the top 8−10 nm is explored under the present measurement conditions, and the observation of oxides of V^{4+} and V^{5+} supports the same. The intensity of the O 1s feature corresponding to long-range ordered species (530.3 eV) is also enhanced, underscoring the sign of progression of oxide formation into deeper layers at the cost of metallic vanadium layers. Although the surface layers are oxidized, a 0.1 mbar O_2 pressure and 825 K temperature are not sufficient to oxidize the vanadium completely to V_2O_5, even within the NAP-XPS probing depth of 8−10 nm. This is in contrast to the complete oxidation of Co, which is fully oxidized to Co_2O_3 even between 400 and 500 K at a 0.1 mbar O_2 partial pressure.[25] A comparative analysis and overall view of O 1s spectra presented in Figures 2 and 4 suggest an interesting point. While it is expected that hydroxide would remain stable below 373 K, the same is not true at high temperatures and hydroxide is expected to decompose in a predominant O_2 environment. However, the possibility of finding O_v is significant, especially when the oxide layers are growing deeper into several atomic layers of vanadium at high temperatures at 0.1 mbar O_2 partial pressure. Indeed, the observation of gradual oxidation from low to high oxidation states at increasing temperatures fully supports this. It is known that those oxide ions in the vicinity of O_v appear between 531 and 532 eV, and it is well documented in the literature,[17,23,35,37] In view of this factor, we attribute the 531.5 eV feature to hydroxide ≤425 K and a combination of hydroxide and oxygen in the neighborhood of O_v between 425 and 625 K; above 625 K, it is attributed only to oxide species that are closer to O_v.

The NAP-UPS VB spectra were also recorded as a function of temperature from 298 to 825 K at a 0.1 mbar O_2 partial pressure, and the results are shown in Figure 5. While the

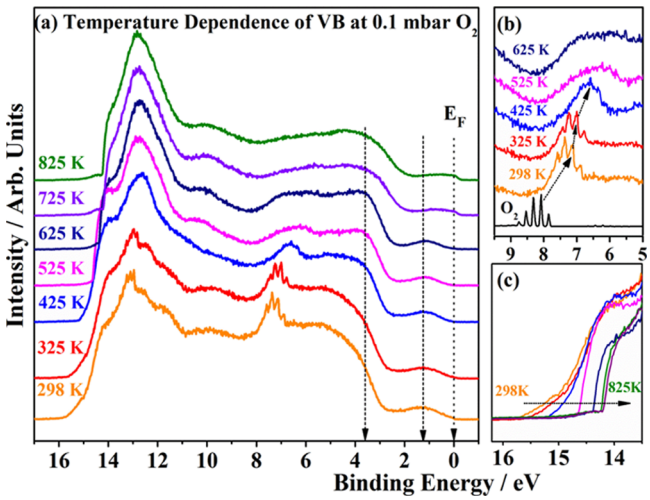

Figure 5. (a) Temperature-dependent NAP-UPS results recorded for V-metal oxidation in the presence of 0.1 mbar O_2 partial pressure. (b) Molecular O_2 vibrational features and (c) changes in the work function, through photoelectron emission offset, are shown on an enlarged scale. Features in (b) are multiplied for clarity; 298 and 325 K spectra are multiplied by a factor of 3, and 425−625 K spectra are multiplied by a factor of 5.

features observed around 1 eV are attributed to V 3d features, the main VB (between 3 and 7 eV) is due to strongly hybridized V 3d−O 2p orbitals. Six important and complementary observations (to NAP-XPS results shown in Figure 4) in Figure 5 are worth highlighting, and they are as follows: (1) a gradual shift was observed in the gas-phase features of O_2 toward lower BEs at high temperatures. A major shift of 0.65 eV in O_2 features was observed when the temperature was increased from 325 to 425 K at 0.1 mbar O_2 partial pressure. (2) In addition to the shift of vibrational features, an enormous broadening was also observed at high temperatures, and the enlarged vibrational features are shown in Figure 5b. This suggests the formation of different oxides on the surface, which makes the surface highly heterogeneous in nature. It is well known that molecular vibrations are sensitive to detect the homogeneous or heterogeneous nature of the surface.[24] (3) A careful analysis of the spectra recorded between 325 and 625 K reveals a low-intensity broad hump at 1 eV, and this is attributed to the V^{3+} feature. While the 1 eV feature shows no changes, the main VB picks up more area and becomes a square feature ≥425 K, compared to that at 298−325 K. (4) Very interestingly, on increasing the temperature, a sharp metallic feature started appearing at ≥725 K near E_F. It is worth mentioning that under similar conditions, NAP-XPS (Figure 4) predominantly shows 4+ and 5+ oxidation states of V. It is known that large V 3d−O 2p hybridization occurs in VO_2 and V_2O_5, with an appearance of the $3d^1L$ feature of VO_2 at E_F.[18] (5) A noticeable VB broadening occurs by 0.6 eV to the lower BE side while increasing the temperature from 625 to 725 K and above. Concurrently, a metallic E_F feature appears and the 1 eV feature is still observed. (6) Figure 5c demonstrates an increase in ϕ from 5.7 to 6.8 eV between 298 to 725−825 K, respectively. This is in good agreement with the $\phi \sim 6.7$ eV reported by Kim et al. for VO_2.[21] Critically, VO_2

https://doi.org/10.1021/acs.jpcc.2c05212
J. Phys. Chem. C 2022, 126, 19136−19146

shows MI phase transition at various temperatures depending on the particle size of vanadium oxide. It is also to be noted that a significantly wide range of work function values is reported for VO_2 as well as metallic V, and it is partly due to various methods employed for ϕ measurements and particle size. The ϕ of VO_2 is shown to change from 5.15 to 5.30 eV between 300 and 375 K.[17]

The sudden appearance of the E_F feature observed at 0 eV supports the metallic nature of VO_2. The changes observed in the E_F are caused by the increased oxygen diffusion in the polycrystalline V-metal foil in the form of VO_2 as a result of heating to high temperatures. An increased rate of oxygen diffusion in polycrystalline metal foil is related to the presence of more number of dangling bonds. Such a phenomenon exists at a lower temperature in the amorphous film and nanoparticles, and it depends on oxidation current, anodic oxidation time, and sample sizes.[38] The rate of oxygen diffusion is reported to be 5−7 times lower with an amorphous vanadium film compared to the polycrystalline V-foil. We speculate the atomic oxygen diffusion into the polycrystalline vanadium foil and mixed VO_x observation leads to the explanation for the observed MI phase transition at high temperature (725 K) in comparison to the previously reported low-temperature MI transition at 340 K with the VO_2 nanodomain.[21] Fast switchable/reversible MI transition makes VO_2 widely employed in applications, such as electronic devices, energy-efficient switches, and ultrafast switches. Furthermore, the charge carrier concentration and dielectric constant of VO_2 in the normal insulating state at ambient temperatures make it applicable to Hall effect devices due to low electron mobility and sensitive temperature dependence of the carrier concentration in VO_2. VO_2 is also used for making heterostructure devices by the deposition of a high-quality thin film of VO_2 on high-mobility semiconductors, such as heavily doped Ge, TiO_2, and Al_2O_3.[1]

3.4. Time-Dependent Study of the V + O_2 Interaction−NAPPES Study. The core-level NAP-XPS and NAP-UPS spectra are recorded during the prolonged oxidation at different time intervals and the NAP-XPS and NAP-UPS results are given in Figures 6 and 7, respectively. In the time-dependent study, the V-foil was exposed to molecular oxygen at 875 K for up to 18 h and spectra were recorded periodically with a significantly long interval. Oxidation from metallic vanadium to a mixture of V_2O_3, VO_2, and V_2O_5 was observed in the earlier results (Figures 2−5). The V-foil could be oxidized to V^{4+} (36.0%) and V^{5+} (41.3%) (Figure 4a) after treatment under a 0.1 mbar O_2 partial pressure at 825 K. By heating the sputter-cleaned vanadium metal foil at a 1 mbar O_2 at 875 K, a minor decrease in the V^{4+} content was observed to 27−35% from 36.0% at 0.1 mbar O_2 at 825 K. Upon continuous oxygen exposure at 1 mbar for up to 18 h, no significant change in the ratio of V^{4+}/V^{5+} was observed. The intensity of V^{4+} and V^{5+} was almost the same, and it is observed within the 5% error limit. V^{5+} was dominant (42−56%), followed by V^{4+} (27−35%) and V^{3+} (17−20%). The oxidation of VO_2 to V_2O_5 is a kinetically slow process, and it requires concurrent high temperatures as well as high pressures (>1 mbar). Nonetheless, the observation of V^{3+} and V^{4+}, even after prolonged exposure to O_2 suggests that oxygen diffusion into the subsurface and bulk layers might be a rate-determining factor toward oxidation to V_2O_5.

The NAP-UPS spectra were recorded periodically to explore the evolution of electronic structure and interface to measure

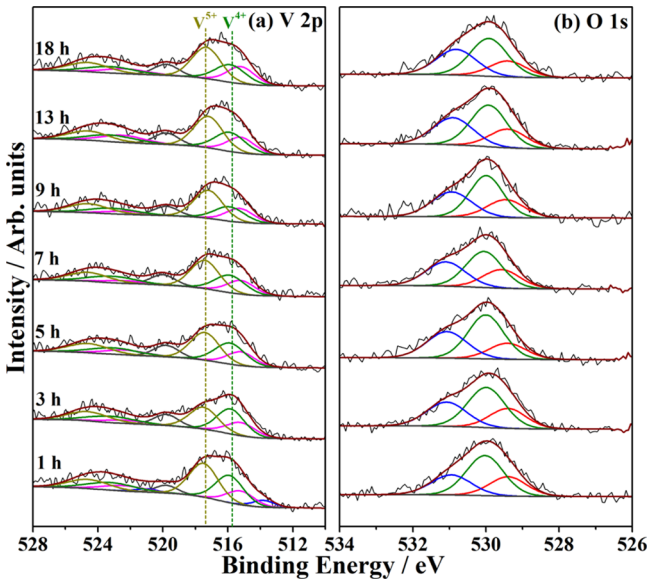

Figure 6. In situ NAP-XPS studies of (a) V 2p and (b) O 1s core-level spectra recorded on vanadium as a function of oxygen exposure time at a 0.1 mbar partial pressure of O_2 at 875 K.

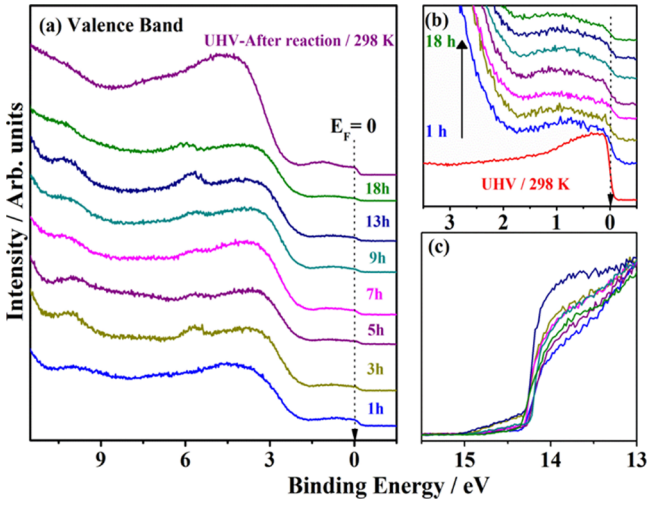

Figure 7. (a) Time-dependent evolution of V-oxidation from V-metal to a mixture of VO_2 and V_2O_5 at 1 mbar/875 K; however, NAP-UPS spectra were recorded at 0.1 mbar/875 K, (b) Fermi energy level, and (c) spectral offset features are shown at an enlarged scale.

the changes in ϕ. The results obtained are shown in Figure 7a−c. After every 2 h of oxygen treatment at 875 K and 1 mbar O_2 partial pressure, the spectrum was recorded at a 0.1 mbar O_2 pressure and compared in Figure 7. The NAP-UPS spectra recorded at 875 K show high E_F intensity, and this corresponds to the metallic nature of VO_2 and is dominant over the surface. This set of spectra are similar to the spectrum given in green/purple color in Figure 5a. Enlarged E_F features are shown in Figure 7b as a function of O_2 treatment at 875 K; however, the results show a very similar E_F pattern hinting at the stability of VO_2 under the measurement conditions. A minor decrease in E_F intensity is observed as the time of O_2 exposure increases. Nonetheless, no change in the photoelectron emission offset was observed (Figure 7c), which also supports the robust nature of VO_2 on the surface. Indeed, it is surprising that VO_2 does not undergo further oxidation, despite prolonged heating;

https://doi.org/10.1021/acs.jpcc.2c05212
J. Phys. Chem. C 2022, 126, 19136−19146

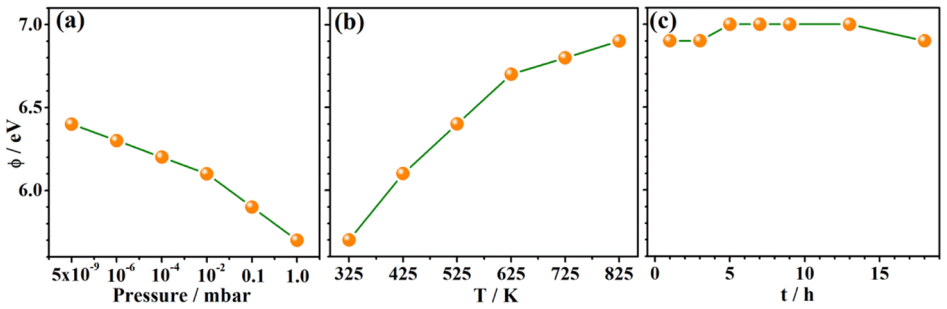

Figure 8. Changes in the work function of VO_x layers during the oxidation of metallic V to VO_x as a function of (a) O_2 partial pressure at 298 K, (b) temperature at a 0.1 mbar O_2 partial pressure, and (c) exposure time to a 1 mbar O_2 partial pressure at 875 K.

we speculate that the metallic character of VO_2 might hinder further oxidation until the oxidation condition becomes more severe. It is also to be noticed that on returning to 298 K under UHV, a metallic feature remains to be seen (dark-purple trace). However, a shift in the main VB to a higher BE suggests a significant change in the nature of surface oxide. A careful look at the O_2 gas-phase vibrational feature shifts to a high BE at t = 18 h, likely hinting at a possibility of the onset of further oxidation.

3.5. Relationship between Surface Composition and Work Function. The changes in the ϕ of the VO_x can be tuned by changing the stoichiometry of the surface.[35,39,40] The ϕ of VO_x at different stages of oxidation and those measured from the offset value of NAP-UPS spectra are plotted in Figure 8 as a function of (a) partial pressure of O_2, (b) temperature at 0.1 mbar O_2 pressure, and (c) time of exposure to O_2 at 1 mbar at 875 K. The change in the ϕ indicated that surface dipole changes with exposure to O_2. At UHV and 298 K, the ϕ of metallic V was observed to be 6.4 eV; however, it varies between 5.9 and 6.8 eV for VO_x. The change in ϕ depends on various factors, such as stoichiometry of VO_x, size of VO_x particles/islands, or growth of VO_x layers and the surrounding environment. With the increase in the O_2 partial pressure from metallic vanadium under UHV conditions to a 1 mbar partial pressure of O_2 at ambient temperature (Figure 8a), a decrease in the ϕ by 0.5 ± 0.05 eV was observed. However, when VO_x obtained in Figure 8a is exposed to a 0.1 mbar O_2 partial pressure at high temperatures, the ϕ increased from 5.9 eV at 298 K to 6.9 eV at 825 K (Figure 8b). However, in the time-dependent study (Figure 8c), the ϕ shows a marginal change of 0.1 eV. It is evident from the above data that the ϕ increases linearly with temperature and decreases linearly with O_2 partial pressure. While the temperature dependence at 0.1 mbar shows an increase in ϕ, metallic VO_2 observed at high temperatures is an unusual phenomenon with transition-metal oxides.

Indeed, VO_2 is an exceptional case; at least we are unaware that any other metal oxide turns metallic at such high temperatures (≥725 K). Furthermore, it is known in the literature that metallic behavior is due to the rutile phase of VO_2 with contribution from V t_{2g} and O 2p orbitals. Indeed, an interesting observation is the MI transition observed at high temperatures but at a 0.1 mbar O_2 partial pressure, while all the literature reports are carried out at ambient pressure with bulk/nano-VO_2 materials. It is also to be reemphasized that the thickness of VO_2 in the present experiments cannot be more than 10 nm, which is the probing depth of near-ambient-pressure XPS and observed along with a significantly larger amount of V_2O_5. Hence, it is very likely that VO_2 is present in the nanodomains with interweaving V_2O_5 under the present experimental conditions. The metallic E_F feature observed at 298 K in Figure 7a (dark-purple trace) could be possibly due to this, which is in contrast to the insulating behavior of bulk VO_2 below 340 K. Another interesting observation is the decrease in ϕ due to increasing O_2 partial pressure, but at 298 K, while ϕ increases with temperature at a 0.1 mbar O_2 partial pressure. While multiple oxidation states of vanadium are observed in both scenarios, the thickness of oxidation was really limited to 3−5 nm at 298 K with underlying metallic vanadium, and the oxidized layers' thickness reaches 10 nm at high temperatures in the latter case with predominant 4+ and 5+ oxidation states. There is a possibility that vanadium oxidation occurs in islands, rather than complete layers and discontinuously at 298 K, which cannot be ruled out. Studies with well-defined single-crystal surfaces might be required to understand this phenomenon.

A bird's eye view of the changes in oxidation states of vanadium as a function of all measurement conditions is shown in Figure 9. Changes in the V^0, V^{2+}, V^{3+}, V^{4+}, and V^{5+} content, which is measured from deconvolution of NAP-XPS results, as a function of (a) O_2 partial pressure at 298 K, (b) temperature at 0.1 mbar O_2 partial pressure, and (c) O_2 exposure time at 1 mbar and 875 K, is shown. Irrespective of the O_2 pressure, metallic vanadium content dominates the surface at 298 K, while all other oxidation states contribute to a comparable extent. This trend completely changes, when the temperature increases at 0.1 mbar O_2 pressure; the metallic vanadium and V^{5+} oxidation state decreases and increases, respectively, when the reaction conditions applied become severe. The metallic feature disappears completely above 625 K. The V^{2+} and V^{3+} content increases initially from 298 to 525 K, and thereafter, it decreases for a further increase in temperature. This underscores that the oxidation of vanadium occurs sequentially from lower to higher oxidation states. The predominant presence of V^{5+} followed by V^{4+} states, along with a minor amount of lower valence oxidation states, even after an 18 h O_2 treatment at 875 K at 1 mbar, reiterates that oxygen diffusion into bulk layers requires more severe conditions toward complete oxidation to V_2O_5. In the lab-based NAPPES system employed for the present measurements, exposure to higher pressure is not possible due to operational limitations.

CONCLUSIONS

In conclusion, we have examined the oxide formation of the V-foil. The surface layers of V-metal are systematically converted to a mixture of various oxides, such as VO, V_2O_3, VO_2, and V_2O_5 by using NAPPES methods by controlled oxidation of the V-foil at near-ambient pressures (0.1 mbar) and temper-

https://doi.org/10.1021/acs.jpcc.2c05212
J. Phys. Chem. C 2022, 126, 19136−19146

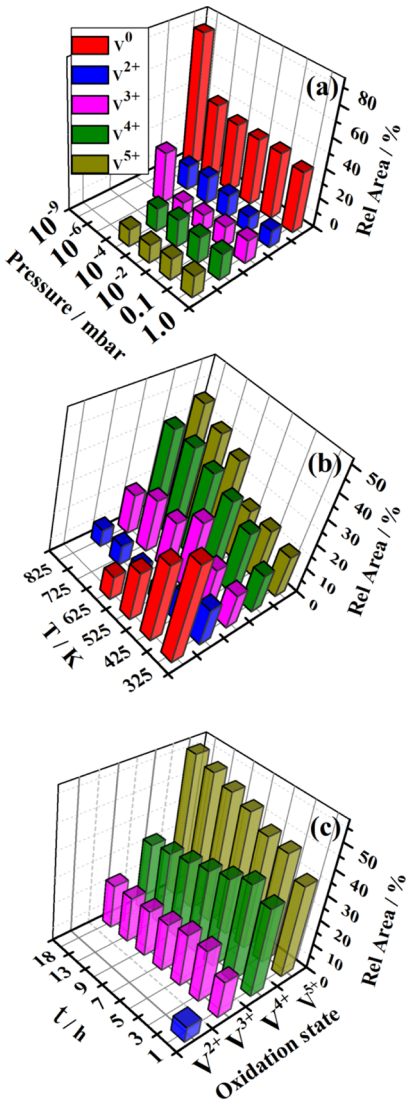

Figure 9. 3D plots of relative area percentage and various oxidation states of vanadium as a function of (a) partial pressure of O_2, (b) temperature, and (c) time.

atures (up to 875 K). V-metal gradually oxidizes to VO and then slowly starts evolving to V_2O_3 and VO_2; approximately 56% of V-metal oxidizes to higher oxidation states (VO_x). Complete oxidation is not observed at 0.1 mbar O_2 pressure and 298 K. At a 0.1 mbar O_2 pressure and a temperature above 625 K, the metallic feature disappears completely and the systematic growth of VO_2 is observed. Furthermore, the transition of V_2O_3 to VO_2 is observed at high temperatures (>725 K) along with MI transition. Although the MI transition was first observed at high temperatures, it is stable even at ambient temperatures, which is worth investigating further. The present investigations reveal not only the formation of VO_x with various stoichiometries but also the diffusion of atomic oxygen into the layers of the V-surface. The oxygen diffusion rate increases at high temperatures and decreases at high pressure, possibly due to the oxide layers, which prevents further oxidation. VO_x formation is further confirmed through a change in ϕ of the surface.

The diffusion of oxygen and VO_x formation is identified through V 3d−O 2p interaction in NAP-UPS. Changes in the width of oxygen vibration features characterize the formation of heterogeneous natures due to the formation of a mixture of VO_x.[26] ϕ is the key electronic property of a surface that mainly depends on the structure and electronic nature of the surface, and it is measured under the realistic conditions or close to them. Furthermore, above 625 K, metallic V predominantly oxidized to a mixture of oxides of V^{3+}, V^{4+}, and V^{5+} oxidation states at a 0.1 mbar partial pressure of O_2. The change in DOS near E_F observed above 723 K at a 0.1 mbar O_2 partial pressure demonstrates the metallic nature due to VO_2 formation. Although other VO_x are present, the metallic feature characterizes the dominance of VO_2, even in the presence of nanodomains of other VO_x. Critically, the metallic nature preserved even at ambient temperature is worth investigating further with other methods, particularly for conductivity and microscopy studies. Indeed, a thin-film form of VO_2 with other VO_x could still be a potential solution for many applications. It is amply clear that the NAPPES study can explore the electronic structure evolution as a function of reaction conditions, and it underscores its relevance to areas such as heterogeneous catalysis and sensing.

■ ASSOCIATED CONTENT

Supporting Information

The Supporting Information is available free of charge at https://pubs.acs.org/doi/10.1021/acs.jpcc.2c05212.

Deconvolution and quantification parameters, mass spectrum for hydrogen back-streaming, and quantification of various V-oxidation states (PDF)

■ AUTHOR INFORMATION

Corresponding Author

Chinnakonda S. Gopinath − *Catalysis and Inorganic Chemistry Division, CSIR—National Chemical Laboratory, Pune 411 008, India; Academy of Scientific and Innovative Research (AcSIR), Ghaziabad 201 002, India;* orcid.org/0000-0002-4525-3912; Email: cs.gopinath@ncl.res.in

Authors

Ravi Ranjan − *Catalysis and Inorganic Chemistry Division, CSIR—National Chemical Laboratory, Pune 411 008, India; Academy of Scientific and Innovative Research (AcSIR), Ghaziabad 201 002, India*

Nitin B. Mhamane − *Catalysis and Inorganic Chemistry Division, CSIR—National Chemical Laboratory, Pune 411 008, India; Academy of Scientific and Innovative Research (AcSIR), Ghaziabad 201 002, India*

Sadhu K. Kolekar − *Catalysis and Inorganic Chemistry Division, CSIR—National Chemical Laboratory, Pune 411 008, India*

Complete contact information is available at: https://pubs.acs.org/10.1021/acs.jpcc.2c05212

Notes

The authors declare no competing financial interest.

■ ACKNOWLEDGMENTS

R.R. and N.B.M. are thankful to the DST-INSPIRE and UGC, New Delhi, respectively, for research fellowships.

REFERENCES

(1) Griffiths, C. H.; Eastwood, H. K. Influence of Stoichiometry on the Metal-Semiconductor Transition in Vanadium Dioxide. *J. Appl. Phys.* **1974**, *45*, 2201−2206.

(2) Whittaker, L.; Zhang, H.; Banerjee, S. VO_2 Nanosheets Exhibiting a Well-Defined Metal-Insulator Phase Transition. *J. Mater. Chem.* **2009**, *19*, 2968−2974.

(3) Sivaranjani, K.; Verma, A.; Gopinath, C. S. Molecular Oxygen-Assisted Oxidative Dehydrogenation of Ethylbenzene to Styrene with Nanocrystalline $Ti_{1-x}V_xO_2$. *Green Chem.* **2012**, *14*, 461−471.

(4) Shiju, N. R.; Anilkumar, M.; Mirajkar, S. P.; Gopinath, C. S.; Rao, B. S.; Satyanarayana, C. V. Oxidative dehydrogenation of ethylbenzene over vanadia-alumina catalysts in the presence of nitrous oxide: structure-activity relationship. *J. Catal.* **2005**, *230*, 484−492.

(5) Talledo, A.; Granqvist, C. G. Electrochromic Vanadium-Pentoxide-Based Films: Structural, Electrochemical, and Optical Properties. *J. Appl. Phys.* **1995**, *77*, 4655−4666.

(6) Devaraji, P.; Sathu, N. K.; Gopinath, C. S. Ambient oxidation of benzene to phenol by photocatalysis on $Au/Ti_{0.98}V_{0.02}O_2$: Role of Holes. *ACS Catal.* **2014**, *4*, 2844−2853.

(7) Herman, I. P. *Electrical and Magnetic Properties*; Springer: Cham, Switzerland, 2016; pp 819−871.

(8) Shik, S.; Suga, S.; Taniguchi, M.; Kanzaki, H. Vacuum-ultraviolet reflectance and photoemission study of the metal-insulator phase transitions in VO_2, V_6O_{13}, and V_2O_3. *Phys. Rev. B: Condens. Matter Mater. Phys.* **1990**, *41*, 4993−5009.

(9) Langeslay, R. R.; Kaphan, D. M.; Marshall, C. L.; Stair, P. C.; Sattelberger, A. P.; Delferro, M. Catalytic Applications of Vanadium: A Mechanistic Perspective. *Chem. Rev.* **2019**, *119*, 2128−2191.

(10) Gopinath, C. S.; Roy, K.; Nagarajan, S. Can We Shift and/or Broaden the Catalysis Regime towards Ambient Temperature? *ChemCatChem* **2015**, *7*, 588−594.

(11) Klein, A.; Körber, C.; Wachau, A.; Säuberlich, F.; Gassenbauer, Y.; Harvey, S. P.; Proffit, D. E.; Mason, T. O. Transparent Conducting Oxides for Photovoltaics: Manipulation of Fermi Level,Work Function and Energy Band Alignment. *Materials* **2010**, *3*, 4892−4914.

(12) Walsh, A.; Catlow, C. R. A. Structure, Stability and Work Functions of the Low Index Surfaces of Pure Indium Oxide and Sn-Doped Indium Oxide (ITO) from Density Functional Theory. *J. Mater. Chem.* **2010**, *20*, 10438−10444.

(13) Son, M. J.; Kim, S.; Kwon, S.; Kim, J. W. Interface Electronic Structures of Organic Light-Emitting Diodes with WO_3 Interlayer: A Study by Photoelectron Spectroscopy. *Org. Electron.* **2009**, *10*, 637−642.

(14) Meyer, J.; Khalandovsky, R.; Görrn, P.; Kahn, A. MoO_3 Films Spin-Coated from a Nanoparticle Suspension for Efficient Hole-Injection in Organic Electronics. *Adv. Mater.* **2011**, *23*, 70−73.

(15) Gopinath, C. S.; Nalajala, N. Scalable and thin film approach for solar hydrogen generation: A review on enhanced photocatalytic water splitting. *J. Mater. Chem. A.* **2021**, *9*, 1353−1371.

(16) Rajaambal, S.; Sivaranjani, K.; Gopinath, C. S. Recent Developments in Solar H_2 Generation from Water Splitting. *J. Chem. Sci.* **2015**, *127*, 33−47.

(17) Ko, C.; Yang, Z.; Ramanathan, S. Work Function of Vanadium Dioxide Thin Films across the Metal-Insulator Transition and the Role of Surface Nonstoichiometry. *ACS Appl. Mater. Interfaces* **2011**, *3*, 3396−3401.

(18) Shao, Z.; Cao, X.; Luo, H.; Jin, P. Recent Progress in the Phase-Transition Mechanism and Modulation of Vanadium Dioxide Materials. *NPG Asia Mater.* **2018**, *10*, 581−605.

(19) Goodenough, J. B. The Two Components of the Crystallographic Transition in VO_2. *J. Solid State Chem.* **1971**, *3*, 490−500.

(20) Shibuya, K.; Kawasaki, M.; Tokura, Y. Metal-Insulator Transition in Epitaxial $V_{1-x}W_xO_2$ ($0 \le x \le 0.33$) Thin Films. *Appl. Phys. Lett.* **2010**, *96*, 022102.

(21) Kim, C. Y.; Slusar, T.; Cho, J.; Kim, H. T. Mott Switching and Structural Transition in the Metal Phase of VO_2 Nanodomain. *ACS Appl. Electron. Mater.* **2021**, *3*, 605−610.

(22) Morin, F. J. Oxides which show metal to insulator transition at the neel temperature. *Phys. Rev. Lett.* **1959**, *3*, 34−36.

(23) Reddy, K. P.; Mhamane, N. B.; Ghosalya, M. K.; Gopinath, C. S. Mapping Valence Band and Interface Electronic Structure Changes during the Oxidation of Mo to MoO_3 via MoO_2 and MoO_3 Reduction to MoO_2: A NAPPES Study. *J. Phys. Chem. C* **2018**, *122*, 23034−23044.

(24) Jain, R.; Reddy, K. P.; Ghosalya, M. K.; Gopinath, C. S. Water Mediated Deactivation of Co_3O_4 Naonrods Catalyst for CO Oxidation and Resumption of Activity at and above 373 K: Electronic Structural Aspects by NAPPES. *J. Phys. Chem. C* **2017**, *121*, 20296−20305.

(25) Reddy, K. P.; Jain, R.; Ghosalya, M. K.; Gopinath, C. S. Metallic Cobalt to Spinel Co_3O_4-Electronic Structure Evolution by near-Ambient Pressure Photoelectron Spectroscopy. *J. Phys. Chem. C* **2017**, *121*, 21472−21481.

(26) Ghosalya, M. K.; Prabhakar Reddy, K.; Mhamane, N. B.; Ranjan, R.; Gopinath, C. S. Gas-Solid Interactions with Reactive and Inert Gas Molecules by NAPUPS: Can Work Function Be a Better Descriptor of Chemical Reactivity? *Phys. Chem. Chem. Phys.* **2020**, *22*, 15528−15540.

(27) Ghosalya, M. K.; Jain, R.; Reddy, K. P.; Gopinath, C. S. Silicon Oxidation by NAPPES: From Dangling Bonds to Oxygen Islands to 2D SiO_x Layer to the Onset of Bulk SiO_2 Formation. *J. Phys. Chem. C* **2018**, *122*, 4331−4338.

(28) Kolekar, S. K.; Dubey, A.; Date, K. S.; Datar, S.; Gopinath, C. S. An Attempt to Correlate Surface Physics with Chemical Properties: Molecular Beam and Kelvin Probe Investigations of $Ce_{1-x}Zr_xO_2$ Thin Films. *Phys. Chem. Chem. Phys.* **2016**, *18*, 27594−27602.

(29) Ghosalya, M. K.; Reddy, K. P.; Jain, R.; Roy, K.; Gopinath, C. S. Subtle Interaction between Ag and O_2: A Near Ambient Pressure UV Photoelectron Spectroscopy (NAP-UPS) investigations. *J. Chem. Sci.* **2018**, *130*, 30.

(30) Roy, K.; Vinod, C. P.; Gopinath, C. S. Design and Performance Aspects of a Custom-Built Ambient Pressure Photoelectron Spectrometer toward Bridging the Pressure Gap: Oxidation of Cu, Ag, and Au Surfaces at 1 mbar O_2 Pressure. *J. Phys. Chem. C* **2013**, *117*, 4717−4726.

(31) Roy, K.; Gopinath, C. S. UV Photoelectron Spectroscopy at near Ambient Pressures: Mapping Valence Band Electronic Structure Changes from Cu to CuO. *Anal. Chem.* **2014**, *86*, 3683−3687.

(32) Fairley, N.; Fernandez, V.; Richard-Plouet, M.; Guillot-Deudon, C.; Walton, J.; Smith, E.; Flahaut, D.; Greiner, M.; Biesinger, M.; Tougaard, S.; Morgan, D.; Baltrusaitis, J. Systematic and collaborative approach to problem solving using X-ray photoelectron spectroscopy. *Appl. Surf. Sci. Adv.* **2021**, *5*, 100112.

(33) Biesinger, M. C.; Payne, B. P.; Grosvenor, A. P.; Lau, L. W. M.; Gerson, A. R.; Smart, R. S. C. Resolving Surface Chemical States in XPS Analysis of First Row Transition Metals, Oxides and Hydroxides: Cr, Mn, Fe, Co and Ni. *Appl. Surf. Sci.* **2011**, *257*, 2717−2730.

(34) Sawatzky, G.; Post, A. D. X-ray photoelectron and Auger spectroscopy Study of some vanadium oxides. *Phys. Rev. B: Condens. Matter Mater. Phys.* **1979**, *20*, 1546−1555.

(35) Wang, R.; Katase, T.; Fu, K. K.; Zhai, T.; Yang, J.; Wang, Q.; Ohta, H.; Koch, N.; Duhm, S. Oxygen Vacancies Allow Tuning the Work Function of Vanadium Dioxide. *Adv. Mater. Interfaces* **2018**, *5*, 1801033.

(36) Roy, K.; Jain, R.; Gopinath, C. S. Sustainable and Near Ambient $DeNO_x$ Under Lean Burn Conditions: A Revisit to NO Reduction on Virgin and Modified Pd (111) Surfaces. *ACS Catal.* **2014**, *4*, 1801−1811.

(37) Mhamane, N. B.; Chetry, S.; Ranjan, R.; Raja, T.; Gopinath, C. S. Sustainable CO_2 Reduction on In_2O_3 with Exclusive CO Selectivity: Catalysis and In Situ Valence Band Photoelectron Spectral Investigations. *ACS Sustainable Chem. Eng.* **2022**, *10*, 3521−3531.

(38) Ilinski, A.; Silva-Andrade, F.; Shadrin, E.; Klimov, V. Variations in optical reflectivity in the semiconductor−metal phase transition of vanadium dioxide. *J. Non-Cryst. Solids* **2004**, *338−340*, 266−268.

https://doi.org/10.1021/acs.jpcc.2c05212
J. Phys. Chem. C 2022, 126, 19136−19146

(39) Wu, Q. H.; Thissen, A.; Jaegermann, W.; Liu, M. Photoelectron Spectroscopy Study of Oxygen Vacancy on Vanadium Oxides Surface. *Appl. Surf. Sci.* **2004**, *236*, 473−478.
(40) Greiner, M. T.; Lu, Z. H. Thin-Film Metal Oxides in Organic Semiconductor Devices: Their Electronic Structures, Work Functions and Interfaces. *NPG Asia Mater.* **2013**, *5*, No. e55.

https://doi.org/10.1021/acs.jpcc.2c05212
J. Phys. Chem. C 2022, 126, 19136−19146

Chemical Engineering Journal 471 (2023) 144459

Contents lists available at ScienceDirect

Chemical Engineering Journal

journal homepage: www.elsevier.com/locate/cej

Co_3O_4 for sustainable CO_2 reduction and possible fine-tuning towards selective CO production

Ravi Ranjan [a,b], Jyoti Tekawadia [a,b], Ruchi Jain [a,b], Nitin B. Mhamane [a,b], Thirumalaiswamy Raja [a,b], Chinnakonda S. Gopinath [a,b,*]

[a] Catalysis and Inorganic Chemistry Division, CSIR - National Chemical Laboratory, Dr. Homi Bhabha Road, Pune 411 008, India
[b] Academy of Scientific and Innovative Research (AcSIR), Ghaziabad 201 002, India

ARTICLE INFO

Keywords:
Heterogeneous catalysis
Carbon neutral economy
RWGS
SDG
Surface science

ABSTRACT

Two main challenges involved in heterogeneous catalytic CO_2 reduction are: (a) decreasing the consumption of H_2 to the minimum required level with possibly the maximum CO_2 conversion, and (b) concurrently enhancing the selectivity of the desired CO, at the cost of methane. Towards meeting these two challenges, Co_3O_4 spinel has been identified as a potential catalyst and it exhibits predominant CO selectivity $\geq$ 673 K at atmospheric pressure. CO_2 conversion begins $\geq$ 523 K, with 100% CO selectivity observed $\geq$ 673 K with CO_2:H_2 = 3:2. Current work shows a sustainable catalytic CO_2 conversion to 100% CO selectivity with Co_3O_4-Nanocube (NC). Critically, CO selectivity and yield is observed to increase at the cost of methane with smaller amount of H_2. 1:1 and 3:2 CO_2:H_2 ratio exhibits 88–100% CO selectivity with 24–32.5% CO_2 conversion between 623 and 823 K. Irrespective of the input CO_2:H_2, ratio of CO_2:H_2 uptake changes from around 1:3 at 523 K to 1:1–1.5 at 823 K with concurrent production of significant methane to predominant CO, respectively. Surface electronic state changes was explored by near ambient pressure photoelectron spectroscopy, and the results suggests that Co_3O_4 is the active phase that promotes CO_2 reduction selectively to CO. Broadening observed with the vibrational feature of the CO_2 molecules at high temperature underscores the heterogeneous character of the catalyst surface, under operating conditions, due to changing electron density. By optimizing the gas hourly space velocity (GHSV), H_2-lean CO_2:H_2 ratio, and the reaction temperature/pressure, 100% CO selectivity could be broadened to a range of operating conditions.

1. Introduction

Carbon dioxide (CO_2) is a colorless and odorless greenhouse gas responsible for ocean acidification and climate change [1]. The burning of fossil fuels in various industries and automobiles has resulted in the massive emission of greenhouse gases, leading to an alarming increase in the concentration of CO_2 in the environment; and critically it continues to increase due to increasing consumption of various commodities and increasing population. [2–5]. To combat this issue, different approaches are being explored to control the concentration of CO_2 in the atmosphere, including carbon capture and storage (CCS) and carbon capture and utilization (CCU). Present work is a part of CCU and focusing only on CO_2 utilization. CCU involves the conversion of CO_2 into valuable chemicals and fuels by various methods. Among these, a promising and scalable route for the conversion of CO_2 to C1-oxygenates, such as CO, methanol, has been widely investigated in recycling technology. While the conversion of CO_2 to methane is also possible, it is not preferred due to the added cost and energy required for compression and transportation. Liquid products, like methanol, are preferred due to their high volumetric energy density. CO is also an important building block molecule, and along with hydrogen, it can be used to produce many liquid chemicals and fuels through Fischer-Tropsch ((FT) synthesis) [6–8]. Transition metal-based catalysts have been found to be a promising approach for the catalytic conversion of CO_2 to achieve high conversion and product selectivity and low cost compared to precious metal catalyst [9,10]. However, there are challenges associated with CO_2 conversion. The CO_2 molecule is symmetric and linear, with a high heat of formation (−395 kJ/mol), and the strong O═C bonds (O═C═O) make it very stable. The enthalpy required to break the O═C bond into CO and O is very high (+293 kJ/mol), making CO_2 activation difficult [11].

The reduction of CO_2 to CO and water via hydrogenation is a well-

* Corresponding author.
E-mail address: cs.gopinath@ncl.res.in (C.S. Gopinath).

https://doi.org/10.1016/j.cej.2023.144459
Received 5 March 2023; Received in revised form 22 June 2023; Accepted 26 June 2023
Available online 28 June 2023

known process called the reverse water gas shift (RWGS) reaction. However, achieving high CO_2 conversion with high selectivity towards CO is a major challenge due to possible methane formation. This issue can be addressed by decreasing the H_2 content and increasing the CO_2 content to suppress the formation of methane and water; indeed adsorbed ratio of reactants is more important than the input feed ratio of reactants. In addition, employing lower than stoichiometric amount of hydrogen would be cost-effective, from an industrial viewpoint. The present work focuses precisely on addressing this challenge, resulting in a significantly large CO_2 conversion to CO with a 1:1 and 3:2 ratio of CO_2:H_2. Furthermore, using less than stoichiometric amounts of H_2 decreases the methane selectivity. Since shale gas reserves are widely available, low volumetric energy density and transportation issues associated with methane may be avoided. Therefore, the catalyst should also possess oxygen storage with redox capability, making Co_3O_4 an ideal catalyst for CO_2 reduction. The process of CO_2 reduction involves three main reactions: CO_2 methanation, RWGS, and methanol formation, as shown in equations (1), (2), and (3), respectively,

$$CO_2 + 4H_2 \rightarrow CH_4 + 2H_2O \quad \Delta H^0{}_{298K} = -165KJ/mol \tag{1}$$

$$CO_2 + H_2 \rightleftharpoons CO + H_2O \quad \Delta H^0_{298K} = 41.2kJ/mol \tag{2}$$

$$CO_2 + 3H_2 \rightarrow CH_3OH + H_2O \quad \Delta H^0_{298K} = -50kJ/mol \tag{3}$$

However, the most desirable pathway is the conversion of CO_2 to CO, which is a key feedstock molecule for the FT process. It is worth noting that even if the current global demand for CH_3OH could be met by CO_2, it would only reduce global CO_2 emissions by 0.1%. Additionally, methanation requires a large amount of H_2, while RWGS requires the least. Therefore, achieving high selectivity towards CO by using the minimum required H_2 would be prudent.

One of the main challenges of RWGS is to ensure the catalyst remains active over a prolonged period. Recent research on active catalysts for CO_2 reduction has focused on optimizing their properties by altering the composition, particle size, and oxidation state [12,13]. For instance, Co-based catalysts with an average particle size of 10 nm exhibited three times higher turnover frequency than those with a 3 nm particle size [14,15]. However, in some recent studies, surface structure and properties have been overlooked, despite the fact that the top few atomic layers of the catalyst surface actively participate in the catalytic reaction [16,17]. Understanding the evolution of surface changes under different reaction conditions is crucial. For example, metallic Co on SiO_2 support is four times more active than oxidized cobalt catalyst for CO_2 reduction [13,18,19]. On the other hand, metallic Co on TiO_2 support has shown to be five times less active than oxidized Co on the same support due to metal-support interaction. The activity of metallic Co on different supports varies, and it may be worthwhile to explore these differences further. Transition metal-based catalysts, such as nickel, cobalt, and ruthenium, have been found to be economical and efficient for CO_2 reduction. While other catalysts, like Cu/ZnO, can partially reduce CO_2 to methanol [16,20], the electronic and geometric structure, caused by a specific morphology of the catalyst, such as Cu/ZnO nanoplates or Cu-Ni/CeO_2 nanotubes, can fine-tune the selectivity of CO_2 reduction [21,22].

Spinel cobalt oxide ($Co^{2+}Co_2^{3+}O_4$), particularly, is a promising active material with tunable redox properties and high potential for catalytic activity in CO_2 reduction. Spinel Co_3O_4 is known to consist tetrahedrally (T_d) coordinated Co^{2+} sites and octahedrally (O_h) coordinated Co^{3+} sites, which exhibit interesting chemistry at the nanoscale. This effects in a high degree of heterogeneity on the catalytically relevant surface structure due to changes in different facets [23–25], point defects [26], and particle size [14]. Recent studies have also shown that the oxide support can significantly influence the product selectivity of CO_2 reduction. For instance, PtCo bimetal supported on TiO_2 (CeO_2 and ZrO_2) exhibits high (low) selectivity to CO (CH_4) [27]. Therefore, in situ spectral studies of a heterogeneous catalyst under relevant conditions or closer to those conditions are important for fundamental understanding of surface chemistry and its correlation to catalytic performance. Identification of the active state of the catalyst under reaction conditions is crucial for further improving its activity and selectivity.

An overall view of literature results [13,14,23,24,28,29], especially based on Co-based catalysts, suggest the following: Generally CO_2 reduction has been carried out with H_2-rich CO_2:H_2 (1:x, $x \geq 3$) feed. In general, metallic Co as an active phase leads to methanation of CO_2 with H_2-rich CO_2:H_2 (1:x, $x \geq 3$) feed; this is due to facile activation of H_2 and CO_2. However, cobalt oxides leads to variety of products and it depends on the nature of the support, reaction conditions, due to strong (weak) CO_2 (H_2) activation on Co-oxides; for example, methanol and C_{2+} alcohols are reported on Co-oxides. Other Co-containing catalysts, such as carbides, lead to light olefins. Generally H_2-rich CO_2 feed on metallic Co or mixed valent cobalt oxide has been employed and no studies are available on stoichiometric or lower than stoichiometric CO_2:H_2 feed ratios. By employing H_2-lean CO_2-feed, maintaining the mixed valent character of cobalt oxide is possible, which can show sustainable CO_2 activation. In addition, high selectivity of a product might be possible by maintaining a single type of crystallographic facet, which is not reported so far; often mixed products formation observed with cobalt oxides makes the products separation inevitable. Indeed, NC morphology is very apt for this, as it exposes only (1 0 0) crystallographic facets on all six sides of NC particles; this type of uniform active sites available abundantly on the catalyst surface is likely to lead to higher activity and the highest selectivity. Although optimizing the reaction conditions could change the activity/selectivity to some extent, it is highly unlikely to achieve the best activity/selectivity without inherent activity of the catalyst. Present work attempted to optimize the reactants and energy, while improving selectivity towards the desired result of producing selective CO. By employing NC morphology of Co_3O_4 with H_2-lean feeds, highly selective CO production is observed in the present work; this also emphasize the need to explore more with H_2-lean feeds.

In the current study, we have investigated the potential of Co_3O_4 NC catalyst for CO_2 reduction under realistic conditions using a fixed bed reactor. Current analysis includes studying the influence of factors such as CO_2:H_2 ratio, temperature, and time on stream (ToS) on the reaction. Reaction results indicate that the highest CO selectivity is achieved at temperatures between 673 and 823 K, particularly when the feed mixture has a H_2:$CO_2 \leq 1$. Additionally, we examined the changes in the nature of the catalyst when a 1:3 CO_2:H_2 feed ratio was employed by utilizing near-ambient pressure photoelectron spectroscopy (NAPPES) at 0.1 mbar pressures up to 675 K. We also assessed the reactivity of the catalyst after reducing Co_3O_4 to CoO and Co metal through in situ reduction in the presence of hydrogen. NAPPES results reveal a significant alteration in the oxidation state of Co and the surface work function of Co_3O_4 NC under realistic conditions, which correlates well with catalysis results. Present findings demonstrate the active state of the catalyst under working conditions and bridge the pressure gap between surface science and real-world catalysis.

2. Experimental and characterization

2.1. Synthesis of Co_3O_4 NC

Co_3O_4 NC was synthesized using the wet chemical synthesis method as reported in the literature [30]. Specifically, a template-free hydrothermal method was employed, with $Co(OAC)_2{\cdot}4H_2O$ (Alfa Aesar) serving as the cobalt precursor. A 2.5 mmol precursor was dissolved in 125 ml of water and stirred at 298 K for 30 min. Aqueous ammonia was then added drop-wise to the solution until the pH reached 9, indicated by a color change from pink-red to blue. The solution was further stirred for 30 min and then transferred into a 200 ml autoclave with a Teflon liner and heated at 453 K for 10 h. The resulting Co_3O_4 solid was filtered and washed multiple times with water. Finally, the sample was calcined

in air at 623 K for 3 h.

2.2. Characterization methods

The powder X-ray diffraction (XRD) measurements were performed on a PANalytical X'pert Pro dual goniometer diffractometer equipped with Cu-Kα (1.5418 Å) radiation, operating at 40 kV and 40 mA in a continuous mode with a scanning rate of 2°/min in the 2θ range from 10° to 80°. The morphology and composition of the freshly prepared sample were characterized using a FEI NOVA NANOSEM 450 scanning electron microscope (SEM) with energy dispersive X-ray (EDX) analysis, and the shape, size, and lattice fringes of Co_3O_4 NC were identified using a FEI Technai TF-20 electron microscope operating at 200 keV with high-resolution transmission electron microscopy (HR-TEM) measurements. The H_2-temperature programmed reduction (H_2-TPR) experiment was carried out using a Micromeritics Autochem 2920 system, equipped with a thermal conductivity detector (TCD). Initially, the fresh catalyst was heated to 573 K in helium (30 ml/min) at a ramping rate of 5 K/min, and kept at 573 K for 30 min before cooling to room temperature. The gas was then changed to 10% H_2 in Ar gas, and the catalyst was heated to 1000 K at a rate of 5 K/min. The H_2 consumption was measured as a function of temperature.

2.3. In-situ XPS and UPS experiments

A NAPPES setup was utilized to investigate changes in oxidation state resulting from interactions between different phases of cobalt oxide and CO_2 and H_2 gases over a wide range of temperatures. The core level and valence band (VB) spectra of Co_3O_4 catalyst were monitored as a function of reaction conditions. Photoelectron spectra were obtained in the 295–675 K temperature range, ranging from ultrahigh vacuum ((UHV) 1×10^{-10} mbar) to 0.1 mbar (reactants) pressures in NAPPES unit equipped with differentially pumped R3000HP (VG Scienta) analyzer, Al-Mg dual anode X-ray source, and a discharge lamp that generated He I ($h\nu = 21.2$ eV) UV radiation to record XPS and VB results, respectively [31,32]. VB spectra were recorded using near ambient pressure ultraviolet photoelectron spectroscopy (NAP-UPS) with a He I photon source at pass energy of 5 eV. NAP-UPS is highly sensitive to surface absorbates and surface changes, providing exclusive information about the top 2 nm of material surfaces. To prepare the sample for NAPPES measurements, 10 mg of catalyst was sonicated in isopropyl alcohol for 10 min., followed-by drop casting on Au foil, and drying at 333 K, and then heated in a muffle furnace at 473 K for 30 min to remove any surface contamination. All in situ experiments were carried out at predominantly at 0.1 mbar pressure, with a CO_2:H_2 ratio of 1:3, and 99.9% pure CO_2 and H_2 was used. It should be noted that 1 mbar CO_2 + H_2 treatment was performed during controlled reduction (Co_3O_4 to CoO and Co); however, any spectra (NAP-XPS and NAP-UPS) were recorded at 0.1 mbar partial pressure. All spectra were calibrated with respect to the E_F of aclean gold foil and normalized against room temperature measurement data. CasaXPS software was used for peak deconvolution and spectral analysis; Shirley background removal was used for background corrections. The goodness of fitting was confirmed with γ^2 below 0.2. All spectra were deconvoluted after subtracting the Shirley-type background.

2.4. CO_2 catalytic reduction

The CO_2 reduction reaction was performed in a fixed-bed down flow reactor with an internal diameter of 12 mm and length of 40 cm at atmospheric pressure. A thermocouple was positioned at the center of the 1 cm^3 catalyst bed. The catalyst particles had a size range of 35–50 mesh and were mixed with alumina pieces of equal volume and particle size, and placed in the uniform heating zone of the tubular reactor. The catalyst was pre-heated in static air to 523 K at a rate of 5 K/min and held at the same temperature for 2 h before the reaction. The experiment was conducted at desired reaction temperatures. The gaseous products were analyzed online using a Trace 3110 gas chromatograph (Thermoscientific) equipped with a thermal conductivity detector (TCD) and a Porapak Q column (column diameter = 0.2 mm and length = 6 m). Before the experiment, a calibrated gas mixture was used to identify the gas components. We evaluated the catalytic activity and selectivity of Co_3O_4 NC at temperatures of 450 and 823 K and with CO_2:H_2 ratios of 1:3, 1:2, 1:1, and 3:2. The CO_2 + H_2 gas mixture was generated using mass flow controllers specific for H_2 and CO_2. It is worth noting that no carrier gas was used with the reactant, which is advantageous from a process standpoint and indicates that product desorption does not require any carrier gas. Before starting any reaction measurements by GC analysis, the reaction temperature was allowed to stabilize for approximately 30 min to reach steady state. The total flow rate of gas mixture was 320 ml/min and the gas hourly space velocity (GHSV) was 19200 h^{-1} for the entire reactor studies. High GHSV ensures that mass transfer resistance has no significant role in the present studies. Time on stream (TOS) was also conducted for 12 h with a 3:2 CO_2:H_2 ratio at temperatures of 623 and 723 K. The reaction conversion and product selectivity were calculated using the following equations:

$$CO_2\ \text{Conversion}\ (\%) = \frac{nCO_2(\text{in}) - nCO_2(\text{out})}{CO_2\ (\text{in})}\ \text{X}\ 100$$

$$H_2\ \text{Conversion}\ (\%) = \frac{nH_2\ (\text{in}) - nH_2\ (\text{out})}{nH_2\ (\text{in})} \times 100$$

$$\text{CO Selectivity}(\%) = \frac{n\text{CO}\ (\text{out})}{n\text{CO}\ (\text{out}) + nCH_4\ (\text{out})} \times 100$$

$$CH_4\ \text{Selectivity}(\%) = \frac{nCH_4(\text{out})}{n\text{CO}\ (\text{out}) + nCH_4\ (\text{out})} \times 100$$

3. Results and discussion

3.1. Texture characterization of Co_3O_4 NC

The X-ray diffraction (XRD) analysis of both the fresh and spent catalysts is shown in Fig. 1; spent catalyst was recovered after the reaction carried out at 723 K for 12 h with 3:2 CO_2:H_2 ratio. The XRD pattern of the fresh catalyst, as shown in Fig. 1a, exhibits characteristic

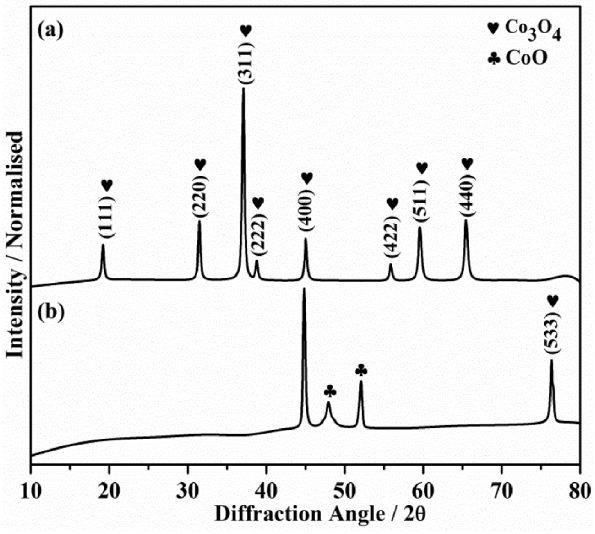

Fig. 1. The X-ray diffraction (XRD) patterns of the Co_3O_4 catalyst are presented, with (a) representing the fresh catalyst and (b) representing the spent catalyst. The spent catalyst was obtained after conducting the CO_2 reduction reaction with a feed ratio of 3:2 of CO_2:H_2 at 723 K for 12 h.

features at 2θ = 19.3, 31.5, 37, 38.8, 45, 55.8, 59.5, and 65.4°, corresponding to the (111), (220), (311), (222), (400), (422), (511), and (400) facets of cubic Co_3O_4, respectively. These observations are consistent with the literature values (JCPDS 65–3103), indicating that the catalyst has a cubic spinel structure. However, after the reaction at 723 K, new facets have emerged, along with an intense (400) feature, as shown in Fig. 1b. The intensity of the (400) facet is the highest and appears as the parent peak, and the peak at 2θ = 47.91° and 52.8° correspond to CoO phase, and peak at 2θ = 76.3 correspond to (533) phase of Co_3O_4crystalfacets were observed in Fig. 1b.

Indeed, this observation suggests a restructuring of the surface and high intensity (400) facet suggests a surface with step like structure on the surface. NC exposes (100) facet on all six sides of the cube and observation of (400) is not unusual; however, disappearance of all other peaks and appearance of CoO features needed more investigation. The particle size and morphology of the fresh and spent Co_3O_4 NC catalysts were examined by TEM, and the results are presented in Fig. 2a-c and 2d-e, respectively. TEM results indicate that the fresh Co_3O_4 material has a cubic morphology, and the high magnification image of a single cube (Fig. 2a) reveals a size of 30–35 nm, suggesting that the NC catalysts are faceted(100) orientation. The particle size was found to be in the range of 20–50 nm, with a predominant size of 30 ± 5 nm. The XRD analysis of Co_3O_4 NC shows that the preferentially exposed plane is (311). The Co_3O_4 morphology should preferentially expose the (100)

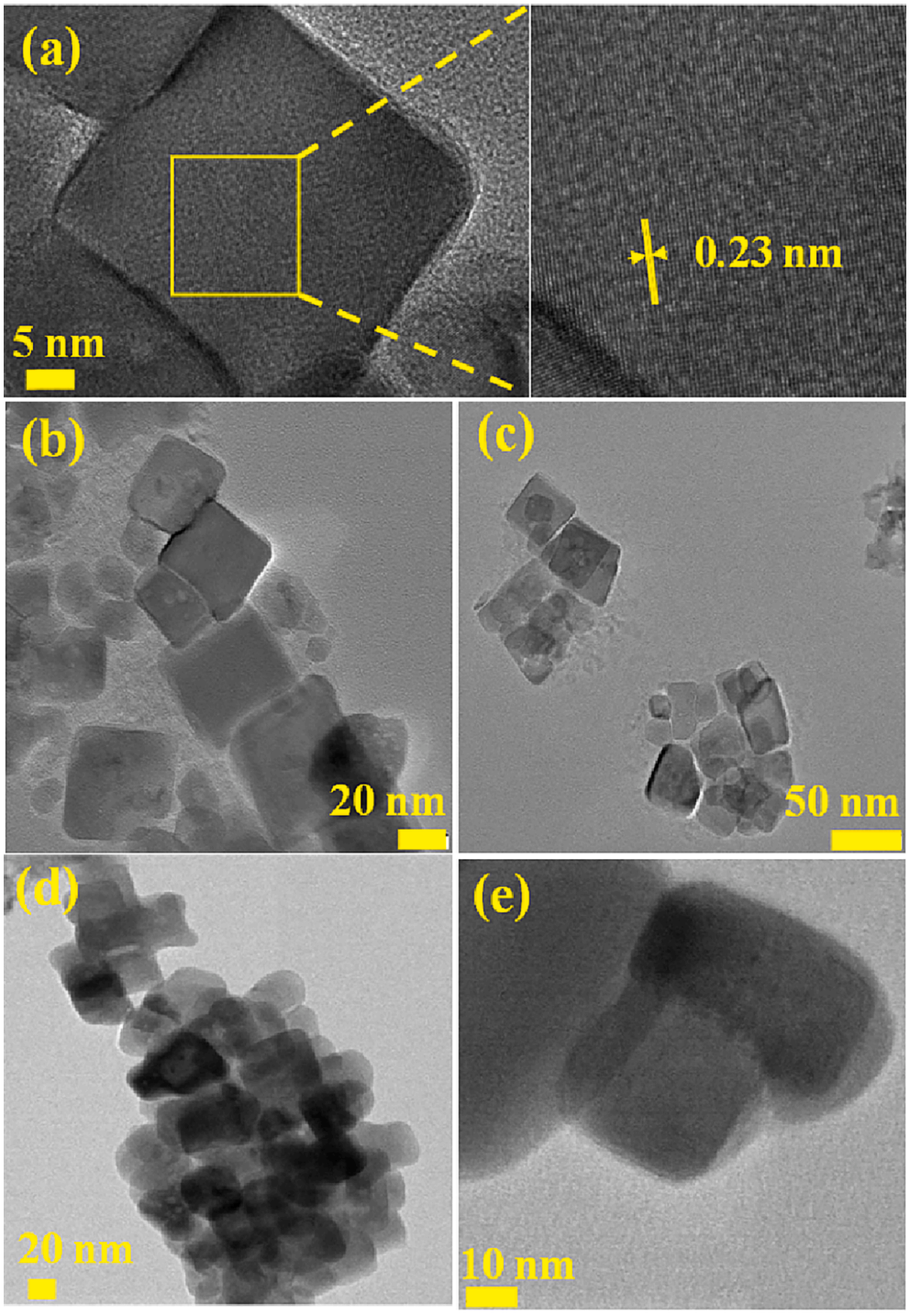

Fig. 2. TEM analysis performed on both the fresh and spent Co_3O_4 NC. **(a)** HR-TEM image of the fresh Co_3O_4 is shown, which displays a cubic morphology with an average particle size of 35 nm. Panels **(b)** and **(c)** show TEM images of the fresh catalyst, revealing particle sizes ranging from 20 to 50 nm, with a predominant size of 30 ± 5 nm. **(d** and **e)** TEM image of the spent catalyst obtained after the CO_2 reduction reaction, performed at 723 K with a 3:2 ratio of CO_2:H_2 feed for 12 h at GHSV 19200 h^{-1}, is presented. The lattice fringes observed in this image correspond to the interplanar distance of (222) facet (d_{222} = 0.23 nm).

facet based on energy considerations, and the lattice fringe confirms the presence of the (1 0 0) facet. Indeed this is a novel aspect of the catalyst, which.

exposes predominantly (1 0 0) facet with single set of activity sites; this aspect helps to achieve high selectivity of CO.The TEM image in Fig. 2d and e shows the mostly cubic morphology of the spent catalyst after reaction with a 3:2 ratio of CO_2:H_2 at 723 K, with an average particle size ~ 30 nm, similar to the fresh Co_3O_4, but with a marginal agglomeration. The TEM image shows the NC with inter-planar distances of 0.23 nm, corresponding to (2 2 2) facet, as shown in Fig. 2.

3.2. H_2-TPR analysis

The reducibility of spinel Co_3O_4 NC was evaluated by conducting H_2-TPR analysis, and the result is shown in Fig. 3. Two distinct reduction features were observed in the temperature range of 450–750 K. A sharp peak at 545 K and a broad reduction feature between 600 and 700 K were observed, with an area ratio of 1:3. No further reduction or hydrogen uptake was observed beyond 723 K, indicating complete reduction of Co_3O_4 to metal. The TPR results suggest a two-step reduction mechanism, where Co_3O_4 is initially reduced to CoO (peak at 545 K), followed by final reduction to metallic Co (between 600 and 700 K) [33,34]. It is worth investigating the possibility of two or more micro reduction steps in a narrow temperature range using careful spectral and structural methods, as indicated by the broad reduction feature. First reduction to CoO hints the possibility of, at least, partial reduction of Co_3O_4 to CoO under the present reaction conditions, since H_2 would be available at ambient pressure. It is to be reiterated that while TPR measurements are made at ambient pressure, NAPPES measurements are made at 0.1 mbar, and hence the pressure dependency to be taken into account while interpreting the results.

3.3. In-situ catalytic activity measurement in NAPPES

To investigate the partial pressures of reactants and products during the experiment, a quadrupole mass spectrometer (QMS) in the NAPPES unit was utilized to record mass spectra. The CO_2 reduction reaction was conducted using CO_2:H_2 = 1:3 between 325 and 675 K at 0.1 mbar pressure. The reactions were performed using fresh Co_3O_4 NC, in situ reduced CoO (prepared from Co_3O_4 by in situ H_2 reduction treatment at 523 K for 3 h), and Co metal (prepared from Co_3O_4 by in situ H_2 reduction treatment at 673 K for 5 h) under dynamic dosing conditions at a total pressure of 0.1 mbar between 375 and 675 K. For simplicity and convenience, the two surfaces will be referred to as CoO and Co, respectively. The QMS was used to observe product evolution, and the results are depicted in Fig. 4. A slight oscillation in all mass species was observed due to the opening of a leak valve to maintain a pressure of 0.1 mbar, with the overall pressure being maintained within 10% of 0.1 mbar. The QMS was kept in the preparation chamber, while the reaction occurred in the main chamber. The output of the first turbo molecular pump in the electrostatic lens regime was directed to the QMS through a leak valve, which may result in diffusion of different components. Given these experimental challenges, any changes observed in QMS results should be considered qualitative. Despite the difficulty of observing CO (which is also a fragment of CO_2 in QMS) in the presence of CO_2, a significant change in spectral data was observed due to CO_2 dissociation on the catalyst surface. Fig. 4 shows the evolution of relevant masses resulting from CO_2 reduction as a function of reaction temperature. Fig. 4a depicts a distinctly different evolution pattern, compared to reactants, and confirms the formation of CO and H_2O from 575 K and above due to CO_2 activation on the Co_3O_4 NC catalyst. The same evolution pattern was observed for CO_2 and amu 16, indicating that the latter is due to atomic oxygen fragment from CO_2 dissociation, rather than methane formation on any catalyst; amu15 results recorded (not shown) did not show any change and supports the above point. The same reaction was performed on in situ prepared CoO and Co metal from spinel Co_3O_4 through H_2reduction, as shown in Fig. 4b and 4c, respectively. The result in Fig. 4b indicates that CoO activates CO_2 from around 525 K, while Co activates CO_2 at 675 K (Fig. 4c). This finding indicates that metallic Co cannot activate CO_2 below 675 K and is therefore unlikely to be an active phase in the present findings. It should also be noted that metallic cobalt is expected to undergo oxidation due to interaction with CO_2 and hence a change in surface nature. As such, the results observed in the mass spectra (Fig. 4) can be considered qualitative. The mass spectra show that CO and H_2O formation occurred at temperatures $\geq$ 475 K (Fig. 4b). This observation indicates that the CoO activates CO_2 at a relatively lower temperature than the spinel Co_3O_4 (Fig. 4a).

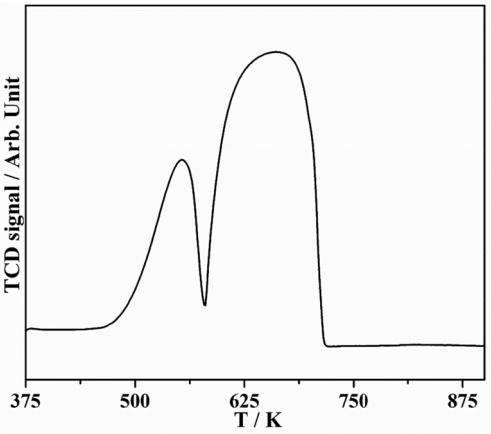

Fig. 3. H_2-TPR profile for Co_3O_4 Nano Cube catalyst.

3.4. In situ NAP-XPS study under reaction condition

To investigate the surface electronic structure of Co_3O_4NC under catalytic reaction conditions, NAPPES experiments were conducted at a pressure of 0.1 mbar with a CO_2:H_2 ratio of 1:3 and at temperatures ranging from 325 to 675 K. Despite the use of low pressure, the results obtained from the NAPPES measurements provided relevant information about surface changes and their correlation to the active state under reaction conditions. Although kinetic changes occur more rapidly at higher pressures, such as 1 bar, the surface chemistry/changes remained the same and were observed in the present measurements. NAP-XPS and NAP-UPS measurements were performed systematically under the same reaction conditions, and the results are depicted in Figs. 5-7 and 8, respectively. Co $2p_{3/2}$ spectra obtained from Co_3O_4 NC, CoO, and fully reduced Co metal surfaces are shown in Fig. 5a, 5b, and 5c, respectively [35]. The (1 0 0) facet of Co_3O_4 is known to exhibit Co^{2+} ions on the surface, whereas Co^{3+} is found in the underlying layers, suggesting that the activity could be predominantly determined by the former ions. However, CoO also exhibits a Co^{2+}-terminated surface that is similar to that of Co_3O_4 and has no Co^{3+} in the layers beneath. In all spectra, Co $2p_{3/2}$ core-level spectra exhibited features at 778.1 eV (red trace) and 780.1 eV (blue trace) corresponding to Co^{3+} (Oh coordination) and Co^{2+} (Td coordination) oxidation states, respectively [36,37]. The UHV spectra recorded at 298 K are shown at the bottom of all panels of Fig. 5, revealing the expected Co^{3+}, Co^{2+}, and weak satellite features, along with a feature at 782.1 eV (olive), which is attributed to Co at defect sites. Marginal changes were observed in the Co$2p_{3/2}$ spectrum up to 475 K at 0.1 mbar pressure, which was comparable to the UHV spectrum. This suggests that the surface remained relatively unaffected and appeared to be comparable to that of the surface at 298 K conditions. However, an increase in Co^{2+} and Co near defect sites content was observed at 575 and 675 K, underscoring reaction-induced changes.

The surface electronic structure of CoO was investigated using the same experimental techniques as for Co_3O_4 NC, and the results are

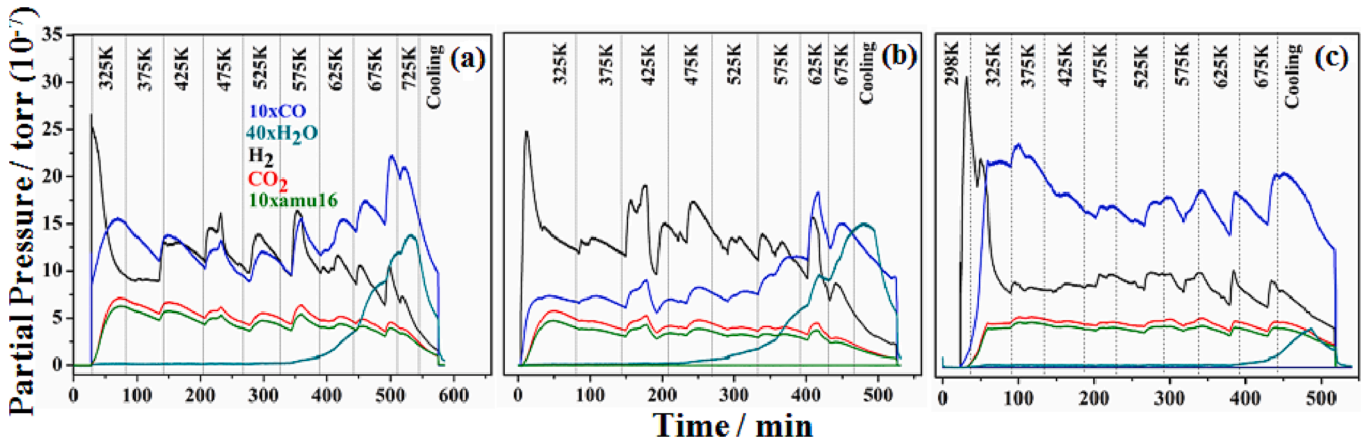

Fig. 4. The mass spectral analysis of the CO_2 reduction reaction was conducted at 0.1 mbar with a 1:3 CO_2:H_2 ratio over the temperature range of 325 to 725 K using **(a)** Co_3O_4 NC catalyst, **(b)** Co_3O_4 reduced to CoO, and **(c)** Co_3O_4 reduced to Co. The partial pressure of CO, H_2O, H_2, CO_2, and amu 16 (O) were represented by blue, cyan, black, red, and olive colors, respectively. To enhance clarity, the partial pressures of CO, amu 16, and H_2O were multiplied by factors of 10, 10, and 40, respectively. The total pressure of the system was maintained at 0.1 mbar. (For interpretation of the references to color in this figure legend, the reader is referred to the web version of this article.)

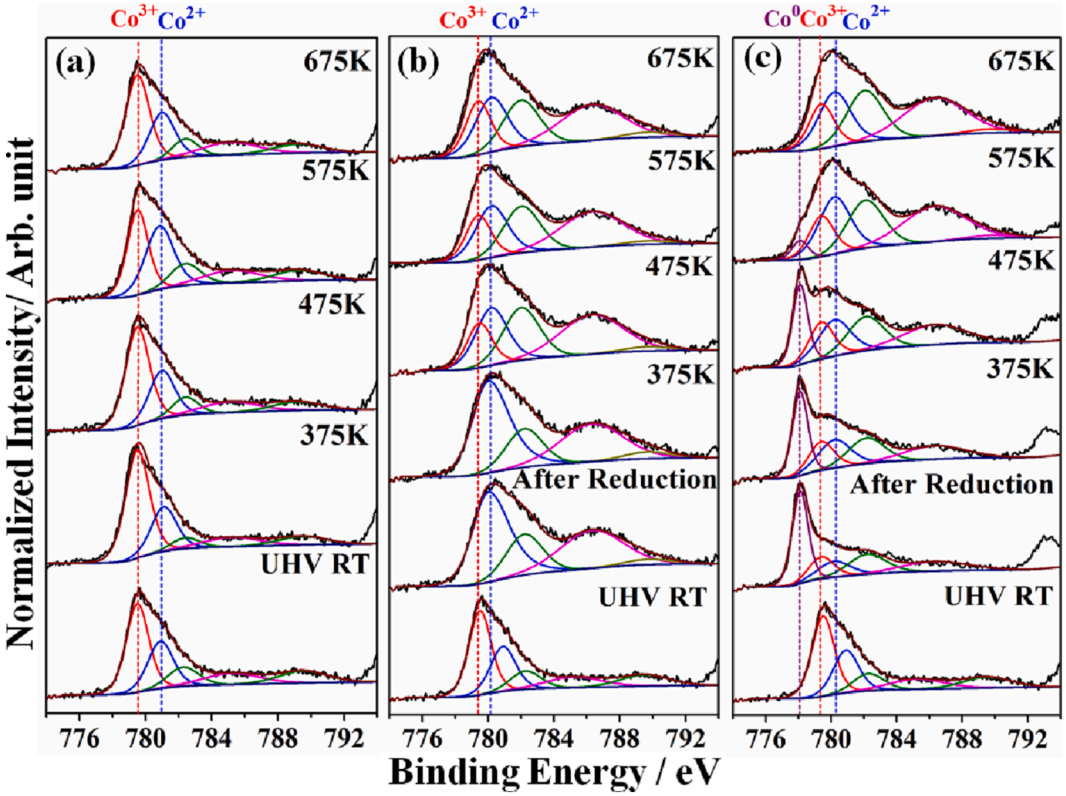

Fig. 5. Deconvoluted Co $2p_{3/2}$ spectra recorded under reaction conditions of 0.1 mbar pressure (CO_2:H_2 = 1:3) and temperature range between 375 and 675 K (a) on Co_3O_4 NC, (b) on in-situ prepared CoO from Co_3O_4, and (c) on in-situ prepared Co metal from Co_3O_4.

presented in Fig. 5b. The spectrum obtained after reduction of Co_3O_4 to CoO is shown as the second spectrum from the bottom in Fig. 5b and denoted as "after reduction". An increase in the intensity of Co^{2+} at 780.1 eV and a high intensity satellite peak at 786.4 eV confirms the reduction of Co_3O_4 to CoO [38]. This observation is further supported by the NAP-UPS results (**Figure S1**). The NAP-XPS measurements were carried out on the CoO surface at 0.1 mbar pressure and in the temperature range of 375 to 675 K. Interestingly, a significant increase in the intensity of Co^{3+} was observed at the expense of the Co^{2+} intensity at temperatures $\geq$ 475 K. The formation of CO and H_2O starts at 475 K, which is 100 K lower than for the spinel Co_3O_4 sample, as observed in Fig. 4b. The ratio of the + 2/+3 oxidation states changes from 2:1 at 475 K to 6:5 at 675 K. The relative percentage area of various cobalt species, obtained after decoupling the NAP-XPS data, is plotted in **Figure S2**. It is noteworthy that the satellite intensity is largely maintained up to 675 K, indicating the equally important role of both Co^{3+} and Co^{2+}; however, a shift in the satellite feature by 0.6 eV to lower binding energy is observed at temperatures $\geq$ 475 K, indicating some electronic changes. It is to be emphasized the necessity of both 2 + and 3 + oxidation states of Co for the CO_2 activation on the catalyst surface, rather than any one of them.

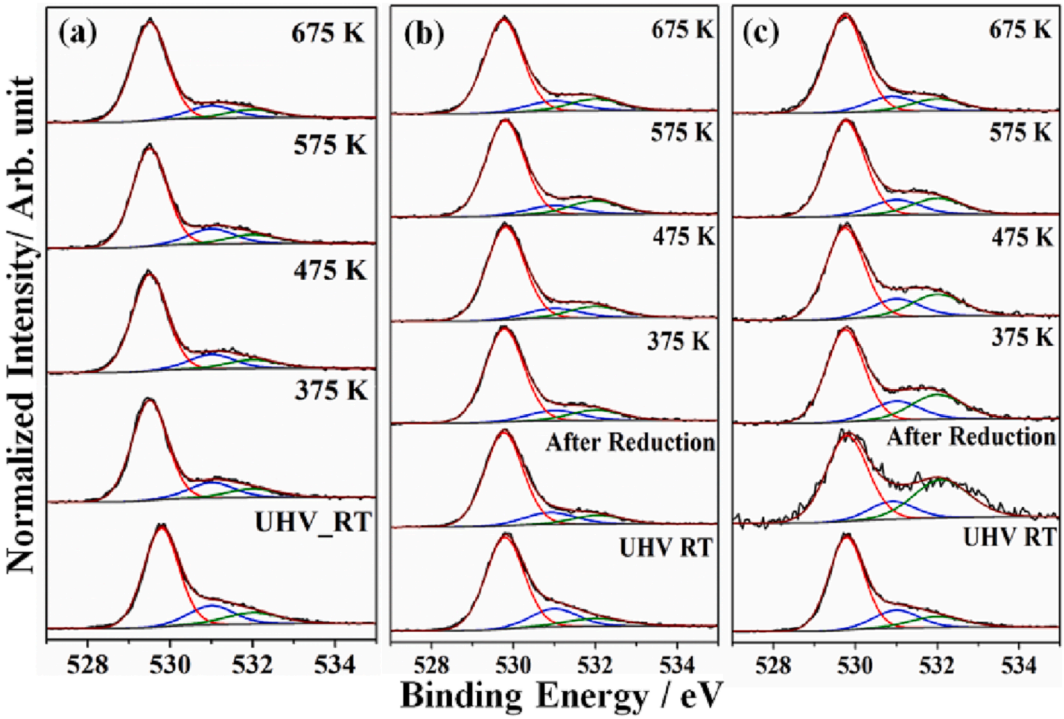

Fig. 6. Shows the O1s spectra recorded under reaction conditions, with a total pressure of 0.1 mbar and temperatures ranging from 375 K to 675 K, on **(a)** Co_3O_4 NC catalyst, **(b)** in situ prepared CoO catalyst, and **(c)** in situ prepared metallic Co catalyst by H_2 reduction. It is worth noting that the low signal-to-noise ratio observed in panel c, after reduction to Co-metal, is attributed to partially reduced or unreduced oxide layers beneath the metal.

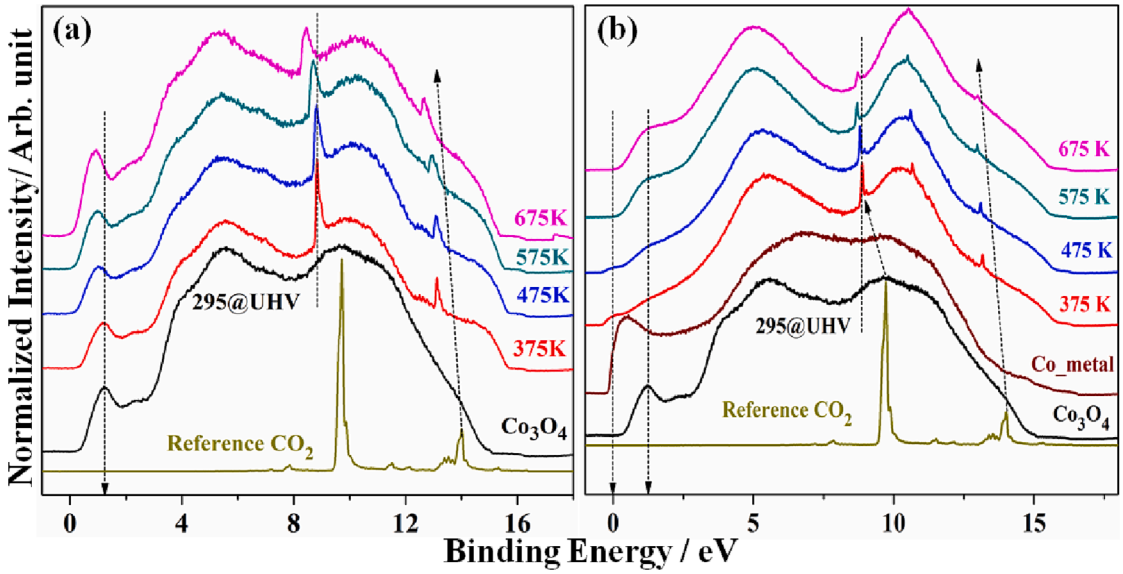

Fig. 7. Ultraviolet photoelectron VB spectra recorded under measurement conditions of 1:3 CO_2/H_2 ratio at 0.1 mbar between 375 and 675 K. NAP-UPS VB features recorded with **(a)** Co_3O_4 NCs, and **(b)** Co_3O_4 reduced to Co metal. The intensity of CO_2 has decreased and broadening in the spectra observed because of formation of CO at high temperature. UVPES recorded for pure gas-phase CO_2, Co_3O_4 and Co_3O_4 reduced to metal are also shown for comparison and as reference.

Although some CoO is observed in XRD result (Fig. 1b), Fig. 5b emphasizes the mixed oxidation states on the surface under the reaction conditions.

Fig. 5c shows the Co $2p_{3/2}$ spectrum obtained after the reduction of Co_3O_4 to metallic Co, and data acquired under reaction conditions. The conversion of spinel Co_3O_4 NCs to metallic cobalt was also confirmed by the NAP-UPS spectrum shown in Fig. 7b (wine red) with a high E_F intensity. The small amount of Co^{2+} and Co^{3+} features observed are attributed to their presence beneath metallic layers. When measurements were made in the presence of CO_2:H_2 (1:3) at 375 K and above, there was a gradual increase in Co^{2+} and Co^{3+} content at the cost of metallic Co, and metallic Co almost disappeared at 675 K. The oxidation of Co indicates that the oxygen atoms available from CO_2 dissociation are used for surface oxidation, with the extent of surface oxidation gradually increasing with temperature and metallic Co disappearing at 675 K. However, metallic Co is preferentially oxidized to Co^{3+} up to 475 K with low intensity satellite, and then Co^{2+} increases, which is supported by the increase in satellite intensity. It is likely that

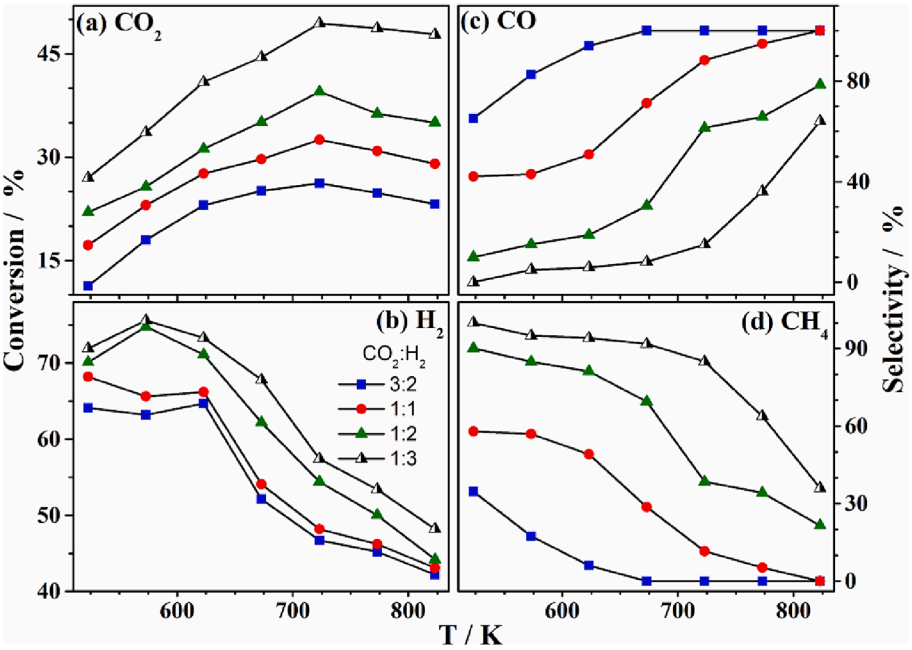

Fig. 8. Presents the results for (a) CO_2 conversion, (b) H_2 conversion, (c) CO selectivity, and (d) CH_4 selectivity under the following reaction conditions: reaction temperature range of 523 K to 823 K, atmospheric pressure, gas flow of 320 ml/min, and GHSV of 19200 h^{-1} for varying CO_2:H_2 ratios of 1:3, 1:2, 1:1, and 3:2.

H_2 from the reactant mixture is playing a role in the reduction of Co^{3+} to Co^{2+} at higher temperatures. It is also worth noting that effective CO_2 reduction starts $\geq$ 625 K, and the chances of metallic Co-formation under reaction conditions and its effect on CO_2 activation are remote.

O1s spectra were recorded under the same conditions as in Fig. 5, and the results are shown in Fig. 6. The features appearing at 529.9 eV (red), 530.5 eV (blue), and 532 eV (olive) belong to lattice oxygen, oxygen near defect sites, and OH, respectively (Fig. 6a-c). Co_3O_4 NCs (Fig. 6a) and CoO (Fig. 6b) show very similar features, indicating that the changes are similar. The O1s spectrum recorded for metallic cobalt (second spectrum from bottom in Fig. 6c) shows some interesting changes. Firstly, the low signal-to-noise ratio of the O1s peak observed after reduction indicates that the complete reduction to Co-metal occurs only on the surface, even lower than the XPS probing depth of 10 nm. This is supported by the high intensity E_F feature observed in NAP-UPS (Fig. 7b), indicating that the underlying layers are not fully reduced, and the 0.1 mbar pressure may not be sufficient to achieve complete reduction. Secondly, there is a sharp increase in the hydroxyl peak after reduction, with an increase in defect sites, which could be due to the interaction with hydrogen. As the reaction proceeds to higher temperatures, the intensity of the hydroxyl features decreases, and the O1s spectrum resembles to that of recorded at 675 K on Co_3O_4 NC or CoO. This is in agreement with changes observed with C 1s spectra recorded under same conditions (Figure S3).

3.5. *In situ NAP-UPS study under reaction condition*

The nature of the catalyst, particularly the VB, under reaction conditions with CO_2:H_2 = 1:3 between 375 and 675 K at a total pressure of 0.1 mbar was explored using NAP-UPS analysis. Fig. 7a and 7b shows the NAP-UPS spectral data recorded on Co_3O_4 NCs and Co_3O_4 reduced to metallic Co, respectively. The UPS result recorded at UHV@295 K shows an onset of VB at 0.37 eV, and a typical Oh Co^{3+} feature was observed at 1.22 eV [39], which is consistent with similar spectral results reported in the literature for Co_3O_4. From the NAP-UPS measurements carried out on Co_3O_4 up to 675 K (Fig. 7a), four critical observations are worth highlighting. First, very similar VB results under reaction conditions were observed compared to those under UHV-RT conditions. Second, a gradual and rigid shift of the entire spectrum to lower binding energy (BE) was observed up to 0.35 eV from UHV-RT to 675 K. For example, Oh Co^{3+} shifted from 1.22 eV under UHV-RT to 0.88 eV at 675 K at 0.1 mbar. Third, an increase in the full-width at half-maximum (FWHM) of the CO_2 vibrational feature was observed with increasing reaction temperature from 160 meV at 375 K to 300 meV at 675 K (Figure S4). Notably, the drastic change in BE and FWHM is directly evident when the temperature increases from 475 to 575 K, which also coincides with the onset of CO_2 reduction activity. Fourth, these observations indicate that the Co_3O_4 surface remains in the same state but with a gradually decreasing work function under the reaction conditions at high temperatures. Furthermore, the increasing FWHM observed at high temperatures for the CO_2 vibrational feature is attributed to an increasing heterogeneity of the surface. It is worth reiterating that NAP-UPS probes a maximum of the top 2 nm layers, while NAP-XPS probes up to 10 nm. It is therefore surprising to observe no major change in the VB pattern, except for the aforementioned points.

Fig. 7b displays similar measurements conducted on Co metal surfaces. The ultraviolet photoelectron spectroscopy (UPS) VB spectrum recorded at room temperature under ultra-high vacuum (UHV-RT) conditions for freshly reduced Co metal is presented as the second spectral trace in Fig. 7b; a sharp E_F feature observed is characteristic of metallic nature [39]. Under the conditions of NAP-UPS measurements, the surface nature of the Co-catalyst gradually transformed from metallic to the oxide phase, and fully supported by the disappearance of E_F intensity and the transformation of the broad VB feature of metallic Co to the evolution of typical O 2p VB. Notably, the typical Oh Co^{3+} began evolving from 575 K and above, indicating the gradual oxidation of the metallic surface to oxide [40]. However, unlike the changes in BE and FWHM of CO_2 vibrational features on Co_3O_4 (Fig. 7a), only a marginal shift in BE (0.16 eV) of CO_2 vibrational feature was observed, with a small change in FWHM (Figure S4). These observations indicate the relatively passive nature of the metallic Co-surface to CO_2 activation, compared to Co_3O_4 NC, at least under the present experimental conditions. Therefore, in light of these observations, catalytic activity measurements were carried out on Co_3O_4 NC under relevant condition at ambient pressure.

3.6. Catalytic activity measurements

The reduction of CO_2 was performed in a fixed bed catalytic reactor under atmospheric pressure in the temperatures range from 523 to 823 K, with various CO_2:H_2 ratios (1:3, 1:2, 1:1, and 3:2), and at a GHSV of 19200 h^{-1}. CO_2 activation was observed to be insignificant below 473 K, and thus, the measurements were limited to 523 to 823 K and the results are shown in Fig. 8. Only products detected were methane, CO, and water. The following results are worth highlighting:

(a) CO_2 conversion increased with rising reaction temperature up to 723 K for all CO_2:H_2 ratios, after which it decreased marginally. In contrast, H_2 conversion remained nearly constant for a given CO_2:H_2 ratio between 523 and 623 K, after which it decreased rapidly with further increase in temperature.
(b) At low temperatures, methane is the preferred product, whereas CO is produced predominantly at high temperatures, regardless of the reactants ratio. A CO_2 rich reactant ratio (CO_2:H_2 = 1:1, 3:2) showed 100% selectivity towards CO. Novelty of the present work partly lies in employing lower content of hydrogen, and still achieving 100 % CO selectivity.
(c) Methanation occurred preferentially with hydrogen-rich feed and at low temperatures, whereas CO was selectively produced with CO_2-rich feed and at relatively high temperatures. For example, a 1:3 ratio of CO_2:H_2 led predominantly to methane, with maximum CO_2 and H_2 conversion of 49.5% and 76.3% at 723 K and 573 K, respectively. In contrast, 3:2 CO_2:H_2 ratio resulted in the maximum CO_2 conversion of 26.2% at 723 K and the maximum H_2 conversion of 64.7% at 623 K, with over 90% CO selectivity and less than 10% methane selectivity.
(d) A decrease in H_2 conversion observed at high temperatures for all CO_2:H_2 ratios support the notion that surface coverage decreased with temperature, thereby enhancing CO production and minimizing methanation. It is likely that hydrogen was used predominantly to remove oxygen dissociated from CO_2 in the form of water under high-temperature conditions. Hence, the ratio of adsorbed surface reactants was likely close to unity. While methane is a thermodynamically stable product, CO is the preferred product, and the current catalyst maximizes its production under the given experimental conditions. As one mole of methane (and two moles of water) formation requires four moles of hydrogen for CO_2 reduction (Eq. (1), it is an expensive process. In addition, there is a possibility that large H_2 conversion conditions might lead to dynamic oxygen vacancy generation on the catalyst surface, which can influence the activity/selectivity.

In Fig. 8a, the catalytic conversion of CO_2 is presented and the results offer additional insights. Below 523 K, there was no substantial CO_2 conversion, which is in agreement with the TPR results depicted in Fig. 3 and confirms that the reaction is initiated by H_2 adsorption and consumption. The maximum CO_2 conversion is observed at 723 K, regardless of the reactant ratio; however, a slight decrease of 3–4 % in CO_2 conversion was observed beyond this temperature. Surprisingly, significant CO_2 (with large H_2) conversion was observed with a less than stoichiometric CO_2:H_2 ratio (3:2), highlighting the preference of hydrogen adsorption on the catalyst sites over CO_2 adsorption at low temperatures. The contact time of high CO_2 (low H_2) with 3:2 and 1:1 ratios assists in achieving high CO yield at 673 K and 823 K, respectively.

Fig. 8b presents the H_2 conversion data, and it shows an opposite trend to that observed in Fig. 8a for CO_2 data. The H_2 conversion decreases for all feed compositions as the reaction temperature increases. The maximum H_2 conversion (75.6%) was observed with CO_2:H_2 = 1:3 at 573 K, which leads to high methane selectivity. Generally, an increase in H_2 content leads to an increase in CO_2 conversion but a decrease in H_2 conversion. The increase in CO_2 conversion can be attributed to the generation of equal or nearly equal amounts of Co^{2+} and Co^{3+} on the CoO surface, which activate CO_2 at relatively low temperature (473 K, Fig. 4b), as observed in QMS. A similar trend is also observed for partially reduced Co_3O_4 catalyst, which shows less CO selectivity compared to CH_4 at high temperature in a fixed-bed reactor study at atmospheric pressure, and it is discussed later.

The results presented in Fig. 8 are displayed in terms of the rate of reactant conversion and product formation. The corresponding plot is shown in Fig. 9, which enables direct comparison with previously published results and complements the findings from Fig. 8. It is observed that CO_2 and H_2 conversions exhibit the same trend, as illustrated in Fig. 8. The highest rate of CO formation is obtained with a 1:3 CO_2:H_2 feed, while also producing methane at 823 K. Exclusive CO (CH_4) production at the lowest temperature of 673 K (523 K) was observed with 3:2 (1:3) CO_2:H_2. The rate of CO formation nearly plateaus between 100 and 120 mmol/h.g_{cat} for the other three CO_2:H_2 feeds between 723 and 823 K. Although no methane production was observed, a minor decreasing trend in the rate of CO production with CO_2:H_2 3:2 above 723 K indicates that the hydrogen-deprived surface is likely to change further. Hydrogen deprived surface is likely to decrease the CO_2 conversion too, especially at 773–823 K. It may be noted that same CO yield (120 mmol/h.g, with a decreasing methane yield from 20 to 0 mmol/h.g) is observed with 1:1 CO_2:H_2 feed between 723 and 823 K; while a marginal decrease in CO yield (with no methane yield) with temperature is observed with 3:2 CO_2:H_2 underscores the hydrogen deprived surface decreases the CO_2 conversion. These observations underscore the necessity of maintaining the redox nature of the surface for sustainability, especially in terms of a combination of the availability of both Co^{2+} and Co^{3+} oxidation states under reaction conditions. It is also highly probable that dynamic changes occur on the catalyst surface, which is worth studying with in situ spectral methods, such as IR.

Catalytic CO_2 reduction reaction was also carried out on pre-reduced catalysts, namely, CoO and metallic Co, with CO_2:H_2 = 3:2 to understand the role of different oxidation states of Co. Same reduction conditions were applied, as given in sec.3.3, but at H_2 flow rate of 25 ml/min, which reduces the Co_3O_4 catalyst. The reaction results obtained with Co-metal and CoO are compared with that of Co_3O_4 (NC) and shown in Fig. 10. Expectedly, the initial activity of CoO (Fig. 10b) and metallic Co (Fig. 10c) is very different at temperatures $\leq$ 673 K, compared to Co_3O_4 (NC) (Fig. 10a). Metallic Co exhibits comparable CO_2 conversion as that of Co_3O_4, even at 523–573 K, but with high methane selectivity, which is in good agreement with the literature reports [13,23]; while Co_3O_4 (NC) exhibits high CO selectivity. Interestingly, low H_2-conversion observed, in spite of high methane selectivity, underscores the oxygen stripped from CO_2 oxidizes the metallic Co to higher oxidation states. This suggests the changes that occur on the catalyst surfaces under H_2-lean conditions. Nonetheless, as the temperature increases, CO selectivity increases at the cost of methane selectivity, indicating the change in the nature of the metallic Co-catalyst. It is also known that H_2-rich feed composition,(1:4 in ref. 23) exhibits high methane selectivity even at high temperatures with metallic Co, while the present results with H_2-lean feed shows high CO selectivity. While exclusive methane selectivity was observed below 673 K with CoO, CO selectivity increases with temperature. Surprisingly, CO_2 conversion observed to be the lowest (8–10 %), along with low H_2 conversion with CoO. Nonetheless, CO (CH_4) selectivity increases (decreases) linearly with temperature, again underscoring the change in the nature of the catalyst surfaces progressively under reaction conditions.

Present set of results given in Fig. 10 suggests the following: (a) In contrast to the literature reports, which employed generally H_2-rich feed compositions (CO_2:H_2 = 1:x; x $\geq$ 2), present H_2-lean reactants feed changes the nature of the catalysts (especially Co-metal) gradually towards higher oxidation state(s). This in turn influences the reactants conversion and products selectivity. (b) While the CO_2 conversion remains observed between 20 and 25 % on Co_3O_4 and Co, it decreased to ~ 5–10 % with CoO. (c) Increase in CO selectivity at the cost of methane with CoO and with Co at high temperature indicates the progressive

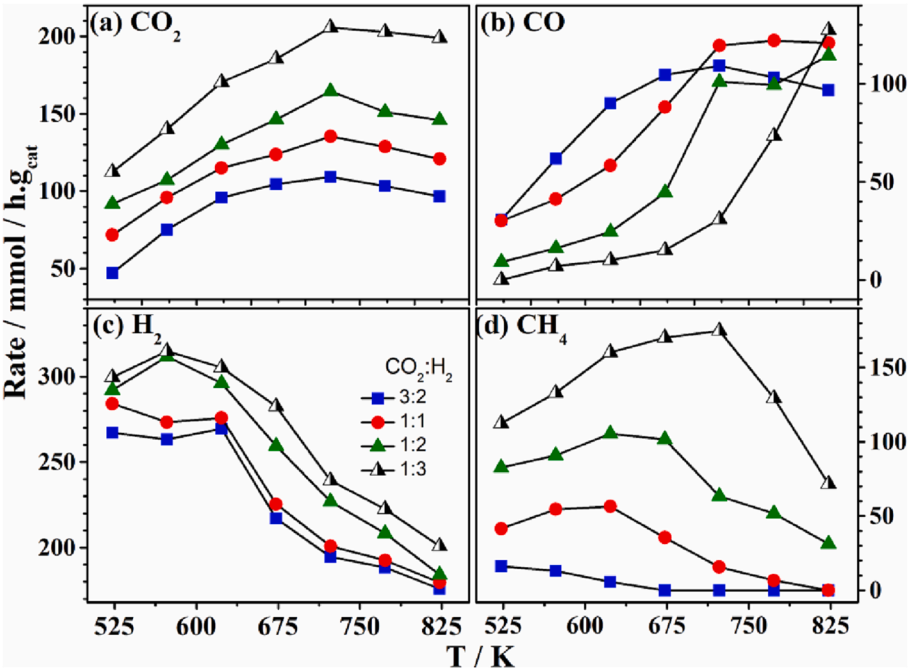

Fig. 9. Rate of CO_2 reduction with $H_2$and products formation is shown as a function of temperature for various CO_2:H_2 ratios. Conversion of (a) CO_2 and(b) H_2, as well as the formation of products (c) CO and(d) CH_4 are separately plotted.

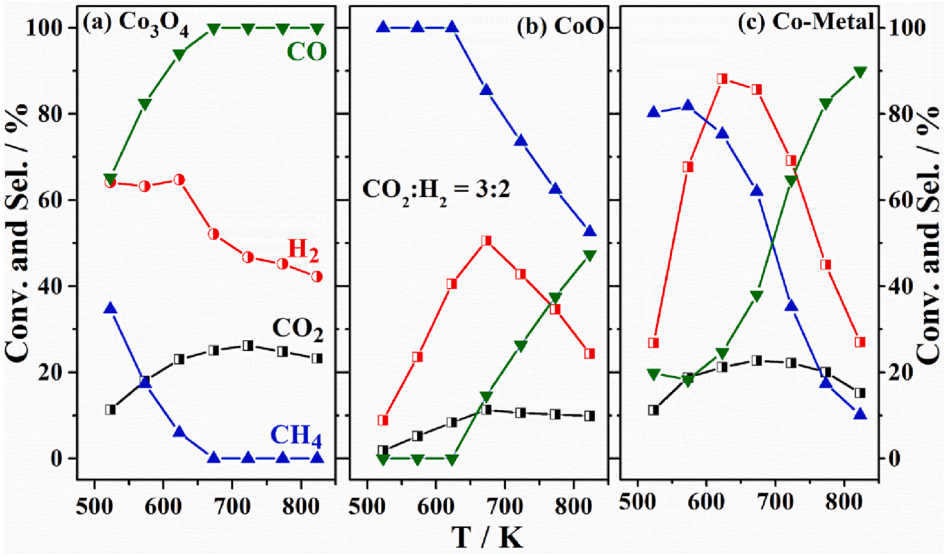

Fig. 10. Comparison of temperature dependent CO_2 reduction activity and selectivity for (a) Co_3O_4, (b) CoO, and (c) Co-metal. Later two were generated by reducing Co_3O_4 in H_2 at 250 and 400 °C for 3 and 5 h, respectively. Note a significant decrease in CO_2 conversion with CoO.

oxidation of the surface towards Co_xO_y; this aspect is confirmed from the XRD pattern recorded with the spent catalyst, collected after the reaction carried out, and discussed later. (d) NC morphology is present only for Co_3O_4, while it changes to random morphology with agglomeration (Figure S5 in supporting information) on reduction to CoO or metallic Co, which also a major reason for changes in the activity observed in Fig. 10b and c panels. This point underscores the importance of NC morphology for 100 % CO selectivity with Co_3O_4. It is also to be pointed out that under NAPPES conditions, reduction was carried out at 0.1 mbar H_2 pressure, which reduces the surface layers and hence it retains the NC morphology. Hence upon reaction at the same pressure, the surface gets oxidized.

XRD pattern of Co_3O_4 (NC) reduced to Co, CoO is plotted along with spent Co-catalyst (after reaction with CO_2:H_2 = 3:2), in Fig. 11. XRD results shown in Fig. 1 is also included for comparison in Fig. 11. Inset shows the enlarged region around 44–45°. First of all it is evident that (4 0 0) facet of metallic Co and Co_3O_4 appears at a difference of 0.4°, and hence they could be easily distinguished. While fresh and spent Co_3O_4 catalysts exhibits (4 0 0) facet at 44.9 deg., reduced Co shows the (4 0 0) facet at 44.4 deg., which is typical for metallic Co [23,41]. More interestingly, after CO_2 reduction reaction was carried out with Co-metal with CO_2:H_2 = 3:2 (Fig. 10c), all diffraction features corresponding to Co_3O_4 and CoO are observed; this is in addition to the metallic Co-features. Very similar XRD pattern was observed with spent CoO catalyst also (not shown). This observation reiterates that under the present experimental conditions with H_2-lean feed, metallic Co-surface

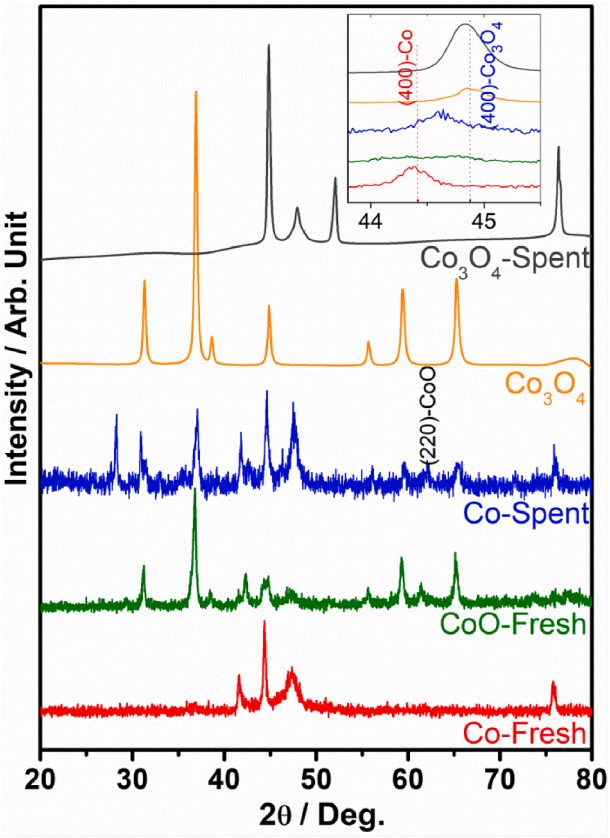

Fig. 11. XRD pattern recorded after Co_3O_4 was reduced to Co, CoO and compared with the fresh Co_3O_4 and spent Co_3O_4 catalysts. Spent Co catalyst, obtained after the reaction results shown in Fig. 10c, XRD pattern was also carried out and compared. Evolution of Co-metal to cobalt oxides is directly evident from the results, due to CO_2-reduction with H_2-lean feed. Inset shows the enlarged pattern around 44–45 deg. to distinguish the (400) facet of metallic Co and Co_3O_4.

undergoes oxidation towards Co_3O_4 along with CoO. Indeed, NAPPES studies have earlier shown the evolution of Co-metal and CoO surfaces towards Co_3O_4 under in-situ measurement conditions (Fig. 5). Another aspect is the presence of many different crystallographic facets on the spent catalyst, after the reaction. Upon reduction of Co_3O_4 to Co, NC morphology disappears completely and TEM analysis indicates a random morphology with Co or CoO (Figure S5). This allows the growth of different facets of Co_3O_4 and CoO. Chain growth of particle (or agglomeration) observed with random morphology in TEM results (Fig. S5), and different crystallographic facets observed in Fig. 11 underscores the activity observed in Fig. 10b and c is due to an averaging effect of different crystallographic sites, which may be considered as comparable to conventionally synthesized Co_3O_4. Although by continuing the reaction for longer time on stream (Fig. 10b and c) catalyst could be fully converted to long-range ordered Co_3O_4; however, NC morphology cannot be restored by simply continuing the reaction. Entirely different activity/selectivity observed in Fig. 10b and c, compared to Fig. 10a attests this conclusion. Indeed selective CO production observed was due to exclusive (100) facets present on NC morphology. This fact also supports the high conversion and exclusive CO selectivity with Co_3O_4 is due to NC morphology with (100) facets, which promotes CO formation. Metallic Co in nanorod and nanoparticle forms was evaluated for CO_2 hydrogenation with CO_2:H_2 = 1:4 [23]. Though both are metallic Co, completely different activity was reported; Co-nanorod exhibits 100 % methane selectivity, while Co-nanoparticles exhibit a reactivity similar to the results shown in Fig. 10c (with high methane selectivity at low temperature, while high CO selectivity at high temperatures). Observations like this along with our present results underscores the importance of adopting suitable nanoscience would lead to the desired results.

3.7. Time on stream

In order to evaluate the feasibility of the Co_3O_4 NC spinel catalyst, a time-on-stream (TOS) study was conducted for the CO_2 reduction reaction with CO_2:H_2 = 3:2 at 723 K for 12 h, and the results are shown in Fig. 12. The Co_3O_4 NC catalyst exhibited a remarkable catalytic activity for the CO_2 reduction to CO, without the formation of methane, and this presents a more cost-effective approach to producing a single product that can be utilized in various applications. The stable CO_2 and H_2 conversion rates were observed to be 98 ± 10 and 160 ± 15 mmol/h.g_{cat} at 723 K within the experimental error limit of 10%, while the CO and CH_4 production rates were 98 ± 5% and 0 mmol/h.g_{cat} at 723 K, respectively. The CO production was maintained at 100% for the entire duration of the study at 723 K with minimal variation, which falls within the acceptable range of error. The catalyst demonstrated sustainable activity and selectivity throughout the entire reaction period at both temperatures. A decrease in H_2 consumption observed between 4 and 7th hour, while constant rate of CO production demonstrates a dynamic change on the surface. Same numbers observed for CO_2 conversion and CO production fully supports the above conclusion. The ToS study shows that the Co_3O_4 NC catalyst exhibits high activity and stability under the CO_2 reduction reaction condition, with no significant change in activity observed.

Moreover, the results suggest that an optimal concentration of cobalt (+2/+3) oxidation state is maintained throughout the reaction, which could be the key to catalytic stability. Furthermore, higher H_2 and CO_2 conversions were observed at CO_2:H_2 = 3:2, along with high CO

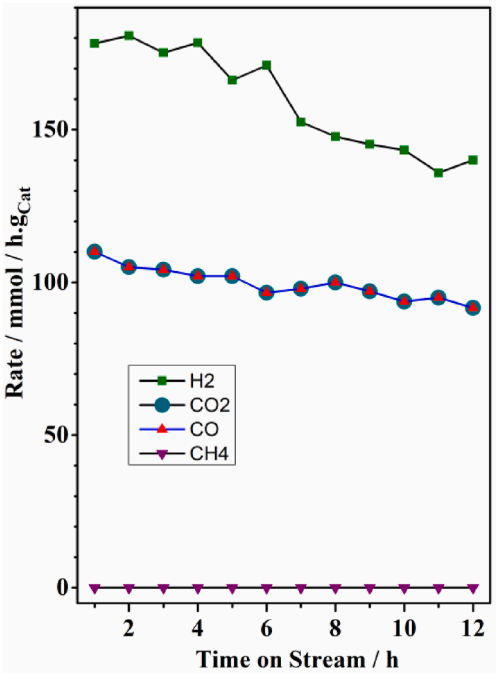

Fig. 12. Time on stream (ToS) studies were conducted to investigate the reactant conversion of CO_2 (represented by the color cyan) and H_2 (represented by the color olive) on Co_3O_4 NC, with the resulting products of CO (represented by the color red) and CH_4 (represented by the color purple), at 723 K and a CO_2:H_2 ratio of 3:2, at a pressure of 1 bar, a flow rate of 320 ml/min, and a gas hourly space velocity (GHSV) of 19200 h^{-1}. The ToS study demonstrated sustainable activity of the catalyst throughout the experimental period. (For interpretation of the references to color in this figure legend, the reader is referred to the web version of this article.)

selectivity. Under H_2-rich conditions, the amount of Co^{2+} concentration on the catalyst surface was higher compared to Co^{3+}, while the opposite trend was observed under CO_2-rich conditions. The CO_2 acted as an oxidizing agent and maintained the optimal concentration of Co^{3+} on the surface, resulting in selective CO production at a relatively lower temperature than under CO_2-lean conditions. Table 1 lists the catalyst activity and selectivity for some of the top performing catalysts for CO_2 reduction reaction from the literature reports. A preliminary analysis of the results demonstrates that the present results for Co_3O_4 NC exhibit a better performance compared to other reported systems. Previous work by our group on Mo_2C reported 44% conversion with 34% CO selectivity with reactant ratio 1: 3 CO_2:H_2 at 623 K [42]; this is only the second report on CO_2 reduction under H_2 lean conditions; another report on In_2O_3 reported 24% CO_2 conversion with 98% CO selectivity at 873 K. However, in the present work, the maximum 26% CO_2 conversion along with 100% CO selectivity observed at 723 K, which is 150 K lower than the previous work reported under comparable conditions [43]. At optimum conditions, Co_3O_4 NC demonstrates the potential to produce exclusively CO, which reduces the separation cost of methane and makes the process more economically viable and sustainable. A significant number of systems show 5–85% CH_4 selectivity, which is not preferred in the RWGS reaction. On the other hand, Ni-CeO_2 shows 40% CO_2 conversion with 1:1 CO_2:H_2 with 100% CO selectivity, but at high temperature (973 K) and lacks sustainability studies [44]. Indeed none of the catalyst systems reported activity with 3:2 CO_2:H_2 feed at any temperatures [44,45,48]. Although ref.45 and 48 employed the lowest ratio (1:1 CO_2:H_2), predominant CO with methane was reported at $\geq$ 823 K. With single type of crystallographic facet (1 0 0) present on Co_3O_4-NC, the present work has overcome the selective production of CO without methane.

4. Conclusion

In this study, we investigated the surface chemistry and catalysis aspects of Co_3O_4 NC for CO_2 reduction, using relevant methods, such as NAP-XPS, UPS, RGA and fixed bed reactor. The results show that the Co_3O_4 spinel phase is sustainable at least up to 773 K under reaction conditions. Under near-ambient pressure and temperature, Co metal surfaces oxidize to CoO and Co_3O_4 during the reaction, underscoring the dynamic changes. Indeed a direct correlation was observed between the findings of NAPPES at 0.1 mbar partial pressure and catalysis at 1 bar along with XRD/TEM characterization. Especially the disappearance of metallic nature of Co and appearance of oxides of cobalt was observed in NAPPES as well as under ambient pressure reaction conditions and further confirmed by XRD. The activation of CO_2 starts at 575 K on freshly prepared Co_3O_4 at 0.1 mbar pressures. The metallic phase of cobalt prepared by H_2 reduction activates CO_2 at 473 K, the oxygen from CO_2 dissociation oxidizes the Co metal surface, resulting in a higher oxidation state at higher temperatures as the reaction proceeds. The oxidation of the Co-metal catalyst surface was characterized by NAP-XPS and NAP-UPS spectra, and XRD. Several interesting results are observed with CO_2 reduction on various oxidation states of cobalt and ex-situ reactor study at 1 bar pressure with varying reactant ratios.

(1) Contrary to some of the reports suggesting that Co metal is active for CO_2 activation and selective towards CO formation, our studies with NAP-XPS and NAP-UPS indicate that a combination of 2 + and 3 + oxidation states of Co activates CO_2 at lower temperatures and exhibits high selectivity to CO production. **(2)** A 1:1 and 3:2 CO_2:H_2 ratio exhibits the best and sustainable performance between 623 and 723 K with 100% CO selectivity at 723 K. The highest CO selectivity was observed at the cost of methanation, and this was observed by employing lower than stoichiometric amounts of H_2 and at moderate temperatures. This point underscores the unique and inherent catalytic activity and selectivity of Co_3O_4-NC. **(3)** There is a dynamic redox interaction between Co^{2+} and Co^{3+} states, which seems to help for high CO selectivity [51]. **(4)** Increases in broadening of CO_2 vibrational features support the formation of CO, which is overlapping with the CO_2 features. Finally, by optimizing the reaction conditions, especially with contact time and fine-tuning the CO_2:H_2 ratio, highly sustainable activity can be achieved around 700 K. By optimizing the pressure to significantly higher levels, it is possible to obtain value-added liquid products as well. Indeed, Co_3O_4 catalyst has already been reported for the direct conversion of CO_2 to methanol, C2 and C3 products, but at high pressures (20 bar and above) [52]. We believe the information provided in this manuscript could be helpful for carbon–neutral economy or carbon-recycling aspects, and more work is desired in that direction. Highly selective CO formation, with or without H_2, could be utilized in the steel industry for steelmaking and to minimize emissions. It is also worth exploring the structure dependent activity of Co_3O_4, especially with different crystallographic facet(s), since there is a possibility to selectively produce one or fewer products.

Declaration of Competing Interest

The authors declare that they have no known competing financial interests or personal relationships that could have appeared to influence the work reported in this paper.

Table 1
Comparison of activity and sustainability reported for CO_2 reduction with different catalyst systems.

Catalyst	T/K	Pressure (bar), GHSV/WHSV/Feed Flow	CO_2:$H_2^{\#}$	CO_2 conv. (%)	CO Sel. (%)	CH_4 Sel. (%)	Sustainability aspects	Ref.
β-Mo_2C	723	1 bar, GHSV: 20,000 /h	1:3	56	61	5–9	Stable activity for 12 h	[42]
In_2O_3	873	1 bar, GHSV:15000 h^{-1}	1:3	49	85	15	Stable performance for 12 h	[43]
			3:2	24	98	2		
Ni-CeO_2	973	1 bar, flow:100 ml min^{-1}	1:1	40	100	0	TOS: N/A	[44]
$BaCe_{0.2}Zr_{0.6}Y_{0.16}Zn_{0.04}O_3$	873	1 bar, Flow: 20 ml/min	1:1	36.3	94	~5	Stable performance for 5 h	[45]
Pt- SiO_2	573	1 bar, WHSV: 119.7 h^{-1}	1:2	3.38	100	0	TOS: N/A	[46]
Pt-TiO_2		WHSV: 24.7 h^{-1}		4.51	99	1		
Cu/SiO_2	573	1 bar, WHSV: 4.32 h^{-1}	1:3	6	98	~2	Marginal decrease in activity in 2 h	[47]
Cu/CeO_2		and 1.08 h^{-1}		18	100	0		
$La_{0.75}Sr_{0.25}FeO_3$	823	1 bar.50 sccm (10% H_2 10% CO_2 v/v)	1:1 Bal. He	15.5	95	~3	TOS: 2.5 h. Stable activity for 2.5 h	[48]
Ni_3-Fe_3/ZrO_2	673	1 bar,40 ml/min,	1:2 Bal. Ar	38.8	12.9	87	Marginal decrease in activity in 14 h	[49]
In_2O_3	873	1 bar, 40 ml/min	1:1	29.63	N/A	N/A	TOS: N/A	[50]
Ga_2O_3				19.08				
Co_3O_4 NC	723	1 bar, GHSV:19200 h^{-1}	1:3	49.4	15	85	Stable performance for 12 h	Present work
			3:2	26.2	100	0		

Balance by N_2/He/Ar.

Data availability

Data will be made available on request.

Acknowledgement

RR, JT and NBM are thankful to DST-INSPIRE, CSIR, and UGC, New Delhi, respectively, for research fellowships.

Appendix A. Supplementary data

Supplementary data to this article can be found online at https://doi.org/10.1016/j.cej.2023.144459.

References

[1] H. Arakawa, M. Aresta, J.N. Armor, M.A. Barteau, E.J. Beckman, A.T. Bell, J. E. Bercaw, C. Creutz, E. Dinjus, D.A. Dixon, K. Domen, D.L. DuBois, J. Eckert, E. Fujita, D.H. Gibson, W.A. Goddard, D.W. Goodman, J. Keller, G.J. Kubas, H. H. Kung, J.E. Lyons, L.E. Manzer, T.J. Marks, K. Morokuma, K.M. Nicholas, R. Periana, L. Que, J. Rostrup-Nielson, W.M.H. Sachtler, L.D. Schmidt, A. Sen, G. A. Somorjai, P.C. Stair, B.R. Stults, W. Tumas, Catalysis research of relevance to carbon management: progress, challenges, and opportunities, Chem. Rev. 101 (2001) 953–996, https://doi.org/10.1021/cr000018s.

[2] N.S. Lewis, D.G. Nocera, Powering the planet: Chemical challenges in solar energy utilization, 103 (2006) 15729-15735. https://doi.org/doi:10.1073/pnas.0603395103.

[3] M. Aresta, A. Dibenedetto, Utilisation of CO_2 as a chemical feedstock: opportunities and challenges, Dalton Trans. 28 (2007) 2975–2992, https://doi.org/10.1039/B700658F.

[4] A.M. Appel, J.E. Bercaw, A.B. Bocarsly, H. Dobbek, D.L. DuBois, M. Dupuis, J. G. Ferry, E. Fujita, R. Hille, P.J.A. Kenis, C.A. Kerfeld, R.H. Morris, C.H.F. Peden, A. R. Portis, S.W. Ragsdale, T.B. Rauchfuss, J.N.H. Reek, L.C. Seefeldt, R.K. Thauer, G. L. Waldrop, Frontiers, opportunities, and challenges in biochemical and chemical catalysis of CO_2 fixation, Chem. Rev. 113 (2013) 6621–6658, https://doi.org/10.1021/cr300463y.

[5] M. Aresta, A. Dibenedetto, A. Angelini, Catalysis for the valorization of exhaust carbon: from CO_2 to chemicals, materials, and fuels. technological use of CO_2, Chem. Rev. 114 (2014) 1709–1742, https://doi.org/10.1021/cr4002758.

[6] W. Wang, S. Wang, X. Ma, J. Gong, Recent advances in catalytic hydrogenation of CO_2, Chem. Soc. Rev. 40 (2011) 3703–3727, https://doi.org/10.1039/C1CS15008A.

[7] H. Ohya, J. Fun, H. Kawamura, K. Itoh, H. Ohashi, M. Aihara, S. Tanisho, Y. Negishi, Methanation of carbon dioxide by using membrane reactor integrated with water vapor permselective membrane and its analysis, J. Membr. Sci. 131 (1997) 237–247, https://doi.org/10.1016/S0376-7388(97)00055-0.

[8] D. Kim, J. Resasco, Y. Yu, A.M. Asiri, P. Yang, Synergistic geometric and electronic effects for electrochemical reduction of carbon dioxide using gold–copper bimetallic nanoparticles, #4948, Nature Commun. 5 (2014), https://doi.org/10.1038/ncomms5948.

[9] W.-H. Wang, Y. Himeda, J.T. Muckerman, G.F. Manbeck, E. Fujita, CO_2 hydrogenation to formate and methanol as an alternative to photo- and electrochemical CO_2 reduction, Chem. Rev. 115 (2015) 12936–12973, https://doi.org/10.1021/acs.chemrev.5b00197.

[10] S. Nitopi, E. Bertheussen, S.B. Scott, X. Liu, A.K. Engstfeld, S. Horch, B. Seger, I.E. L. Stephens, K. Chan, C. Hahn, J.K. Nørskov, T.F. Jaramillo, I. Chorkendorff, Progress and perspectives of electrochemical CO_2 reduction on copper in aqueous electrolyte, Chem. Rev. 119 (2019) 7610–7672, https://doi.org/10.1021/acs.chemrev.8b00705.

[11] M.C.J. Bradford, M.A. Vannice, CO_2 reforming of CH_4, Catal. Rev. 41 (1999) 1–42, https://doi.org/10.1081/CR-100101948.

[12] K. An, G.A. Somorjai, Nanocatalysis I: synthesis of metal and bimetallic nanoparticles and porous oxides and their catalytic reaction studies, Catal. Lett. 145 (2015) 233–248, https://doi.org/10.1007/s10562-014-1399-x.

[13] G. Melaet, W.T. Ralston, C.-S. Li, S. Alayoglu, K. An, N. Musselwhite, B. Kalkan, G. A. Somorjai, Evidence of highly active cobalt oxide catalyst for the Fischer-Tropsch synthesis and CO_2 hydrogenation, J. Am. Chem. Soc. 136 (2014) 2260–2263, https://doi.org/10.1021/ja412447q.

[14] V. Iablokov, S.K. Beaumont, S. Alayoglu, V.V. Pushkarev, C. Specht, J. Gao, A. P. Alivisatos, N. Kruse, G.A. Somorjai, Size-controlled model Co nanoparticle catalysts for CO_2 hydrogenation: synthesis, characterization, and catalytic reactions, Nano Lett. 12 (2012) 3091–3096, https://doi.org/10.1021/nl300973b.

[15] J.P. den Breejen, P.B. Radstake, G.L. Bezemer, J.H. Bitter, V. Frøseth, A. Holmen, K. P. de Jong, On the origin of the cobalt particle size effects in Fischer−Tropsch catalysis, J. Am. Chem. Soc. 131 (2009) 7197–7203, https://doi.org/10.1021/ja901006x.

[16] Y. Zhu, S. Zhang, Y. Ye, X. Zhang, L. Wang, W. Zhu, F. Cheng, F. Tao, Catalytic conversion of carbon dioxide to methane on ruthenium-cobalt bimetallic nanocatalysts and correlation between surface chemistry of catalysts under reaction conditions and catalytic performances, ACS Catal. 2 (2012) 2403–2408, https://doi.org/10.1021/cs3005242.

[17] D.I. Enache, B. Rebours, M. Roy-Auberger, R. Revel, In situ XRD study of the influence of thermal treatment on the characteristics and the catalytic properties of cobalt-based Fischer-Tropsch catalysts, J. Catal 205 (2002) 346–353, https://doi.org/10.1006/jcat.2001.3462.

[18] W.K. Jozwiak, E. Szubiakiewicz, J. Góralski, A. Klonkowski, T. Paryjczak, Physico-chemical and catalytic study of the Co/SiO_2 catalysts, Kinet. Catal. 45 (2004) 247–255, https://doi.org/10.1023/B:KICA.0000023799.93711.58.

[19] J. Lahtinen, T. Anraku, G.A. Somorjai, C, CO and CO_2 hydrogenation on cobalt foil model catalysts: evidence for the need of CoO reduction, Catal. Lett. 25 (1994) 241–255, https://doi.org/10.1007/BF00816304.

[20] G.D. Weatherbee, C.H. Bartholomew, Hydrogenation of CO_2 on group VIII metals: II. Kinetics and mechanism of CO_2 hydrogenation on nickel, J. Catal. 77 (1982) 460–472, https://doi.org/10.1016/0021-9517(82)90186-5.

[21] S. Velu, K. Suzuki, C.S. Gopinath, H. Yoshida, T. Hattori, XPS, XANES and EXAFS investigations of CuO/ZnO/Al_2O_3/ZrO_2 mixed oxide catalysts, Phys. Chem. Chem. Phys. 4 (2002) 1990–1999, https://doi.org/10.1039/B109766K.

[22] M.S. Duyar, C. Tsai, J.L. Snider, J.A. Singh, A. Gallo, J.S. Yoo, A.J. Medford, F. Abild-Pedersen, F. Studt, J. Kibsgaard, S.F. Bent, J.K. Nørskov, T.F. Jaramillo, A highly active molybdenum phosphide catalyst for methanol synthesis from CO and CO_2, Angew. Chem. Int. Ed. 57 (2018) 15045–15050, https://doi.org/10.1002/anie.201806583.

[23] J.D. Jimenez, C. Wen, J. Lauterbach, Design of highly active cobalt catalysts for CO_2 hydrogenation via the tailoring of surface orientation of nanostructures, Catal. Sci. Tech. 9 (2019) 1970–1978, https://doi.org/10.1039/C9CY00402E.

[24] J. Jimenez, A. Bird, M. Santos Santiago, C. Wen, J. Lauterbach, Supported cobalt nanorod catalysts for carbon dioxide hydrogenation, Energy Tech. 5 (2017) 884–891, https://doi.org/10.1002/ente.201600575.

[25] I.H. Kim, H.O. Seo, E.J. Park, S.W. Han, Y.D. Kim, Low temperature CO oxidation over iron oxide nanoparticles decorating internal structures of a mesoporous alumina, Sci. Rep. 7 (2017) 40497, https://doi.org/10.1038/srep40497.

[26] J. Wu, C. Wen, X. Zou, J. Jimenez, J. Sun, Y. Xia, M.-T. Fonseca Rodrigues, S. Vinod, J. Zhong, N. Chopra, I.N. Odeh, G. Ding, J. Lauterbach, P.M. Ajayan, Carbon dioxide hydrogenation over a metal-free carbon-based catalyst, ACS Catal. 7 (2017) 4497–4503, https://doi.org/10.1021/acscatal.7b00729.

[27] S. Kattel, P. Liu, J.G. Chen, Tuning selectivity of CO_2 hydrogenation reactions at the metal/oxide interface, J. Am. Chem. Soc. 139 (2017) 9739–9754, https://doi.org/10.1021/jacs.7b05362.

[28] T. Fan, H. Liu, S. Shao, Y. Gong, G. Li, Z. Tang, Cobalt catalysts enable selective hydrogenation of CO_2 toward diverse products: Recent progress and perspective, J. Phys. Chem. Lett. 12 (2021) 10486–10496, https://doi.org/10.1021/acs.jpclett.1c03043.

[29] S. Navarro-Jaen, M. Virginie, I. Bonin, M. Robert, R. Wojcieszak, A.Y. Khodakov, Highlights and challenges in the selective reduction of carbon dioxide to methanol, Nature Chem. 5 (2021) 564–579, https://doi.org/10.1038/s41570-021-00289-y.

[30] M.T. Makhlouf, B.M. Abu-Zied, T.H. Mansoure, Nanocrystalline Co_3O_4 fabricated via the combustion method, Met. Mater. Int. 19 (2013) 489–495, https://doi.org/10.1007/s12540-013-3017-7.

[31] K. Roy, C.P. Vinod, C.S. Gopinath, Design and performance aspects of a custom-built ambient pressure photoelectron spectrometer toward bridging the pressure gap: oxidation of Cu, Ag, and Au surfaces at 1 mbar O_2 pressure, J. Phys. Chem. C 117 (2013) 4717–4726, https://doi.org/10.1021/jp312706s.

[32] K. Roy, C.S. Gopinath, UV Photoelectron spectroscopy at near ambient pressures: mapping valence band electronic structure changes from Cu to CuO, Anal. Chem. 86 (2014) 3683–3687, https://doi.org/10.1021/ac4041026.

[33] G. Zhou, T. Wu, H. Xie, X. Zheng, Effects of structure on the carbon dioxide methanation performance of Co-based catalysts, Int. J. Hydrogen Energy 38 (2013) 10012–10018, https://doi.org/10.1016/j.ijhydene.2013.05.130.

[34] B.A. Sexton, A.E. Hughes, T.W. Turney, An XPS and TPR study of the reduction of promoted cobalt-kieselguhr Fischer-Tropsch catalysts, J. Catal. 97 (1986) 390–406, https://doi.org/10.1016/0021-9517(86)90011-4.

[35] R. Shi, G. Chen, W. Ma, D. Zhang, G. Qiu, X. Liu, Shape-controlled synthesis and characterization of cobalt oxides hollow spheres and octahedra, Dalton Trans. 41 (2012) 5981–5987, https://doi.org/10.1039/C2DT12403C.

[36] L.F. Liotta, G. Di Carlo, G. Pantaleo, A.M. Venezia, G. Deganello, Co_3O_4/CeO_2 composite oxides for methane emissions abatement: Relationship between Co_3O_4–CeO_2 interaction and catalytic activity, Appl. Catal. B: Environ. 66 (2006) 217–227, https://doi.org/10.1016/j.apcatb.2006.03.018.

[37] M.C. Biesinger, B.P. Payne, A.P. Grosvenor, L.W.M. Lau, A.R. Gerson, R.S.C. Smart, Resolving surface chemical states in XPS analysis of first row transition metals, oxides and hydroxides: Cr, Mn, Fe, Co and Ni, Appl. Surf. Sci. 257 (2011) 2717–2730, https://doi.org/10.1016/j.apsusc.2010.10.051.

[38] T. Mathew, N.R. Shiju, K. Sreekumar, B.S. Rao, C.S. Gopinath, Cu–Co synergism in $Cu_{1-x}Co_xFe_2O_4$—catalysis and XPS aspects, J. Catal. 210 (2002) 405–417, https://doi.org/10.1006/jcat.2002.3712.

[39] A. Dubey, K.P. Reddy, C.S. Gopinath, Ambient CO oxidation on in-situ generated Co3O4 spinel surfaces with random morphology, ChemSel 2 (2017) 533–536, https://doi.org/10.1002/slct.201602010.

[40] K.P. Reddy, R. Jain, M.K. Ghosalya, C.S. Gopinath, Metallic cobalt to spinel Co_3O_4—electronic structure evolution by near-ambient pressure photoelectron spectroscopy, J. Phys. Chem. C 121 (2017) 21472–21481, https://doi.org/10.1021/acs.jpcc.7b06661.

[41] N.A.M. Barakat, M.S. Khil, F.A. Sheikh, H.Y. Kim, Synthesis and optical properties of two cobalt oxides (CoO and Co_3O_4) nanofibers produced by electrospinning process, J. Phys. Chem. C 112 (2008) 12225–12233, https://doi.org/10.1021/jp8027353.

[42] K.P. Reddy, S. Dama, N.B. Mhamane, M.K. Ghosalya, T. Raja, C.V. Satyanarayana, C.S. Gopinath, Molybdenum carbide catalyst for the reduction of CO_2 to CO: surface science aspects by NAPPES and catalysis studies, Dalton Trans. 48 (2019) 12199–12209, https://doi.org/10.1039/C9DT01774G.

[43] N.B. Mhamane, S. Chetry, R. Ranjan, T. Raja, C.S. Gopinath, Sustainable CO_2 reduction on In2O3 with exclusive CO selectivity: catalysis and in situ valence band photoelectron spectral investigations, ACS Sus. Chem. Engn. 10 (2022) 3521–3531, https://doi.org/10.1021/acssuschemeng.1c07897.

[44] L. Wang, H. Liu, Y. Liu, Y. Chen, S. Yang, Effect of precipitants on Ni-CeO_2 catalysts prepared by a co-precipitation method for the reverse water-gas shift reaction, J. Rare Earths 31 (2013) 969–974, https://doi.org/10.1016/S1002-0721(13)60014-9.

[45] D.H. Kim, J.L. Park, E.J. Park, Y.D. Kim, S. Uhm, Dopant Effect of Barium Zirconate-Based Perovskite-Type Catalysts for the Intermediate-Temperature Reverse Water Gas Shift Reaction, ACS Catal. 4 (2014) 3117–3122, https://doi.org/10.1021/cs500476e.

[46] S. Kattel, B. Yan, J.G. Chen, P. Liu, CO_2 hydrogenation on Pt, Pt/SiO2 and Pt/TiO2: Importance of synergy between Pt and oxide support, J. Catal. 343 (2016) 115–126, https://doi.org/10.1016/j.jcat.2015.12.019.

[47] S.-C. Yang, S.H. Pang, T.P. Sulmonetti, W.-N. Su, J.-F. Lee, B.-J. Hwang, C. W. Jones, Synergy between Ceria Oxygen Vacancies and Cu Nanoparticles Facilitates the Catalytic Conversion of CO_2 to CO under Mild Conditions, ACS Catal. 8 (2018) 12056–12066, https://doi.org/10.1021/acscatal.8b04219.

[48] Y.A. Daza, J.N. Kuhn, CO_2 conversion by reverse water gas shift catalysis: comparison of catalysts, mechanisms and their consequences for CO_2 conversion to liquid fuels, RSC Adv. 6 (2016) 49675–49691, https://doi.org/10.1039/C6RA05414E.

[49] B. Yan, B. Zhao, S. Kattel, Q. Wu, S. Yao, D. Su, J.G. Chen, Tuning CO_2 hydrogenation selectivity via metal-oxide interfacial sites, J. Catal. 374 (2019) 60–71, https://doi.org/10.1016/j.jcat.2019.04.036.

[50] Q. Sun, J. Ye, C.-J. Liu, Q. Ge, In2O3 as a promising catalyst for CO_2 utilization: A case study with reverse water gas shift over In_2O_3, Greenhouse Gases: Sci. Tech. 4 (2014) 140–144, https://doi.org/10.1002/ghg.1401.

[51] R. Jain, C.S. Gopinath, New strategy toward a dual functional nanocatalyst at ambient conditions: influence of the Pd–Co interface in the catalytic activity of Pd@Co core-shell nanoparticles, ACS Appl. Mater. Interfaces 10 (2018) 41268–41278, https://doi.org/10.1021/acsami.8b12940.

[52] I.C.T. Have, J.J.G. Kromwijk, M. Monai, D. Ferri, E.B. Sterk, F. Meirer, B. M. Weckhuysen, Uncovering the reaction mechanism behind CoO as active phase for CO_2 hydrogenation, Nat. Commun. 13 (1) (2022), https://doi.org/10.1038/s41467-022-27981-x.